Charles University

Faculty of Mathematics and Physics

DOCTORAL THESIS

2023

Miłosz Wcisło

FACULTY OF MATHEMATICS AND PHYSICS
Charles University

DOCTORAL THESIS

Miłosz Wcisło

Seismic waves in inhomogeneous, weakly dissipative, anisotropic media

Department of Geophysics

Supervisor of the doctoral thesis: RNDr. Ivan Pšenčík, CSc

Study programme: Physics

Specialization: Geophysics

Prague 2023

In Prague 25.05.2023   Miłosz Wcisło

I would like to express my deep gratitude for the help and guidance provided by Ivan Pšenčík during my doctoral studies. His insistence on maintaining the highest standards and his transfer of valuable knowledge have greatly benefited me throughout the course of my studies. I am confident that the lessons and guidance I received from Ivan will yield fruitful results in the future.

Title: Seismic waves in inhomogeneous, weakly dissipative, anisotropic media

Author: Mgr. Miłosz Wcisło

Department: Department of Geophysics

Supervisor of the doctoral thesis: RNDr. Ivan Pšenčík, CSc

Abstract:

The thesis consists of two parts: theoretical and part devoted to applications. In the theoretical part, it is shown that the so-called Weak Attenuation Concept (WAC), in which attenuation is considered as a perturbation of a reference elastic state, guarantees applicability of the ray method to most models of realistic, laterally varying layered, isotropic or anisotropic attenuative media. This conclusion follows from comparisons of ray results with an independent full-wave method, which is, unfortunately, applicable only to isotropic media. Another important finding is that the so-called correspondence principle, broadly used in studies of attenuative media, must be used with care because in some situations, it may lead to incorrect results. In the part devoted to applications, the important results are presentations of successful applications of the peak-frequency method. The method is shown to be a useful tool in studying attenuation using microseismic events. It allows relatively simple estimate of the so-called global attenuation factor t^*, from which estimates of attenuation can be made. In general, estimated values of t^* can be used for attenuation tomography which can be done using similar principles as in the tomography of seismic velocities. The peak-frequency method is mostly used in the thesis to estimate effective Q values over a studied region. The presented results indicate that the analysis of peak frequencies can be useful in studies of source properties as well, particularly in studies of source directivity due to direction of rupture propagation. The analysis of peak frequencies is performed using datasets collected in three different regions of the world. One dataset is taken from western Bohemia, where it was recorded during one of the frequently observed natural earthquake swarms. Another dataset comes from Italy from the region with intensive microseismicity caused by the wastewater injection. The last dataset comes from

China from the region with microseismicity caused by hydraulic stimulation of shales. All the above results, both theoretical and observational, form a useful base for further more detailed studies.

Název: Seismické vlny v nehomogenních, slabě absorbujících, anizotropních prostředích

Autor: Mgr. Miłosz Wcisło

Katedra: Katedra geofyziky

Vedoucí disertační práce: RNDr. Ivan Pšenčík, CSc

Abstrakt:

Disertace má dvě části, teoretickou a aplikační. V teoretické části je ukázáno, že použití tzv. konceptu slabého útlumu (WAC), ve kterém se útlum považuje za perturbaci referenčního elastického stavu, zaručuje použitelnost paprskové teorie pro většinu modelů realistických, laterálně nehomogenních, vrstevnatých, izotropních nebo anizotropních absorbujících prostředí. Tento závěr vyplývá ze srovnání výsledků paprskových výpočtů s výsledky přesnější vlnové metody, která je, bohužel, použitelná jen v izotropních prostředích. Jiné důležité zjištění je, že tzv. korespondenční princip, široce užívaný při studiích absorbujících prostředí, musí být používán opatrně, protože v některých případech může jeho užití vést k nesprávným výsledkům. Důležité výsledky aplikační části disertace jsou úspěšné aplikace přístupu nazvaného "peak-frequency" metoda. Ukazuje se, že tato metoda je vhodná zejména při studiu mikroseismických jevů. Metoda umožňuje relativně jednoduché určení tzv. faktoru globálního útlumu t^*, z kterého je možné určit míru útlumu studovaného prostředí. V principu by bylo možné použít t^* pro určení rozložení útlumu jako se používají časy šíření v tomografických studiích pro určení rozložení seismických rychlostí. V disertaci je ale "peak-frequency" metoda užita většinou pro určení efektivní hodnoty útlumu charakterizující celou studovanou oblast. Uvedené výsledky naznačují, že "peak-frequency" metoda může být také užitečná při studiu směrovosti seismického zdroje způsobené šířením trhliny podél zlomu. Metoda "peak-frequency" je použita na data získaná na třech různých místech světa. Jedna datová sada pochází ze západních Čech, kde byla získána během jednoho z častých zemětřesných rojů. Jiná pochází z Itálie, z oblasti zvýšené mikroseismicity způsobené vstřikováním odpadních vod při těžbě ropy do země. Poslední data pochází z Číny, z

oblasti s mikroseismicitou způsobenou hydraulickým štěpením při získávání plynu z břidlic. Všechny výše popsané výsledky, teoretické i z aplikací, představují užitečný základ pro další, detailnejsi studia.

Klíčová slova:

Útlum, Koncept Slabého Útlumu, Paprsková Metoda, Anizotropie, Frekvence, Směrovost Zdroje

Contents

Introduction

Seismic waves provide valuable information about the source and the medium between the source and receiver. They provide insight into the Earth at different scales. The strongest natural sources, such as earthquakes with high magnitudes, allow us studying the general structure of the Earth. Weaker earthquakes enable study of regional structures and are typically used to study the properties of the upper mantle and, in particular, the Earth's crust. More detailed studies on a smaller scale can be conducted using microseismicity, understood here as small earthquakes with moment magnitude M_W less than 3. Microseismic events occur commonly in all seismically active regions. With the rise of non-conventional oil and gas extraction from, often strongly anisotropic shale reservoirs, microseismic data related to induced seismicity are becoming more common. Besides the use of typical surface arrays, borehole arrays are often used in studies involving induced microseismicity as well. This enables recording of microearthquakes with magnitudes $M_W<0$.

The frequency range of waves generated by natural and induced microseismicity is broad. The dominant frequencies of these waves are in the range of tens, or even hundreds of Hertz (in case of events that we can detect using arrays placed inside boreholes), much higher than dominant frequencies of waves excited by large earthquakes. When working with waves dominated by high frequencies, we need to put an emphasis on analysis of anelastic (intrinsic, not caused by scattering) seismic attenuation, which is not so significant factor in studies of large earthquakes. Attenuation reduces high frequencies faster than low frequencies. We should also note that the upper crust, where small sources detectable at the surface are placed, is characterized by stronger attenuation than the deep crust. Strong effects of attenuation on high frequencies provide an opportunity for a more detailed description of attenuation as a property of a medium, e.g., by analysis of the dominant/peak frequencies of waves. Regions, where stronger seismic attenuation is found are commonly used as indicators of the presence of saturated rocks. This is

important, for example, in industrial seismic studies related to the exploration for oil and gas, but also in studies concerning geothermal energy.

Wavefields can be modelled using ray method. Given that ray method is a high- frequency approximation, it can be very suitable to use it in studies connected to natural and induced microseismicity. The strength of attenuation inside Earth crust is of magnitude that allows to consider attenuation as perturbation of elasticity. Therefore, we can apply so-called Weak Attenuation Concept (WAC) to existing ray codes to allow calculation of wavefields in inhomogeneous, anisotropic and attenuative media. Application of WAC allows working with real rays, which is much simpler than working with complex rays. We demonstrate, that the attenuation effects on reflection/transmission coefficients are not negligible only in the critical region, where ray method does not provide accurate results, and is thus inapplicable anyway. Nevertheless, we provide approximate formula that allows computation of reflection/transmission coefficients of SH-SH waves at the interface between isotropic, attenuative media. Application of WAC allows the use of high-frequency methods for relatively accurate computations of wave propagation in layered media. Without great efforts, a similar procedure as used for the calculation of SH-SH coefficients, can be applied to more complex situations including interfaces between anisotropic media. Currently there is a limited body of research, which presents attenuation anisotropy in media through real datasets. Theoretical studies can provide useful insight for further studies concerning real media. Highly anisotropic shales could likely be the object of this type of analysis.

The main part of the presented doctoral thesis (Chapters 1 to 6) is based on material published in five out of ten peer-reviewed articles that I authored or co-authored during my studies. In addition, it includes material from articles in three reports of the Seismic Waves in Complex 3-D Structures consortium.

In Chapter 1, we describe the application of the Weak Attenuation Concept in smooth media. We implement WAC in the program package ANRAY, which now allows the calculation of ray synthetic seismograms of waves propagating in layered, attenuative, isotropic, and anisotropic media. In Chapter 1, we study the effects of attenuation on waves propagating in isotropic and anisotropic models of smooth

attenuative media, and show that the WAC can be applied even if media are characterized by relatively low, in Earth's crust context, value of Q. We also discuss how waves are affected by attenuation in different frequency-dependent attenuation models and speculate on how anisotropy of attenuation can affect the results of inversion for the seismic source parameters.

In Chapter 2, we discuss the effects of attenuation on reflection/transmission process. For better insight, we implemented the WAC to the simplest case of reflection/transmission, SH-SH wave, at the interface between two isotropic media. The application of the Weak Attenuation Concept to this problem indicates that the correspondence principle may fail for overcritical incidence. Despite this, we provide working formulae for the reflection/transmission coefficients that deliver satisfactory results in both sub- and overcritical region. The formulae are implemented in the SEIS program package, which, after modification, allows the computation of SH-wave ray synthetic seismograms in 2D isotropic, layered, inhomogeneous and attenuative media. We analyze the results provided by SEIS and benchmark them with independent full-wave method. The comparison shows that the effects of attenuation on the reflection/transmission process are small when compared with effects inside layers, and the only region where they can noticeably affect reflected/transmitted waves is the vicinity of the critical incidence where the ray theory provides unreliable results anyway.

In Chapter 3, we introduce the peak-frequency method, which allows the estimation of the global absorption factor t^* and from it a Q factor of the medium using P- and S-waves excited by microseismic events. We describe how the method should be applied and what its limitations are. We briefly discuss how more detailed studies of the attenuation of media, such as tomography and measurement of Q in the source area, could be performed.

In Chapter 4 we show the application of the peak-frequency method to the data of the 2008 seismic swarm that took place in West Bohemia, one of the few seismically active regions in the Czech Republic. We show that the peak-frequency method can be successfully applied and can provide detailed insight that allows a discussion of possible temporal changes of attenuation related to upper mantle/deep

crust fluids that are likely causing the swarms. We also perform a measurement of the attenuation in the source area, which indicates that the focal zone is more attenuative than the surrounding medium.

In Chapter 5, we show the application of the peak-frequency method to the dataset from the High Agri Valley, located in southern Italy. Microseismicity in this region is induced by the injection of the wastewater that is produced during the oil extraction back to the reservoir. Analysis of attenuation reveals an attenuation anomaly in the vicinity of the injection well. The attenuation anomaly correlates with the anomaly of the V_P/V_S that we analyzed as well. We show that the V_P/V_S anomaly is affected by the temporal parameters of the injection. At the same time, we conclude that most likely, the discovered anomaly is at least partially a result of differences in rock properties above the reservoir.

In Chapter 6 we analyze peak frequencies from dataset recorded during hydraulic stimulation of shales in northern China. The study reveals that the measured peak frequencies are not only controlled by attenuation but also by the source effects. The distribution of peak frequencies is analyzed to reveal the source directivity of the event. The source mechanism of the event is estimated and represents a starting point for performing a modeling that includes parameters such as rupture duration, rupture direction, and attenuation of the medium. This allows the identification of the true fault plane of the event and other properties of the source. A simple correction for the directivity effects on amplitudes used for mechanism inversion is proposed. The analysis of the peak frequencies, treated as a proxy for the frequency content of waves, is shown to be more beneficial in the studies of the source-directivity of small events than the analysis of amplitudes.

The thesis is closed with brief conclusions drawn from the results presented in the dissertation.

List of publications that form a basis of the dissertation:

Wcisło, M. and Pšenčík, I. (2017). Seismic waves in inhomogeneous, weakly dissipative, anisotropic media; preliminary tests with P waves, *Seismic Waves in Complex 3-D Structures*, 27, 83-92.

Wcisło, M. (2018). Effects of attenuation, velocity and density on SH-wave reflection/transmission coefficients in isotropic, weakly attenuating media, *Seismic Waves in Complex 3-D Structures*, 28, 135-168.

Wcisło, M., L. Eisner, J. Málek, T. Fischer, J. Vlček, and G. Kletetschka (2018). Attenuation in West Bohemia: Evidence of high attenuation in the Nový Kostel focal zone and temporal change consistent with CO2 degassing, *Bulletin of Seismological Society of America*, 108(1), 450–458, doi: 10.1785/0120180143.

Wcisło, M., Stabile, T.A., Telesca, L. and Eisner, L. (2018). Variations of attenuation and VP/VS ratio in the vicinity of wastewater injection: a case study of Costa Molina 2 well (High Agri Valley, Italy), *Geophysics*, 83(2), B25-B31, doi: 10.1190/geo2017-0123.1.

Wcisło, M., Eisner, L., Málek, L., Fischer, T., Vlček, J. and Kletetschka, G. (2020). Reply to "Comment on 'Attenuation in West Bohemia: Evidence of High Attenuation in the Nový Kostel Focal Zone and Temporal Change Consistent with CO2 Degassing' by M. Wcisło, L. Eisner, J. Málek, T. Fischer, J. Vlček, and G. Kletetschka" by Morozov, *Bulletin of Seismological Society of America,* 110 (1), 375–380, doi: 10.1785/0120190100.

Pšenčík, I., **Wcisło, M.** and Daley, P.F. (2021). SH plane-wave reflection/transmission coefficients in isotropic, attenuating media, *Journal of Seismology*, 26, 15-34, doi: 10.1007/s10950-021-10052-x.

Pšenčík, I. and **Wcisło, M.** (2022) Comparison of ray and full-wave synthetic seismograms of reflected SH waves in attenuating media, *Seismic Waves in Complex 3-D Structures*, 31, 83-92.

Wcisło, M., Staněk, F., Gallovič, F., Wu, S. and Pšenčík, I. (2023). Induced Microseismic Event with Strong Rupture Directivity and Superimposed Attenuation Effects, Seismological Research Letters, 94(3), 1455-1466, doi: 10.1785/0220220229.

Chapter 1

Attenuation in smooth media

1.1 Weak attenuation concept in smooth media

In elastodynamic theory, properties of an elastic, anisotropic medium are described by the stiffness tensor c_{ijkl} and the density ρ. The so-called density-normalized stiffness tensor $a_{ijkl} = c_{ijkl}/\rho$ is frequently used as well. The stiffness tensor consists of 81 elements, but due to symmetries of the tensor, only 21 elements are independent (Aki and Richards, 2002). For study of seismic wave propagation in attenuative media, the so-called correspondence principle is often used, according to which a real-valued stiffness tensor is replaced by complex-valued counterpart: $c_{ijkl} = c_{ijkl}^{R} + ic_{ijkl}^{I}$, see, for example, Bland (1960), Carcione (2014), Borcherdt (2020). It means that in order to describe wave propagation using ray theory, one should work with complex rays. Use of complex rays is, however, complicated. Complex rays were used in a limited number of cases, see, e.g., Einziger and Felsen (1982), Thomson (1997). For media with formally weak attenuation, i.e., for media with quality factor Q>>1, which includes most media encountered in seismic practice, Kravtsov & Orlov, (1990) proposed to treat attenuation as a perturbation of an elastic state. This approximation is also sometimes referred to as Weak Attenuation Concept (WAC). Moczo et al. (1987) and Gajewski & Pšenčík (1992) applied the proposed WAC successfully to laterally varying isotropic and anisotropic attenuative media. Let's note, that the effects of attenuation on reflection/transmission at the interface between the layers within the framework of the WAC were ignored in their studies. Basic idea of the WAC (for more details, see Kravtsov & Orlov, 1990 or Červený, 2001) is assumption that imaginary parts of the complex-valued density-normalized stiffness tensor are considerably smaller than their real parts:

$$a_{ijkl}^{I} \ll a_{ijkl}^{R}. \tag{1.1}$$

It means that attenuation can be considered as a perturbation of the reference elastic case. The perturbation a_{ijkl}^I generates perturbation $i\tau^I$ of real valued traveltimes τ^R. The imaginary perturbation term affects the amplitudes, while the ray tracing and ray traveltimes τ^R remain real and the same as in the reference elastic case, thus avoiding complicating complex-valued ray tracing. In WAC, the i-th component of the displacement vector $\mathbf{u}(\mathbf{x}, \mathbf{t})$ of the elastodynamic equation in the zero-order ray approximation WAC reads:

$$u_i(x_j, t) = U_i(x_j)\exp\{-i\omega[t - \tau^R(x_j) - i\tau^I(x_j)]\}. \tag{1.2}$$

$u(x_j)$ is the i-th component of the amplitude vector, ω is circular frequency, τ^R is traveltime, and $i\tau^I$ is traveltime perturbation. Perturbation method for anisotropic, attenuative media (Jech and Pšenčík, 1989; Gajewski & Pšenčík, 1992) provides the first order perturbation formula for complex traveltime $\tau^R + i\tau^I$ along the ray in the reference elastic medium:

$$\tau^R(x_j) + i\tau^I(x_j) = \int_{\tau_0}^{\tau}(1 + \frac{1}{2}ia_{ijkl}^I p_i p_l g_j g_k)d\tau^R. \tag{1.3}$$

In equation (1.3), p and g are slowness and polarization vectors of propagating wave, τ_0 is the initial time and τ is the arrival time. Perturbations of traveltime may be also expressed in terms of perturbations of ray velocity. Let's consider complex ray velocity v of an anelastic medium: $v = v^R - iv^I$, with small imaginary part v^I. Then $\tau^R + i\tau^I$ equals:

$$\tau^R(x_j) + i\tau^I(x_j) = \int_{\tau_0}^{\tau}(1 + i\frac{v^I}{v^R})d\tau^R. \tag{1.4}$$

Let us introduce the approximate (neglecting higher-order terms) relation between complex ray velocity v and quality factor Q introduced by e.g. Aki & Richards (2002):

$$v = v^R - iv^I = v^R[1 - \frac{i}{2}Q^{-1}]. \tag{1.5}$$

From (1.3), (1.4) and (1.5) we arrive to:

$$Q^{-1} = a_{ijkl}^I p_i p_l g_j g_k \tag{1.6}$$

Behavior of quality factor Q in eq. (1.6) is generally anisotropic. Therefore, Q depends on the direction of propagation of the seismic wave. Isotropic attenuation is obtained if the imaginary part of the a_{ijkl} tensor is linearly scaled in regard to its real counterpart:

$$a_{ijkl}^{I} = c a_{ijkl}^{R}, \qquad\qquad (1.7)$$

with constant c equal to Q^{-1}. From equations (1.2-1.4) and (1.6), the i-th component of displacement vector of a wave propagating in an attenuating, inhomogeneous, anisotropic medium reads:

$$u_i(x_j, t) = U_i(x_j) \exp\{-i\omega[t - \tau^R(x_j)] - \tfrac{1}{2}\omega t^*(x_j)\}. \qquad (1.8)$$

Here t^* is the so-called global absorption factor that describes accumulated attenuation along the ray path:

$$t^*(x_j) = 2\tau^I(x_j) = \int_{\tau_0}^{\tau} a_{ijkl}^{I}(x_j) p_i p_l g_j g_k d\tau^R = \int_{\tau_0}^{\tau} \frac{d\tau^R}{Q(x_j)}. \qquad (1.9)$$

The factor t^* is computed by quadratures along a real valued ray in the elastic reference medium.

Frequency-independent a_{ijkl} does not preserve the causality of a wave i.e. the calculated waveform begins before the actual arrival of a wave, which implies that frequency independent dispersion model is not self-consistent. In order to obtain causal waves, frequency-dependent $a_{ijkl}(\omega)$ has to be used. The most commonly used model in seismology and seismic data processing is the Futterman model (Futterman, 1962). First order approximation of the velocity in Futterman model reads:

$$v(\omega) = v(\omega_r)[1 + \frac{1}{\pi Q(\omega_r)} \ln\left(\frac{\omega}{\omega_r}\right) + \frac{i}{2Q(\omega_r)}] . \qquad (1.10)$$

Here ω_r is the reference frequency. The ray displacement vector in the Futterman model reads:

$$u_i(x_j, t) = U_i(x_j) \exp\{-i\omega\left[t - \tau^R(x_j) + \frac{t^*}{\pi}\ln\frac{\omega}{\omega_r}\right] - \tfrac{1}{2}\omega t^*(x_j)\}. \qquad (1.11)$$

As earlier noted, the real part of the perturbation term in the exponent – in Futterman model - $\frac{t^*}{\pi}\ln\frac{\omega}{\omega_r}$ controls the arrival time of a particular frequency component of a wave. In the Futterman model, the phase velocity at frequencies above the ω_r is greater than at frequencies below ω_r. Therefore, the arrival of calculated wave can start at an earlier time than the ray time computed at the reference frequency. The arrival time is strictly connected to velocity at given frequency.

1.2 Implementation of the WAC in the ANRAY program package

The above described theory was implemented to the ANRAY program package (Gajewski & Pšenčík, 1987, 1990). ANRAY package is designed to compute traveltimes, ray amplitudes, and ray synthetic seismograms in 3D layered models with isotropic and anisotropic layers of arbitrary anisotropy. The code can be used in the intial-value as well as two-point ray tracing mode. The key step in the modification was implementing computation of t^* along the ray as defined in eq. (1.9). After modification (Wcisło and Pšenčík, 2017), ANRAY package allows to calculate ray synthetic seismograms of waves propagating in smooth, laterally varying, attenuative, isotropic and anisotropic media.

1.2.1 Isotropic attenuation

Below we use synthetic seismograms computed with the modified ANRAY program package to illustrate how attenuation affects waves and compare them with results obtained in elastic reference media. For tests, we use the configuration shown in Figure 1.1.
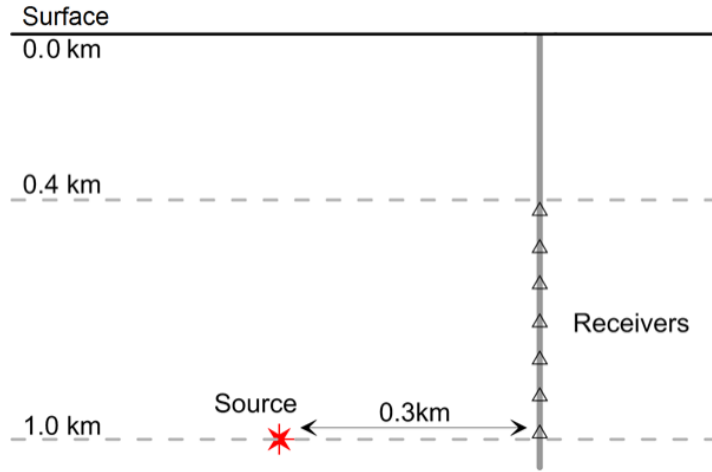
Figure 1.1. Configuration used in the calculation of synthetic seismograms shown in Figs 1.2-1.5. Spacing between receivers is equal 0.05km.

Similar configuration is often encountered during the borehole monitoring of induced seismicity caused by hydraulic stimulation. 13 receivers are placed in the vertical borehole with the upper-most receiver at the depth of 0.4km, with a step between receivers equal to 0.05km. Explosive source is located at the same depth as the deepest receiver of the array – at 1km. The horizontal distance of the source from the borehole is 0.3km. Müller (Fuchs and Müller, 1971) signal with prevailing frequency of 100 Hz and 2 maxima is used as the source-time function. Models used for tests are vertically inhomogeneous and transversely isotropic with vertical axis of symmetry (VTI). To compute synthetic seismograms, we use Futterman dispersion formula (1.10) with reference frequency ω_r equal to 100 Hz. Non-zero elements of the real-value density-normalized stiffness tensors (measured in km^{2}s^{-2}), in Voigt notation and at the reference frequency ω_r are:

at the surface: a_{11}^R=11.56, a_{33}^R=8.25, a_{13}^R=2.13, a_{44}^R=4.00, a_{66}^R=5.60;

at the 2 km depth: a_{11}^R=16.64, a_{33}^R=11.89, a_{13}^R=3.074, a_{44}^R=5.76, a_{66}^R=8.064.

Both sets of parameters describe VTI medium with anisotropy strength ~20%. Density-normalized parameters inside layers are determined by a vertical linear interpolation between interfaces. As a result, a medium with a vertical gradient is obtained. Seismograms are calculated for four different values of isotropic Q, see equation (1.7), equal 200, 100, 50 and 25. The imaginary counterparts of real-valued Voigt parameters listed above, for Q=100 are:

11

at the surface: a_{11}^I=0.1156, a_{33}^I=0.0825, a_{13}^I=0.0213, a_{44}^I=0.040, a_{66}^I=0.056;

at 2 km depth: a_{11}^I=0.1664, a_{33}^I=0.1189, a_{13}^I=0.0307, a_{44}^I=0.0576, a_{66}^I=0.0806.

Figures 1.2-1.5 show radial and vertical components (transverse component is zero) of the P-wave displacement vector for models computed in vertically inhomogeneous VTI media with varying strength of attenuation. Figures include as well results obtained for elastic refence model ($Q=\infty$). In Figures 1.2 and 1.3, we include seismograms with Q=200 and 50; in Figures 1.4 and 1.5, Q=100 and 25. The same amplitude scaling is used for all plots. Note that in our calculations we neglect the effects of the anisotropy on the point-source radiation (Shekar and Tsvankin, 2014). From Figures 1.2-1.5, we see that attenuation substantially affects amplitudes of obtained seismograms. For example, the maximum amplitude of the radial component for the set corresponding to Q=25 is 2.7 times smaller than for the elastic case. The relative difference between elastic and anelastic cases increases with distance as traveltime and t^* increase. Due to velocity varying with frequency in Futterman dispersion model, arrival times of waves change slightly too. Furthermore, waveforms change with increasing t^* as well - the waves are prolongated and loose the sinusoidal shape of the source signal, and become asymmetric.

To better illustrate how attenuation affects the waveform, we show waves computed in models with different Q in Figure 1.6. The maximum amplitudes of presented waves are normalized to the size of the frame, which makes the comparison of waveforms easier. From eq. (1.11), we see that in Futterman model the factors influencing the waveform are traveltime t and t^*. The top plot in Figure 1.6 shows computed wave which propagated through an elastic medium (infinite Q, t^*=0) for 0.25s. The waveform is the same as at the source. Then we show results for Q=100 (t^*=0.0025) and Q=50 (t^*=0.005) calculated using Futterman model. We clearly see that the waveform computed in medium with lower Q is longer, with greater difference between maxima. In Figure 1.6, we also include the seismograms computed using frequency-independent complex velocity (non-causal attenuation, grey curves). The non-causal attenuation results in elongation of the waveform and earlier arrival of the wave, albeit not due to changes of velocity at given frequency (therefore the arrival is no causal). The waveform keeps being symmetric.

Figure 1.2. Synthetic seismograms (radial component) at receivers from the configuration shown in Figure 1.1 in the model of vertically inhomogeneous VTI medium with isotropic Q. Green - elastic case, red - Q=200, black – Q=50.

Figure 1.3. Synthetic seismograms (vertical component) at receivers from the configuration shown in Figure 1.1 in the model of vertically inhomogeneous VTI medium with isotropic Q. Green - elastic case, red - Q=200, black – Q=50. Amplitudes are doubled with respect to Fig. 1.2.

13

Figure 1.4. Synthetic seismograms (radial component) at receivers from the configuration shown in Figure 1.1 in the model of vertically inhomogeneous VTI medium with isotropic Q. Green - elastic case, red - Q=100, black – Q=25.
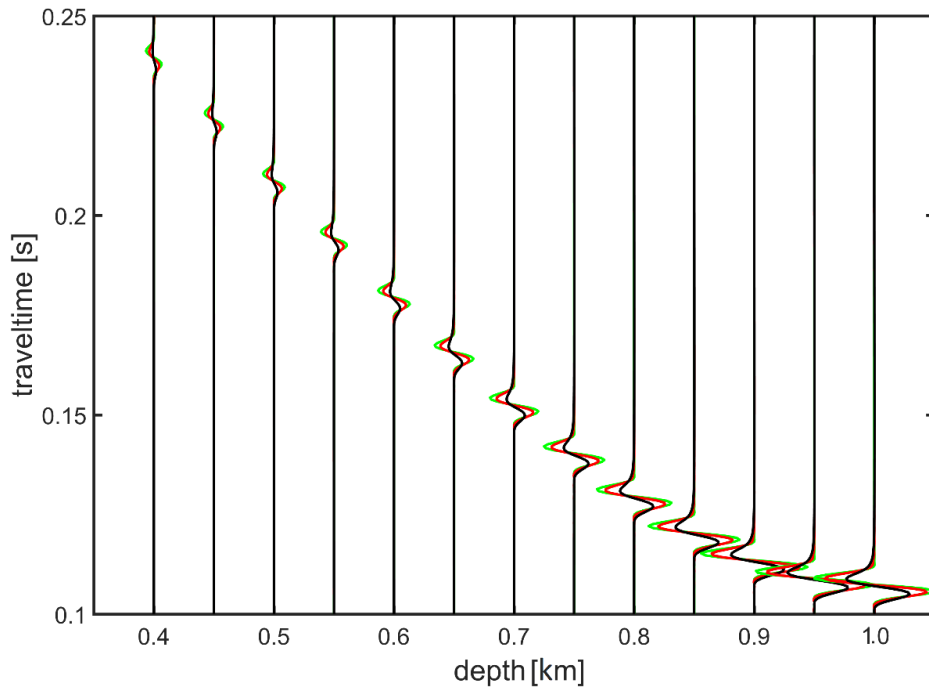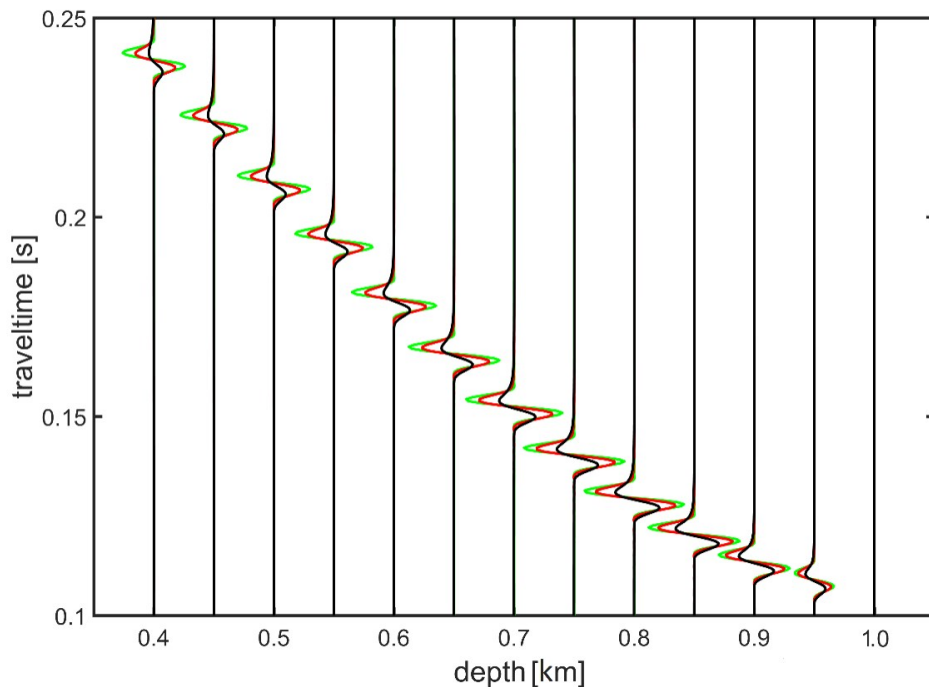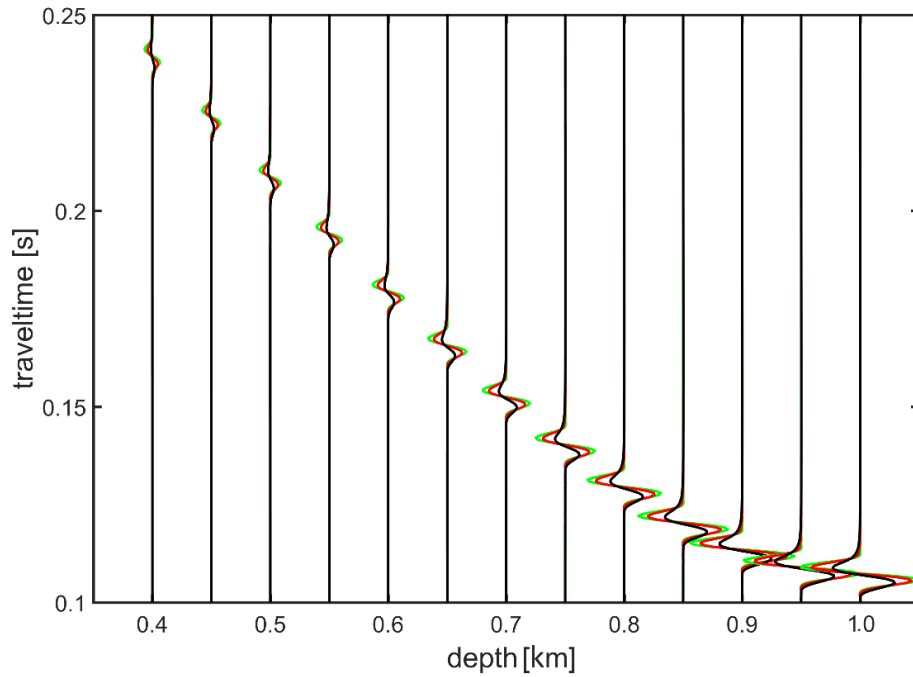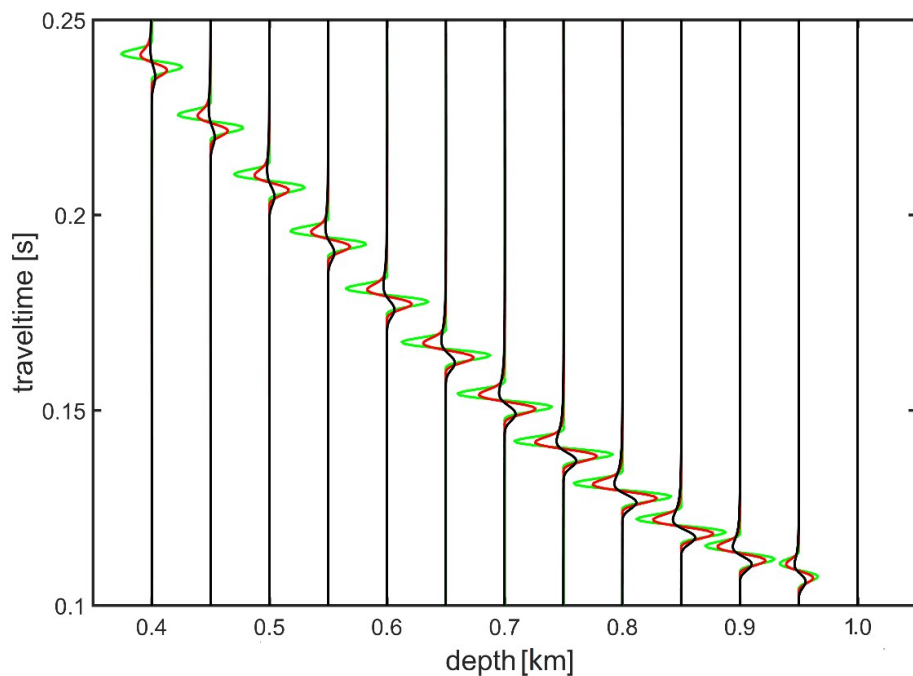

Figure 1.5. Synthetic seismograms (vertical component) at receivers from the configuration shown in Figure 1.1 in the model of vertically inhomogeneous VTI medium with isotropic Q. Green - elastic case, red - Q=100, black – Q=25. Amplitudes are doubled with respect to Fig. 1.4.

14
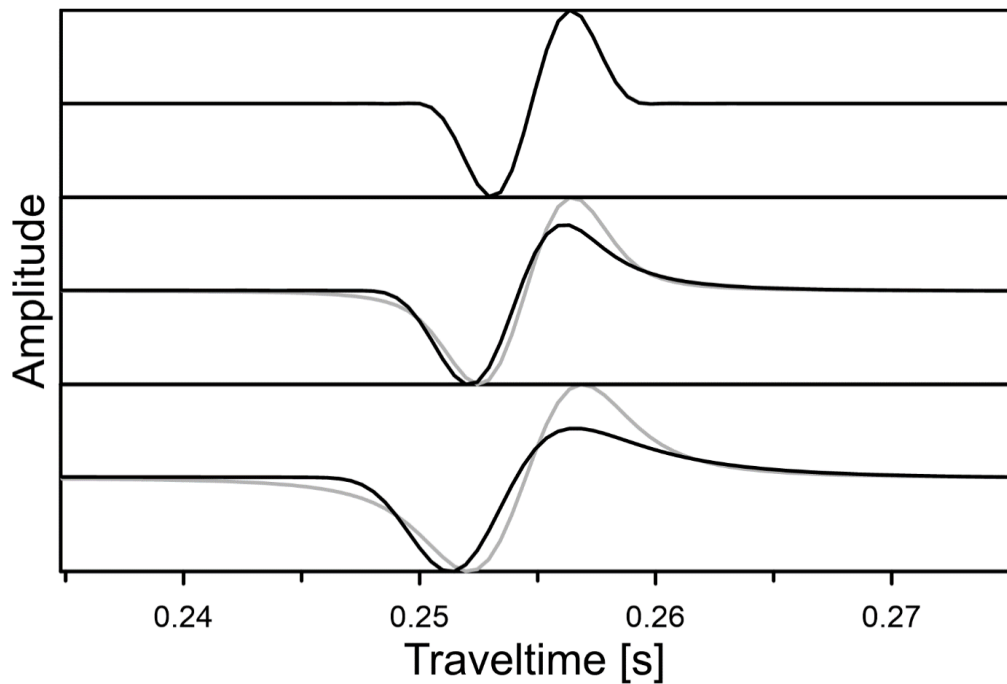
Figure 1.6. Comparison of waveforms computed in elastic (top panel) medium, (shape equivalent to source signal used in Figures 1.2-1.5) and attenuated waves resulting from propagation in isotropic, homogeneous medium with Q=100 (middle panel) and 50 (bottom panel) at 100 Hz reference frequency, using Futterman model. Black seismograms: Futterman model, grey seismograms: frequency independent Q (non-causal absorption). Waves are scaled so that the greatest amplitude in each case reaches size of the frame.

1.2.2 Anisotropic attenuation

In the previous paragraph we considered the influence of the isotropic attenuation on waves in a medium with velocity anisotropy. As strength of attenuation is usually inversely proportional to the increase of the seismic velocity (Zhang & Steward, 2008), it is likely that the rocks, which manifest anisotropy in velocities, manifest anisotropy in attenuation as well. Some theoretical studies, e.g. Červený & Pšenčík (2005, 2008) showed that variations of attenuation due to anisotropy may be, in fact, quite pronounced and may exceed directional changes of seismic velocities. In their studies they have used two models. The first model corresponds to quartz grain rock with two sets of pores (spherical and randomly oriented flat pores) with relatively high concentration of nearly fully aligned flat cracks (Jakobsen et al., 2003). The non-zero (transverse isotropy symmetry) elements of density-normalized complex

stiffness matrix for this rock model read: $a_{11}=14.4+i0.144$, $a_{33}=9.0+i0.09$, $a_{13}=4.5+i0.045$, $a_{44}=2.25+i-0.0225$, $a_{66}=5+0.05$.

Second model is a model of a sedimentary rock. It is a modification of the model proposed by Zhu and Tsvankin (2006) and Vavryčuk (2007), used by Červený and Pšenčík (2008). The non-zero (transverse isotropy symmetry) elements of normalized complex stiffness matrix read: $a_{11}=46.63+i0.4663$, $a_{33}=19.93+i0.1993$, $a_{13}=4.27+i0.0427$, $a_{44}=13.44+i0.1344$, $a_{66}=20.32+i0.2032$.

In Figure 1.7, we show polar diagrams of P-wave ray velocities (top) and of inverse quality factors Q^{-1} (bottom) for the above mentioned VTI models. For the model of quartz grain rock, the angular changes of attenuation are significant, with
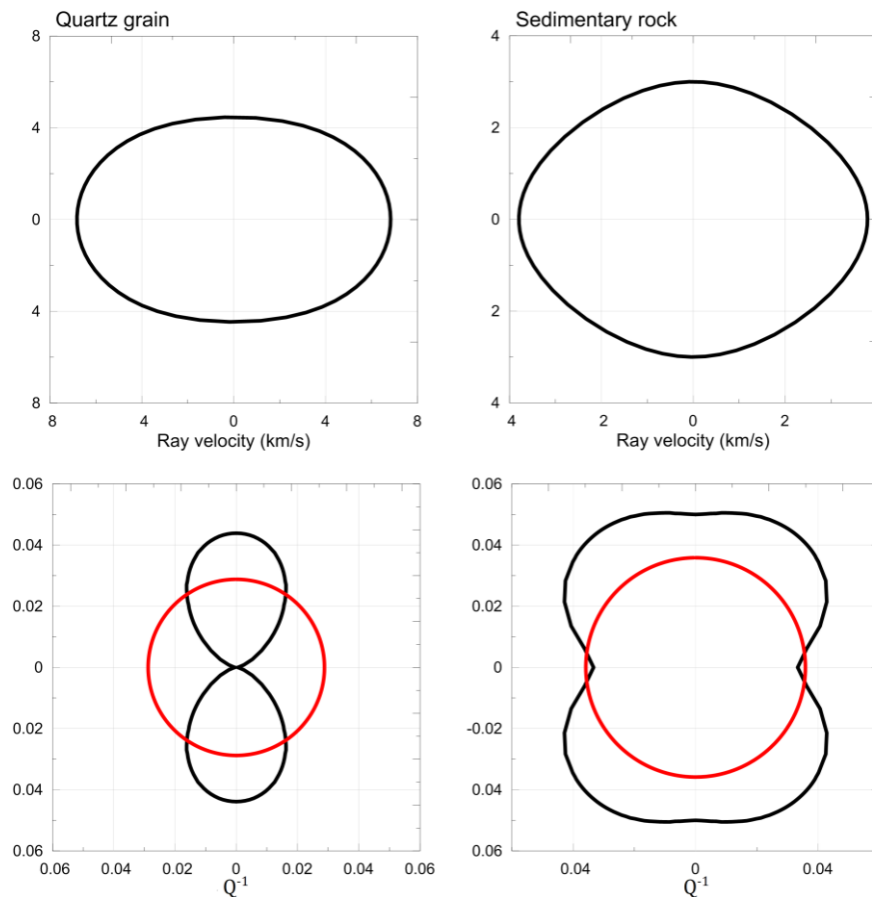

Figure 1.7. Polar diagrams of P-wave ray velocities (top panels) and of Q^{-1} (bottom panels) for the quartz grain rock (left) and the sedimentary rock (right) specified in the text above. The red circles in the bottom panels show isotropic Q^{-1} used to construct the benchmark seismograms in Figures 1.8-1.11.

distinct lobes of strong attenuation along the axis of symmetry and negligible value of Q^{-1} in horizontal direction. While, it is very unlikely to encounter such a pure rock without any silt content, we just want illustrate how strong variations of attenuation can be. The second model of the sedimentary rock is more likely to represent a real medium.

In Figures 1.8-1.11, we show effects of anisotropic attenuation on P-wave ray synthetic seismograms in homogeneous models composed of the quartz grain rock and the sedimentary rock for the configuration of Figure 1.1 (explosive source with source time function the same as in Figures 1.2-1.6). Seismograms for models with anisotropic attenuation are black. For comparison, red seismograms in the background are calculated with the use of the isotropic attenuation (eq. 1.7) equal to median value of Q for the set of receivers shown in Figure 1.1. Isotropic reference Q is Q=34.7 for the quartz grain rock and Q=18.6 for the sedimentary rock. Seismograms for each rock model preserve amplitude variations. Seismograms computed for the quartz grain rock model show, that the influence of attenuation on seismic amplitudes can be very pronounced. While the results for the sedimentary rock model do not show such a strong effect, they are visible as well. To see effects of attenuation anisotropy we need to have at the disposal results for multiple receivers. We can see, that the pattern of changes of maximum amplitudes for different values of Q in sets of seismograms for models with isotropic attenuation (shown in Figure 1.2-1.5) vary, but these changes are increased for models with anisotropic attenuation (shown in Figures 1.8-1.11). Strong Q amplifies differences of amplitudes for receivers placed at varying distance to the source, but anisotropy of attenuation can make these differences even more (or less, even in case of generally strong attenuation) pronounced.

Figure 1.8. Ray synthetic seismograms (radial component) for the quartz grain rock with anisotropic attenuation (black). Red seismograms are computed for velocity model of quartz grain rock but with isotropic (Q=34.7) attenuation.
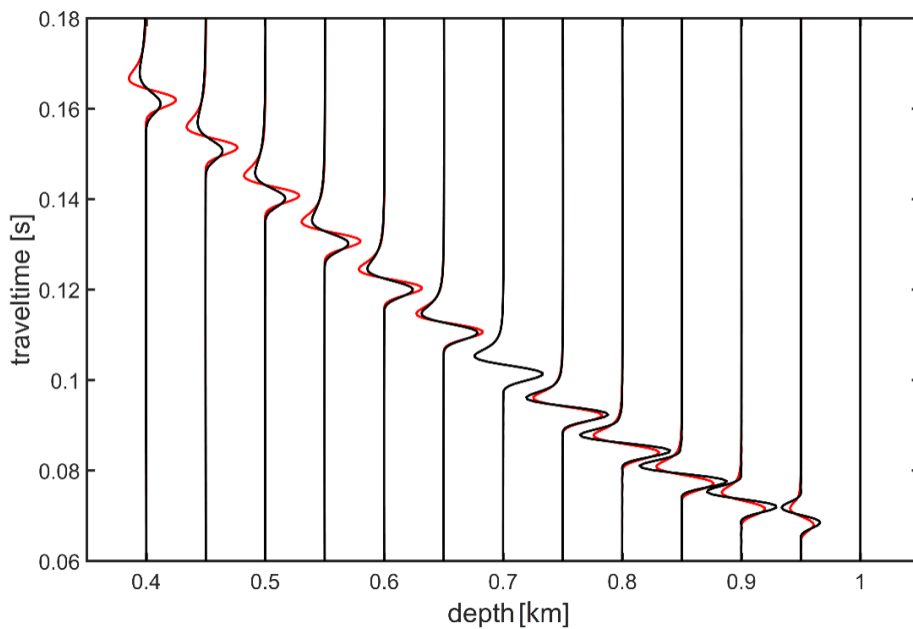
Figure 1.9. Ray synthetic seismograms (vertical component) for the quartz grain rock with anisotropic attenuation (black). Red seismograms are computed for velocity model of quartz grain rock but with isotropic (Q=34.7) attenuation. The amplitudes are doubled with respect to Fig. 1.8.

18
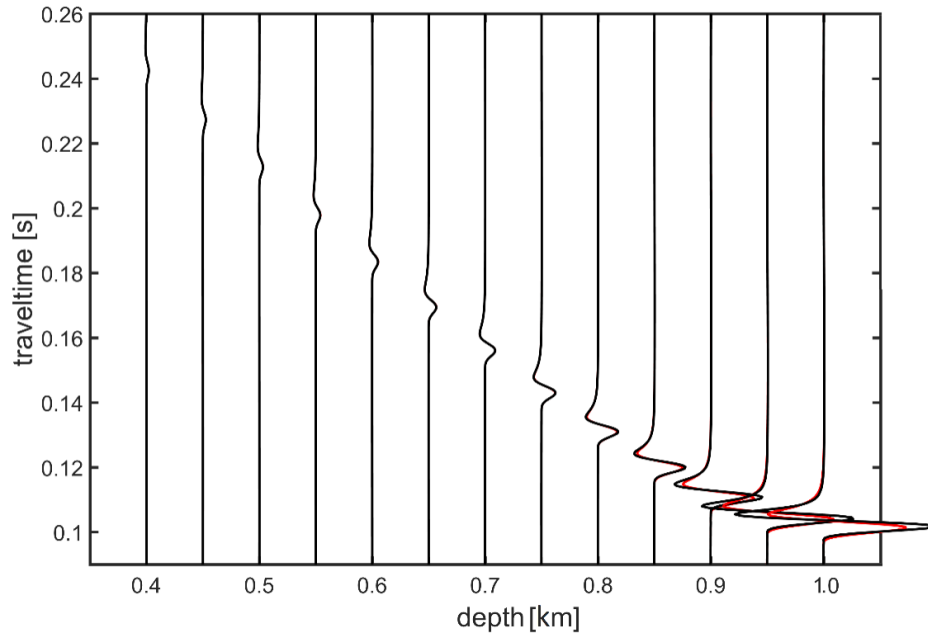
Figure 1.10. Ray synthetic seismograms (radial component) for the sedimentary rock with anisotropic attenuation (black). Red seismograms are computed for velocity model of sedimentary rock but with isotropic (Q=27.9) attenuation.
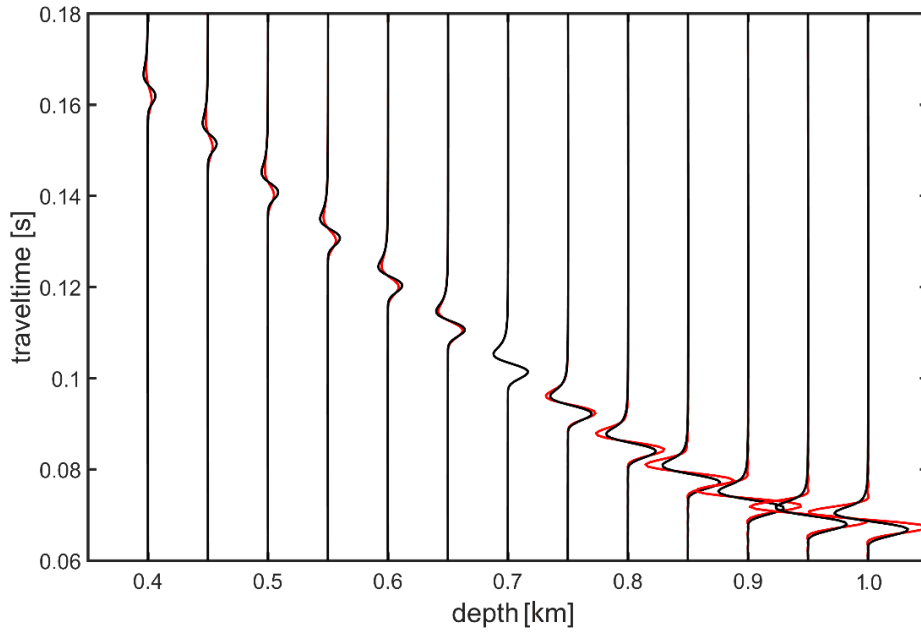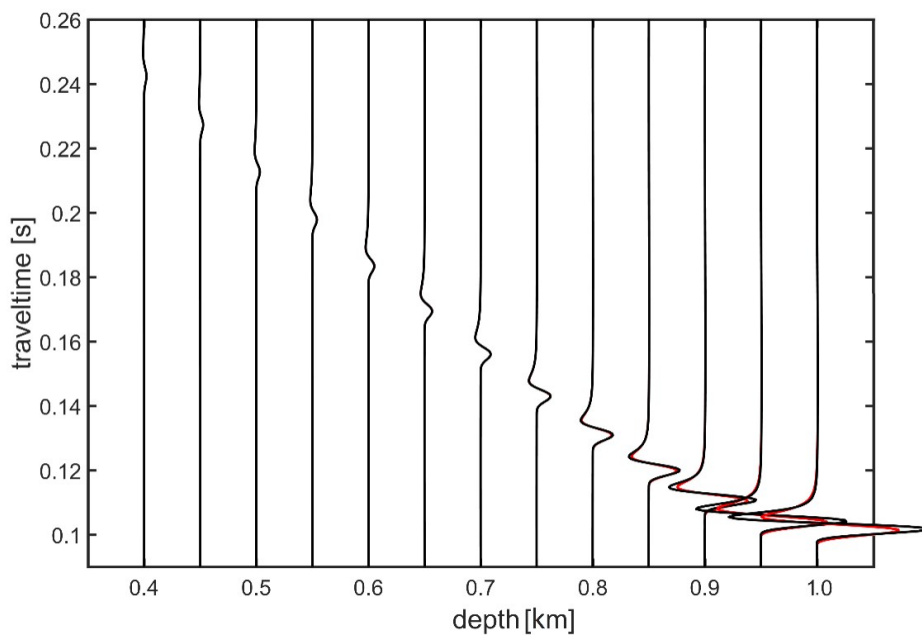

Figure 1.11. Ray synthetic seismograms (radial component) for the sedimentary rock with anisotropic attenuation (black). Red seismograms are computed for velocity model of sedimentary rock but with isotropic (Q=27.9) attenuation. The amplitudes are doubled with respect to Fig. 1.10.

19

An example of an area where attenuation anisotropy can be important to study is a problem of source mechanism inversion. Earthquakes have unique radiation patterns with particular orientation, share of double couple, compensated linear vector dipole, and isotropic components. Radiation pattern, therefore, gives us information about, e.g., orientation of the fault plane. The example of pure shear, point source radiation pattern of a P-wave is shown in Figure 1.12. The point source approximation is broadly used in microseismic studies, in which we deal with frequencies allowing the use of the ray method. The amplitude of the arriving wave significantly depends on the take-off angle. Distribution of maximum amplitudes of P- and S-wave arrivals gives us information about the source mechanism. Propagation effects, including attenuation, influence the pattern of true, but also synthetically modeled in the inversion process maximum amplitudes. Poorly selected medium properties for the inversion affect modeled amplitudes and are detrimental to the inversion result.
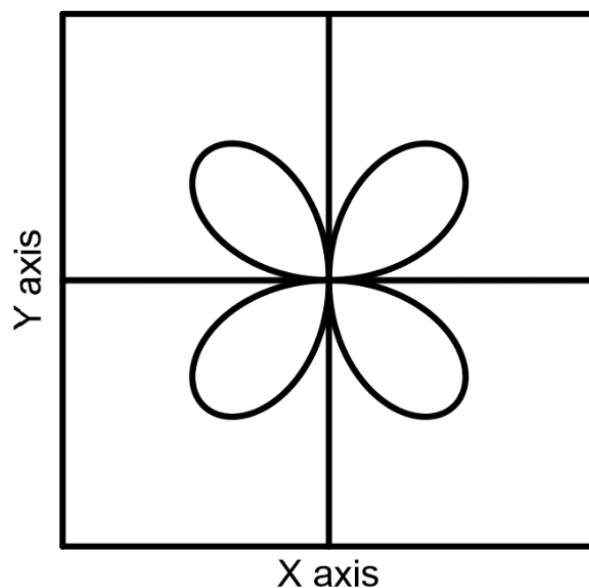
Figure 1.12. Standard P-wave radiation pattern of a shear source – a cross section along the fault plane (situated in the horizontal, X-Y plane) with the horizontal rake direction (0 deg). Changing the rake direction results in rotation of the pattern within the plane.

We briefly illustrate combined influence of radiation pattern and attenuation on distribution and size of maximum amplitudes of P-wave arrivals by showing

seismograms (radial components) in Figures 1.13 and 1.14. They are computed using different types of point sources. The models used in computation are again as above - quartz grain rock and sedimentary rock. In Figures 1.13 and 1.14, we compare the results obtained for isotropic radiation and anisotropic attenuation with results for shear (double – couple) sources (fault plane situated in horizontal (X-Y) plane, varying rake: 40, 30 and -30 deg) in media with isotropic attenuation. We see clear changes in amplitude distribution due to radiation pattern. As shown In Figures 1.8-1.11, variations of maximum amplitudes occur due to attenuation as well. What cannot be affected by attenuation are polarity changes of direct arrivals, which are visible in Figures 1.13 and 1.14 in seismograms corresponding to the double-couple sources.
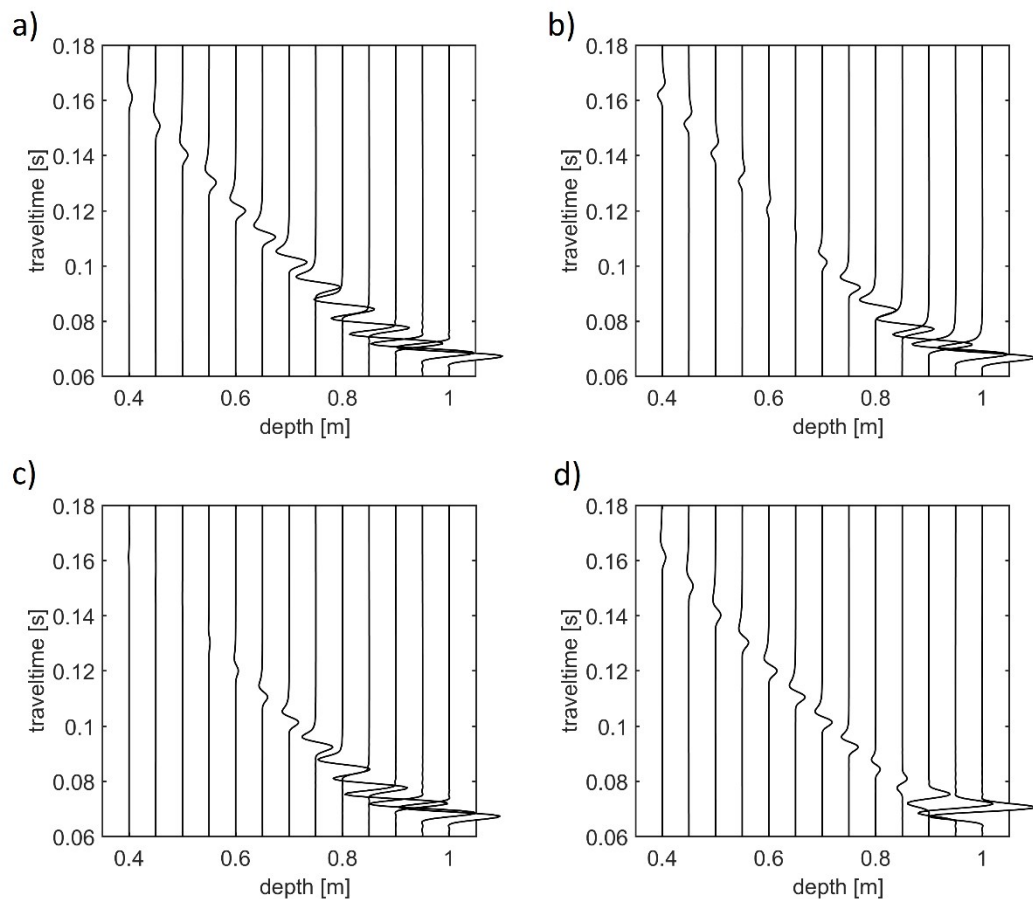
Figure 1.13. Ray synthetic seismograms (radial components) for the quartz grain rock model. a) anisotropic attenuation and isotropic radiation. b-d) results for the isotropic attenuation (Q=34.7) and a double couple radiation: fault plane situated in horizontal X-Y plane. Rake angle varies: b) 40deg, c) 30deg, d) -30deg.

21
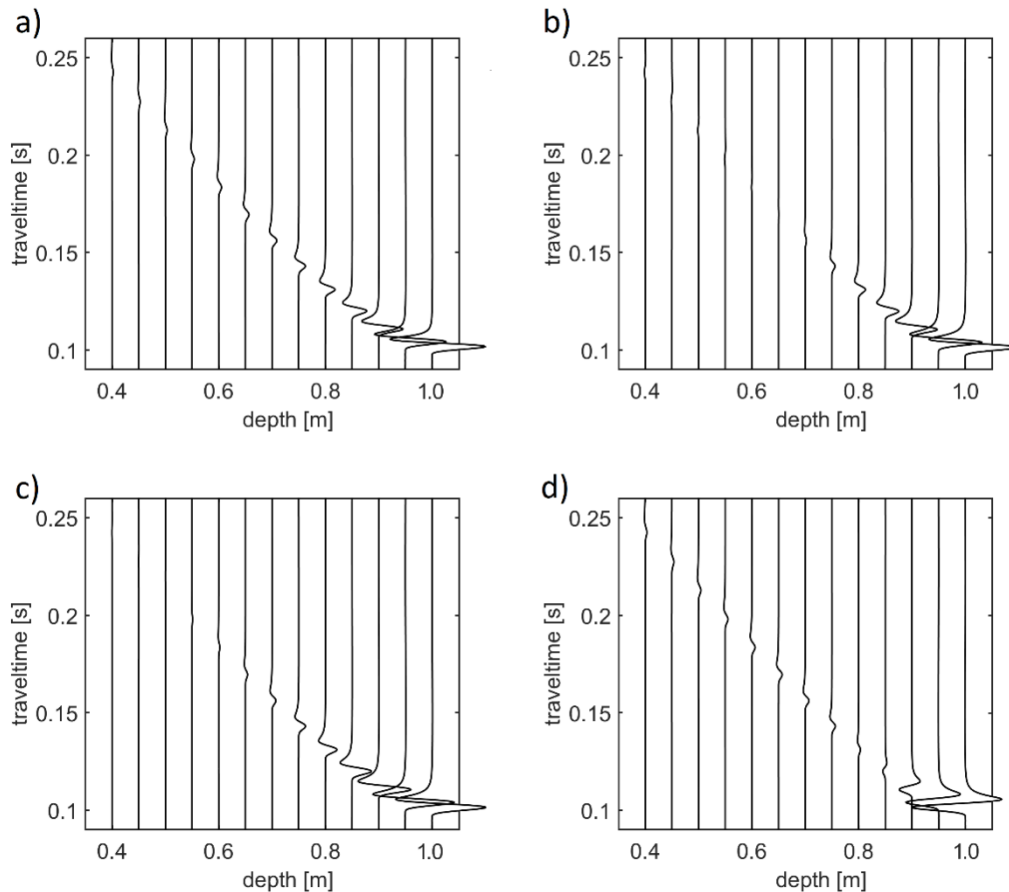
Figure 1.14. Ray synthetic seismograms (radial components) for the sedimentary rock model. a) anisotropic attenuation and isotropic radiation. b-d) results for the isotropic attenuation (Q=27.9), and a double couple radiation: fault plane situated in horizontal X-Y plane. Rake angle varies: b) 40deg, c) 30deg, d) -30deg.

In the inversion of the source mechanism, the input data are usually maximum amplitudes of direct arrivals. In Figure 1.15 we show maximum amplitudes of arrivals included in Figures 1.8, 1.10, 1.13 and 1.14 (note that these are radial components only) as a function of traveltime. While maximum amplitudes generally decrease due to geometrical spreading and attenuation, the exact pattern varies for each presented case, including case with anisotropic attenuation. If we work with limited number of parameters, e.g., we assume in synthetic modeling of amplitudes that the attenuation is isotropic, then, the change of the pattern of maximum amplitudes due to attenuation anisotropy has to be explained with the use of other parameters changing the outcome of the inversion. In case of poor receiver coverage, the change

22

of the outcome of the source mechanism inversion may be manifested even through different orientation of the source fault plane. In case of good receiver coverage, the change of the outcome should not exceed changes in source-mechanism decomposition (e.g. increased non-double couple component of the solution: Staněk et al., 2013) and increased uncertainty of the solution. Studies involving data recorded by arrays placed in borehole, e.g., during monitoring of hydraulic stimulation of shales, which tend to be highly anisotropic, could benefit from analysis of attenuation anisotropy. Especially in cases, when no polarity reversals are recorded. The detailed analysis of the extend of influence of attenuation model selection on the source mechanism inversion is beyond the scope of this dissertation.
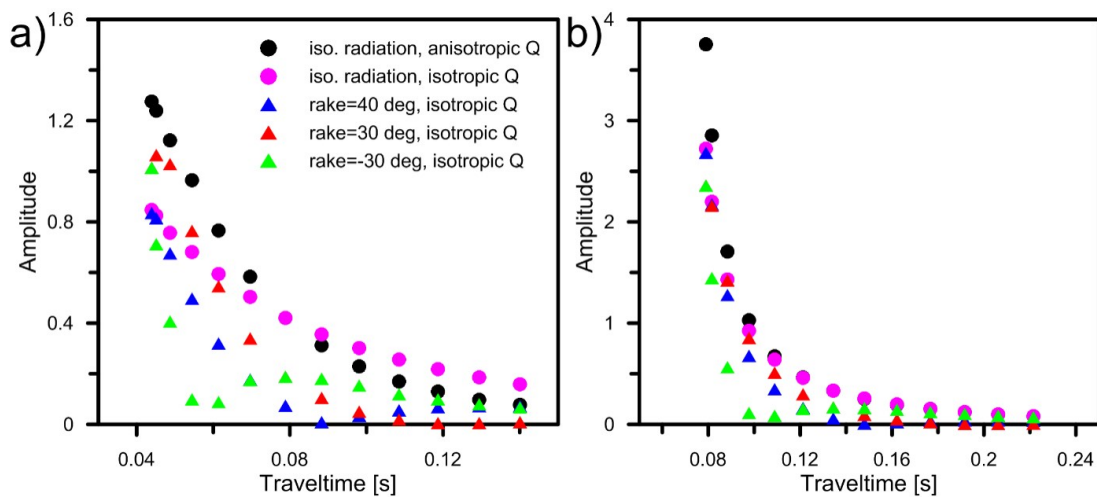
Figure 1.15. Maximum amplitudes as a function of traveltime of the seismograms presented in a) Figs 1.8 and 1.13 (quartz rock model), b) Figs. 1.10 and 1.14 (sedimentary rock model).

1.3 Different frequency dependent attenuation models

In the previous tests, approximate Futterman attenuation model (eq. 1.10) was used in order to calculate causal arrivals. In addition to the Futterman model, there are multiple attenuation models describing dispersive properties of media (Ursin & Toverud, 2002). In this part, we show how the use of particular model may affect computed seismograms. We compare results obtained with Futterman model with results obtained with Maxwell model (Carcione, 2014) and Standard Linear Solid (SLS), also known as Zener model (Ben-Menahem and Singh, 1981). The Maxwell model is the simplest form of empirical viscoelastic models and it can be represented

23

by a spring and a dashpot connected in a series. It is described as a model with isotropic stress. The Maxwell model does not allow to describe creep or recovery, but it describes well the behavior of fluids. SLS model is more complex. It can be represented by springs and dashpots placed both in series and in parallel. The SLS model is the simplest model to describe creep and stress relaxation. The SLS model is, after Futterman model, most frequently used in seismic studies and seismology.

In the Maxwell model the complex valued phase velocity reads:

$$v_p(\omega) = v_p(\omega_r)\sqrt{\frac{Q(\omega_r)}{Q(\omega_r) - i\frac{\omega_r}{\omega}}} \qquad (1.12)$$

Here ω_r is reference frequency. In the SLS model the complex valued phase velocity reads:

$$v_p(\omega) = [v_{pr}(1 - \frac{(\frac{\omega}{\omega_r})^2}{Q(\omega_r)[1 + (\frac{\omega}{\omega_r})^2]})^{-1}][1 + \frac{i}{2}(Q(\omega_r)\frac{2\frac{\omega}{\omega_r}}{1 + (\frac{\omega}{\omega_r})^2})^{-1}]. \qquad (1.13)$$

Note that the relation between a ray velocity v and phase velocity v_p is:

$$\frac{1}{v(\omega)} = \frac{1}{v_{p(\omega)}}[1 - \frac{\omega}{v_p(\omega)}\frac{dv_p(\omega)}{d\omega}]. \qquad (1.14)$$

In SLS model, the reference frequency ω_r is tied to the relaxation time t_r (Ursin & Toverud, 2002). Let's note that reference phase velocity v_{pr} in the definition of the SLS model in eq. (1.13) is not equivalent to $v_p(\omega_r)$. For selected value of v_{pr}, the value of $v_p(\omega_r)$ is slightly higher. The difference between v_{pr} and $v_p(\omega_r)$ increases with for models with stronger attenuation. This is important to know if we wish to create a model with particular value of velocity at the reference frequency.

Examples of behavior of $v_p(\omega)$ and $Q(\omega)$ in Futterman, Maxwell, and SLS models are shown in Fig. 1.16. The reference frequency ω_r is 60 Hz and $v_p(\omega_r)$=2km/s and $Q(\omega_r)$=40. In case of SLS model, it means that reference velocity v_{pr} must be set to 1.975km/s. Let's recall that the changes of phase velocity affect τ^R and the changes of Q affect t^*. Fig. 1.16 shows that for Maxwell model, Q increases linearly with increasing frequency but the phase velocity is nearly constant (except
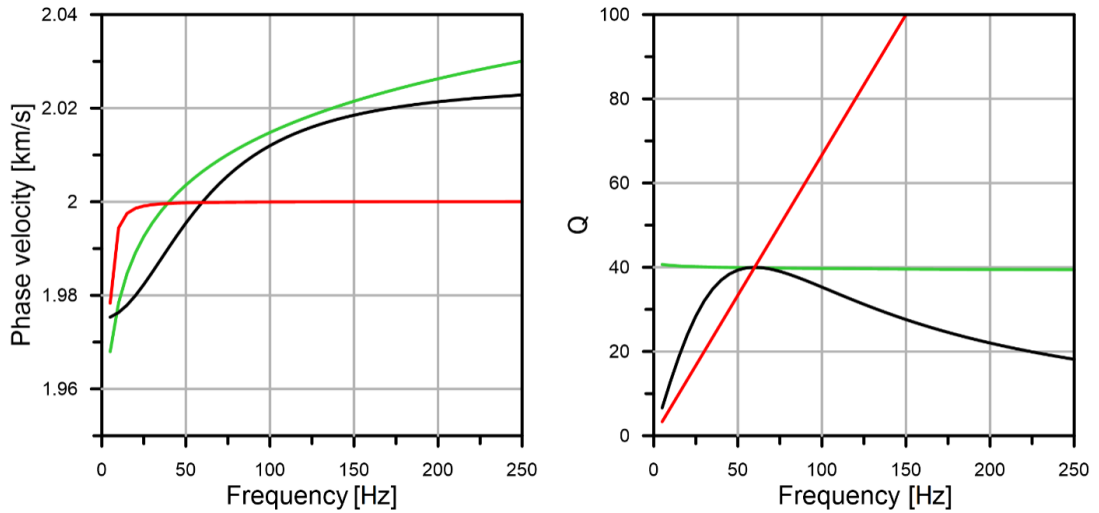
Fig 1.16. Phase velocities (left panel) and Q factors (right panel) as a function of frequency for different attenuation models. Futterman model in green, Maxwell model in red: reference frequency ω_r equal 60Hz, $v_p(\omega_r)$=2.0 km/s and $Q(\omega_r)$=40. SLS model (eq. 13) in black is computed for the relaxation time t_r=1/60s, v_{pr}=1.975km/s and $Q(\omega_r)$=40.

low frequencies). Increase of the Q cancels the effect of increasing frequency in the exponent when Maxwell model is inserted into eq. (1.8). This results in the de facto preservation of the form of the source wavelet during the propagation. Although very simple Maxwell model does not describe solid media well, conservation of the source wavelet makes the use of the Maxwell model useful in, e.g., theoretical studies of phase changes due to reflection of waves at interfaces. The changes in waveforms are then due to the phase of reflection coefficients. We use this advantage in further parts of the thesis.

Different frequency-dependent velocity and attenuation affect waves. We show an example of seismograms using attenuation models, with variations of $v_p(\omega)$ and $Q(\omega)$ presented in Figure 1.16. The computations are done for an isotropic, attenuative, homogeneous medium. Simple source-receiver configuration includes source and 5 receivers, all placed along the horizontal profile, with receivers located at offsets increasing by 0.1km. Explosive source and Müller signal with prevailing frequency equal 60Hz and 2 maxima as the source-time function is used. Seismograms are shown in Figure 1.17. Each model results in different waveforms

25

and maximum amplitudes. The SLS and Futterman models provide relatively similar waveforms. Naturally, the difference between Maxwell and other models' waveforms grows with increasing offset.
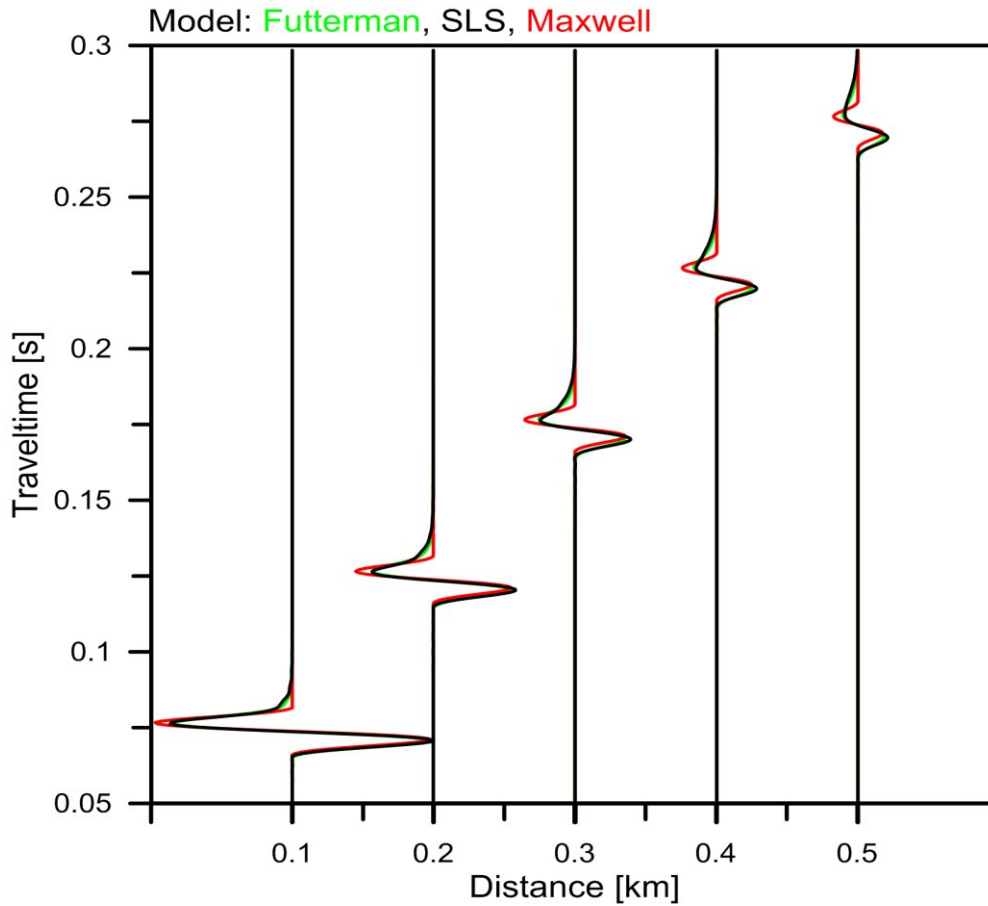
Figure 1.17. Synthetic seismograms (radial components) for Futterman model (eq. 1.10) in green, Maxwell model (eq. 1.12) in red: reference frequency equal 60Hz, $v_p(\omega_r)$=2.0 km/s and $Q(\omega_r)$=40. SLS model (eq. 1.13) in black is computed for the t_r equal 1/60s, v_{pr}=1.975km/s and $Q(\omega_r)$=40.

1.4 Limits of the WAC

WAC, as a perturbation theory, can be used only if $a_{ijkl}^I \ll a_{ijkl}^R$. In practice we can tie the limit of the applicability of the method to the Q value. To see what are the limits of the applicability of the WAC we compare the results obtained with the use of modified ANRAY program package with the full-wave synthetic seismograms computed by the procedure based on the Fourier and Chebyshev pseudospectral

26

methods to compute the spatial derivatives. The procedure is called domain decomposition in computational acoustics. It has been used extensively to model elastic and electromagnetic waves (Carcione and Helle, 2004; Carcione et al., 2014). The medium is covered by grid. The solution on each grid is obtained by using the Runge-Kutta method as a time-stepping algorithm and the Fourier and Chebyshev differential operators to compute the spatial derivatives (Carcione, 2014). The method, which implements the boundary conditions explicitly, has been verified extensively (Sidler and Carcione, 2007; Sidler et al. 2008; Ursin et al. 2017). This modelling can be considered exact within the limits of computer precision, when the temporal and spatial discretization is chosen properly to avoid aliasing and numerical dispersion.

The computations are done in the simple configuration including source and single receiver placed along horizontal line with offset of 0.405 km. Four models are computed using Maxwell attenuation model. In each case, density ρ=2.4 kg/cm^3, SH-wave velocity β=2km/s and Q varies and is equal 40, 30, 20, 10 at reference frequency of 60Hz.

An explosive point source with Ricker signal with dominant frequency of 60Hz as the source-time function is used. In 2D full-wave models, Ricker signal loses its symmetry and has a slowly decaying tail (this is the consequence of the fact that the signal is the time convolution of the wavelet and two-dimensional Green function). The source signal used in the ray method computation was adjusted accordingly.

Seismograms for models with decreasing value of Q are shown in Figure 1.8 (amplitudes are normalized). We can see that in the model with Q=40, the difference between the ray and the full-wave approach is almost invisible. As we move to the models with lower values of Q, we start to notice that there are slight differences close to the extremes, but even for Q=10, the differences are negligible. It means that **WAC is applicable for most of real media**, as majority of rocks has Q higher than 10.
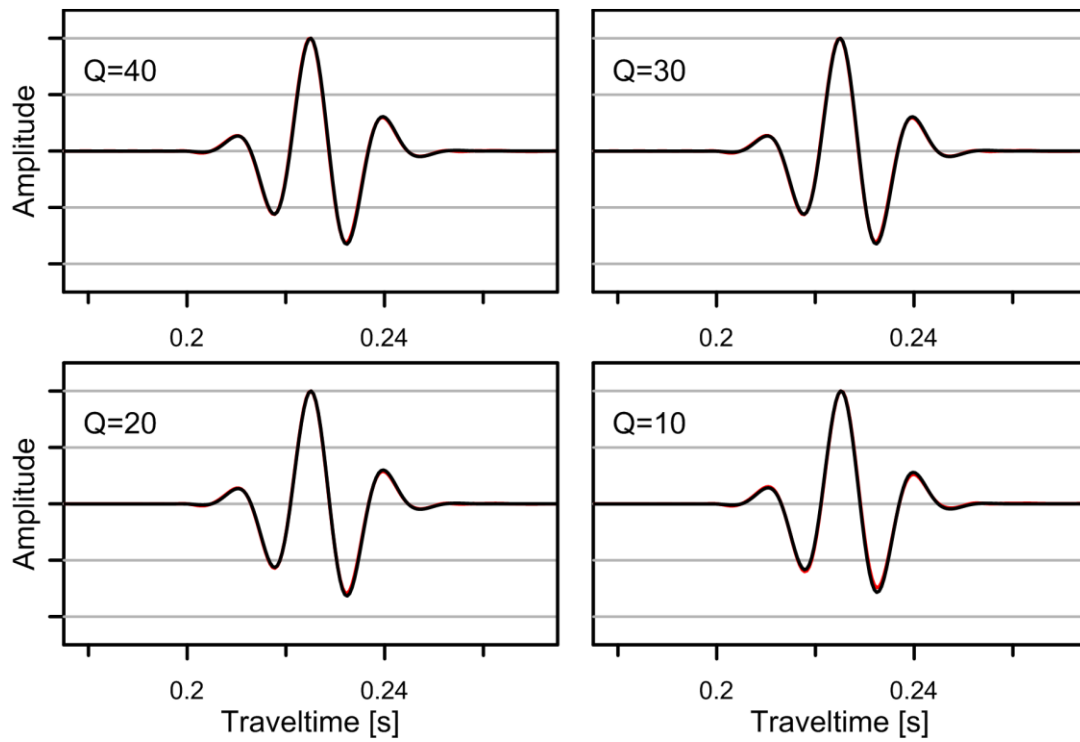
Figure 1.18. Comparison of seismograms computed using ray method with WAC (black) with exact benchmark (full-wave method - red background). Seismograms are normalized.

Chapter 2

SH-waves in attenuative, isotropic, layered media

Real media are often layered, therefore, to properly describe the influence of attenuation on wavefields, it is required to study the effect of attenuation not only during propagation of a wave inside the layers, but also, at interfaces between them. Here we concentrate on the simplest case of reflection and transmission (R/T) of an SH wave at an interface between two isotropic, attenuative media. This problem has been studied, among many others, by Buchen (1971), Borcherdt (1977), Krebes (1983), Richards (1984), Brokešová and Červený (1998), Ruud (2006), and Krebes and Daley (2007), Sidler et al. (2008), Vavryčuk (2010), Daley and Krebes (2015) or Ursin et al. (2017). The problem is also discussed in several textbooks, see, e.g., Carcione (2014) or Borcherdt (2020). Here we will focus on application of the weak attenuation concept (WAC) – a perturbation method in calculation of the reflection/transmission (R/T) coefficients, as it was done by Pšenčík et al. (2022). In addition to WAC applied to smooth media (as shown in Chapter 1) it allows modelling using ray method to be performed for layered, attenuative media.

2.1 SH-wave reflection/transmission coefficients in attenuative media

2.1.1 Theory

SH-wave reflection and transmission (R/T) displacement coefficients in elastic media can be expressed as (Borcherdt 2020, eqs 5.4.18 and 5.4.19):

$$R = \frac{\rho_1 \beta_1^2 p_i N_i - \rho_2 \beta_2^2 p_k^{(t)} N_k}{\rho_1 \beta_1^2 p_i N_i + \rho_2 \beta_2^2 p_k^{(t)} N_k}, \qquad T = \frac{2\rho_1 \beta_1^2 p_i N_i}{\rho_1 \beta_1^2 p_i N_i + \rho_2 \beta_2^2 p_k^{(t)} N_k}. \qquad (2.1)$$

Here ρ_i and β_i denote the density and S-wave velocity in the i-th halfspace/layer (both terms will be used in this chapter), i=1,2, where 1 indicates the halfspace from where the wave is incident at the interface separating two half-spaces, and 2 indicates the other half-space. p and $p^{(t)}$ denote slowness vectors of the incident and

transmitted SH-waves. N denotes the unit normal to the interface (positive against the direction of propagation of incident wave). Slowness vectors of the incident and transmitted waves have the crucial effect on the R/T coefficients. As in the previous chapter that concerned the smooth medium, we use the correspondence principle. Therefore, slowness vectors in the attenuative media are complex valued:

$$p_i = P_i + iA_i, \qquad p_i^{(t)} = P_i^{(t)} + iA_i^{(t)} . \qquad (2.2)$$

Real valued part **P** of slowness vector is called propagation vector, and imaginary part A is called attenuation vector. If both these parts are parallel, the wave is called homogeneous, if they are not parallel, the wave is called inhomogeneous. The inhomogeneity may be described by the attenuation angle γ (angle between attenuation and propagation vectors) or by the inhomogeneity factor D. For the relation between the factor D and the attenuation angle γ for SH waves in an isotropic viscoelastic medium, see equations (7) and (12) of Červený and Pšencík (2005). In elastic media, the only situation, where we deal with non-zero attenuation vector, is the case of transmitted wave for overcritical incidence (evanescent wave). In attenuative media, the imaginary part of complex velocity is non-zero, therefore, the attenuation vector is non-zero in all cases. By inserting complex velocity (eq. 1.5) and slowness vector (eq. 2.2) into eq. (2.1), we arrive to the general form for SH-wave reflection and transmission coefficients in isotropic attenuative medium:

$$R = \frac{\rho_1 \beta_1^2 (1 - iQ_1^{-1})(P_i + iA_i)N_i - \rho_2 \beta_2^2 (1 - iQ_2^{-1})(P_i^{(t)} + iA_i^{(t)})N_i}{\rho_1 \beta_1^2 (1 - iQ_1^{-1})(P_i + iA_i)N_i + \rho_2 \beta_2^2 (1 - iQ_2^{-1})(P_i^{(t)} + iA_i^{(t)})N_i},$$

$$(2.3)$$

$$T = \frac{2\rho_1 \beta_1^2 (1 - iQ_1^{-1})(P_i + iA_i)N_i}{\rho_1 \beta_1^2 (1 - iQ_1^{-1})(P_i + iA_i)N_i + \rho_2 \beta_2^2 (1 - iQ_2^{-1})(P_i^{(t)} + iA_i^{(t)})N_i} .$$

Here Q_1 and Q_2 are quality factors of first and second half-space respectively. Slowness vectors of incident and generated homogeneous and inhomogeneous waves at an interface separating two weakly attenuating media need to satisfy 3 conditions:

a) the approximate constraint relation resulting from the corresponding equation of motion;

b) Snell's law, which requires equality of tangential components of complex-valued slowness vectors of the incident and generated waves;

c) the radiation condition, which requires decay of amplitudes of generated waves away from the interface.

Pšenčík et al. (2022) derived expressions for slowness vectors that satisfy the above conditions. First order expression for the slowness vector p of incident wave is following:

$$p_i = P_i + iA_i = P_i + i\left(\frac{1}{2}Q_1^{-1}P_i + Dm_i\right). \tag{2.4}$$

m is a unit vector perpendicular to the direction of propagation vector which multiplied by inhomogeneity factor D describes the inhomogeneity of slowness vector. Computation of the slowness vector of the transmitted wave in an attenuative medium is more complicated. It is useful to study separately the expressions for $\mathbf{P}^{(t)}$ and $\mathbf{A}^{(t)}$ components of the slowness vector $\mathbf{p}^{(t)}$ in sub- and overcritical regions (understood as sub- and overcritical regions in the reference elastic medium). For subcritical incidence they have a form:

$$P_i^{(t)} = P_i + \beta_1^{-1}X_1N_i - \beta_2^{-1}X_2N_i,$$

$$\tag{2.5}$$

$$A_i^{(t)} = A_i + \beta_1^{-1}\xi N_i - \beta_2^{-1}\xi^{(t)}N_i.$$

For overcritical incidence the equations read:

$$P_i^{(t)} = P_i + \beta_1^{-1}X_1N_i + \beta_2^{-1}\xi^{(t)}N_i,$$

$$\tag{2.6}$$

$$A_i^{t)} = A_i + \beta_1^{-1}\xi N_i - \beta_2^{-1}X_2N_i.$$

In equations (2.5) and (2.6) quantities X_1 and X_2 are the square roots frequently used in the studies of reflection and transmission in elastic media:

$$X_1 = (1 - \beta_1^2 p^2)^{1/2},$$

$$\text{(2.7)}$$

$$X_2 = (1 - \beta_2^2 p^2)^{1/2}.$$

Here p denotes ray parameter that reads:

$$p = \sin \theta / \beta_1 \qquad \text{(2.8)}$$

The symbol θ in equation (2.7) denotes the incidence angle. If $\beta_2 > \beta_1$, the term X_2 becomes imaginary for the overcritical incidence in the reference elastic medium. In this case, we have:

$$X_2 = i\dot{X}_2 = i(\beta_2^2 p^2 - 1)^{1/2}, \qquad \text{(2.9)}$$

where $\dot{X}_2$ is real valued. The term ξ in equation (2.6) can be determined from the specification of the incident wave (see eq. 2.4):

$$\xi = \frac{1}{2} Q_1^{-1} X_1 - \beta_1 D m_i N_i. \qquad \text{(2.10)}$$

The quantity $\xi^{(t)}$ that is used in the evaluation of attenuation vector for the subcritical incidence in eq. (2.5) reads:

$$\xi^{(t)} = \frac{1}{2} Z X_2^{-1}. \qquad \text{(2.11)}$$

$\xi^{(t)}$ is singular at the critical incidence, and therefore we can expect that it will not be evaluated correctly in the vicinity of the critical incidence as well. It will lead to inaccuracy of R/T coefficients, in which $\xi^{(t)}$ appears. In the overcritical region, we use $\xi^{(t)}$ introduced in eq. (2.6) to evaluate the propagation vector:

$$\xi^{(t)} = -\frac{1}{2} Z X_2^{-1}. \qquad \text{(2.12)}$$

In equations (2.11) and (2.12), we deal with the quantity Z:

$$Z = Q_2^{-1} - Q_1^{-1} \beta_2^2 p^2 - 2 X_1 \beta_1^{-1} \beta_2^2 D m_i N_i. \qquad \text{(2.13)}$$

32

For homogeneous incident wave (D=0), the quantity Z is positive for normal incidence. For $\beta_1 < \beta_2$ (when critical incidence exists), it may become negative for higher incidence angles. Equations (2.4–2.13), inserted into equations (2.3) allow us to calculate SH plane wave reflection/transmission coefficients in the frame of the WAC. The coefficients are singular at the angle corresponding to critical incidence in the reference elastic medium, therefore, their accuracy is limited also in the vicinity of this angle. Pšenčík et al. (2022) have showed that for the subcritical incidence, equations (2.3) provide satisfactory results. Problems arise in the vicinity of the critical incidence and onwards for models with $\beta_1 < \beta_2$ and $Q_1 < Q_2$, (common case) . Z changes its sign in the subcritical region and the obtained results computed in the overcritical region are non-physical, namely:

-propagation vector of transmitted wave points back to the medium, in which incident wave propagates. This is in contradiction to finding of Borcherdt (2020), according to which propagation vector must point to the medium where transmitted wave propagates;

-attenuation vector of transmitted wave behaves in a discontinuous way at the interface when passing from the subcritical to the overcritical region;

-resulting modulus of the reflection coefficient exceeds 1.

These problems indicate that the correspondence principle that was used in the derivation of the coefficients may not be applicable in some cases for the overcritical incidence. Pšenčík et al. (2022) proposed a modification of the formulae, which leads to acceptable results, through artificially changing the sign of Z, see eq. (2-13) once it turns negative in subcritical region. This fixes above mentioned problems, but at the price of violating some of constraint relations. The issue is described in more detail by Pšenčík et al. (2022).

2.1.2 Incident homogeneous waves

Below we show an example of comparison of coefficients computed using WAC and coefficients computed by an independent method proposed by Daley and

Krebes (2015), who calculate R/T coefficients without the use of the correspondence principle. The coefficients for elastic reference are included as well. The three models that we use are based on models proposed by Brokešová and Červený (1998), therefore we mark them BC1, BC2 and BC3. Their parameters are given in Table 2.1. Subscript 1 indicates half-space in which incident wave propagates, subscript 2 indicates the half-space, in which the transmitted wave propagates. In each case, $\beta_2 > \beta_1$, therefore the critical incidence occurs. Model BC1 has $Q_1 > Q_2$ and does not require artificial change of Z in the computations. We need to note that model with lower value of Q for half-spaces characterized by higher β is not very common. Models BC2 and BC3 have higher value of Q for half-space with higher β, therefore they do require change of the sign of Z. Model BC3 shows the case with relatively low values of Q's. Figure 2.1 shows the term Z as a function of the incidence angle for models BC1 and BC2. We can see that the term Z changes its sign in the overcritical region for the model BC1 and in the subcritical region for the model BC2. Figure 2.2 shows the slowness vectors of transmitted wave for models BC1 and BC2 for varying angle of incidence. We can see that the attenuation vector abruptly changes the orientation at the critical incidence for the model BC2. While only slightly, the propagation vector for the overcritical incidence points back to the first half-space for the model BC2 which contradicts findings of Borcherdt (2020) findings.

Model	β_1 [km/s]	β_2 [km/s]	ρ_1 [g/cm³]	ρ_2 [g/cm³]	Q_1	Q_2
BC1	3.698	4.618	2.98	3.3	75	50
BC2	3.698	4.618	2.98	3.3	50	75
BC3	1.44	2.08	2.0	2.0	15	22

Table 2.1: Parameters of models consisting of two half-spaces used in tests.
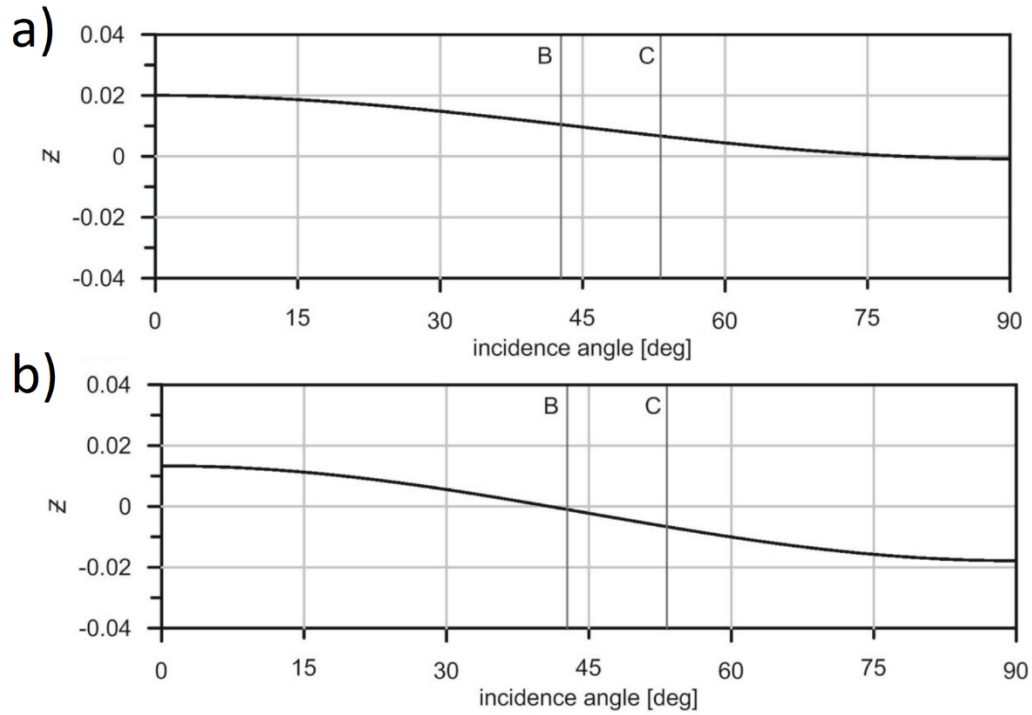
Figure 2.1. The term Z, see eq. (2.13), as a function of the incidence angle for incident homogeneous wave for the model a) BC1, b) BC2. Vertical lines B and C indicate positions of the Brewster and critical angles in the reference elastic medium, respectively.
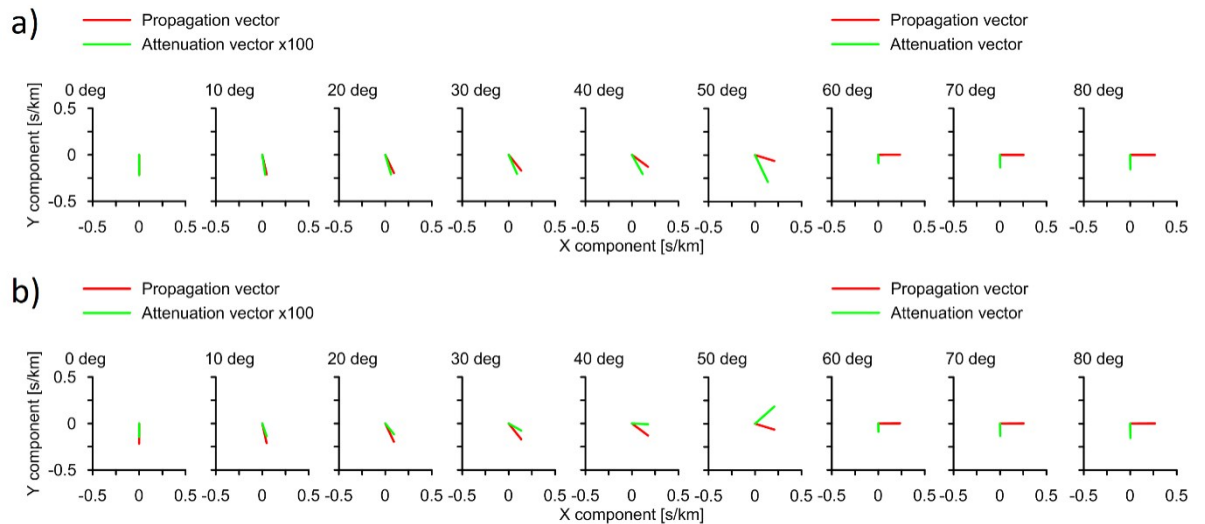
Figure 2.2. Propagation (red) and attenuation (green; amplified in the subcritical region) vectors of the transmitted wave generated by the incident homogeneous wave for model a) BC1, b) BC2. The critical angle for both models is at ~44 deg.

Figure 2.3 shows reflection coefficients calculated for the model BC1. We may see that the results obtained using eq. (2.3) (dotted red) fit almost perfectly results computed using the approach of Daley and Krebes (2015) (dashed green). The only slight difference can be observed in the phase frame in the vicinity of the Brewster and critical angles, where the WAC approximation and the ray theory does not work properly. As observed previously (Brokešová and Červený 1998), attenuation smoothes amplitude and phase of the coefficient corresponding to the elastic case. This smoothing, although hardly visible in the modulus frame, also includes

Figure 2.3. Comparison of moduli (top) and phases (bottom) of the SH plane-wave reflection coefficients for the model BC1. Elastic reference (solid black), Daley and Krebes (2015) (dashed green), equation (2.3) (dotted red). Incident homogeneous wave.

the vicinity of the Brewster angle. Due to this smoothing, the modulus of the reflection coefficient in the anelastic medium is non-zero at the Brewster angle, although only negligibly. By comparing red and green curves with the black curve corresponding to the reference elastic case, we can see that except the vicinity of the Brewster

Figure 2.4. Comparison of moduli (top) and phases (bottom) of the SH plane-wave reflection coefficients in the model BC2. Elastic reference (solid black), Daley and Krebes (2015) (dashed green), equation (2.3) (dotted red). Incident homogeneous wave.

and critical angles, modulus in the overcritical region differs although not significantly. In Fig. 2.4, the same results as in Fig. 2.3 are shown, but for the model

37

BC2. We can see a perfect coincidence of the WAC (red dotted) and Daley and Krebes (2015) (green dashed) curves in the subcritical region. In the overcritical region we can, however, observe significant differences in the modulus (WAC modulus greater than 1), which decrease with the increasing

Figure 2.5. Comparison of moduli (top) and phases (bottom) of the SH plane-wave reflection coefficients in the model BC2. Elastic reference (solid black), Daley and Krebes (2015) (dashed green), equation (2.3) with change of sign of Z when it becomes negative (dotted red). Incident homogeneous wave.

angle of incidence. It is the consequence of the abrupt change of the orientation of the attenuation vector for angles of incidence varying from the subcritical to the overcritical incidence, and also of the unacceptable orientation of the propagation vector of the transmitted wave into the upper half-space as shown in the Figure 2.2. Artificial change of the sign of Z, mentioned above, does allow to obtain as good results for model BC2 as in the

Figure 2.6. Comparison of moduli (top) and phases (bottom) of the SH plane-wave transmission coefficients in the model BC2. Elastic reference (solid black), Daley and Krebes (2015) (dashed green), equation (2.3) (dotted red). Incident homogeneous wave.
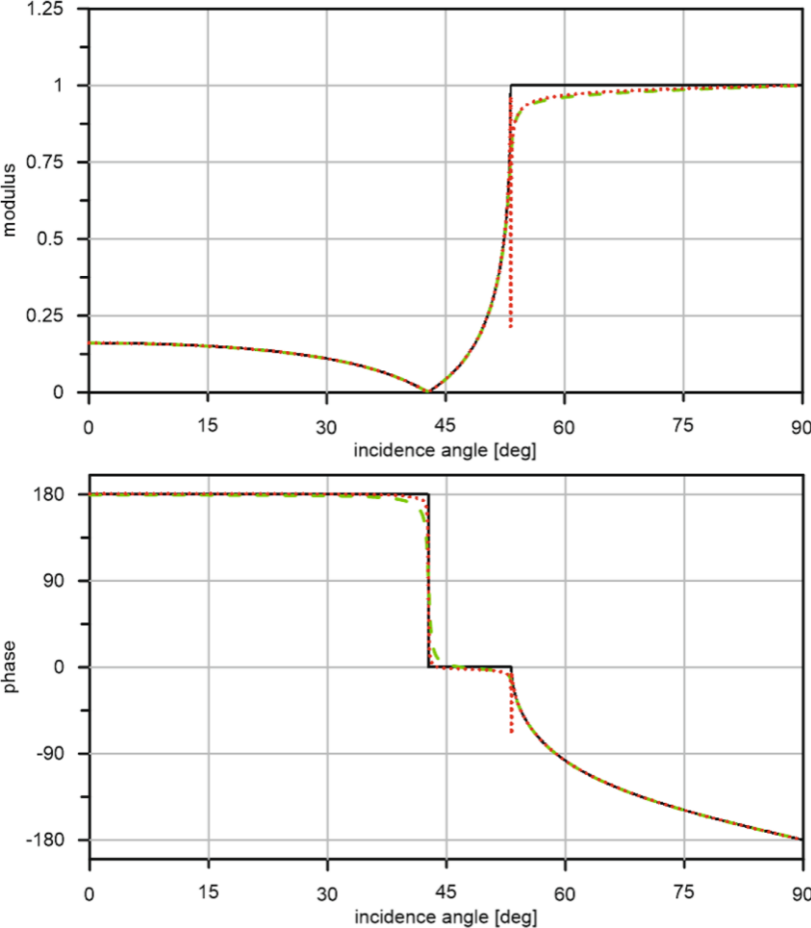
Figure 2.7. Comparison of moduli (top) and phases (bottom) of the SH plane-wave transmission coefficients in the model BC2. Elastic reference (solid black), Daley and Krebes (2015) (dashed green), equation (2.3) with change of sign of Z when it becomes negative (dotted red). Incident homogeneous wave.

case of the model BC1. Figure 2.5 shows the reflection coefficients for the model BC2 when artificial change of the sign of Z is applied. Figures 2.6 and 2.7 are analogous to Figures 2.4 and 2.5, but they show transmission coefficients for the model BC2. Note that the maximum amplitude of the transmission coefficient cannot exceed two.

40

Figure 2.6 violates this indicating a problem as in the case of reflection coefficient in Figure 2.4. In Figure 2.7, the artificial change of the sign of Z once it becomes negative does improve the result again. Figure 2.8 shows results for the model BC3 with low values of Q in both layers. Artificial modification of the quantity Z is applied. Moduli in the subcritical region and phases in the overcritical region fit perfectly.
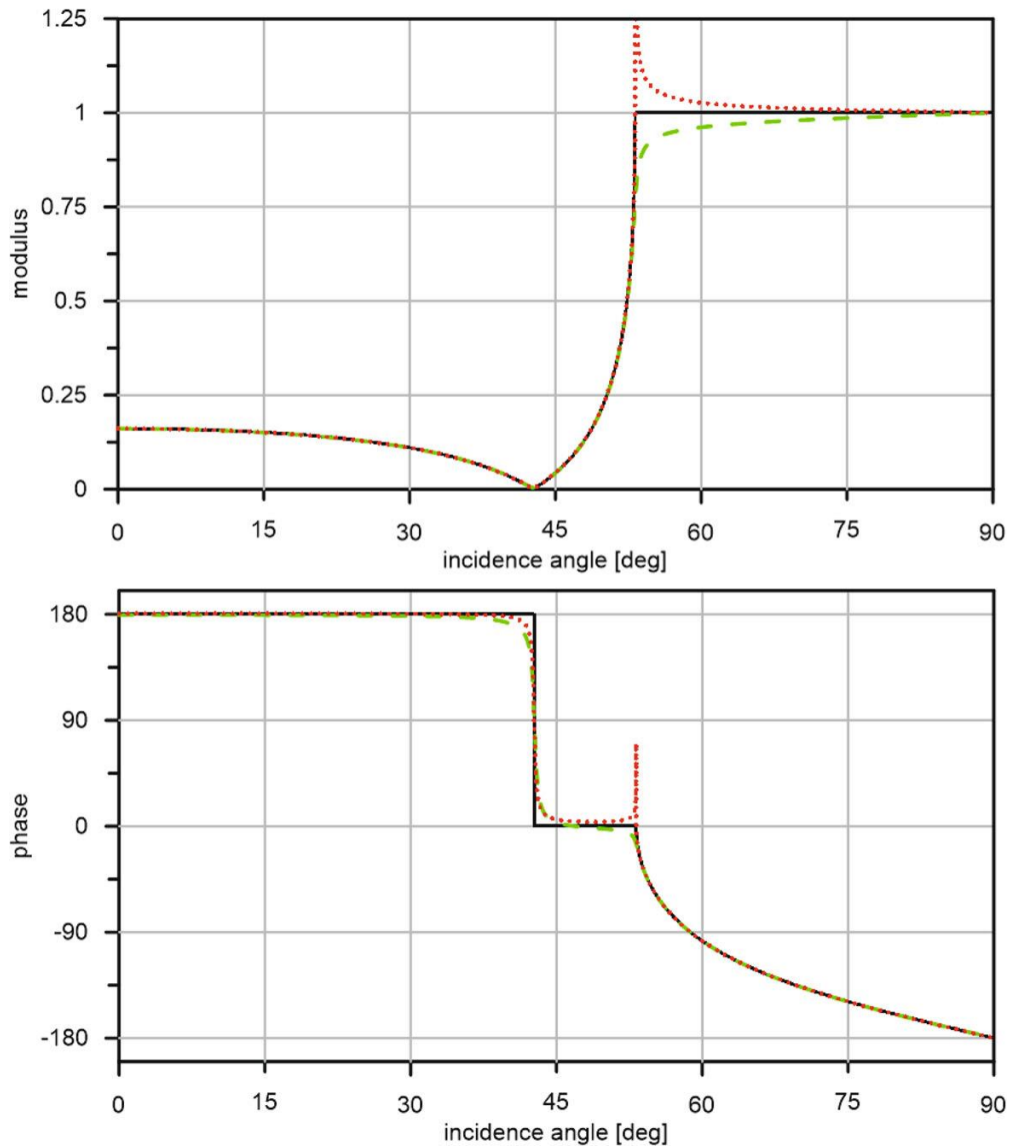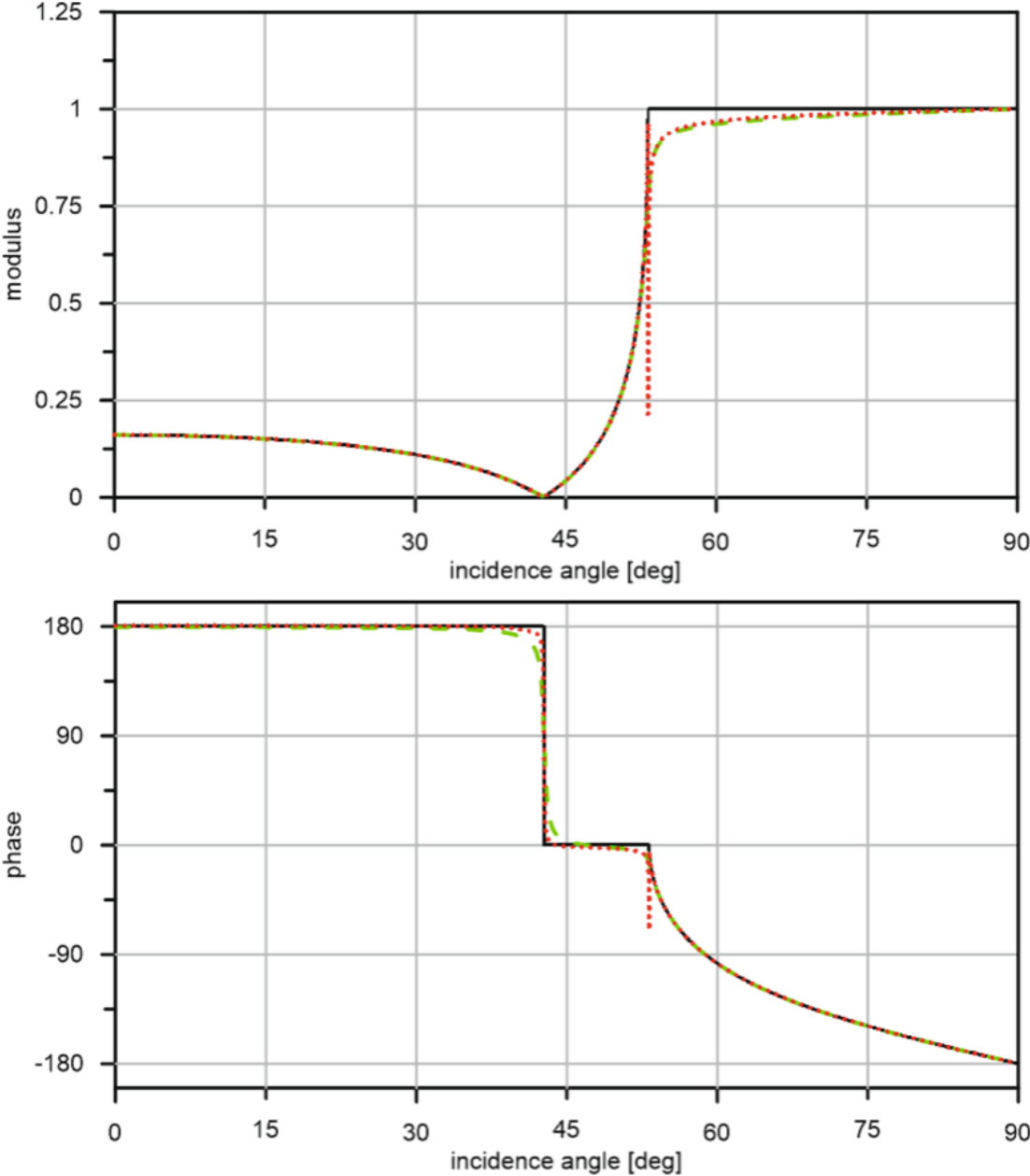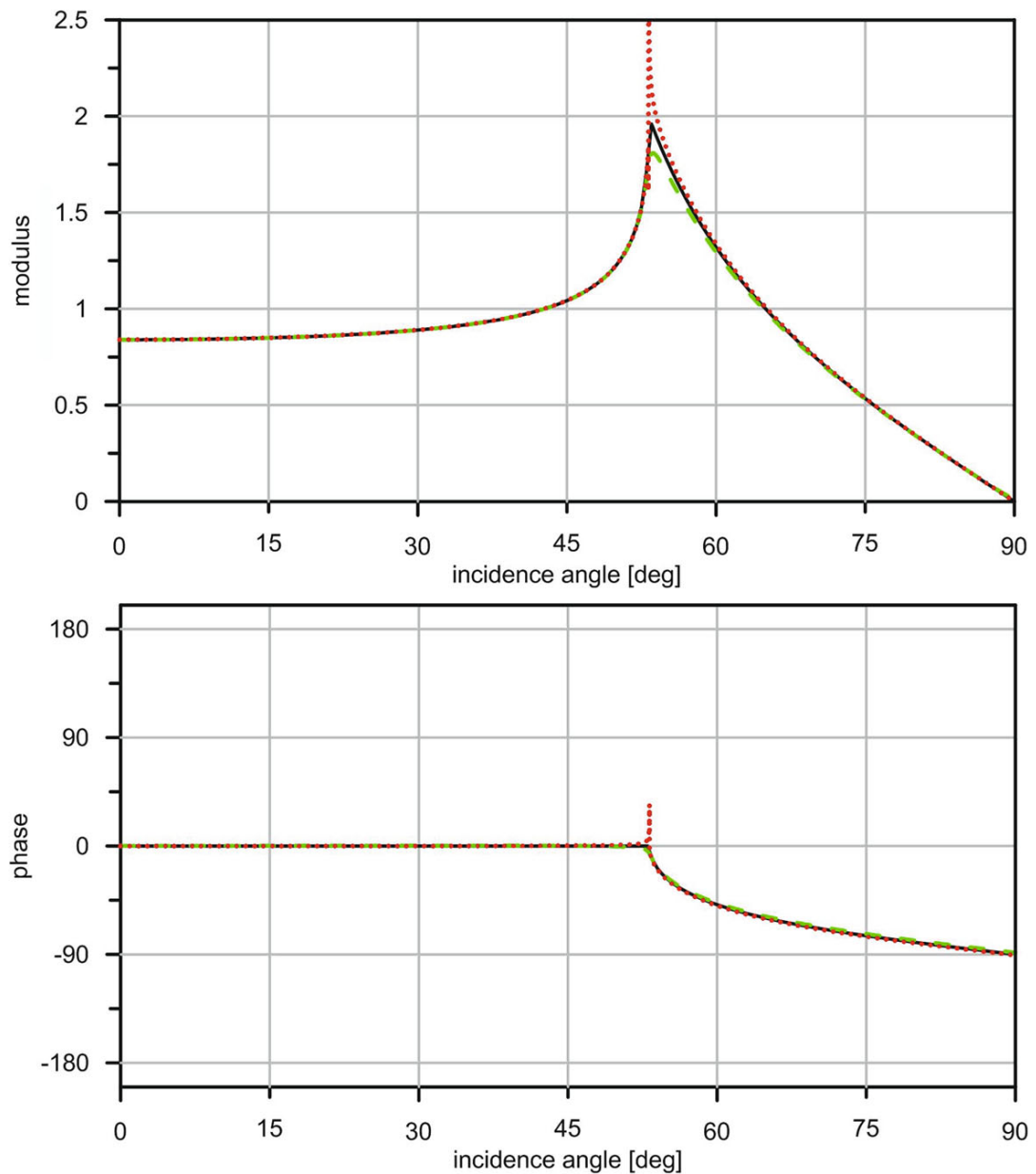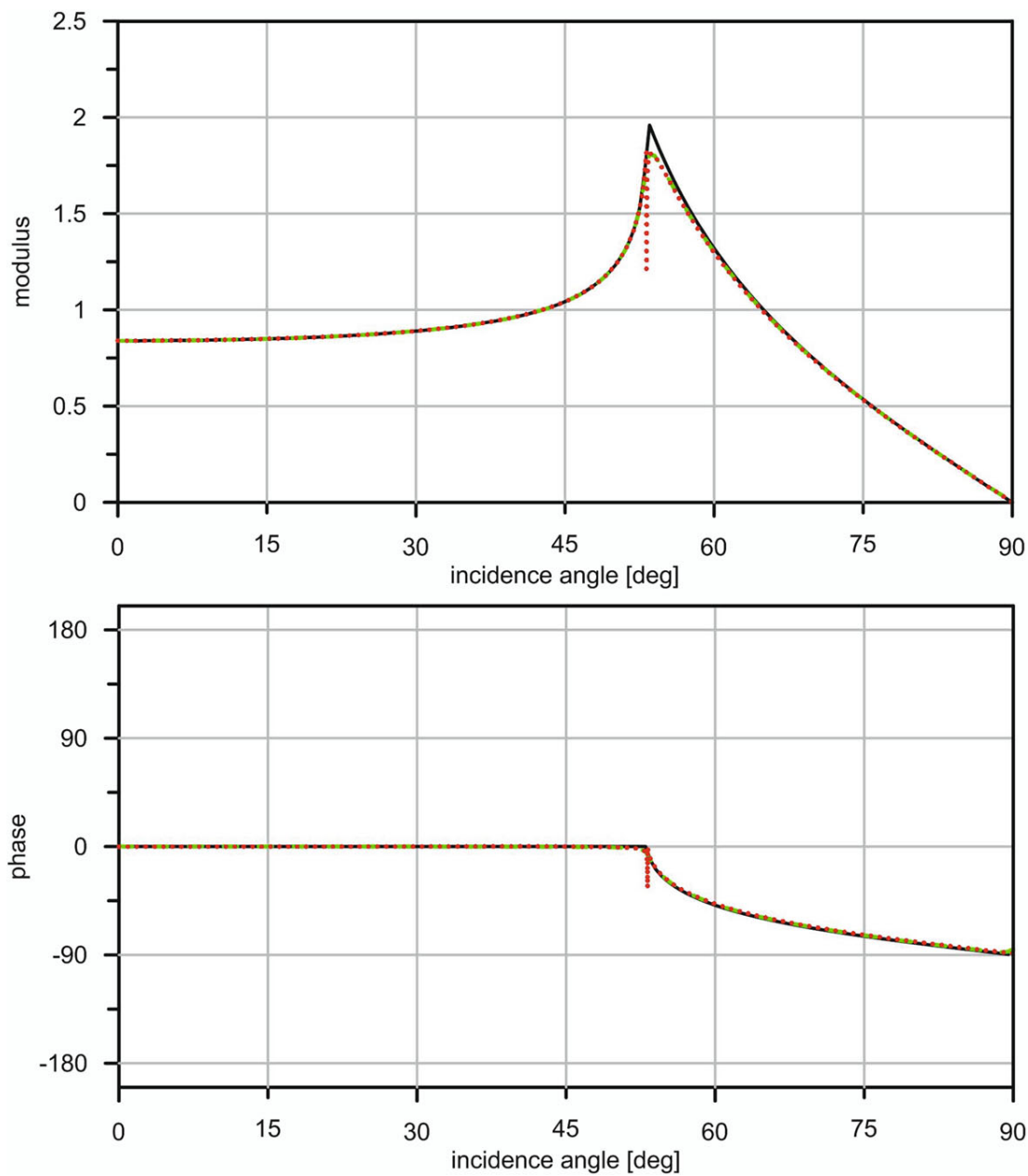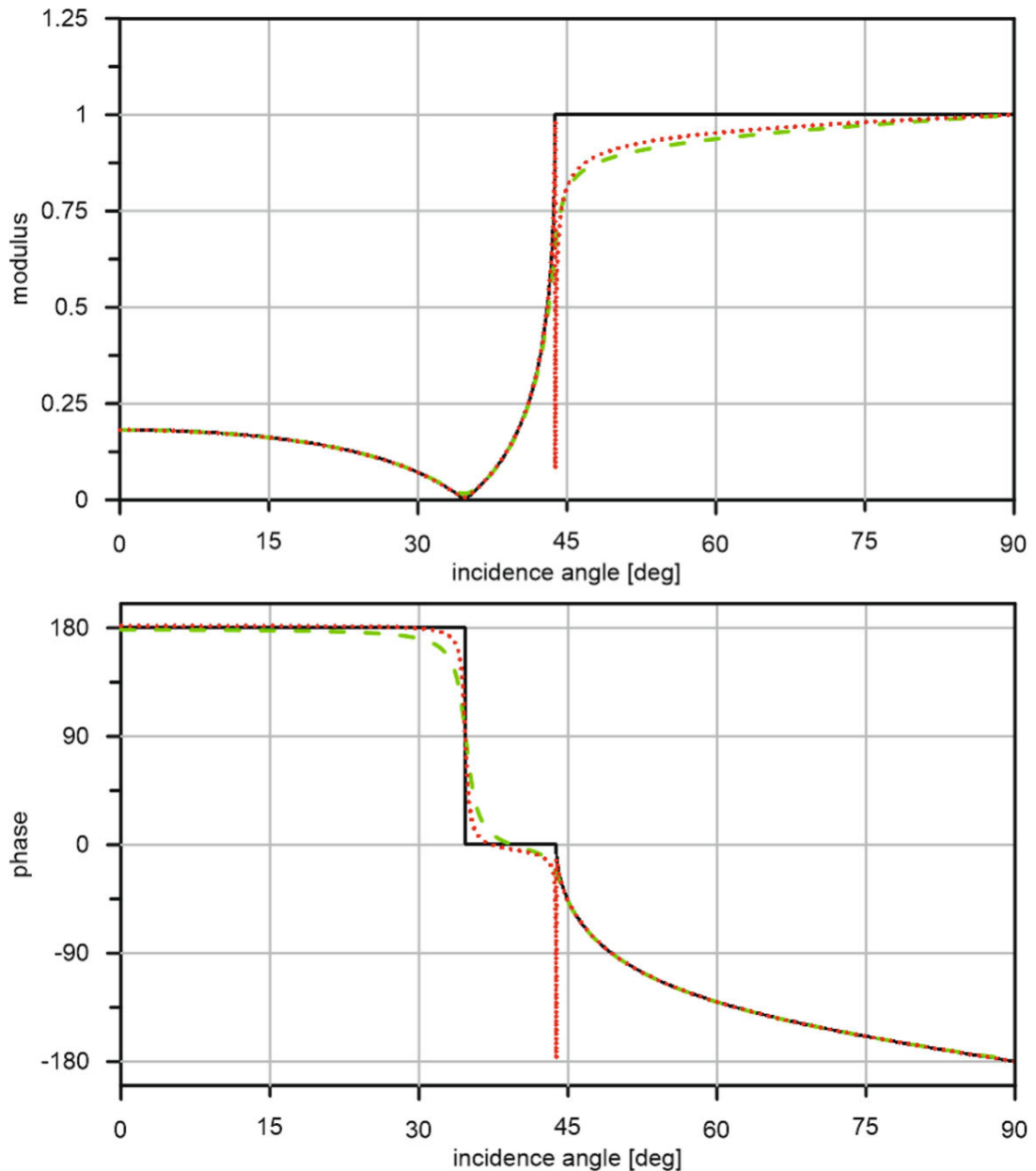

Figure 2.8. Comparison of moduli (top) and phases (bottom) of the SH plane-wave reflection coefficients in the model BC3. Elastic reference (solid black), Daley and Krebs (2015) (dashed green), equation (2.3) with change of sign of Z when it becomes negative (dotted red). Incident homogeneous wave.

41

Comparison of moduli in the overcritical and of phases in the subcritical region shows some differences. They, however, only slightly exceed the differences observable in Figures 2.3 and 2.5, generated for a considerably weaker attenuation. The difference of the modulus of reflection coefficient calculated for the model BC3 with stronger attenuation and of the coefficient calculated for the reference elastic case (black solid) extends farther into the overcritical region. Altogether we can say that comparison with results of independent approach of Daley and Krebes (2015) indicates that WAC approach shows good fit even for interface between media with significantly low values of Q. Let us emphasize that significant majority of rocks (with exceptions of e.g. poorly consolidated near surface sediments) has Q values higher than that of the model BC3. As shown in Chapter 1, Section 4, the ray method with WAC applied in smooth medium provides satisfactory results as well for low values of Q used in the model BC3. Therefore, we can expect tha,t in general, attenuation should not be a limiting factor for using the ray method with WAC.

Let us briefly discuss the factors which affect differences between WAC R/T coefficients when compared to coefficients calculated for elastic reference. From figures 2.5 and 2.8 it seems, that stronger attenuation of media results in stronger influence on R/T coefficients. Yet, the influence of attenuation is slightly more complicated. Pšenčík et al. (2022) have shown that the R/T coefficient at interface between media characterized by the same strength of attenuation have the R/T coefficients equivalent to the coefficients computed for the reference elastic medium. The greater the contrast in strength of attenuation between the layers, the greater the effect of attenuation on R/T coefficients. Therefore, effects of attenuation on R/T coefficients may be very small if contrast of attenuation between layers is very small even if both media are strongly attenuative. Note that it is the best to consider the contrast in strength of attenuation in relation to the difference in Q^{-1} (i.e. attenuation factor A) between layers, see eq. (2.3). This means that, contrast of attenuation considered in Q^{-1} between layers with $Q_1=40$ and $Q_2=10$ is greater than between layers characterized by $Q_1=40$ and $Q_2=1000$. Besides attenuation, there are also other factors involved in computation of SH-wave reflection and transmission coefficients – SH-velocity β and density ρ. Below we

42

briefly illustrate how changes of these coefficients influence effects of attenuation on R/T coefficients. As a benchmark we use elastic reference. The parameters of the models used in tests are shown in Table 2.2. The parameters of the upper half-space are the same for all models. Lower half-space has default values of parameters equal β_2 = 2.5 km/s, ρ_2=2.25g/cm^3 and Q_2=75. We test five values of each of the parameters describing lower half-space layer: β_2, ρ_2, and Q_2 to see how the change of a single parameter affects the R/T coefficients. When we vary one parameter, the other two parameters attain their default values. Note that in each case $\beta_2 > \beta_1$ so that the critical incidence is present.

	β [km/s]	ρ [g/cm^3]	Q
Upper half-space	2.0	2.0	50
Lower half-space	2.05/2.25/**2.5**/2.75/3.0	1.75/2.0/**2.25**/2.5/2.75	25/50/**75**/100/125

Table 2.2. Parameters of the models used in tests. Bold font in cells describing lower half-space indicate default value.

Analysis of Figures 2.3-2.8 where WAC coefficients were shown indicates that for moduli of the R/T coefficients, the visible difference between WAC and elastic reference is present in 2 regions. First is vicinity of the Brewster angle (the moduli of WAC coefficients there are non-zero) and second is the vicinity of the critical angle and behind. The differences between WAC and elastic reference around Brewster angle are very small, therefore we do not focus on this region. Differences from the vicinity of the critical angle onwards are much greater. Results provided using the approach of Daley and Krebes (2015) show that the greatest difference between elastic and anelastic moduli is directly at the critical incidence. Nevertheless, the ray method and equation (2.3) fail in the vicinity of the critical angle. In Figure 2.9 we show the zoom of the modulus calculated for model BC2 around the critical incidence. From Figures 2.3-2.9 we can see, that the interval before the critical incidence where results of Daley and Krebes deviate from elastic reference is very short. At the same time the WAC coefficient in this region is affected by the singularity and provides erroneous results. Therefore, we do not focus on region

before the critical incidence in our tests. Obviously, WAC coefficient is affected by the singularity directly behind critical incidence as well. In Figure 2.10 we summarize the results of tests. To avoid showing region with erroneous results, in Figure 2.10 we show effects of the attenuation on moduli of R/T starting from the critical incidence +1 degree. Effects of attenuation are illustrated as a difference between moduli calculated for elastic reference and WAC. The graphs are calculated (when possible) up to 30 deg above the critical incidence. Note that when we change value of β_2, the critical incidence varies: for β_2=2.05 km/s critical angle is at ~88 degrees, for β_2=3.0 km/s it is at 41 degrees.
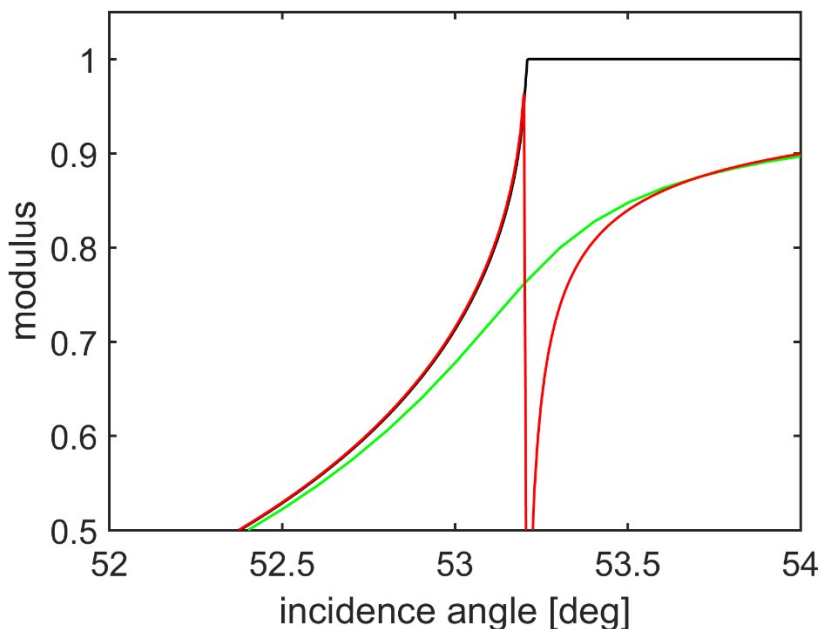
Figure 2.9. Zoom of the Figure 2.5a showing results around the critical incidence. Moduli of the model BC2 calculated for elastic reference (black), Daley and Krebes aproach (2015) (green) and equation (2.3) with change of sign of Z when it becomes negative (red). Incident homogeneous wave.

We can see that when we change β_2, the effects of attenuation on R/T coefficients are stronger if β_2 is closer to β_1. Again, for $\beta_1 \sim \beta_2$ the critical angle is placed at incidence close to 90 deg, therefore this increased effect can be observed only for very distant offsets. Changing values of density only, does not affect coefficients in a significant way. As expected contrast in strength of attenuation at the interface is important factor influencing coefficients. Let's note again that

contrast of the strength of attenuation should be regarded in relation to Q^{-1}. Then, for the first half-space with $Q_1=50$, the attenuation effects on moduli of R/T coefficient is stronger for model with $Q_2=25$, than for model with $Q_2=125$. This also means that model with $Q_2=125$ provides greater differences when compared to elastic moduli than models with $Q_2=75$ or 100. We can also note that attenuation affects more moduli of reflection than moduli of transmission.
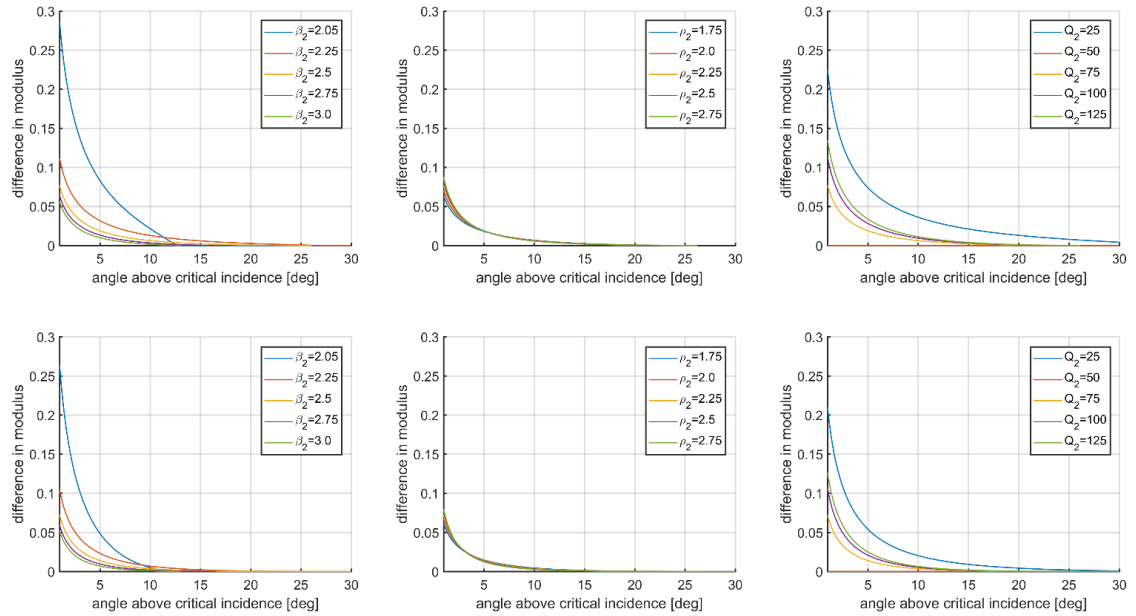
Figure 2.10. Differences between moduli of elastic and anelastic coefficients calculated using eq. (2.3) for angles starting at 1 degree behind critical incidence and onward. Parameters of the used models are shown in Table 2.2. Each panel shows results for models with changes of single parameter in second half-space: β_2 (left panels), ρ_2 (middle panels) and Q_2 (right panels). a) reflection and b) transmission.

2.1.3 Incident inhomogeneous waves

As discussed in the Section 2.1.1, waves are inhomogeneous when the propagation and attenuation vectors do not point in the same direction. Transmitted waves are mostly inhomogeneous even if waves generating them homogeneous. For example, after hitting an interface, the incident homogeneous wave generates a transmitted homogeneous wave only at the 0 deg incidence. In this case The inhomogeneity of transmitted wave increases with angle of incidence as shown in Figure 2.2. Equation (2.3) allows calculation of the reflection and transmission

coefficients for the incident inhomogeneous waves. Figures 2.11 show reflection coefficients calculated for the model BC2 for inhomogeneity angles γ=15, 30 and 45 deg and Figure 2.12 for γ=-15, -30 and -45 deg. Figures 2.13 and 2.14 show transmission coefficients for cases corresponding to Figures 2.11 and 2.12, respectively. The artificial change of the sign of Z is applied when necessary.
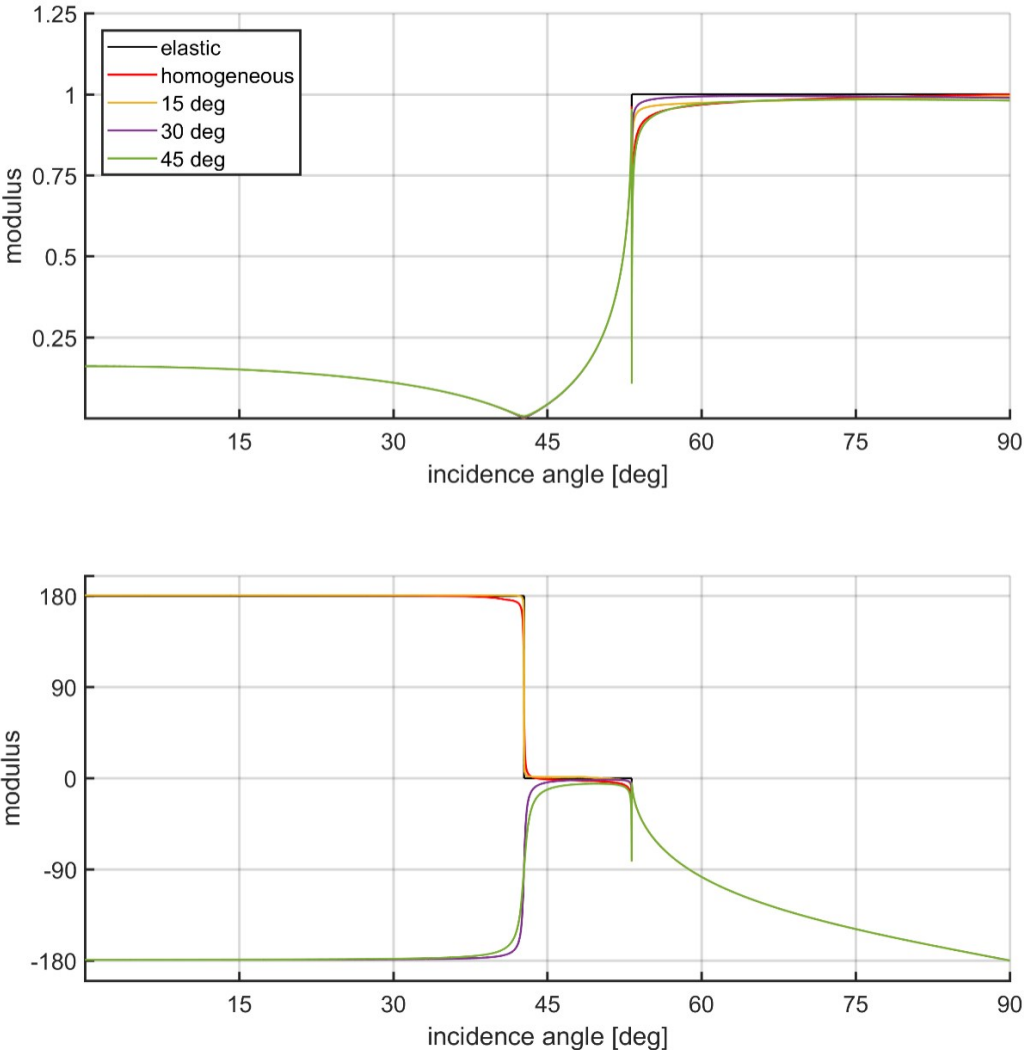
Figure 2.11. Comparison of moduli (top) and phases (bottom) of WAC SH plane-wave reflection coefficients in the model BC2 for varying inhomogeneity of the incident wave: γ = 15, γ = 30 and γ = 45 deg. Curves for elastic reference and for homogeneous incident wave are included for comparison.

Figure 2.12. Comparison of moduli (top) and phases (bottom) of WAC SH plane-wave reflection coefficient sin the model BC2 for varying inhomogeneity of the incident wave: γ = -15, γ = -30 and γ =-45 deg. Curves for elastic reference and for homogeneous incident wave are included for comparison.

Figure 2.13. Comparison of moduli (top) and phases (bottom) of WAC SH plane-wave transmission coefficients in the model BC2 for varying inhomogeneity of the incident wave: $\gamma = 15$, $\gamma = 30$ and $\gamma = 45$ deg. Curves for elastic reference and for homogeneous incident wave are included for comparison.
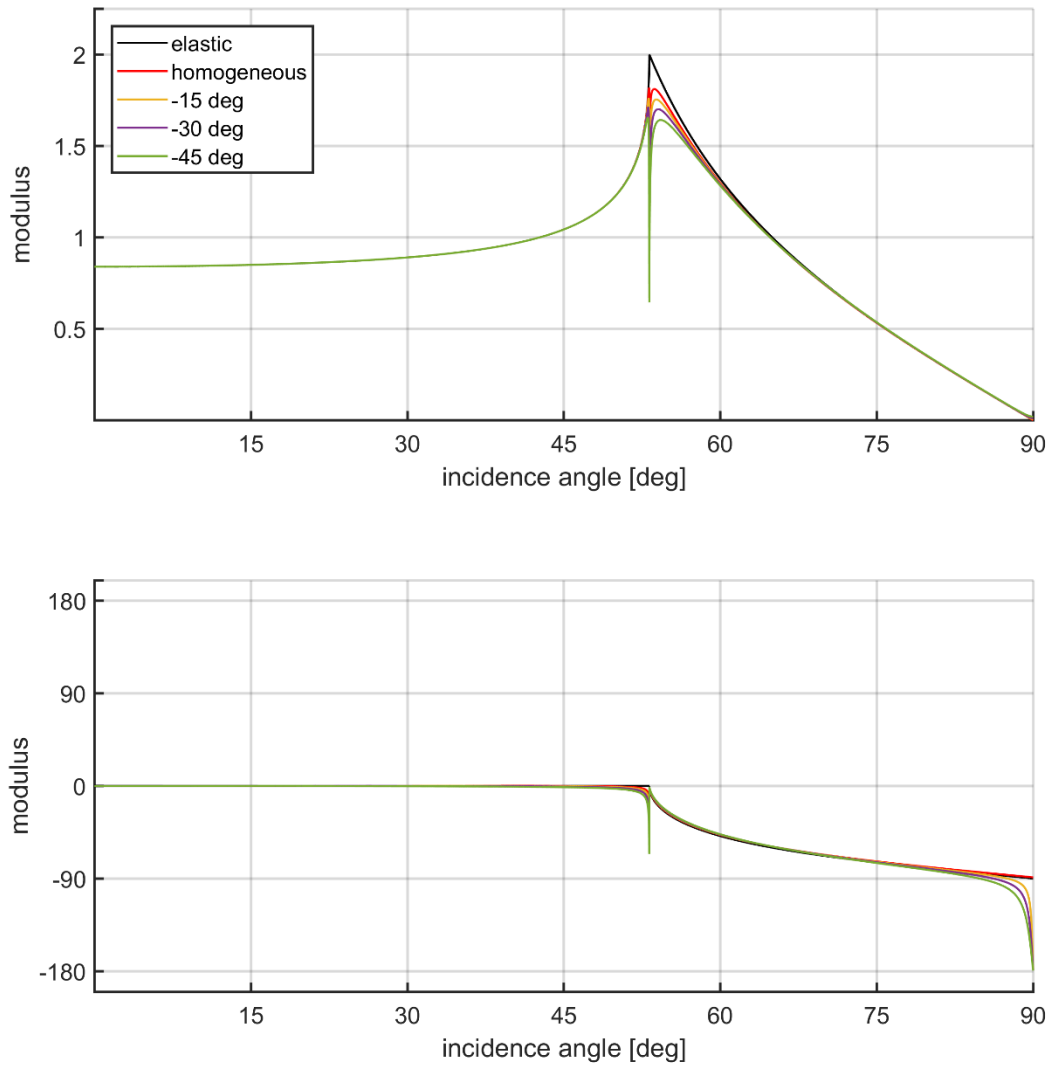
Figure 2.14. Comparison of moduli (top) and phases (bottom) of WAC SH plane-wave transmission coefficients in the model BC2 for varying inhomogeneity of the incident wave: γ = -15, γ = -30 and γ =-45 deg. Curves for elastic reference and for homogeneous incident wave are included for comparison.

For reflection coefficients in the subcritical region, moduli corresponding to incident inhomogeneous wave, similarly to moduli for incident homogeneous wave, closely follow the curves corresponding to the elastic reference. For phases of the coefficients in the subcritical region, noticeable differences are present starting from the vicinity of the Brewster up to critical angle. Around the Brewster angle, where the differences in phase of the coefficient are significant, the amplitudes of reflected

waves are very small. However, closer to critical incidence, where moduli are relatively high, differences between phase of the coefficient computing using WAC and elastic reference are relatively small. Inhomogeneity slightly influences the moduli of coefficients from the critical region onwards. When investigating transmission coefficients, we see, that inhomogeneity affects the differences between moduli of elastic reference and moduli of WAC coefficients in the vicinity of the critical incidence. Interestingly when examining phase of the transmission coefficients, we see that for incidence angles close to 90 degrees, there is substantial deviation of phases of inhomogeneous waves from the elastic reference case. We can note, that the increase of inhomogeneity does not automatically translate to stronger attenuation effects at the interface (understood as difference between WAC coefficients and elastic reference). For example, the coefficient for γ =15 deg is closer to the elastic reference than coefficient for incident homogeneous wave (γ =0). In Figure 2.30, we may also see that for model BC2, for angles significantly above the critical angle, the modulus of the reflection coefficient slightly exceeds 1, which is a failure of the WAC.

2.2 SH-wave seismograms in attenuative, isotropic media with interfaces

Equations (2.3–2.13) that allow computation of SH-wave R/T coefficients in the attenuative, isotropic media with interfaces were implemented into the SEIS software package (Červený and Pšenčík, 1984), which was originally only able to deal with effects of attenuation in a smooth medium. Modified SEIS package allows now calculation of SH-wave ray synthetic seismograms in 2D isotropic, layered, inhomogeneous, and attenuative media. We compare results obtained with the modified SEIS software package with results of full-wave method developed by Carcione et al. (2006) that was already used as an exact benchmark for the ray method in Chapter 1, section 4. First, we show the results of the test of a reflection from a single interface. We also discuss the issue of the frequency-dependent attenuation and its effect on reflection/transmission coefficients. Further we present results of tests of reflection from the bottom interface in the model with two interfaces

2.2.1 Seismograms of reflected wave in medium with a single interface

The first model used for testing consists of two half-spaces separated by a horizontal interface as shown in Figure 2.15. The source and a set of receivers are all distributed along a horizontal profile in the upper half-space. No free-surface effects are considered at receivers. The offset of the first receiver from the source is 0.005 km, the separation of receivers is 0.02 km. The reflector is situated at a depth of 0.248 km below the receiver profile. Each half-space is described by three parameters: SH velocity β and quality factor Q that are defined at the reference frequency ω_r = 2π60 rad/s (60 Hz), and density ρ. The Maxwell attenuation model described in Chapter 1, Section 3 by equation (1.12) is used in the tests of seismograms throughout this chapter. We consider three models (M1, M2, M3). Values of β, Q and ρ specifying these models are given in Table 2.3. The models differ by Q values. S-wave velocities and densities are the same, therefore the offset of the critical point on the receiver profile in all models is the same and is located at ~0.506km. In order to make models as simple as possible, the densities are chosen so that the Brewster angle is avoided.
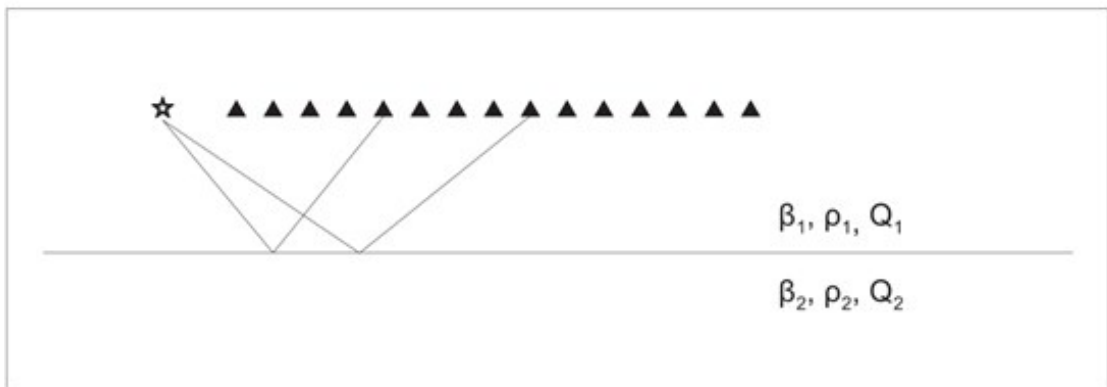
Figure 2.15. Configuration used in tests. The depth of the reflector below the source-receiver profile is 0.248 km. Values of parameters of the half-spaces are given in Table 2.3.

Model	β_1 [km/s]	β_2 [km/s]	ρ_1 [g/cm^3]	ρ_2 [g/cm^3]	Q_1	Q_2
M1	2.0	2.8	2.4	1.5	∞	∞
M2	2.0	2.8	2.4	1.5	∞	60
M3	2.0	2.8	2.4	1.5	40	60

Table 2.3. Parameters of models used in computations of seismograms using ray method and full-wave method as a benchmark.

Results for the model M1, in which both half-spaces are elastic, allows us to evaluate the accuracy of the ray method in elastic medium, where the WAC does not play a role. Results for the model M2 indicate what is the effect of the attenuation at the interface only. Results for the model M3 shows combined effects of the attenuation on waves within the medium and at the interface. Figure 2.16 shows the reflection coefficients for all three models. We may see that attenuation in the model M2 has the strongest effect on reflection coefficient – the contrast of the attenuation strength at the interface is greater than for model M3. Seismograms are generated by a point source with unit isotropic radiation pattern and Ricker signal with dominant frequency of 60 Hz as source-time function. The source-time function is adjusted to compute seismograms in 2D models using the ray method similarly as it was done in the Chapter 1, Section 4.
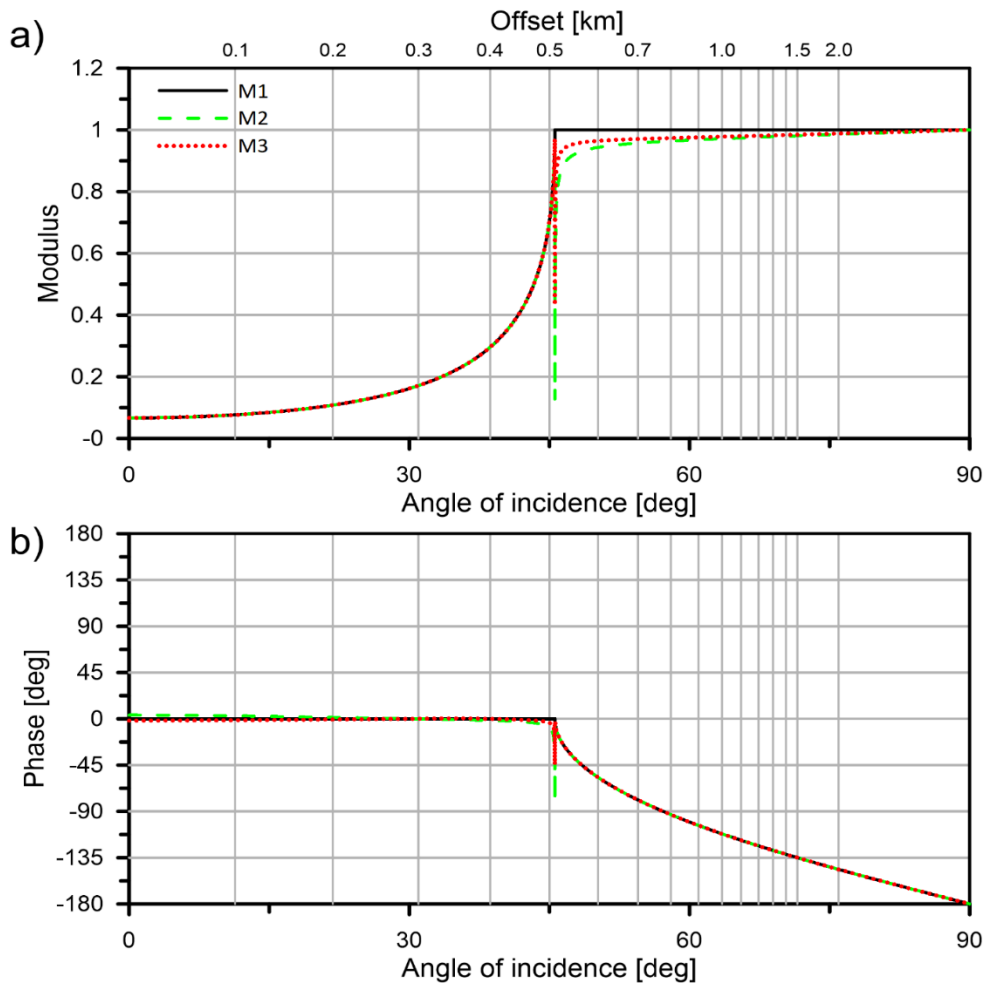
Figure 2.16. SH-wave reflection coefficients for models M1, M2 and M3 at the reference frequency of 60Hz; a) moduli and b) phases.

In the following plots, we present comparison of full-wave SH-wave seismograms (red) overlaid by SH-wave ray seismograms (black). The ray seismograms are computed using single-frequency reflection coefficients computed for medium parameters at the reference frequency of 60 Hz. Unless stated otherwise, the same scaling factor is used in presented seismograms.

Figure 2.17 shows the seismograms computed in model M1 (both half-spaces are elastic). We see that up to the vicinity of the critical angle, there is almost a perfect fit of ray and full wave seismograms. Some (red) disturbances are observed as later arrivals behind the reflected wave. These are "ghost" waves caused by numerical errors in the full-wave computations. Some differences between ray and full-wave synthetic seismograms exist in the vicinity (particularly behind) of critical

angle that is indicated by full triangle. They are caused by limited applicability of the ray method in this region. Differences are caused by the head wave, which is correctly calculated in the full-wave seismograms, but missing in ray results. For offsets larger than 0.9 km, the head wave starts to separate from the reflected wave and appears before the main arrival. In this region we can observe again a perfect fit of ray and full-wave reflected waves.

Figure 2.17. Full-wave seismograms (red) overlaid by ray seismograms (black) in model M1 with both half-spaces elastic. Full triangle indicates the position of the critical point. Red arrivals preceding the reflections behind the critical point are head wave. Later red arrivals are numerical errors of the full-wave method.

Seismograms computed for larger offsets are not shown here. The reason is the fact that waveforms of reflected waves generated by both codes at larger offsets are practically identical. Comparison of ray and full wave seismograms in Figure 2.17 serves as a reference for comparisons of seismograms affected by attenuation.

Seismograms shown in Figure 2.18 are generated in model M2, in which the upper half-space remains elastic and the bottom half-space is anelastic. The only way how attenuation can affect seismograms of reflected wave in model M2 is at the reflection point. Differences of similar magnitude as for model M1 can be observed in the critical region, in which the ray results are unacceptable anyway. Comparison

54

of Figures 2.17 and 2.18 indicates that Gajewski and Pšenčík (1992) did not make a significant mistake when they ignored effects of attenuation on the reflection/transmission in their study.

Figure 2.19 shows the comparison of full wave and ray seismograms in model M3 with both half-spaces attenuating. Due to significant effects of attenuation on the propagation of the wave in the upper half-space, amplitudes of arriving waves shown for the model M3 are significantly smaller than for models M1 and M2. Therefore, seismograms in Figure 2.19 have their amplitudes doubled so that the differences between the ray method and full-wave method are clearly visible. Figure 2.19 show how strongly the attenuation affects propagating waves, but also indicates if application of WAC approximation is detrimental to accuracy of the ray method. As in previous figures, we can observe very good fit of full-wave and ray seismograms outside the critical region. We can see that attenuation suppressed the "ghost" waves generated by the full-wave code and also reduced amplitudes of head wave, which is hardly observable.
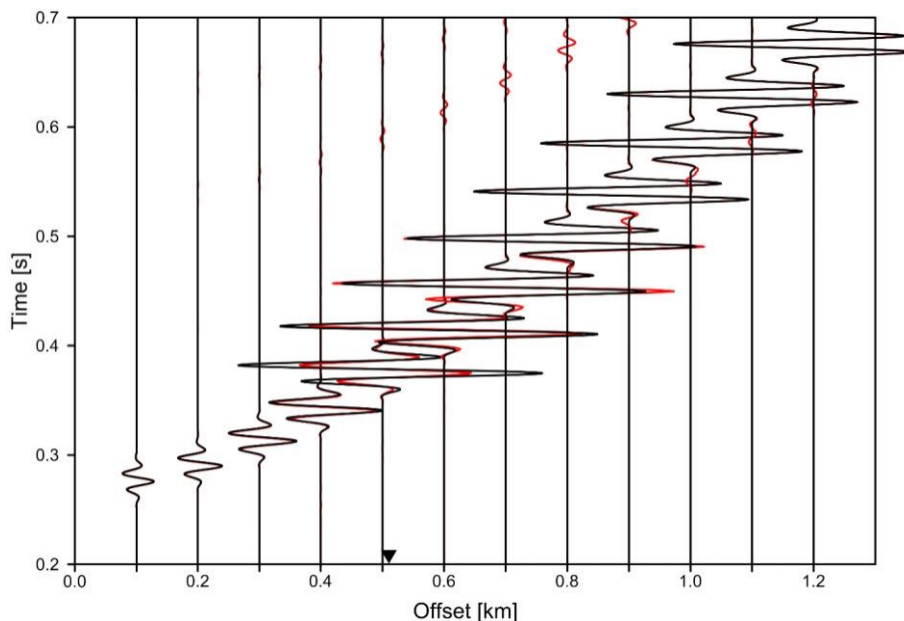
Figure 2.18. Full wave seismograms (red) overlaid by ray seismograms (black) in model M2 (first half-space elastic, second anelastic). Full triangle indicates the position of the critical point. Red arrivals preceding the reflections behind the critical point are the head wave. Later red arrivals are numerical errors of the full-wave method.
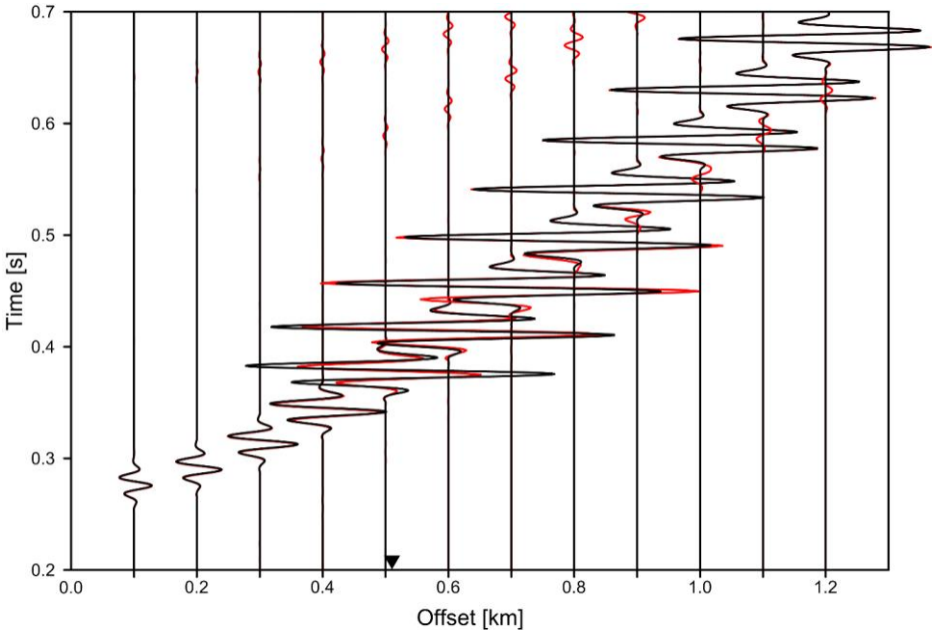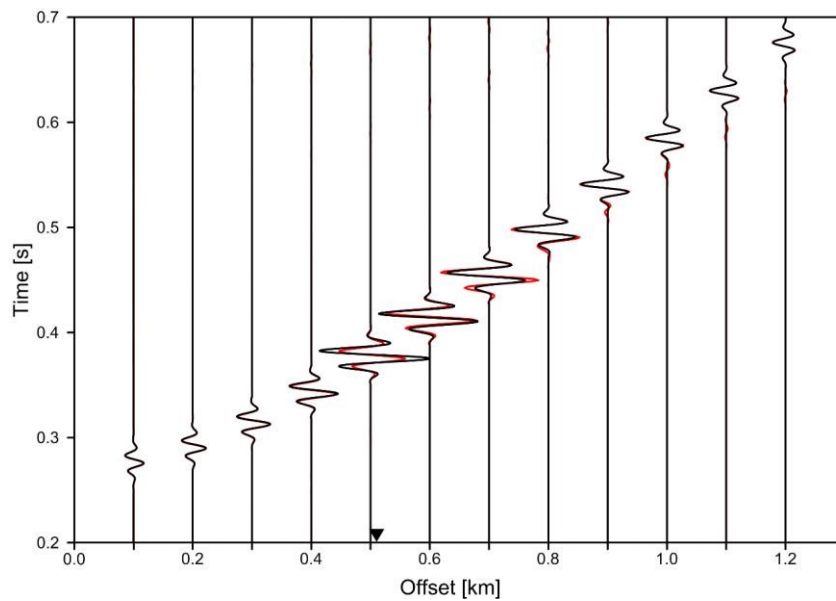
Figure 2.19: Full-wave seismograms (red) overlaid by ray seismograms (black) in model M3 with both half-spaces anelastic; doubled amplitudes. Full triangle indicates the position of the critical point.

So far, we presented comparisons of synthetic seismograms. Equally valuable are comparisons of maximum spectral amplitudes. Figures 2.20, 2.21 and 2.22 show comparisons of ray (black) and full-wave (red) maximum spectral amplitudes for models M1, M2 and M3, respectively. They show the above discussed incorrect behavior of the ray results in the vicinity of the critical incidence. This region is sampled more densely. Specifically, one can observe increase of ray amplitudes to infinity from the subcritical region and their slow smooth decay in the overcritical region. On the contrary, the full-wave results behind the critical incidence display oscillations caused by the existence of the head wave. The oscillations further away for offsets larger than 1.5 km are numerical errors (ghost waves).

56
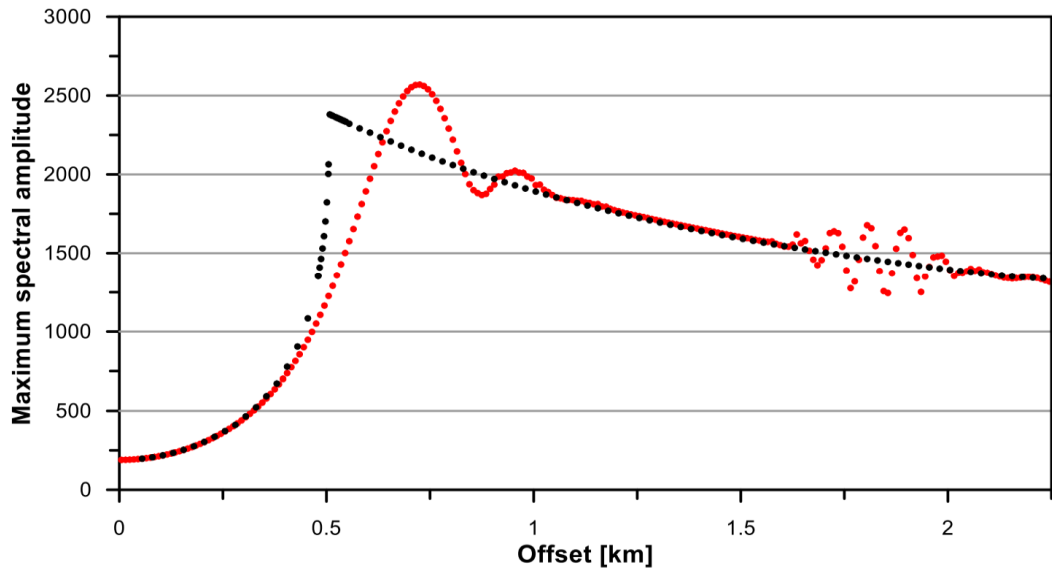
Figure 2.20. Maximum spectral amplitudes for model M1 calculated by the full wave method (red) and by the ray method (black). Note the differences in the vicinity of critical point (~0.506 km) and in the overcritical region (1.5-2 km). In the former case, they are caused by ignoring head wave ignored in ray computations, in the latter case, they are caused by numerical errors in the full wave computations.
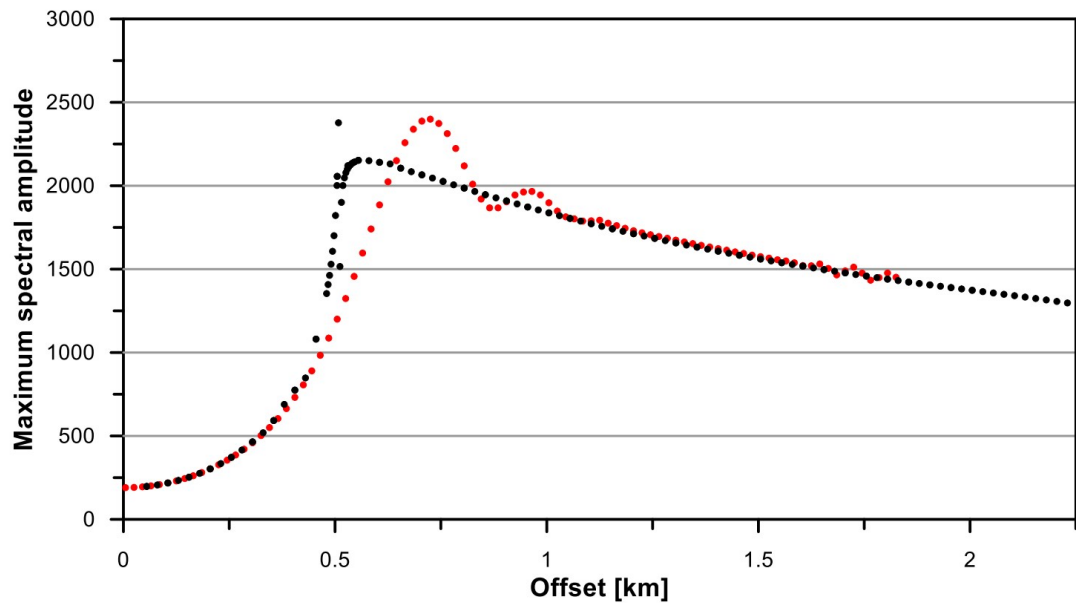
Figure 2.21. Maximum spectral amplitudes for model M2 calculated by the full wave method (red) and by the ray method with WAC (black). Note the differences around the critical point (0.506 km). Note suppressed ghost waves for offsets >1.5 km (due to propagation in the second layer, which is attenuative in model M2).

57
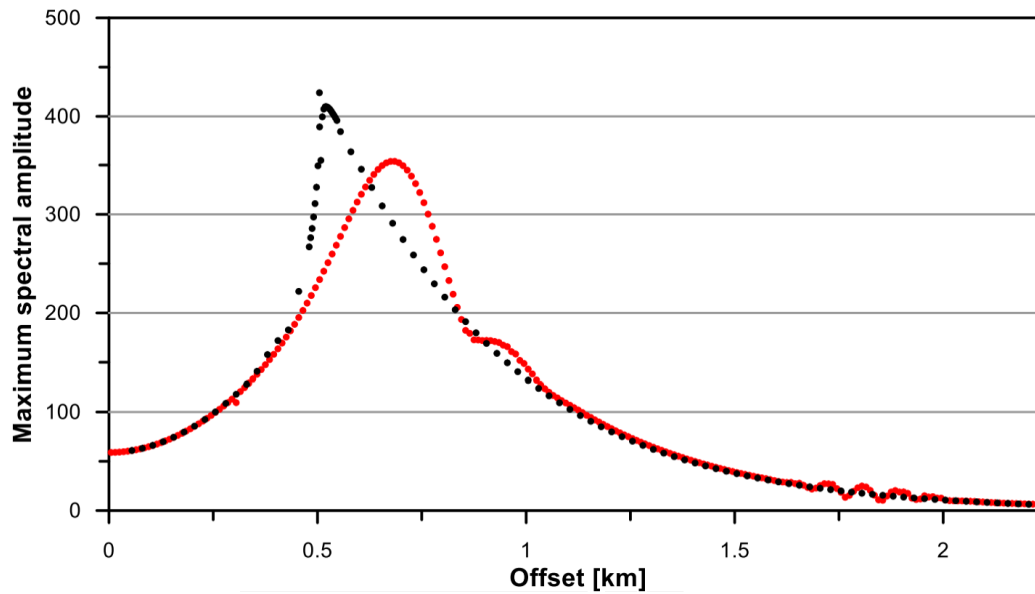
Figure 2.22: Maximum spectral amplitudes for model M3 calculated with the full wave method (red) and by the ray method (black). Note reduced amplitude scale with respect to Figures 2.20 and 2.21.

2.2.2 Frequency dependency of the SH-wave reflection coefficients

In Chapter 1, we have shown that in order to obtain causal arrivals, we need to use models of attenuation and velocity that are frequency dependent. Therefore, at each frequency there is generally a different value of the R/T coefficient. The results shown in Figures 2.17 to 2.22 for the ray method were computed using reflection coefficients calculated for a single (reference) frequency ω_r value. Here, we would like to estimate the error that was introduced by ignoring frequency dependency of the R/T coefficients. In Chapter 1, we introduced three dispersion models: Futterman, SLS and Maxwell model. Figure 2.23 shows how the phase velocity and Q vary in model M3 when Futterman, SLS and Maxwell models are applied. We see that between 1-250Hz, the phase velocities vary only by up to ~3%, but Q changes can be very pronounced for SLS and, in particular, for Maxwell model. Figures 2.24 (Futterman model), 2.25 (SLS model) and 2.26 (Maxwell model) show moduli and phases of reflection coefficients for model M3 computed for frequencies equal 20, 40, 60, 80 and 100 Hz. We see that for these frequencies the reflection coefficients are only slightly dependent on the frequency – the greatest variations of

58

moduli of coefficients calculated for different frequencies are from the vicinity of the critical angle onwards for the Maxwell model. This is due to strongest variations of Q ith frequency as shown in Figure 2.23
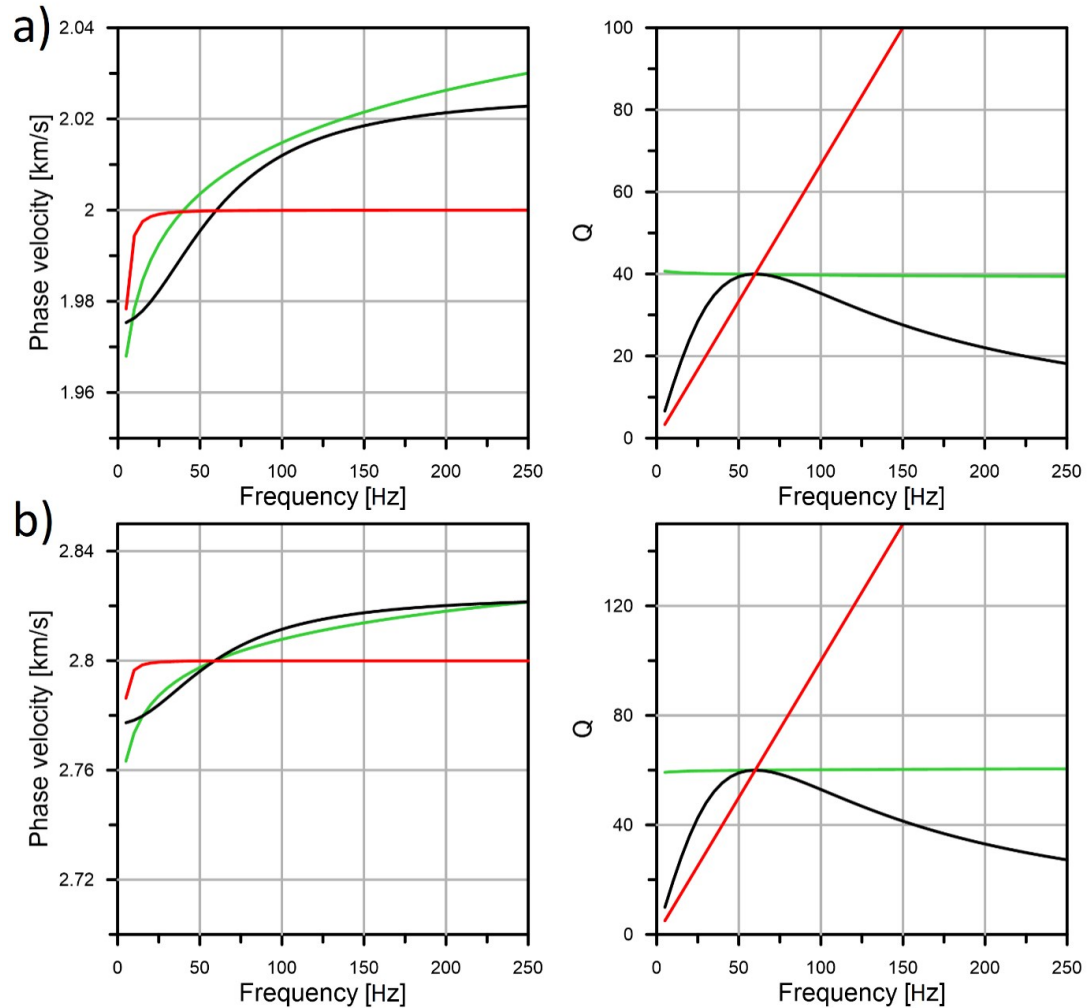
Figure 2.23. Phase velocities (left panels) and Q factors (right panels) for Futterman model (green), SLS model (black) and Maxwell model (red) in model M3; a) properties of the first half-space: Futterman and Maxwell models: reference frequency ω_r =2π60 rad/s (60Hz): $v_p(\omega_r)$=2.0 km/s and $Q(\omega_r)$=40. SLS model is computed for the relaxation time t_r=1/60s, V_{pr}=1.975km/s and $Q(\omega_r)$=40; b) properties of the second half-space: Futterman and Maxwell models at ω_r=2π60 rad/s (60Hz): $v_p(\omega_r)$=2.8 km/s and $Q(\omega_r)$=60. SLS model is computed for the relaxation time t_r = 1/60s, V_{pr}=2.777km/s and $Q(\omega_r)$=60.
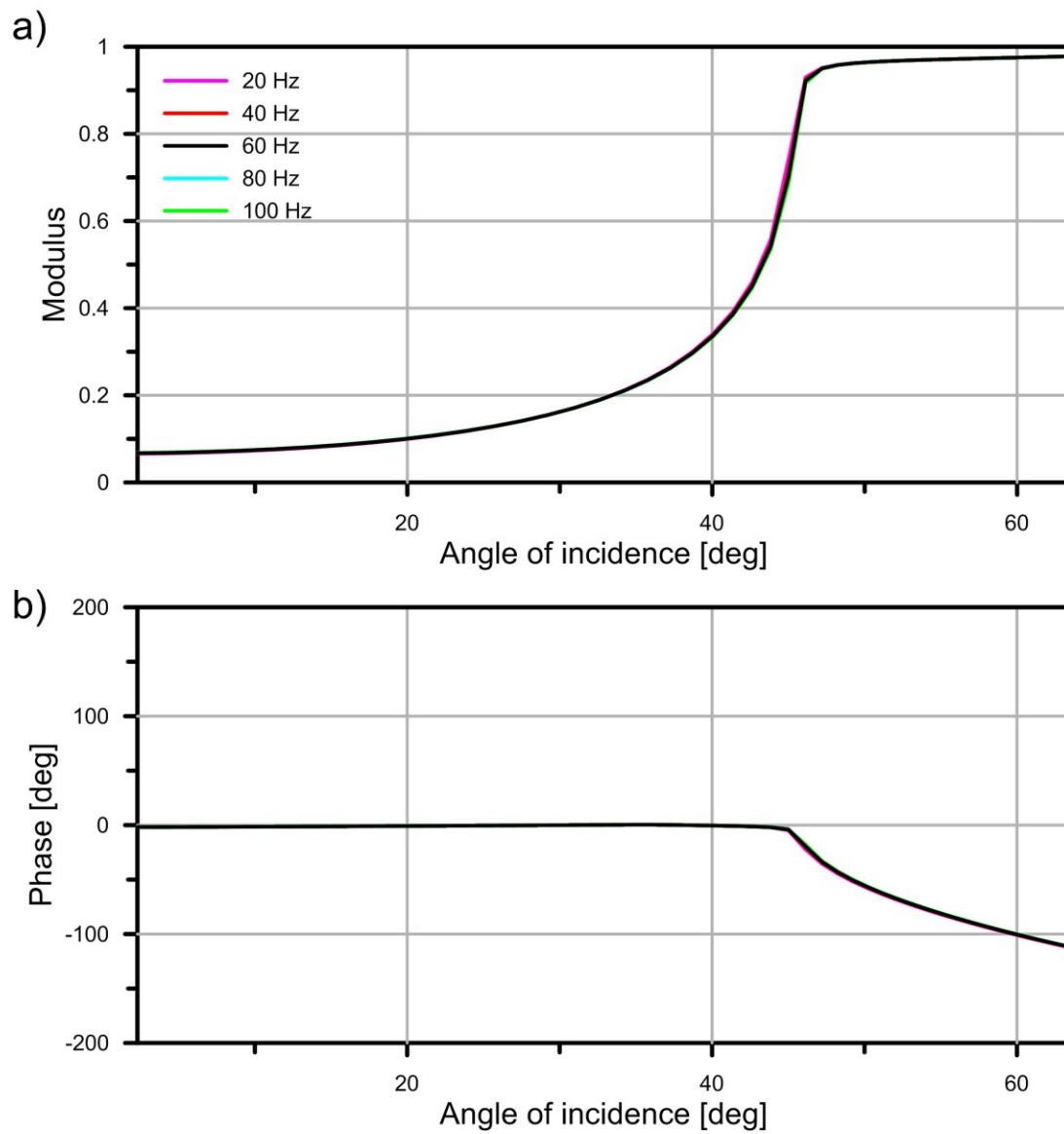
Figure 2.24. a) Moduli and b) phases of SH plane-wave reflection coefficients for the model M3 calculated at 20, 40, 60, 80 and 100 Hz for the model M3 with Futterman dispersion.
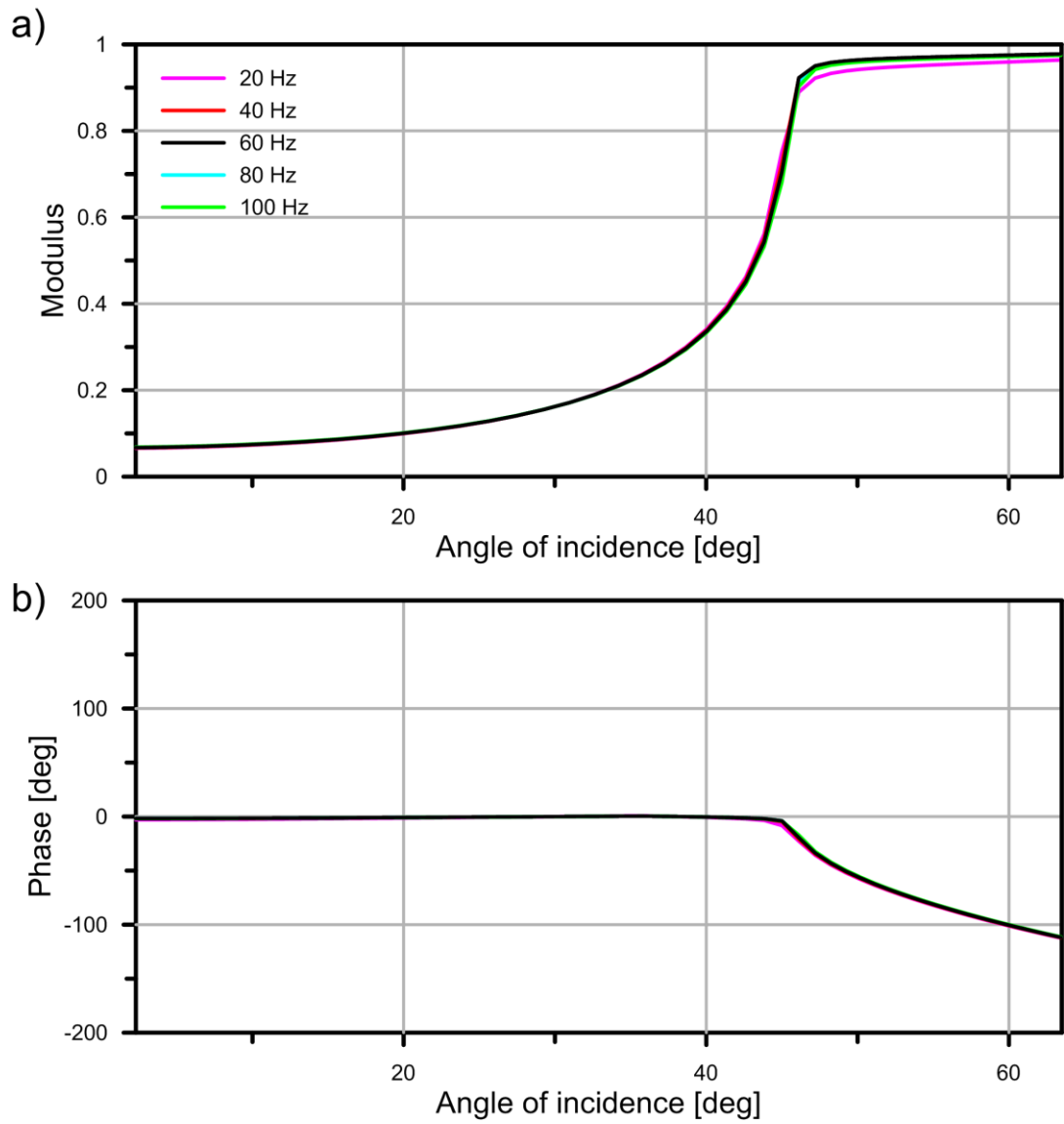
Figure 2.25. a) Moduli and b) phases of the SH plane-wave reflection coefficients for the model M3 calculated at 20, 40, 60, 80 and 100 Hz for model M3 with SLS dispersion.

a)

b)
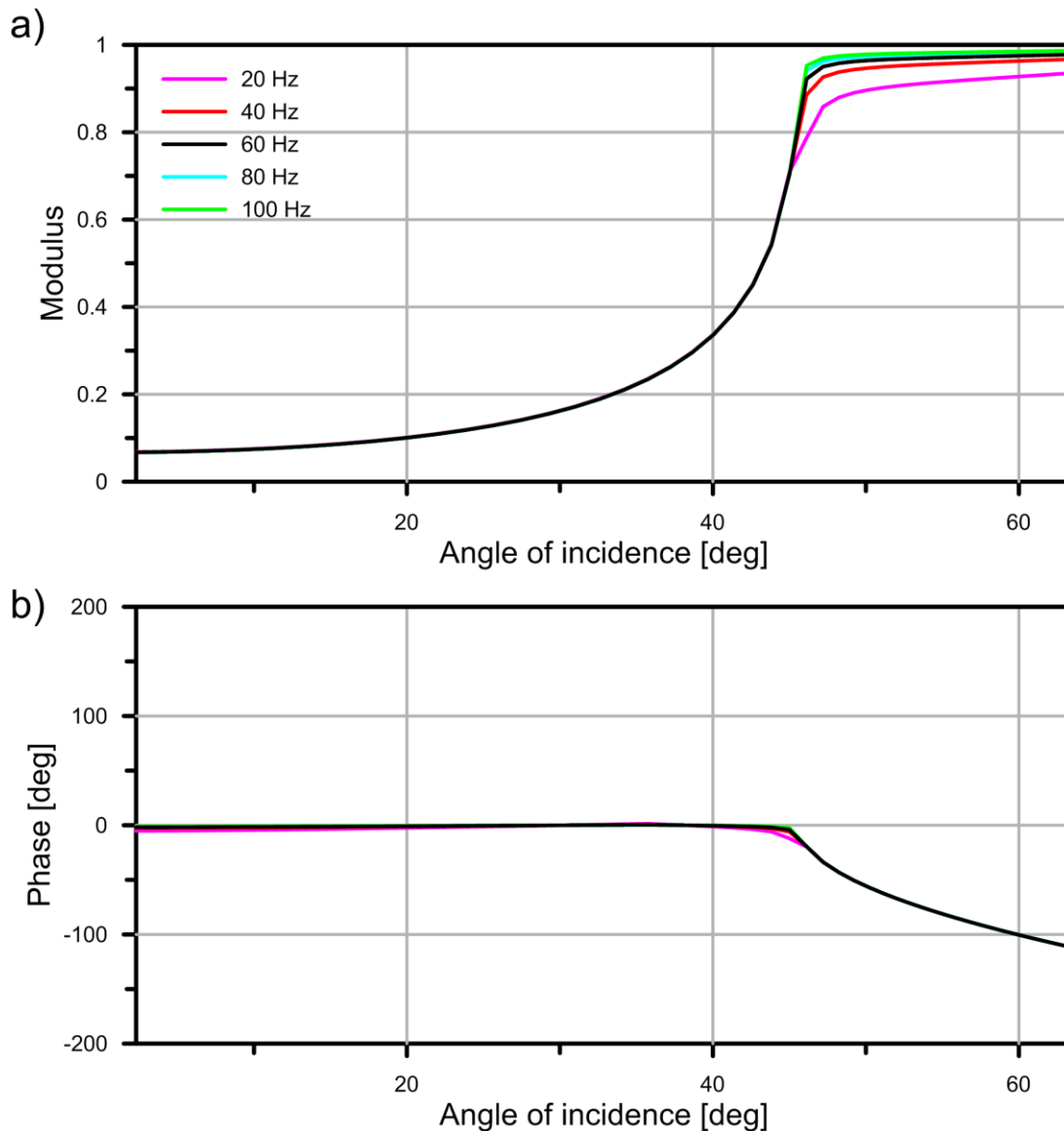
Figure 2.26. a) Moduli and b) phases of SH plane-wave reflection coefficients for the model M3 calculated at 20, 40, 60, 80 and 100 Hz for model M3 with Maxwell dispersion.

Figures 2.27 (Futterman model), 2.28 (SLS model), 2.29 (Maxwell model) show seismograms calculated using ray method with frequency-independent (black) reflection coefficients overlying seismograms with frequency-dependent reflection coefficients (red) in the model M3. We see that presented seismograms are not distinguishable. The only slightly visible difference between both sets of seismograms is at the trace closest to the critical reflection calculated for the elastic reference model. The difference for the SLS model is slightly bigger than for the Maxwell and Futterman models.

62
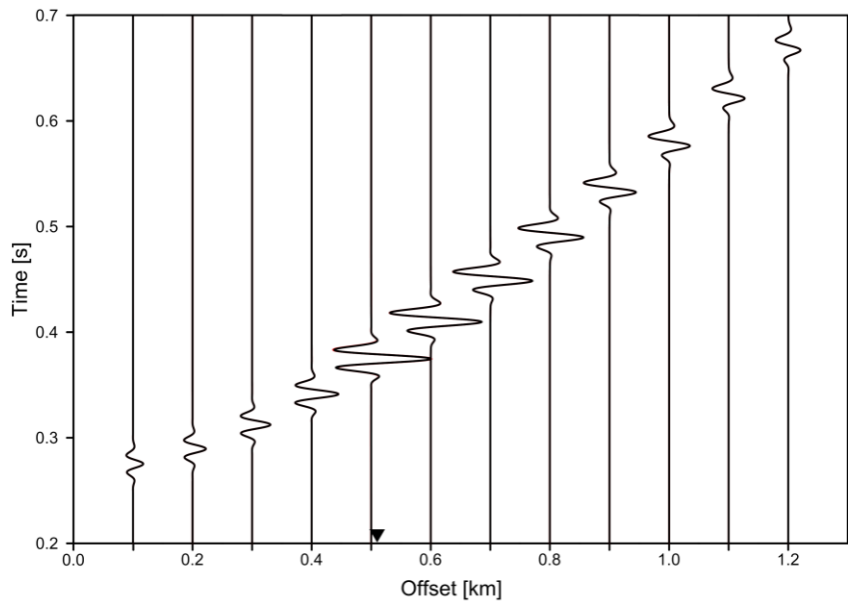
Figure 2.27. Seismograms computed in M3 model, Futterman dispersion. Black – seismograms calculated using frequency-independent reflection coefficient calculated at reference frequency of 60Hz, red – seismograms calculated using frequency-dependent reflection coefficient. Full triangle indicates critical incidence in the elastic reference model.
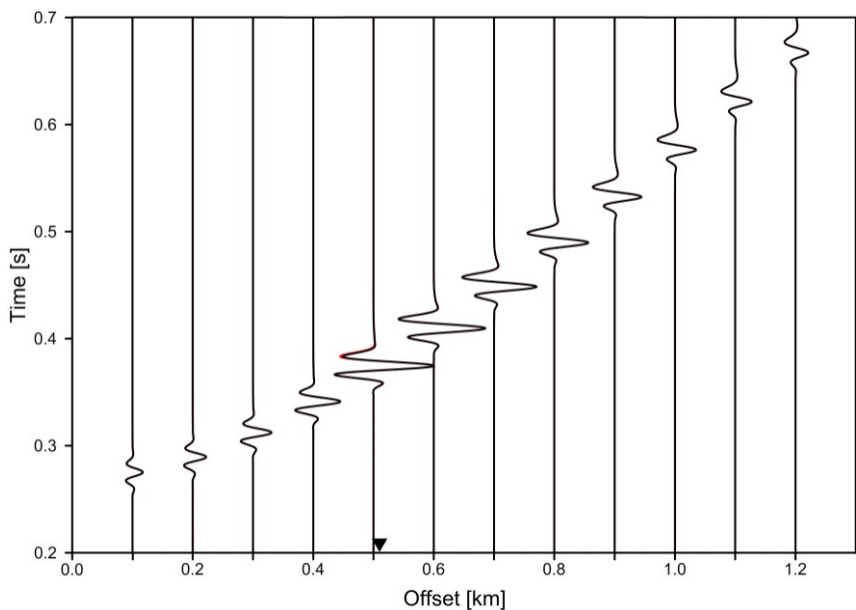
Figure 2.28. Seismograms computed in M3 model, SLS dispersion. Black – seismograms calculated using frequency-independent reflection coefficient calculated at reference frequency of 60Hz , red – seismograms calculated using frequency-dependent reflection coefficient. Full triangle indicates critical incidence in the elastic reference model.

63
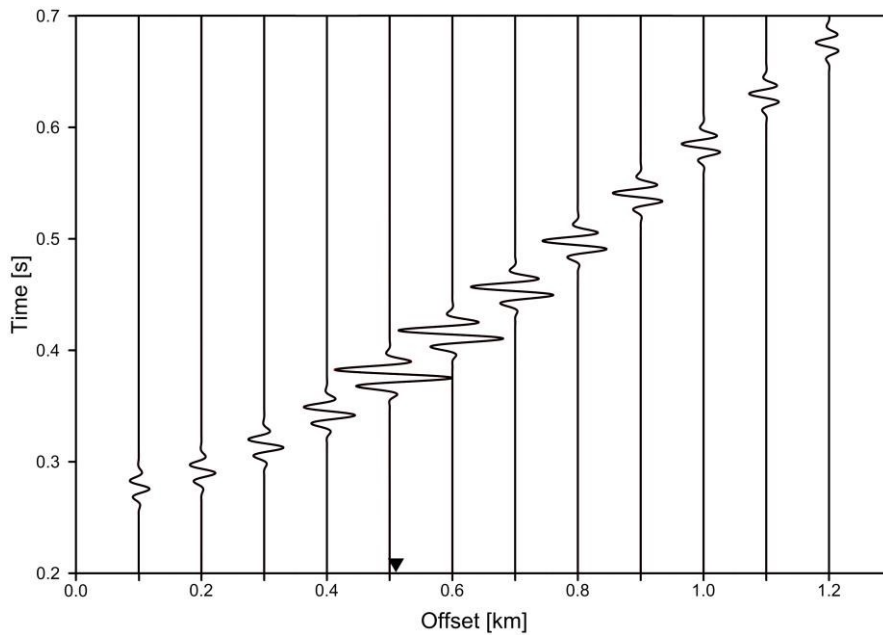
Figure 2.29. Seismograms computed in M3 model, Maxwell dispersion. Black – seismograms calculated using frequency-independent reflection coefficient calculated at reference frequency of 60Hz , red – seismograms calculated using frequency-dependent reflection coefficient. Full triangle indicates critical incidence in the elastic reference model.

Figures 2.30 - 2.32 show maximum spectral amplitudes computed using seismograms shown in Figures 2.27 - 2.29 for extended offset range. We see that besides direct vicinity of the critical angle, there are no visible differences between cases with frequency-independent and frequency-dependent reflection coefficients. Because results with frequency-independent coefficients are basically identical with frequency-dependent, we shall use the former ones in the following tests.

64
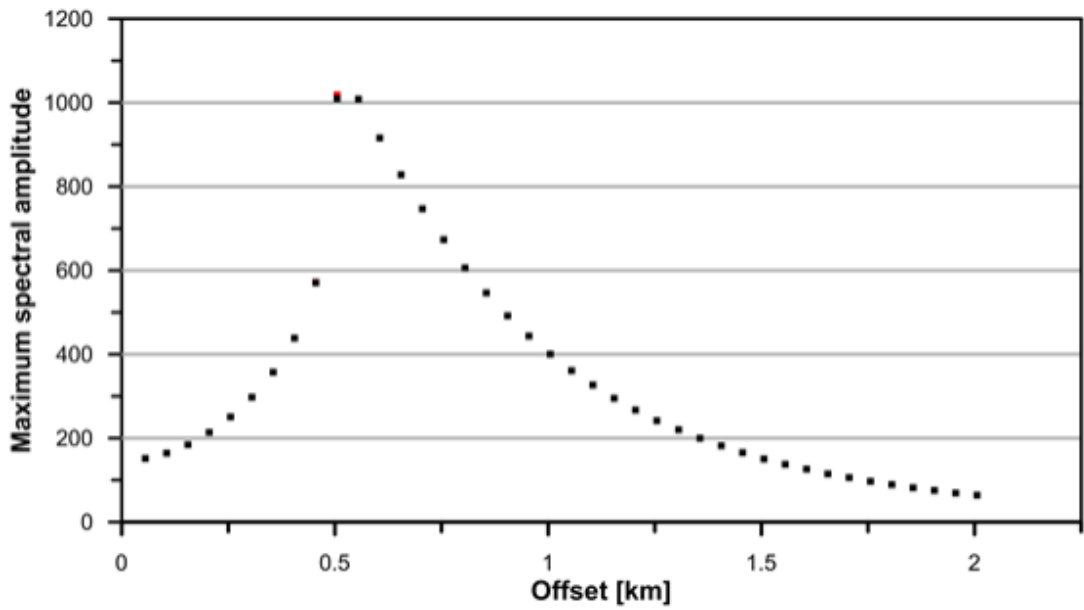
Figure 2.30. Maximum spectral amplitudes calculated using ray method for model M3, Futterman dispersion.. Black - results for frequency-independent reflection coefficient calculated at reference frequency of 60 Hz , red – results calculated for frequency-dependent reflection coefficient.
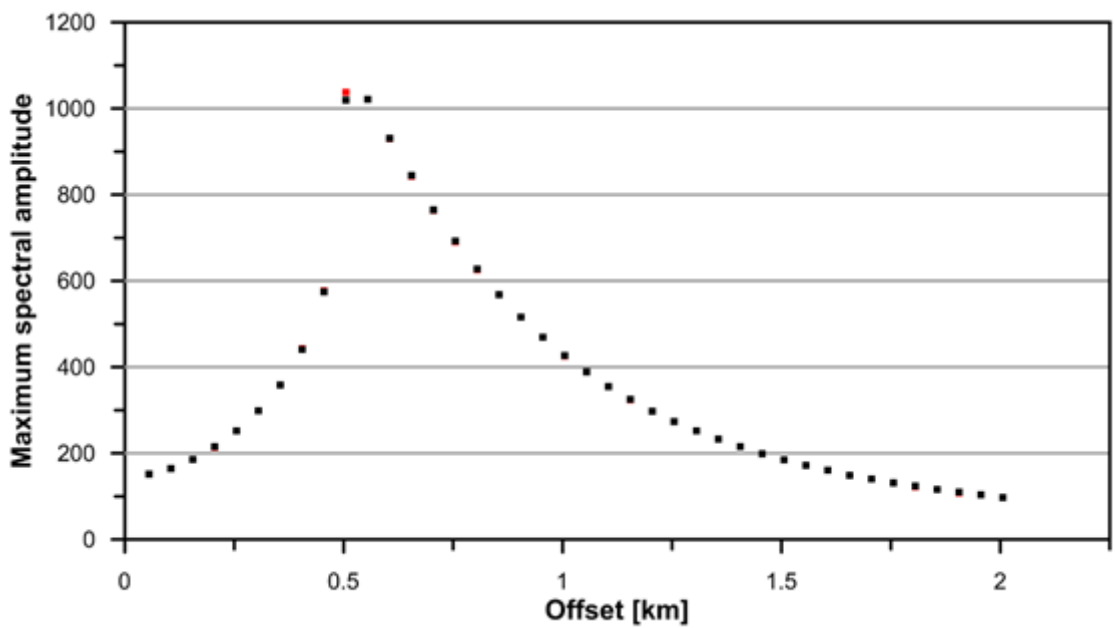
Figure 2.31. Maximum spectral amplitudes calculated using ray method for model M3, SLS dispersion. Black - results for frequency-independent reflection coefficient calculated at reference frequency 60Hz, red – results calculated for frequency-dependent reflection coefficient.
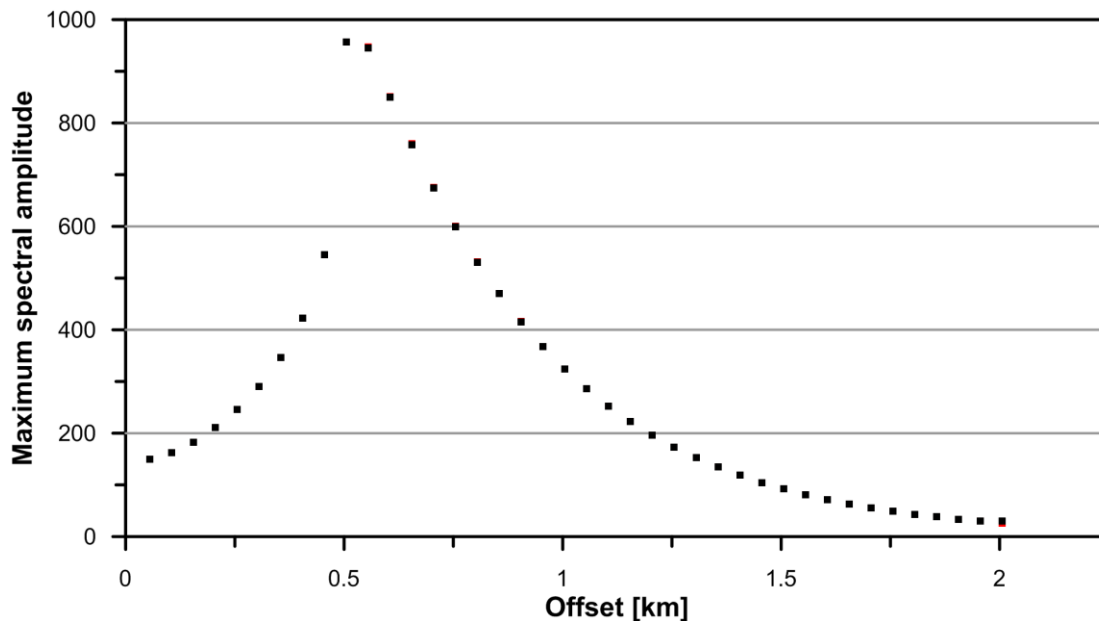
Figure 2.32. Maximum spectral amplitudes calculated using ray method for model M3. Maxwell dispersion. Black - results for frequency-independent reflection coefficient calculated at reference frequency 60Hz , red – results calculated for frequency-dependent reflection coefficient.

2.2.3 Seismograms of reflected waves in medium with two interfaces

In chapter 2.1, we indicated that the waves generated by the incidence of a homogeneous wave at an interface can be inhomogeneous i.e. propagation and attenuation vectors of slowness do not point in the same direction. The transmitted waves are mostly inhomogeneous, as, e.g., homogeneous incident wave generates homogeneous transmitted wave only for the normal incidence. Examples shown in Figures 2.11-2.14 suggest that inhomogeneity of waves play a role in attenuative media. The ray method does not allow computations of inhomogeneous waves. Therefore, it is questionable if WAC (in which inhomogeneous waves are not explicitly incorporated) will work properly in situations, in which inhomogeneous waves exist. To check this, we prepared a simple model with two interfaces, in which reflections from the bottom interface are mostly generated by inhomogeneous waves, see Fig.2.2. The geometry of the model used in the tests is similar to geometry shown in

Figure 2.15, with an additional interface placed 0.25 km below the first interface. Similarly, to earlier tests, first we work with elastic model (N1) and then with model with attenuation (N2). Seismograms are computed using the Maxwell dispersion model with β and Q specified for ω_r = 60 Hz. The parameters of models N1 and N2 are given in Table 2.4. Similarly, to models M1-M3, we compute seismograms using unit isotropic radiation pattern and Ricker signal with dominant frequency of 60 Hz as source time function. The source time function used in calculations for ray method is again modified for the 2D case. Results calculated using the ray method are benchmarked with results obtained by full-wave method.

Model	β_1	β_2	β_3	ρ_1	ρ_2	ρ_3	Q_1	Q_2	Q_3
N1	2.0	2.1	3.2	2.4	2.5	1.5	∞	∞	∞
N2	2.0	2.1	3.2	2.4	2.5	1.5	40	70	120

Table 2.4. Parameters of models N1 and N2 that include two interfaces.

In Figures 2.33 and 2.34, we compare seismograms computed for wave reflected from the bottom interface using ray method (black seismograms) that overlay results obtained using full-wave method (red seismograms) computed for models N1 and N2. Figure 2.35 shows results for model N2 but with WAC not applied at the interfaces for the ray method (full-wave method results are the same as in Figure 2.34). In Figures 2.33-2.35 we removed the wave reflected from the first interface from full-wave seismograms. Scaling in Figures 2.33 and 2.34 is set so that the maximum amplitude for the full wave method corresponds to the difference between traces. Scaling factor for Figure 2.35 is the same as for Figure 2.34.
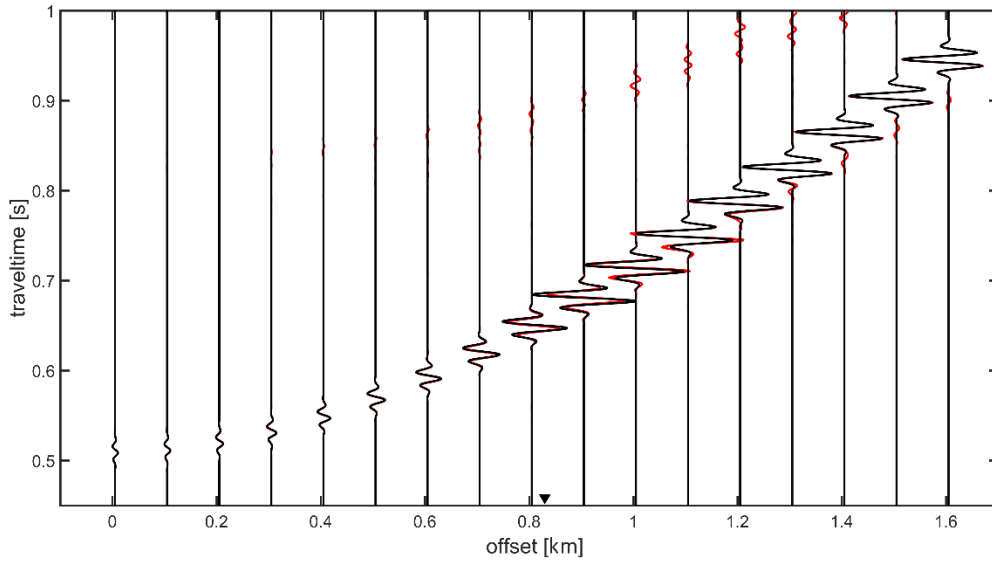
Figure 2.33: Full-wave seismograms of the wave reflected from the bottom interface (red) overlaid by ray seismograms (black) in elastic model N1. Full triangle indicates the position of the critical point of the wave reflected at the bottom interface.
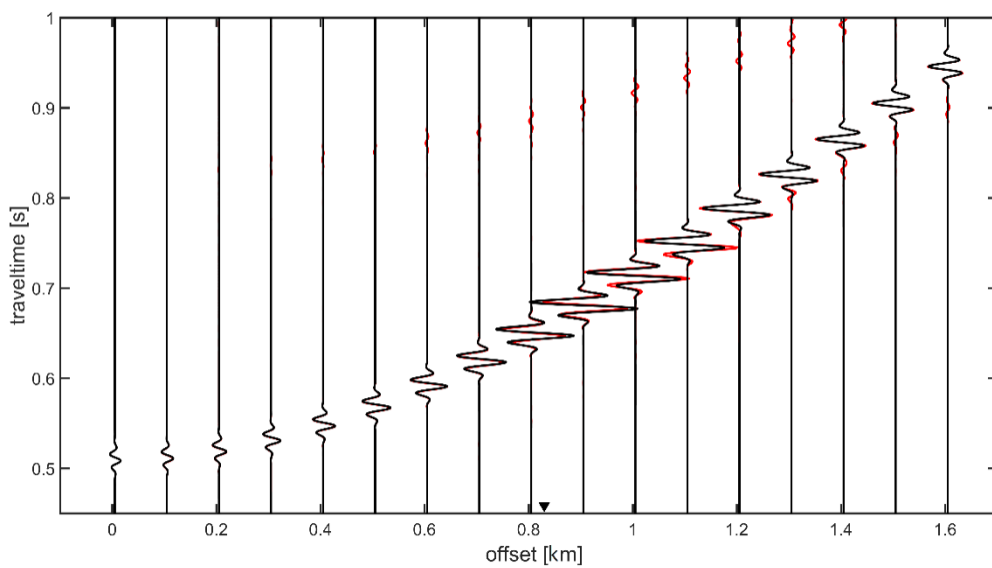
Figure 2.34: Full-wave seismograms of the wave reflected from the bottom interface (red) overlaid by ray seismograms with WAC (black) in anelastic model N2. Full triangle indicates the position of the critical point of the wave reflected at the bottom interface.
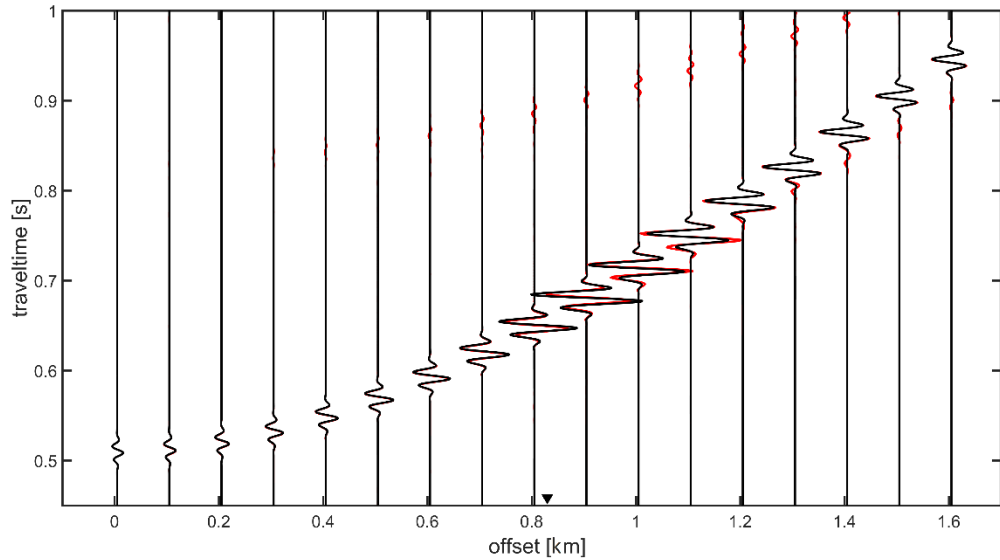
Figure 2.35: Full wave seismograms of the wave reflected from the bottom interface (red) overlaid by ray seismograms with WAC (black) in anelastic model N2. Results of the ray method neglect the influence of attenuation at the interfaces. Full triangle indicates the position of the critical point of the wave reflected at the bottom interface.

By examining Figures 2.33-2.35, we may see that the differences between the ray method and full-wave benchmark are of similar magnitude as in case of models M1-M3. We can see that the only visible differences are in the critical region. Ignoring the effects of attenuation at interfaces, does not introduce visible changes outside of the critical incidence. The effects of attenuation inside layers are much stronger than effects of attenuation at interfaces.

Figures 2.36 and 2.37 show maximum spectral amplitudes for models N1 and N2. Inf Fig. 2.37, effects of attenuation at the interface are both considered and neglected. We may see that the differences between results of ray and full-wave maximum spectral amplitudes are similar to those for models M1-M3. From results of presented tests it seems that WAC can be used even in layered media without significant loss of accuracy. Of course, further tests to confirm this claim are necessary.
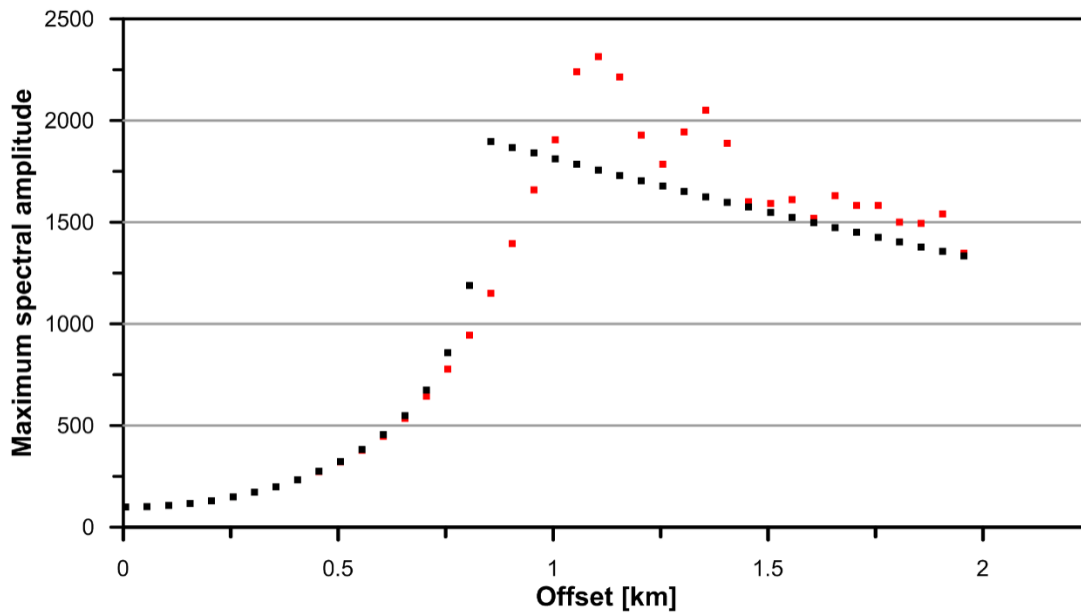
Figure 2.36: Maximum spectral amplitudes for model N1 calculated by the full wave method (red) and by the ray method with WAC (black).
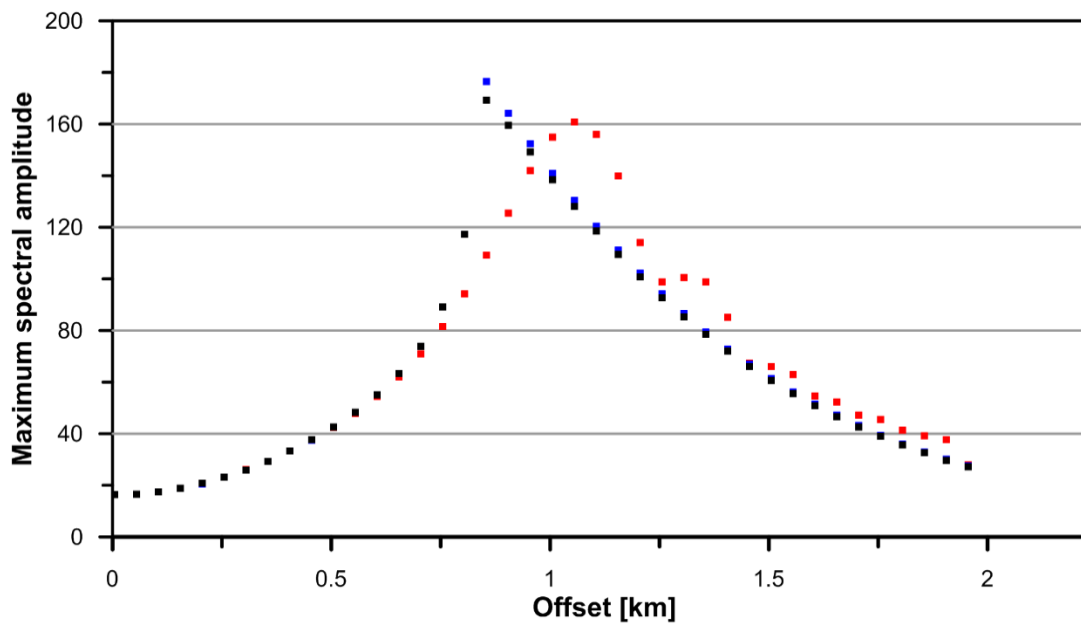
Figure 2.37: Maximum spectral amplitudes for model N2 calculated by the full wave method (red), by ray method with WAC (black) and ray method with WAC applied only inside layers (blue).

Chapter 3

Determination of the effective Q using peak frequencies of microseismic events

3.1 Introduction

Microseismicity is a subsection of seismology dealing with very weak earthquakes with rupture durations lasting only a small fraction of a second and rupture sizes counted in meters. Waves generated by these earthquakes have their spectra dominated by high frequencies. This is different from stronger earthquakes (studied by global seismology) with rupture duration usually counted in seconds which, therefore, generate seismic waves with spectra dominated by relatively low frequencies. Further, during the propagation, effects of attenuation influence waves and as shown, e.g., in eq. (1.8), its influence grows exponentially with increasing frequency. Let us consider a wave propagating in an attenuative medium which at some point was cumulatively affected by attenuation corresponding to global absorption factor, see eq. (1.9), t^*=0.01s. This value of t^* can be a result of e.g., a wave propagating through the medium with constant Q=100 for 1 second (representative example for microseismic studies). In such a medium, the spectral amplitude of the wave is reduced due to attenuation by 1% at 1 Hz, by 27% at 10 Hz, by 54% at 25 Hz and by 79% at 50 Hz. This example clearly shows that the attenuation in comparison to e.g. geometrical spreading likely plays significantly greater role in studies of waves dominated by high-frequencies, therefore is more important in analysis of microseismicity than in analysis of strong earthquakes. In studies of microseismic event source properties, effects of attenuation have to be considered carefully as they affect the inverted source properties in a substantial way. On the other hand, strong influence of attenuation, which may significantly distort observed waves, gives an opportunity for creation of more detailed attenuation model of medium. For strong earthquakes dominance of low frequencies limits the resolution of

attenuation models of the medium – the effects of attenuation can easily be attributed to other factors (e.g. magnitude of event).

3.2 Theory

Observed wave has its source spectrum $\Omega(f)$ (f- frequency) convolved with propagation effects. The frequency-independent (scaling) effects are geometrical spreading G, but also (approximately, as shown in Chapter 2) R/T coefficients. Attenuation $A(f)$, as earlier discussed in the Chapter 1, affects the displacement spectrum in a frequency dependent way. The instrument recording the wave arrival has a frequency dependent response function $I(f)$. Spectrum of a recorded wave $W(f)$ then may be written in a form:

$$W(f) = \Omega(f)GA(f)I(f). \qquad (3.1)$$

The response function $I(f)$ of a recording instrument is in principle known. It is accounted for during the initial, hardware processing, therefore we will not discuss it or take it into account further in this study. It means that only the source spectrum $\Omega(f)$ and the attenuation $A(f)$ control the shape of the spectrum of recorded waves. Let us focus on the source spectrum first. Earthquakes of all sizes are dominated by shear failures mostly happening on a single fault plane (e.g., Rutledge and Phillips, 2003; Eisner et al., 2010). Models describing shear sources have flat particle displacement spectrum at low frequencies (Aki & Richards, 2002), which at higher frequencies is limited by the rise time (duration of a slip) and rupture duration (depending on rupture speed and fault size) of earthquake. As a result, a sharp slope change of spectral power density at frequency called corner frequency f_C occurs. The displacement amplitude spectrum Ω_D at the source of a shear event is constant (flat) and equal to seismic moment M_0 up to the corner frequency. Above the corner frequency, a sharp decline of spectral amplitude takes place:

$$\Omega_D(f) = M_0 \qquad\qquad f < f_C,$$

$$(3.2)$$

$$\Omega_D(f) = \frac{M_0}{\left(\frac{f^2}{f_C^2}\right)} \qquad\qquad f \geq f_C.$$

The observed wave is usually recorded by instruments which measure particle velocity (accelerometers are used mostly to provide data about large earthquakes).

The velocity spectrum $\Omega_V(f)$ (derivative of a displacement spectrum) at the source reads:

$$\Omega_V(f) = 2\pi f M_0 \qquad\qquad f < f_C,$$

(3.3)

$$\Omega_V(f) = 2\pi f \frac{M_0}{\left(\frac{f^2}{f_C^2}\right)} \qquad\qquad f \geq f_C.$$

The frequency, at which the velocity spectrum of a wave peaks, hereafter will be called peak frequency f_{peak}. The velocity spectrum of a wave in direct vicinity of the source peaks at the corner frequency, which is a property of a source. An example of a displacement and velocity spectra for an earthquake with a shear source with corner frequency at 100 Hz and $M_0=1$ is shown in Figure 3.1.
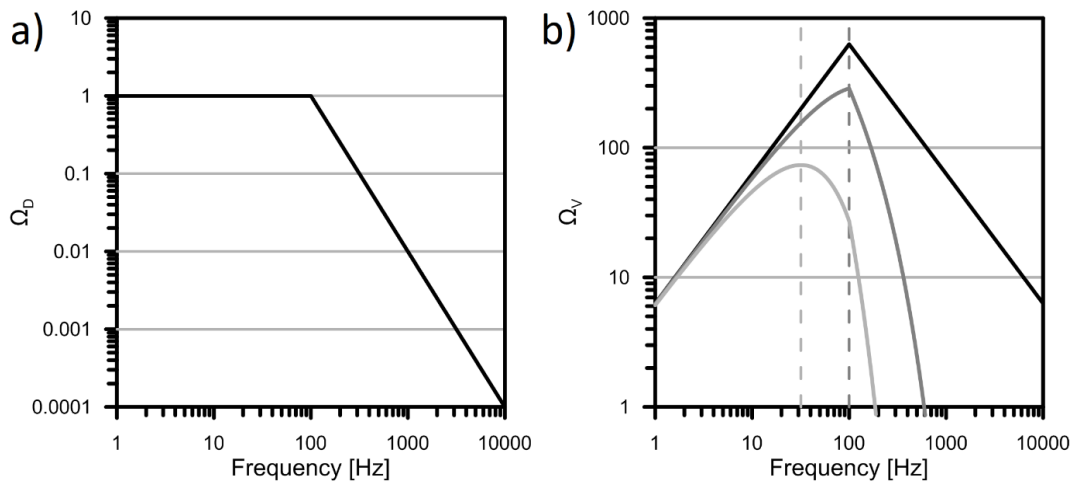
Figure 3.1. a) Source displacement spectrum Ω_D as described by eq. (3.2), for event with corner frequency equal 100Hz and $M_0=1$ b) (black) source velocity spectrum Ω_V as described by eq. (3.3), corresponding to displacement source spectrum in a). Attenuated velocity spectrum with $t^*=0.0025$s (dark grey) and with $t^*=0.01$s (light grey). Dashed lines indicate frequencies corresponding to f_{peak}.

As the wave propagates, the amplitude is reduced by both factors G and $A(f)$. Given that G does not depend on frequency, only attenuation $A(f)$ can affect the peak frequency. As shown in Chapter 1, attenuation has an effect on the waves that is cumulative along the propagation path and it is controlled by the global absorption factor. For frequency independent attenuation, but also for a commonly used Futterman model, the spectral amplitudes decrease exponentially as $e^{-\pi f t^*}$. Neglecting

the term $2\pi M_0$ of eq. (3.3), which is yet another, scaling factor, the observed amplitude of velocity spectrum W_V of a wave has the form:

$$W_V(f) = fe^{-\pi ft^*} \qquad\qquad f \le f_C,$$

$$(3.4)$$

$$W_V(f) = fe^{-\pi ft^*}\, \frac{1}{\left(\frac{f2}{f_C^2}\right)} \qquad\qquad f > f_C.$$

As earlier noted, the peak frequency in a direct vicinity of the source is equal to corner frequency. In a hypothetical elastic medium, the peak frequency remains equal to corner frequency. However, during propagation in attenuative media, high frequencies are attenuated faster, thus, $f_{peak} \le f_C$. For $f_{peak} < f_C$ the peak frequency of direct wave can be determined by finding maximum of the function:

$$(fe^{-\pi ft^*}). \qquad\qquad (3.5)$$

This function peaks for:

$$f_{peak} = \frac{1}{\pi t^*}. \qquad\qquad (3.6)$$

Using eqs. (1.9) and (3.6), we can easily calculate effective (averaged along the ray path) Q of the medium based on peak frequency of a wave:

$$Q = \pi t f_{peak}. \qquad\qquad (3.7)$$

Here t is traveltime along above-mentioned ray path. Further, we call this way of estimation of effective Q the peak frequency method. Note, that eqs. (3.6) and therefore (3.7) cannot be used universally because velocity spectrum described by eq. (3.4), peaks at f_C for small values of t^*. This is illustrated in Figure 3.1b, where besides the source spectrum, we show spectra affected by attenuation only (other factors, including geometrical spreading are disregarded), with $t^*=0.0025s$ and 0.01s. While the curve with $t^*= 0.01s$ has its peak frequency at ~32Hz, which agrees with eq. (3.6), the curve corresponding to $t^*=0.0025s$ peaks at 100Hz – corner frequency of the source, not 127Hz, as implied by eq. (3.6). Therefore, peak frequency of event with source velocity spectrum given by eq. (3.3), can be expressed as:

$$f_{peak} = \min\left(f_C, \frac{1}{\pi t^*}\right). \qquad\qquad (3.8)$$

Eq. (3.8) fully describes the behavior of the peak frequency of a wave with the source velocity spectrum described by eq. (3.3). Let us note, that we can use peak-frequency method to evaluate t^* and effective Q only if we are already at the point

74

where peak frequency of propagating wave follows the $\frac{1}{\pi t^*}$ decrease. In practice peak-frequency method can be used only at some distance from the source that implies some minimal value of t^* a wave accumulate between the source and receiver. The distance from the source depends on the quality factor of the medium in the region and corner frequency (magnitude) of the event. The examples of the theoretical changes of peak frequency as a function of frequency-independent t^* for events with corner frequencies f_c equal 1000, 500, 100 and 50 Hz are shown in Figure 3.2. The selected values of f_c are typical for microseismic monitoring. In the surface microseismic surveys, peak frequencies may reach 100 Hz. In borehole monitoring, where we deal with much smaller distances to the recording array, we can detect much smaller events. Recorded peak frequencies of these very small events may reach close to 1000 Hz (e.g., Wandycz et al., 2019; Maxwell et al., 2010) which implies even higher values of f_c.

Determination of the corner frequency of the event is difficult, and before measuring values of peak frequency we do not know if it is controlled by attenuation only, or by the corner frequency (eq. 3.8). Moreover, in order to determine corner frequency of the event, it is usually necessary to evaluate Q of the medium which we seek. Nevertheless, once we measure many values of peak frequency in given dataset, it is possible to test if t^* only controls the peak frequency, and we can use eq. (3.6). The following tests may be done. If we deal with multiple events recorded by a single station, we can create a plot of measured f_{peak} vs magnitudes of selected events. If values of peak frequencies do not decrease with magnitude M, it means that peak frequencies are likely controlled by attenuation, see eq. (3.6). If we deal with a single event, but multiple receivers, we can check if peak frequencies follow relation with traveltime shown in eq. (3.7).
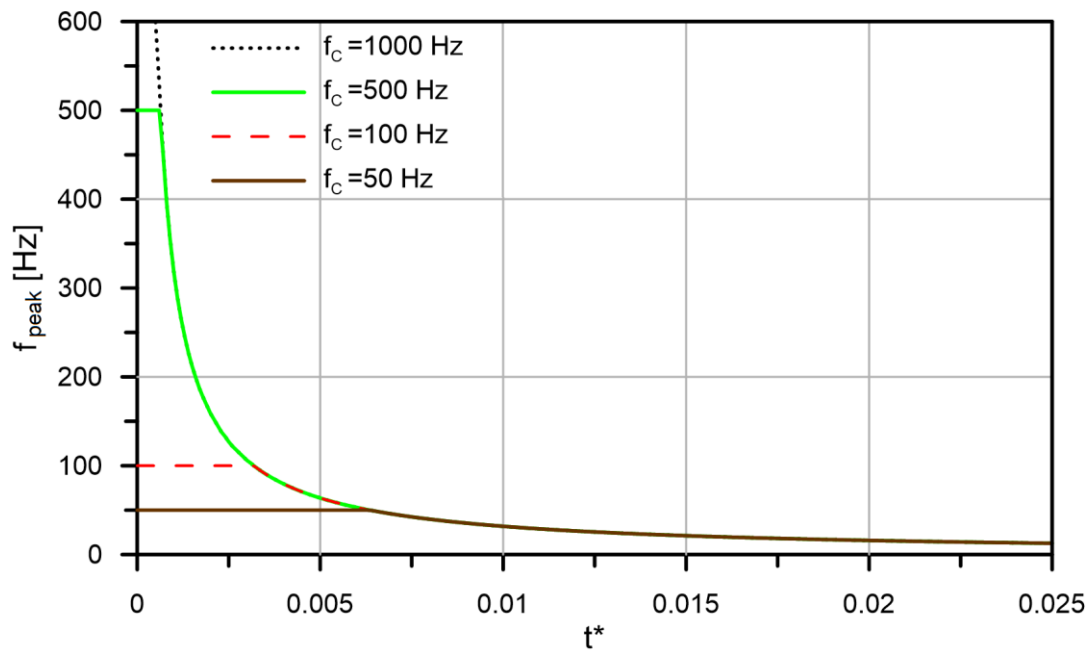
Figure 3.2. The peak frequency f_{peak} as a function of frequency independent global absorption factor t^* for events with different corner frequencies f_C with source spectra described by eqs. (3.3).

In chapters 4, 5, and 6, we show the application of the peak frequency method for datasets gathered in West Bohemia, Czech Republic (natural seismicity), Agri Valley, Italy and North China (induced seismicity). The analysis of the data from the first two locations shows the successful application of the peak frequency method – eqs. (3.6) and (3.7) to evaluate t^* and effective Q – eq. (3.7). The dataset from North China illustrates the case where the measured peak frequencies are affected by both: source corner frequency and attenuation.

3.3 Measurement of peak frequency

The measurement of f_{peak} can be done in the frequency domain, but also in the time domain. The first step is always a selection of clear, single direct arrival. An example of such an arrival is shown in Figure 3.3a (the arrival was recorded at the station Luby during seismic swarm in West Bohemia in 2008, see Fischer et al., 2014).

To determine the peak frequency in the frequency domain, we select an interval from the seismogram that includes direct arrival, then the cosine filter is

76

applied outside this interval. The next step is Fourier-transformation of the signal into frequency domain and the determination of the frequency corresponding to the maximum of the amplitude spectrum. The spectrum corresponding to the signal in Figure 3.3a, with the peak frequency marked is shown in Figure 3.3b.
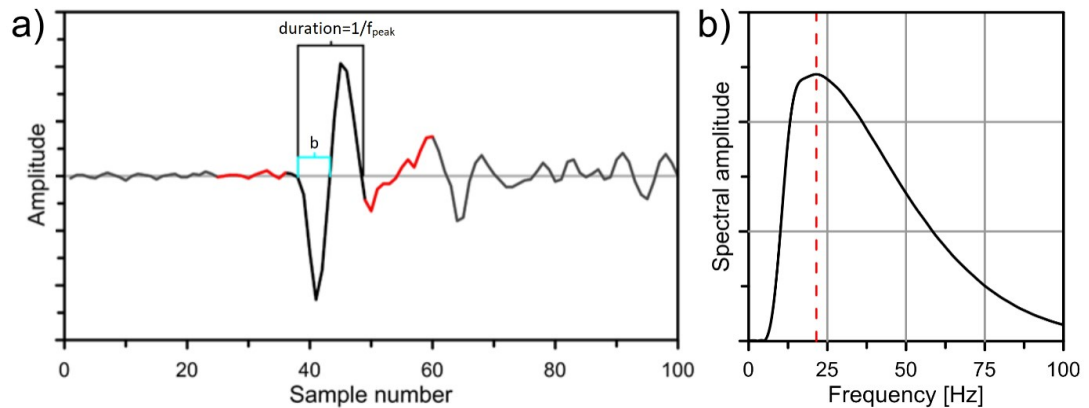
Figure 3.3. a) Example of direct wave arrival suitable for measurement of f_{peak}. Black part of the seismogram in the center is the direct arrival - useful signal that is kept without changes, red color indicates the parts of the signal where cosine filter is applied. Outside this interval, signal used in the Fourier transform is zeroed before calculating amplitude spectrum of the wave. Brackets indicate intervals used for measurement in time domain (full duration – black, half period – cyan). b) Amplitude spectrum of the arrival. Red dashed line indicates the peak frequency.

In time domain, the beginning and the end of the direct arrival is determined by visual inspection of the signal, the inverse of the duration time is then the peak frequency, see Fig. 3a. Wcisło and Eisner (2016, 2019) have shown that measurements in both domains provide consistent results. Another alternative in time domain is to determine the duration between the onset and the first zero crossing (half period) of the direct arrival – cyan interval in Fig. 3.3a. Using half periods is particularly useful if selected arrival is distorted in its second part by following arrivals. Wcisło and Eisner (2016) have shown that using half period provides consistent results with using the whole duration of direct arrival.

On the contrary to clear, single direct arrival shown in Figure 3.3a, in Figure 3.4 we show examples of arrivals that cannot be used in peak frequency method.

They were recorded at the station Květná during seismic swarm in West Bohemia in 2008. These arrivals are dominated by guided near-surface waves and single, first direct arrival cannot be identified, therefore they are not suitable for the peak frequency method.
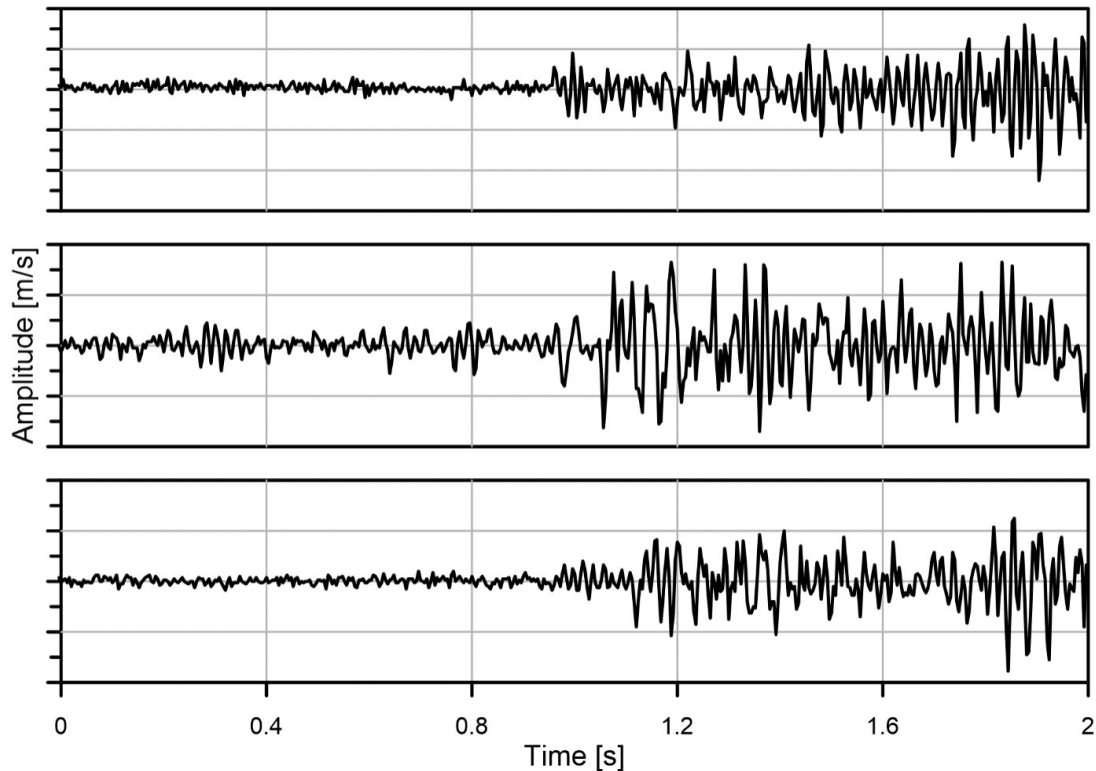
Fig. 3.4. Examples of three P- wave arrivals (vertical component) not suitable for application of peak frequency method.

3.4 Peak frequencies in other source spectrum models

Morozov (2014) have pointed out that eq. (3.8) is valid only if we assume that the source spectrum is described by eq. (3.3). Therefore, we looked for other popular source spectra models, which in some cases may be better approximation of real earthquake. The most common model is a model with continuous derivative of displacement with respect to frequency, proposed by Brune (Brune, 1970). The source displacement spectrum in the Brune model is described as:

$$\Omega_D(f) = \frac{M_0}{(1+(\frac{f}{f_C})^{2\gamma})^{1/\gamma}} \cdot \qquad (3.9)$$

γ is a constant controlling the sharpness of the transition from constant values of the spectrum to decrease with -2 slope (in log-log scale) close to the corner frequency.

Brune (1970) proposed $\gamma=1$, but $\gamma=2$ is used as well as it often provides better fit to the data, see, e.g., Abercrombie (1995), Ide et al. (2003) or Tomic et al. (2009). The source spectra for the same f_c and M_0 as in Figure 3.1, but for Brune model computed using $\gamma=1$ and $\gamma=2$ are shown in Figures 3.5a (displacement) and 3-5b (velocity). The spectra computed using eqs. (3.2) and (3.3) are included for reference. We can see that the greatest difference between these models of velocity spectrum is in the vicinity of the corner frequency. Spectrum for Brune model with $\gamma=2$ is closer to eqs. (3.2) than spectrum for Brune model with $\gamma=1$. For frequencies $f \ll f_c$ and $f \gg f_c$ spectra behave similarly. Figure 3.5b shows the attenuated velocity spectra with the same t^* values as in Figure 3.1b. We can see that even for small values of t^*, e.g. 0.0025s, the maximum of the spectrum for Brune models is shifted to lower frequencies than the corner frequency. The peak frequency in Brune model does not change as predicted by eq. (3.8). Discrepancy between the behavior of peak frequency for Brune model and eq. (3.8) arises for small values of t^*. Nevertheless,
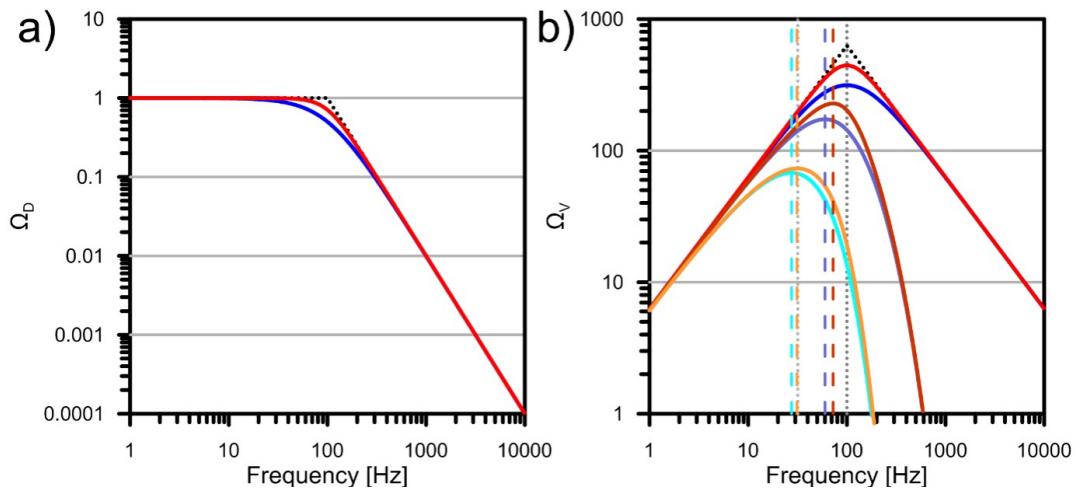
Figure 3.5. a) Brune source displacement spectra as described by eq. (3.9), for event with $f_c=100$Hz and $M_0=1$. Blue curve shows results calculated for $\gamma=1$, red for $\gamma=2$. For the reference, dotted line indicates the spectrum computed using eq. (3.2). b) source velocity spectra corresponding to source displacement spectra shown in a) - curves with the same colours. Attenuated spectra with $t^*=0.0025$s ($\gamma=1$: brick red, $\gamma=2$: twilight blue) and with $t^*=0.01$s ($\gamma=1$: light orange, $\gamma=2$: cyan). Dashed lines indicate frequencies at which the amplitude spectrum peaks. Additional dotted lines indicate the peak frequencies obtained for the reference model from eq (3.2).

79

this difference starts to diminish once we move to frequencies, at which both models are similar. Eqs. (3.2) and (3.9) provide almost identical values for much lower than corner frequency, therefore, the pattern of the decrease of f_{peak} with growing t^* converge to behavior described by eq. (3.6). Fig. 3.6 shows how the relative differences in peak frequencies predicted by each model decrease as we move to lower frequencies. To make the picture valid for all values of f_C, the horizontal axis is defined as f_{peak}/f_C in [%] with f_{peak} being peak frequency predicted by eq. (3.6). With increasing t^* the predicted behavior of f_{peak} for all models converge to behavior of eq. (3.6). We can conclude that the selection of the model does not matter much for greater values of t^*. On the contrary, for small values of t^*, and thus peak frequencies that are close to corner frequency, selection of the model is important. The true spectrum at the source is unknown, and therefore, the tests described at the end of the section 3.2 (preparation of plots of measured f_{peak} vs magnitude and vs traveltime) in order to see if f_{peak} is controlled by attenuation should be performed for all datasets.
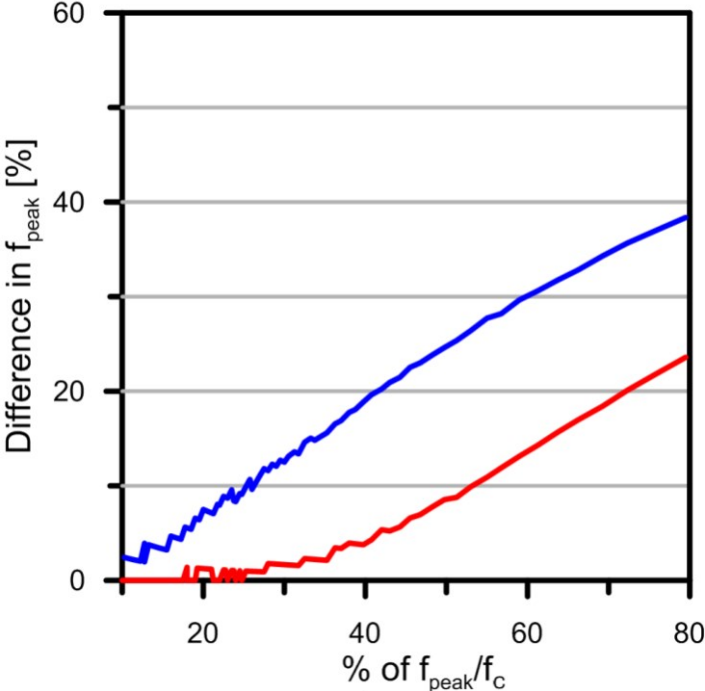
Figure 3.6. Relative difference between peak frequencies predicted for source model described by eq. (3.2) and Brune source models described by eq. (3.9) with $\gamma=1$ (blue curve) and $\gamma=2$ (red curve) as a function of ratio of f_{peak} changing during propagation and f_C at the source. f_{peak} is peak frequency predicted by eq. (3.6).

3.5 Attenuation tomography

Detailed analysis of the distribution of any parameter of the medium requires multiple measurements. This is obviously also the case in studies of attenuation of the medium. Let us assume that we have at our disposal a high number of direct arrivals whose peak frequencies are controlled by attenuation and we apply eq. (3.6) to evaluate t^*. t^* has a similar character as traveltime, therefore, inversion methods used to determine velocity models in traveltime studies, can be extended to the Q factor inversion in t^* studies. To make a tomographic study, we divide a medium into layers (1D studies), or cells (2D or 3D studies) and invert for the sought parameter in each cell. The integral in eq. (1.9) must be discretized. For simplicity, let's work with attenuation parameter $A=1/Q$ (similarly, as we deal with slowness in traveltime tomography). In isotropic media, divided into i layers/cells, t^* is then equal:

$$t^* = \sum_{i=1}^{N} A_i t_i. \qquad\qquad\qquad (3.10)$$

A_i is attenuation parameter characterizing the i-th layer/cell and t_i is traveltime a wave propagating along given ray path spends in the cell. The multiplication t_i and A_i provides t^* of the wave within i-th layer/cell. In order to be able to find the values of A_i within cells we need to work with values of t^* estimated from arrivals that correspond to many source-receiver pairs. Let us assume that we work with an array of seismic stations and number of microseismic events. In total, they provide J estimates of t^*. It is possible then to create a set of linear equations with A_i as unknowns. The set of equations has a form:

$$A_1 t_{11} + A_2 t_{21} \dots + A_i t_{ij} = t_j^*, \qquad 1 \leq j \leq J, \qquad (3.11)$$

where t_j^* is obtained from j-th source-receiver pair measurement. This set of equations, can be solved using the least square method.

3.5.1 Solution of the set of equations

Solution of the eqs. (3.11) presents a classical least square problem. In the inverse problem literature (Tarantola, 2005), the vector containing data - in our case estimated t^*'s - is denoted as **d**, matrix with the set of known parameters –

traveltimes within each cell – is **G,** and vector with unknowns – attenuation parameters A - is denoted as **m**. Then, the set of equations (3.11) can be rewritten as:

$$Gm=d \,.$$ (3.12)

In practice, both d and G, which are input data are estimated with some uncertainty. We include their uncertainties in so called covariance matrixes. Covariance matrix C_d (diagonal matrix) element-by-element describes uncertainties of measured t^* included in d and covariance matrix **C_G** describes uncertainties of estimated traveltimes included in G. In t^* tomography problem, the uncertainty of measured t^*'s (~10% of true t^* for datasets with high signal-to-noise ratio, Wcisło and Eisner, 2018) is about an order of magnitude higher than the uncertainty of estimated traveltimes within cells (mostly due to errors in velocity model). This means, that the accuracy of the solution is mainly affected by uncertainty of attenuation measurement with very minor effect caused by uncertainty of traveltime estimates. Therefore, we neglect the C_G, and we only work with the uncertainty of the vector d - C_d.

The least square problem also frequently involves the use of so called a priori information – information allowing initial estimate of the value of sought parameters – in case of t^* tomography, we can use, e.g., average value of attenuation parameter A implied by the data, or typical strength of attenuation in the type of the medium we are studying, etc. The priori information (model) is included in vector denoted as m_{prior} and can be considered a starting point for the inversion. The uncertainty of the priori information is included in the covariance matrix $C_{mprior.}$ The priori information can be used as well to determine the bounds (maximum and minimum value) of the possible solution. It can be set, e.g., so that it limits (through the covariance matrix C_{mprior}) the inversion output only to positive values of A parameter. In the inverse method literature, the output of the inversion if a priori model is used is called a posteriori model – here denoted **m**. The posteriori model $\widetilde{m}$ which is a solution of the least square problem is given by the expression (Tarantola, 2005):

$$\mathbf{m} = \mathbf{m_{prior}} + (\mathbf{G^t C_d^{-1}} + \mathbf{C_{mprior}^{-1}})^{-1}\mathbf{G^t C_d^{-1}}(\mathbf{d} - \mathbf{Gm_{prior}}).$$ (3.13)

Here an indice t is an operation indicating transposition of a matrix. To evaluate the quality (how well the particular elements of the model were resolved) of the obtained

solution included in $\dot{\mathbf{m}}$ we calculate a so called posteriori covariance matrix $\mathbf{C_m}$ (diagonal matrix). It is given by the expression:

$$\mathbf{C_m} = (\mathbf{G^t C_d^{-1} G} + \mathbf{C_{mprior}^{-1}})^{-1}.$$ (3.14)

If a diagonal element of the $\mathbf{C_m}$ matrix is small, it means that the corresponding cell has the attenuation parameter resolved well. On the contrary if a diagonal element of the matrix $\mathbf{C_m}$ is large and similar to the value in corresponding cell of a priori covariance matrix C_{mprior} then the value within the cell is not reliably inverted.

As noted above the solution of a least-square problem included in eq. (3.13) does not consider the minor influence of uncertainty of estimated within cells traveltimes. If we include the uncertainties of calculated traveltimes in the inversion the problem would become non-linear. Such a solution has to be sought in an iterative way. The iterative scheme similar to the one presented by Tarantola (2005), chapter 3.2.3, describing the non-linear t* tomography is used by Wcisło and Eisner (2018).

The greatest limitation of the t* tomography is above-mentioned high uncertainty of t* measurements and limited number of events that allow t* estimation when compared to number of events available in traveltime tomography. Nevertheless, attenuation tomography attracts increasing attention of seismologists. Recently number of tomographic studies, including even 3D tomography, were published, e.g., Mousavi et al. (2017), Prudencio et al. (2015a;b).

3.6 Simple measurement of attenuation in the source area

Eq. (3.13) provides general solution for the problem of t* tomography. Wcisło and Eisner (2018) shown that in certain cases, when we deal with clustered seismicity, the limited ray illumination of the studied area does not allow to obtain reliable solution even for 1D tomography. Still, even relatively small separation of the event's hypocenters allows extraction of more detailed information about Q of the medium, in particular Q in the source area.

Assume, we observe two events, recorded by a single receiver. The events have different hypocenters located within the same cluster. This means that we can assume that the waves from the two sources propagate along nearly the same path.

t_1 and t_2 are traveltimes of event 1 and 2 respectively. Event 2 is located deeper as illustrated in Figure 3.7. The medium between hypocenter of event 1 and the receiver is characterized by the effective quality factor Q_1, therefore $t_1^*=t_1/Q_1$. Medium between hypocenter of event 2 and the receiver is characterized by the effective quality factor Q_2. Assuming that between hypocenter 1 and the receiver both wave propagate along nearly identical paths, we can express t_2^* as:

$$t_2^* = \frac{t_2}{Q_2} = \frac{t_1}{Q_1} + \frac{\Delta t}{Q_{source}} \qquad (3.14)$$

where $\Delta t = t_2 - t_1$, and Q_{source} is the effective attenuation along the path of the ray between hypocenters of events 1 and 2. Using equations (3.6) and (3.7) we can find, that f_{peak_2} of event 2 is:

$$f_{peak_2} = \frac{1}{\pi(\frac{t_1}{Q_1} + \frac{\Delta t}{Q_{source}})}, \qquad (3.15)$$

Therefore, the attenuation factor Q_{source} can be calculated using the observed peak frequencies of events 1 and 2:

$$Q_{source} = \frac{\pi \Delta t_{2,1}}{\frac{1}{f_{peak_2}} - \frac{1}{f_{peak_1}}}. \qquad (3.16)$$
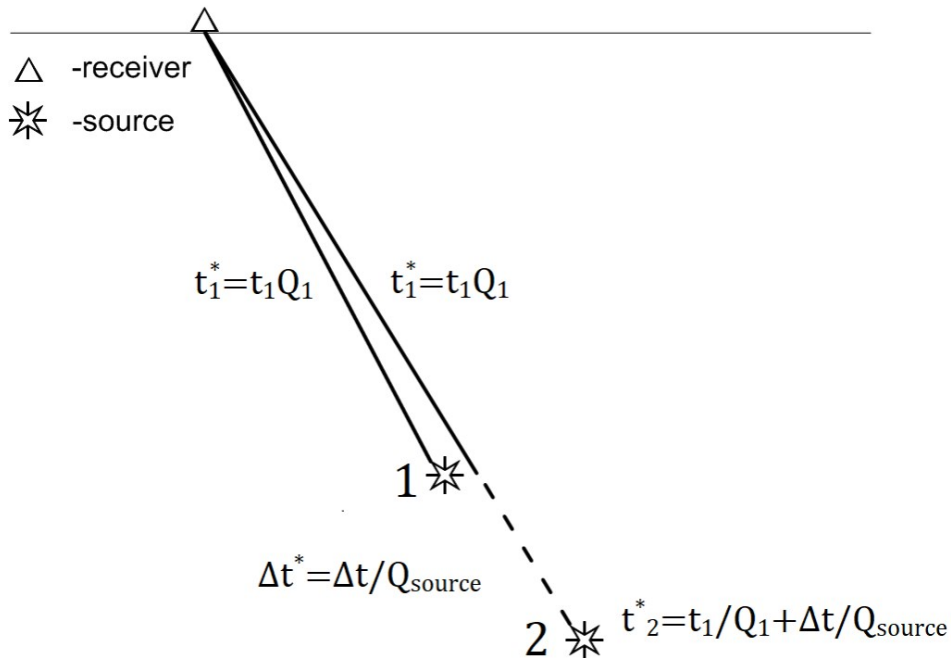
Figure 3.7. The principle of Q_{source} measurement.

The relatively high scatter (uncertainty) of t^* measurements is an issue in this type of analysis as in tomographic studies. To obtain robust values of inverted $Q_{source,}$ we should use multiple source-receiver pairs. Because the uncertainty of the t^* measurements is high, using pairs with almost exactly the same location of hypocenter is problematic, therefore it is good to select events that have some difference in depth/offset, e.g., from the top and the bottom of the cluster. Such selection provides more robust results than random selection which includes all events in the cluster.

The estimation of Q in the source area is important if we suspect that the properties of the medium in it are different. This happens for seismicity occurring in media with presence of fluids/gases. This is often the case when we work with induced seismicity in the areas where hydraulic stimulation was performed. Naturally occurring seismicity can be influenced by the movements of fluids as well. The analysis of the dataset from West Bohemia described in chapter 4 includes an example of the measurement of the Q in the source zone.

Chapter 4

Analysis of attenuation from data of 2008 seismic swarm in West Bohemia – Czech Republic

4.1 West Bohemia

Bohemia (WB) is a seismically active region in Central Europe (Fig. 4.1). Its intra-continental seismicity is manifested by seismic swarms with M_L up to 5. The main seismic activity occurs repeatedly in the Nový Kostel focal zone, on the fault system striking NNW-SSE (more than 80% of seismic energy was released in this zone in the last 25 years; Fischer and Michálek, 2008). The origin of the seismic swarms in WB is enigmatic. The currently accepted ideas indicate that the activity is not only triggered by intraplate loading (Fischer and Horálek, 2005) but also by an injection of lower-crustal/upper-mantle-derived fluids (Hainzl and Fischer, 2002; Bräuer et al., 2009). This interpretation stems from the $^3He/^4He$ ratios observed in the degassing center placed in the Cheb Basin (up to ~300 m thick basin consisting of quaternary and tertiary sediments located west of the Počátky-Plesná fault) where the emanation of CO_2 gas is present in the form of wet and dry mofettes (Weinlich et al., 1999; Faber et al., 2009). The total CO_2 annual degassing rate is estimated to be about 90 000 tons for the whole area (Weinlich et al., 1999), but the new estimates give larger values of about 60 000 tons for a single mofetta field in Hartoušov (Nickschick et al., 2015). The geochemical studies based on helium and carbon isotope ratios show that the produced CO_2 is of a deep upper mantle origin (Bräuer et al., 2003 and 2011) and during its migration to the surface it could take part in the seismogenic process. This was indicated by variations in the gas isotopic signature by Bräuer et al. (2005, 2009 and 2011) and groundwater level changes by Koch et al. (2011) during the earthquake swarm activity. The most pronounced seismogenic anomaly of CO_2 production was observed in the Hartoušov mofetta field, where the gas flow increased by a factor of 2 and 5 after the 2008 swarm and 2014 mainshock-aftershock sequence, respectively.
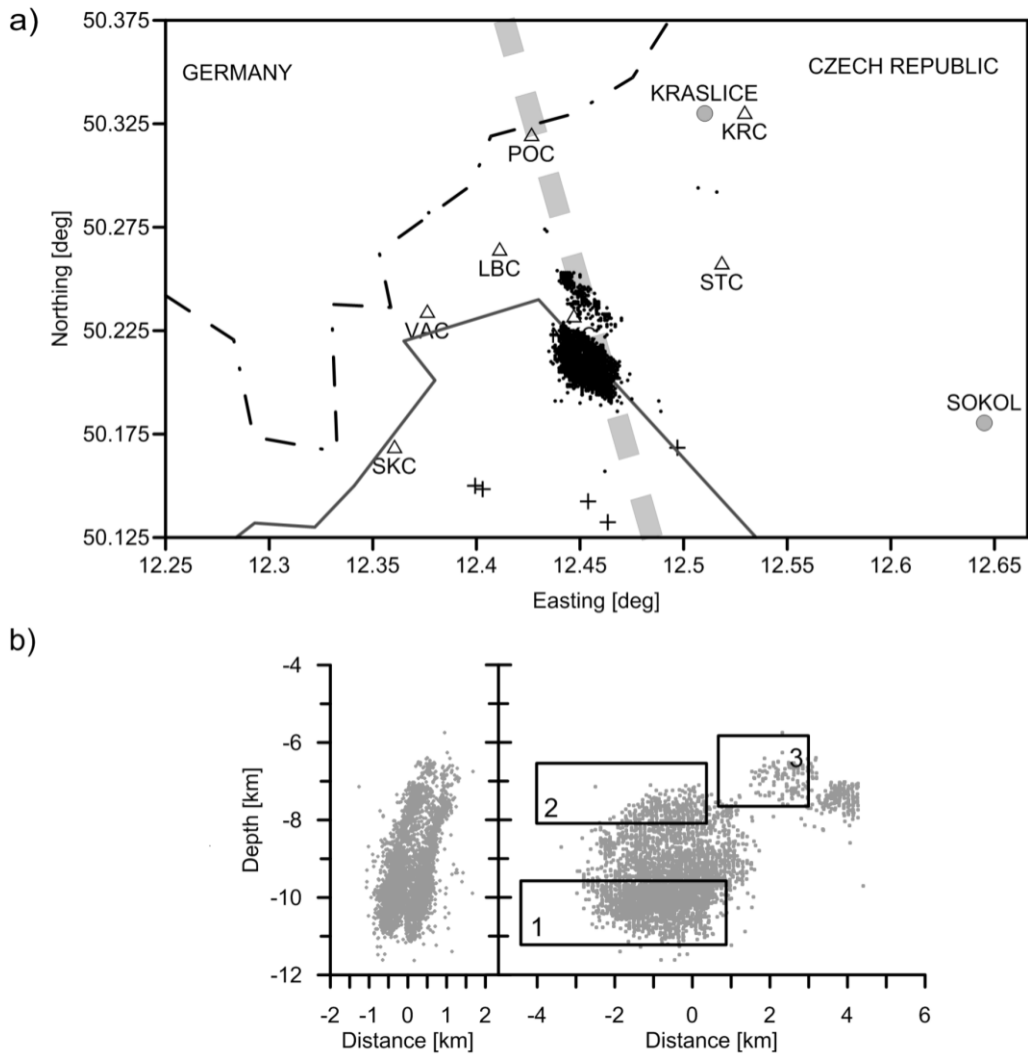
Figure 4.1. a) The West Bohemia (WB) region with the indicated location of stations (triangles), epicenters of events located during the 2008 swarm (black dots), high CO_2 emanation mofettas (crosses), and the direction of the main fault system (dashed gray line). b) Spatial distribution of earthquake hypocenters along the main fault system. Left panel indicates vertical section perpendicular and right panel parallel to the Nový Kostel focal zone. The black rectangle labeled 1 indicates the location of events for October 10 and 19, labeled 2 for October 28, and labeled 3 for December 14, 2008.

The seismic swarms in WB have been continuously monitored over the last three decades using the WEBNET local network (Horálek et al., 1996). Recently, the problem of seismic attenuation in the region attracted more attention, and resulted in several studies. Bachura and Fischer (2015) used coda waves of 13 events to calculate coda Q in the WB region. Mousavi et al. (2017) performed tomographic

87

study showing that attenuation in the Nový Kostel focal zone is stronger than outside of the focal zone. In this chapter, we investigate seismic attenuation and its temporal changes that are likely to be related to the observed seismic swarm that occurred in 2008.

4.2 Dataset

We study P- and S-wave attenuation of the WB region using data from the 2008 swarm (Fischer et al., 2014). Specifically, we focus on the data collected on October 10 and on October 28, 2008, as the largest number of recorded events was recorded during these days (Fig. 4.2). Additionally, we use data collected on October 19 and December 14 with fewer events analysed. The magnitudes of earthquakes detected and located during those days vary from $M_L < 0$ to M_L 3.2. We use data from 7 nearest WEBNET stations: Kraslice (KRC), Luby (LBC), Nový Kostel (NKC), Skalná (SKC), Vackov (VAC), Počátky (POC) and Studenec (STC) which provided clear, single, direct arrivals.
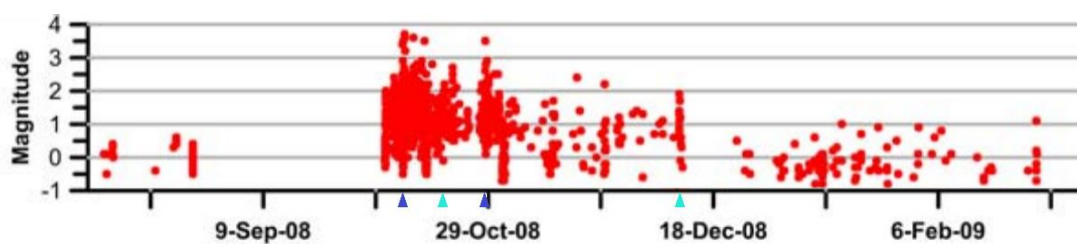
Figure 4.2. Time evolution of the 2008 swarm with indicated events' magnitudes from the WEBNET catalogue. Blue triangles indicate October 10 and 28 with events which were primary object of the analysis, light blue triangles indicate October 19 and December 14 with events, which were used as auxiliary.

Examples of direct wave arrivals used in this study are shown in Figure 4.3. For each station, we selected events with a high signal-to-noise ratio and clear, single, direct wave arrivals. We relocated selected events using P- and S-wave arrival times chosen from at least 4 stations and using the velocity model of WB (Málek et al. 2005). The calculated locations correspond well to locations of the WEBNET catalogue which, however, does not include all events used in our analysis. Events recorded during October 10 have similarly located epicentres to events recorded

during October 28, but their hypocenters are at different depths. The average depth for the selected earthquakes of October 10 is 10.25 km (standard deviation of 0.47 km), and the average depth of the selected earthquakes from October 28 is 8.10 km (standard deviation 0.41 km). Figure 4.4 shows the locations of earthquakes used in the study.
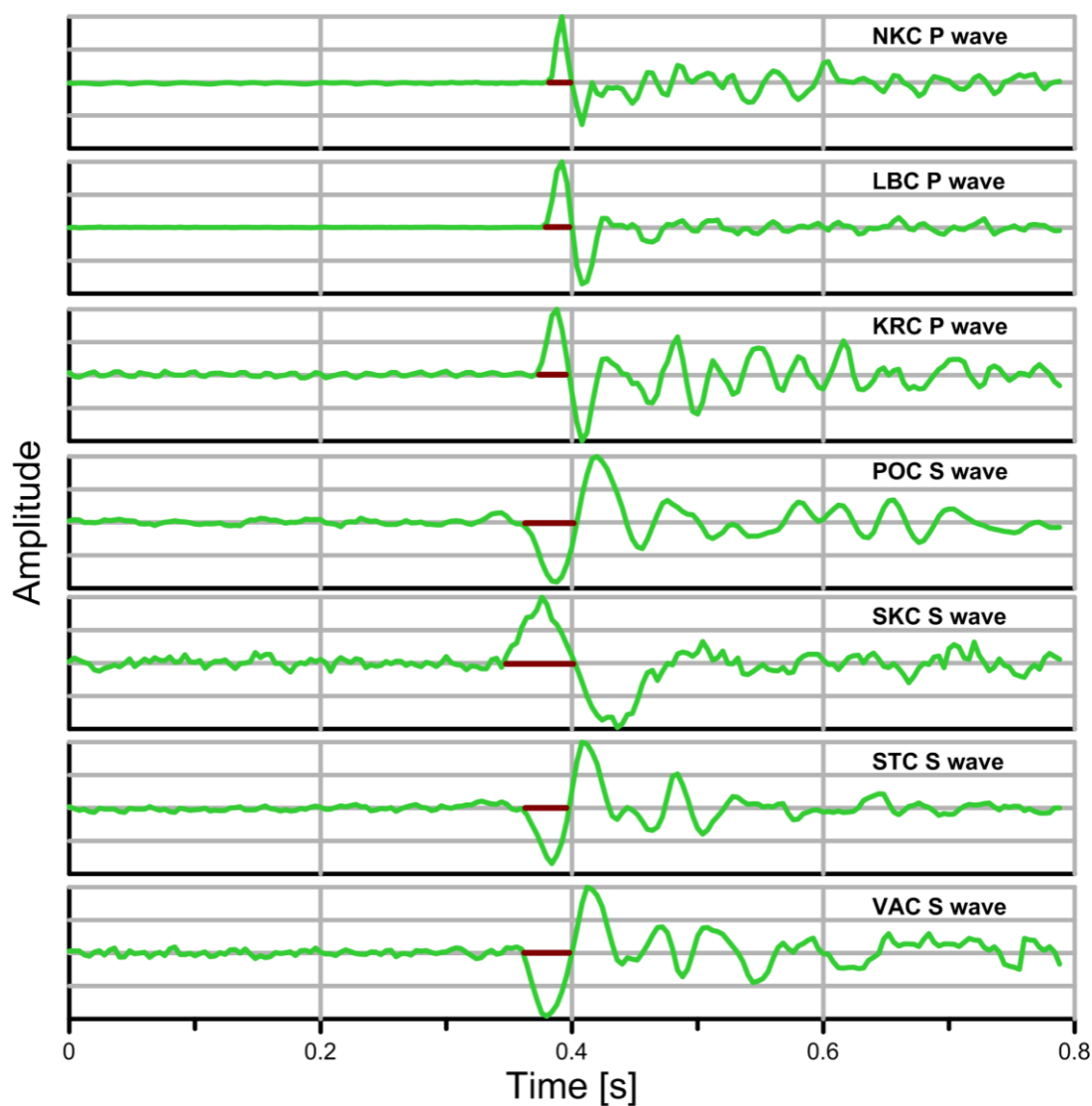
Figure 4.3. Examples of the waveforms used for the peak frequency measurement, cherry red lines show half-periods used to evaluate f_{peak}.
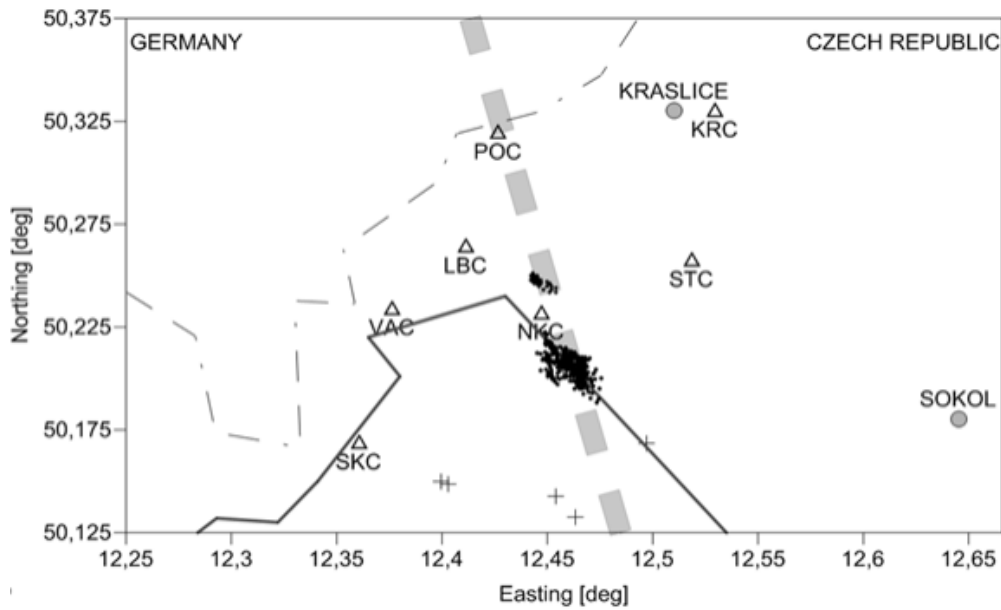
Figure 4.4. Location of epicentres (black dots) of events used in this study. High CO2 emanation mofettas are marked as crosses, and the direction of the main fault system is marked as thick dashed gray line.

4.3 Results

In order to determine the effective Q factor, we selected at least 35 high signal-to-noise ratio waveforms per station for a given day. We did not use the largest observed events as the corner frequencies of these events are relatively low and could affect the measured peak frequencies at the stations. In general, this restriction led us to the use of events of magnitude $M_L<1.0$. Moreover, we ensured that for stations close to the focal zone (especially the NKC station), only smaller events were used as, according to Michálek and Fischer (2013), events of $M_L\sim1.0$ have corner frequency of approximately 35 Hz – similar to the P-wave peak frequencies of the nearby stations. Figure 4.5 shows measured peak frequencies versus M_L for stations LBC (P-waves) and STC (S-waves). As shown in Chapter 3, section 2, this plot allows to examine if the peak frequencies are affected by corner frequency (depending on the magnitude of the event) and should not be used to estimate t^* and effective Q of the medium. We can see that events selected in this study (black dots) have their peak frequencies independent of the magnitude, therefore they are considered to be solely controlled by attenuation. In Figure 4.5 we also included peak frequencies for stronger events than those used in the study (grey dots). P-wave peak frequencies

for station LBC start to decrease with growing magnitude at $M_L \sim 1.8\text{-}2$. The decrease behind this threshold clearly shows how f_{peak} can depend on the magnitude of the event. S-wave peak frequencies measured at the STC station do not change with magnitude even for $M_L = 2.4$ (STC is located in a similar distance to epicenters as station LBC, but the propagation time of S-waves is much greater, therefore the t^*'s for direct waves at this station are greater). Results shown in Figure 4.5 clearly show that events selected in this study can be reliably used to estimate t^* and evaluate effective Q in the region.
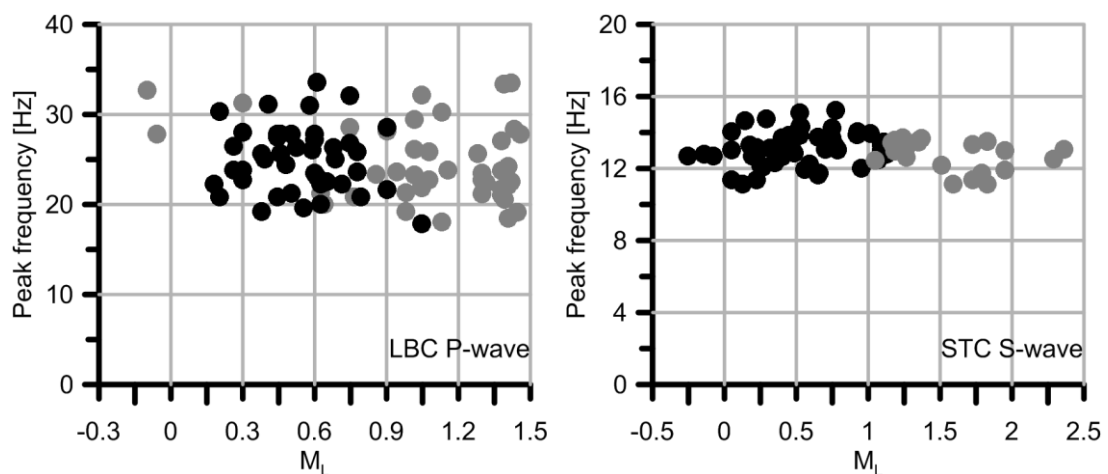
Figure 4.5. Measured peak frequencies versus magnitudes M_L for stations LBC (P-wave) and STC (S-wave) recorded on 28th of October 2008. Black dots indicate events used in the study, grey dots indicate additional measurements that include significantly stronger events as well.

For five of the seven selected stations, we were not able to reliably invert for both Q_P and Q_S factors, but only for one of the factors. Either recorded direct P- or S-waves at a given station had a low signal-to-noise ratio or they were contaminated by guided waves. Figure 4.6 shows all measured values of peak frequencies for selected stations as a function of traveltime. Let's note that in general, the measured peak frequencies decrease with increasing traveltime, which further confirms that they are controlled by attenuation. Interestingly, if we focus on stations individually, we may see that in some cases we get consistently different values of f_{peak} for stations with similar traveltimes (see difference between S-wave peak frequencies for station

STC and SKC). This is an indication that there are differences in the strength of Q in the region. Interestingly, in some cases – e.g. for stations LBC or VAC, we obtain clouds of peak frequencies of similar values for events recorded during both 10.10 and 28.10 despite differences in traveltimes (caused by different depths of hypocenters, as shown in Figure 4.1b). Figure 4.7 shows average values of effective Q calculated using eq. (3.7) from t^*'s measured from peak frequencies shown in Figure 4.6. It shows that in our measurements, we observe statistically significant differences in estimated Q between stations but also between the two selected dates. This, what can seem like a temporal change between October 10 and 28 is especially pronounced for stations NKC (October 10 – lower Q), LBC, VAC, SKC and POC (October 10 – higher Q). In the following paragraphs, we discuss in detail possible reasons for these observations.
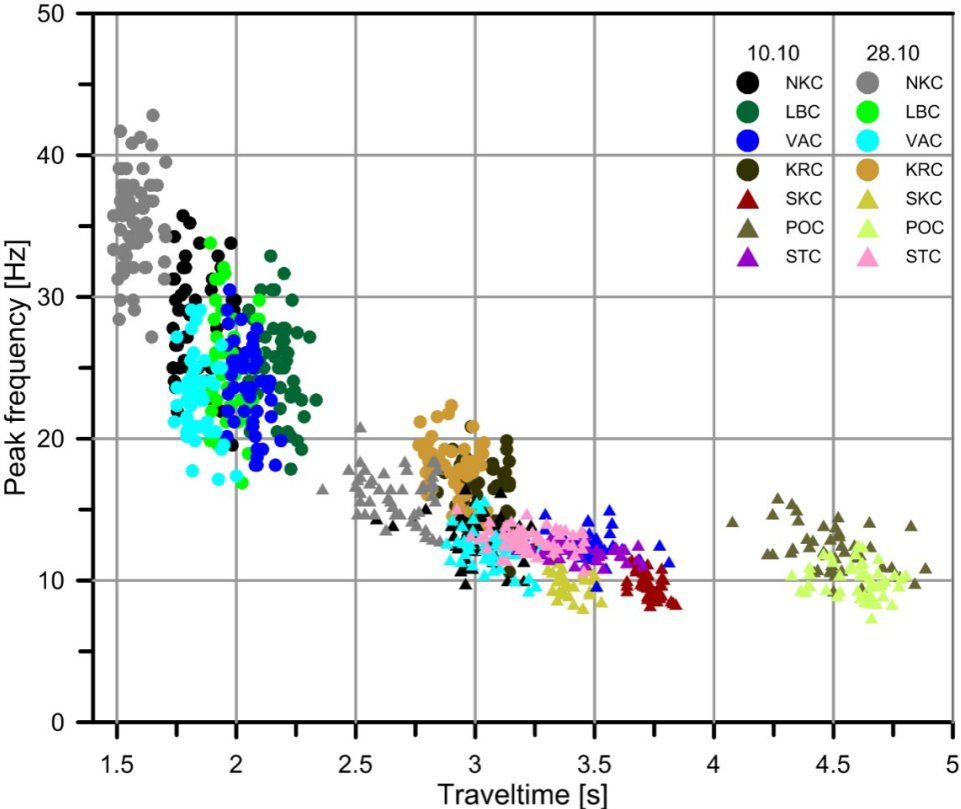
Figure 4.6. Measured peak frequencies as function of traveltimes for stations used in the study. Circles indicate measurement of P-waves, triangles S-waves (note that the legend entrees include only one of these symbols). Measured events that occurred on October 10 are marked with different colors than events that occurred on October 28. Note that for stations NKC and VAC, it was possible to make measurements of both P- and S-waves.
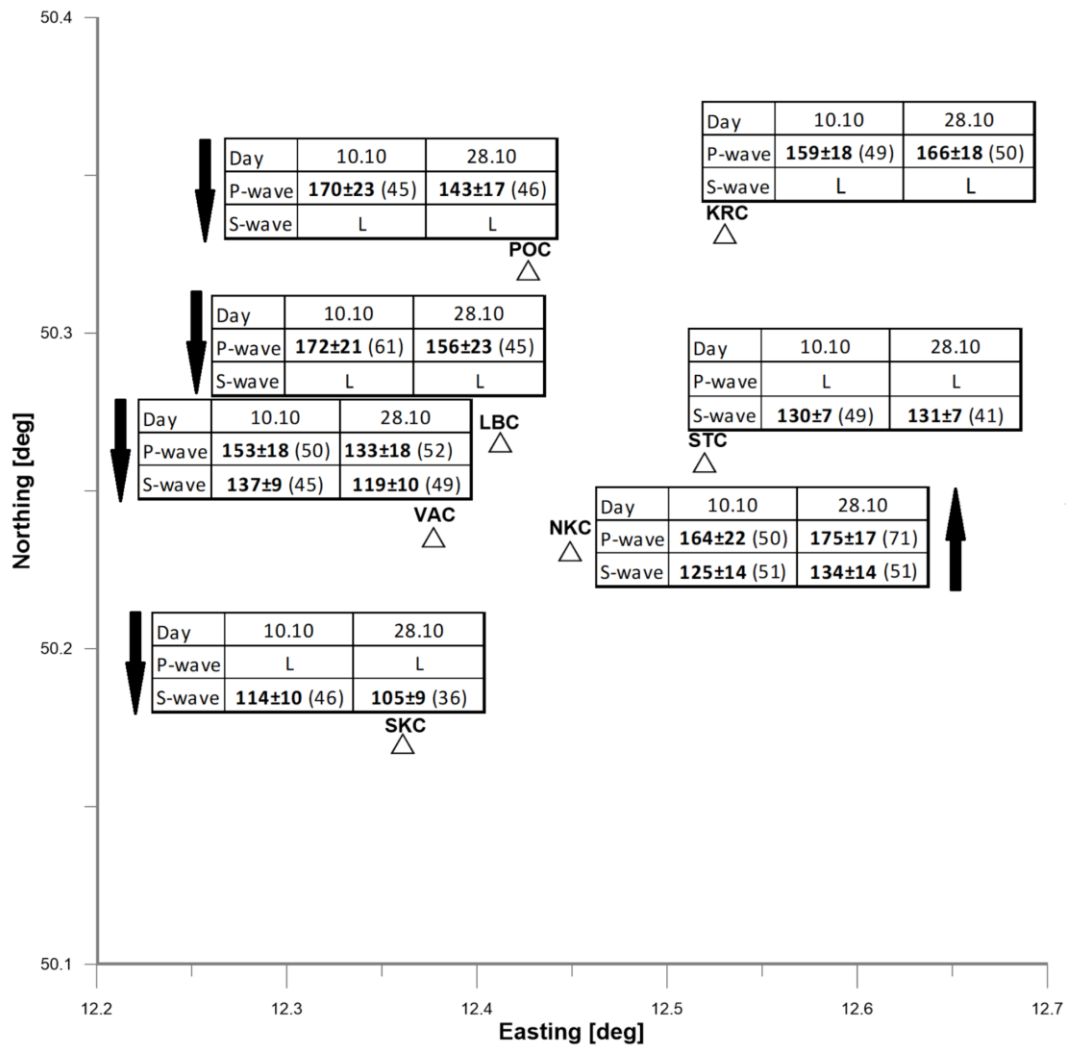
Figure 4.7. Estimated effective Q_P and Q_S values. Numbers in brackets indicate the number of used events. L indicates the insufficient quality of the data for Q determination. Stations are represented by triangles with three letter identifiers. Arrows indicate significant change (increase or decrease) of measured Q between October 10 and October 28, 2008, with t-test confidence level above 99.75%.

4.4 Interpretation of results

As noted earlier, both effective Q_P and Q_S determined from the data recorded at the NKC station are lower for the events of October 10, than for events of October 28 (with statistical t-test confidence level above 99.75% for both sets). The NKC station is located almost directly above the studied part of the focal zone of the

swarm. The proximity of the epicenters to NKC station results in nearly vertical ray paths. Given that the Nový Kostel focal zone itself is also nearly vertical as shown on the crossections in Figure 4.1b, the difference in traveltimes for earthquakes recorded during October 10 and 28 is due to the difference in depths of their hypocenters. The waves generated by deeper events of October 10 and recorded at the NKC station propagate first through the fault zone and then their ray paths are similar to ray paths of shallower events of 28th of October. The Nový Kostel fault zone is highly fractured and probably filled with fluids (Fischer et al. 2017). The influence of cracks on attenuation of seismic waves is a well-described phenomenon. Namely, presence of cracks in a medium result in higher attenuation (Caleap et al., 2009). In contrast to deeper parts, the rocks in the shallower parts near the Nový Kostel area are probably not significantly fractured or permeable as no CO_2 flow was observed in the vicinity of NKC (Faber et al., 2009). Therefore, different values of Q estimated using events recorded during October 10 and 28, are probably not caused by temporal changes of medium properties, but are due to different depths of the events' hypocenters. Waves generated by earthquakes that occurred during October 10 propagated through big portion of the focal zone, which is likely to be characterized by high attenuation.

Station NKC and events that occurred during October 10 and 28 have suitable geometry that allows us to estimate the Q factor in the focal zone of the swarm using approach that relies on partial overlay of ray paths for different events, see Chapter 3, section 6. To apply this approach, we use all combinations of earthquakes of October 10 and 28 recorded at station NKC that were used in this study. The peak frequencies for the P- and S- waves recorded by the NKC station and the resulting quality factors in the Nový Kostel focal zone are shown in Figure 4.8a. The calculated from all selected couples of events median value of Q in the focal zone for the Q_P is ~119, and the median value for the Q_S is ~84. The measurement of Q in the focal zone using only the average peak frequency and travel time for direct waves recorded during October 10 and 28 provides virtually the same values of Q. This means that the attenuation in the source region is higher for both P- and S- waves than for the overlying rocks (Q_P=175, Q_S=134 for shallow events of October 28). Lower Q in the focal zone is consistent with the expected presence of fluids and compressed CO_2 -

filled cracks. Reduced values of Q in the source region were later confirmed by findings of Kriegerowski et al. (2019), who used independent alternative method (based on event couple spectral ratio) and the data from 2008 swarm as well.
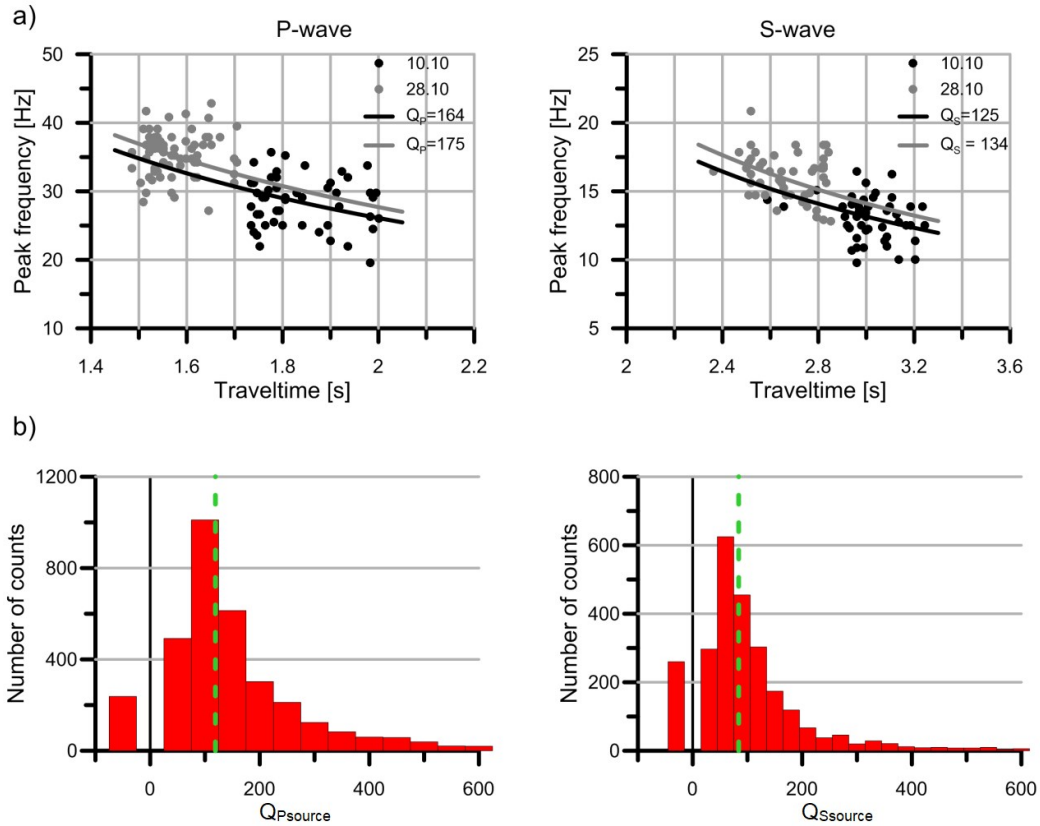
Figure 4.8. a) P- and S-wave peak frequencies estimated at the NKC station as a function of traveltime for events recorded on October 10 and 28. Solid curves represent theoretical decay of peak frequency with time, seeequation (3.7) using median of estimated values of Q_P and Q_S values for each day; b) histograms showing P- and S-wave Q_{source} factors determined from each couple of sources whose peak frequencies are shown in (a). Dashed lines indicate the median Q_P and Q_S at the source (see equation 3.16) equal 119 and 84 respectively. Negative values of Q are produced by noise in the data.

4.4.1 Decrease of the effective Q between October 10 and 28, 2008

In Fig. 4.7, we showed statistically lower Q estimated from recordings of October 28 than Q estimated during October 10 for stations LBC, POC, SKC and VAC. The decrease of Q factor values for the events of October 28 has the t-test confidence level above 99.75% for each station, which indicates that it is not the result of noise

in the data. The decrease of Q is also reflected in distribution of the peak frequency as a function of traveltime shown in Figure 4.9. It includes separate graph for each station (with exception of earlier discussed NKC station –graphs for this station are shown in Figure 4.8a). We may see that for each day, for a given station, there is a general trend of decrease of peak frequencies with increasing traveltime. Nevertheless, for stations LBC, POC, SKC and VAC this trend is interrupted - clouds corresponding to October 10 is shifted up in relation to the cloud corresponding to October 28. This produces above noted lower value of Q for October 28. There is no shift visible in the graph for stations KRC and STC - the peak frequency continuously decreases with increasing traveltime. We can note that median effective Q estimated from peak frequencies for station KRC differs between October 10 and 28 only by 4.5%, which is significantly less than in the case of other stations mentioned earlier. The statistical t-test indicates that the difference is not significant, therefore the difference is likely caused by the noise in the data. Except the case of the data recorded at the POC station, which will be described further below, it is very unlikely that the observed change in effective Q is merely a result of earlier noted different depths of the events during the two investigated days. In this case, one would expect higher peak frequencies for shallower October 28 events as their wave paths are shorter. It should be so even if the deeper rocks are less attenuating (unlike the case of the station NKC, ray paths of waves propagating to stations SKC, VAC and LBC leave almost immediately the focal zone). Despite this, the measured median peak frequencies are slightly higher for the October 10 events. The resulting differences in the estimated quality factors must therefore result from temporal changes in attenuation in considered regions. In the following, we propose an explanation of the temporal increase in seismic attenuation observed at stations SKC, VAC, LBC and POC that is consistent with available literature describing West Bohemia earthquake swarm region and 2008 swarm.
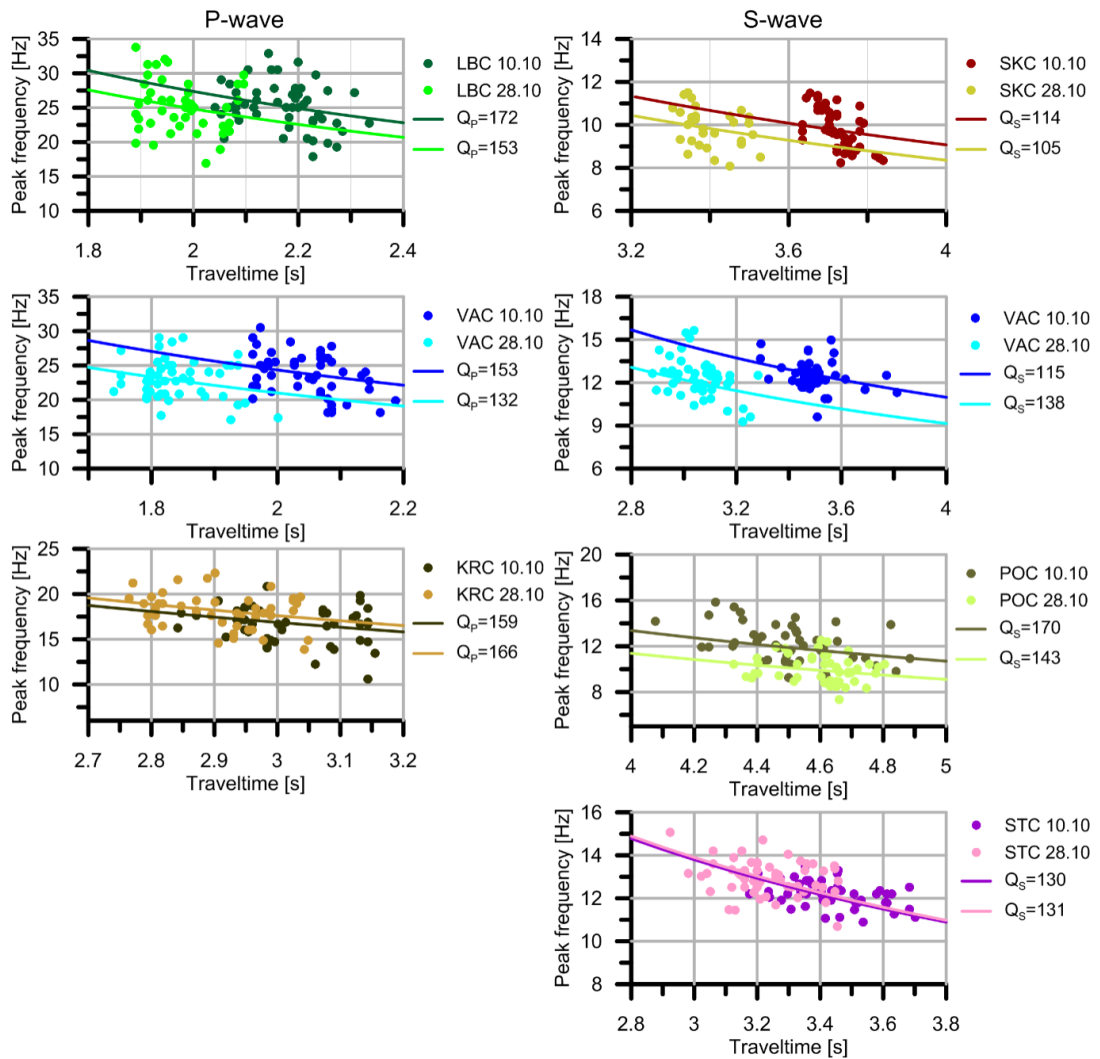
Figure. 4.9. Peak frequencies as a function of traveltimes for stations used in the study (NKC station is shown in Fig. 4.8a) along with a theoretical peak frequencies (solid curves) corresponding to the median effective Q factor for each of the two days.

4.4.2 Interpretation of the Temporal Change in Attenuation

The temporal change of attenuation may be connected to the swarm origin itself. The origin of the WB earthquake swarms is attributed to the migration of fluids (water and CO_2) originating in the lower crust/upper mantle (Bräuer, 2009; Fischer et al., 2014 and 2017). Because the presence of fluids can increase the intrinsic attenuation of the medium, the increase of the fluid activity may be the reason for the increase in the measured attenuation. The presence of the compressed gases/fluids in the medium is manifested through the emanations of CO_2 of upper mantle/lower crust origin. Degassing process has been monitored in the region at

several dry mofettas and mineral springs over the past two decades (Faber et al., 2009; Koch et al. 2011; Fischer et al., 2017).

According to Fischer et al. (2017), there was a substantial increase in CO_2 flow in the Cheb basin mofettas during the 2008 swarm; the CO_2 bubble fraction in the Hartoušov mofetta increased by approximately 35% between October 10 and 28 as shown in Fig. 4.10. A similar, even more significant CO_2 flow increase was observed during the 2014 aftershock sequence in the same mofetta. It was interpreted as a release of the lower-crust CO_2 reservoir through the fault-valve model (Fischer et al., 2017).
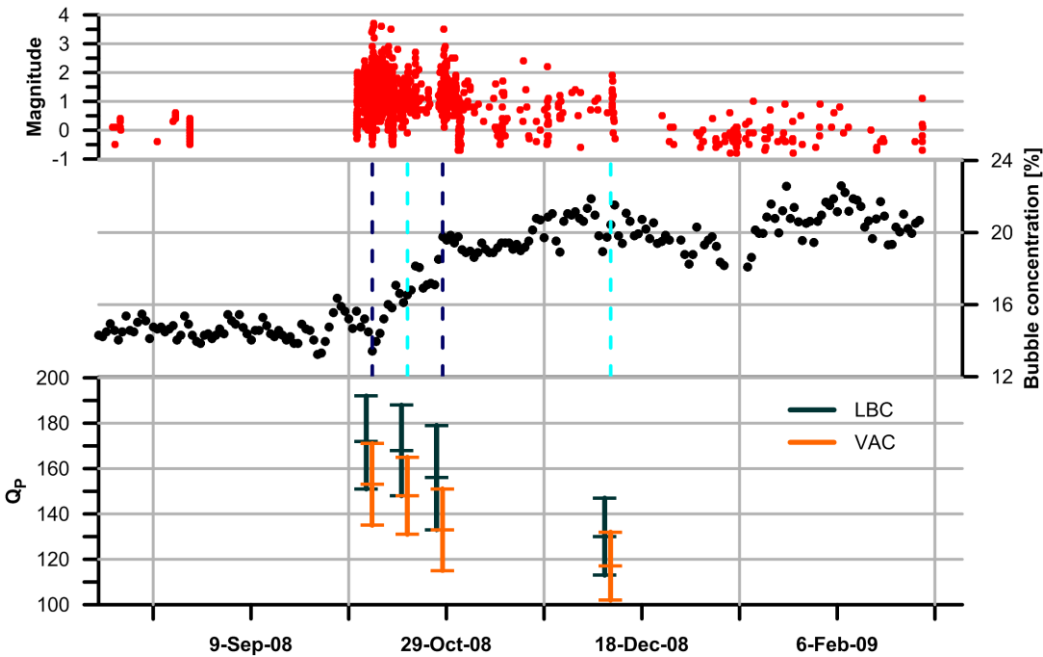
Figure. 4.10. Upper panel – time distribution of earthquakes from the WEBNET catalogue during the 2008 swarm, see Figure 4.2. Middle panel - change in the CO_2 emanation during the 2008 swarm, dashed lines indicate dates during which the analyzed events were recorded (navy blue indicates October 10 and 28 used for all stations and cyan marks October 19 and December 14 used for additional analysis at LBC and VAC stations). Lower panel: median±standard deviation values of measured Q_P at stations LBC and VAC.

Apparently, the presence of CO_2, which is compressible in the medium at the depth of ~10km (Zhu et al., 2017), may influence attenuation characteristics of the medium. High attenuation of gas-filled rocks is a characteristic commonly observed

in industrial seismic applications where gas chimneys above oil reservoirs often attenuate seismic waves, see e.g., Ebrom, (2004). Tisato et al. (2015) and Zhu et al. (2017) showed that partial saturation of CO_2 in the medium results in increased attenuation of rocks for frequencies including the frequency range of this study. This is consistent with changes of Q found in this study. Also, according to Walls et al. (2006) and Lei and Xue (2009), the increase of CO_2 saturation in the pore space of the medium may result in increased attenuation.

We are reluctant to assume that the change in the CO_2 flow is the sole reason for the measured change of attenuation. We have no information whether the fractures, through which CO_2 migrates, have high enough density and proper distribution to affect the attenuation. Moreover, the most powerful CO_2 mofettas are situated south of the stations that we used in our study; therefore, it is not reasonable to assume that changes of attenuation at stations like LBC are solely due to the influence of CO_2. In any case, we can conclude that the changes in the measured CO_2 flow and its connection to the swarm activity are a good indicator that fluid-involving processes are present in the region and may influence the medium in the vicinity of the Nový Kostel focal zone resulting in an increased attenuation of waves propagating to the west from the sources. To verify whether the discussed changes of Q indicate the presence of such processes, we made additional measurements of attenuation for events recorded on October 19 and in the late stage of the swarm on December 14, 2008. For this purpose, we used P waves recorded at stations VAC and LBC, as they show high quality waveforms suitable for Q determination (40 and 30 waveforms for station LBC, 30 and 35 for station VAC on October 19 and December 14 respectively). The results are shown at the bottom of Fig. 4.10. It turns out that results for both stations show a monotonous Q_P decrease for the whole period from October 10 to December 14, which confirms observations from section 4.4.2 and correlates well with the increase in the CO_2 flow rate observed by Fischer et al. (2017). The possibility of temporal changes is also consistent with findings of Bachura and Fischer (2016) who provided evidence for temporal changes in values of the VP/VS ratio inside the fault zone during the 2014 swarm.

The decrease of the effective Q factor for the POC station between October 10 and October 28 may be explained in an alternative way, which is related to the

99

position of the station in the relation to focal zone and events used for the peak frequency estimates. Station POC lies on the Počátky-Plesná fault, in the extension of the Nový Kostel fault zone, see Figure 4.1a. The events that occurred during October 10 that we used for estimates of Q at the POC station were recorded few hours later than the majority of events selected for other stations as the recording at POC was interrupted during that day. Epicenters of events used in the study at stations POC and LBC (located close to the Počátky-Plesná fault as well) are shown in Figure 4.11. In contrast to the station LBC, the epicenters of events recorded during October 10 that we selected at station POC are slightly shifted to the north in relation to events that we selected at other stations during both October 10 and 28. The epicentral distance of events used at POC for October 10 is shorter on average by 1.5 km than that of events used for Q measurements at this station on October 28. It means that the waves recorded at POC on October 28 propagated ~1.5 km more within the focal zone than waves recorded at POC on October 10. The case of the POC station is in this way similar to the earlier described case of the NKC station (section 4.4.1). This may, at least partially, explain the difference in the measured effective Q's at the POC station.
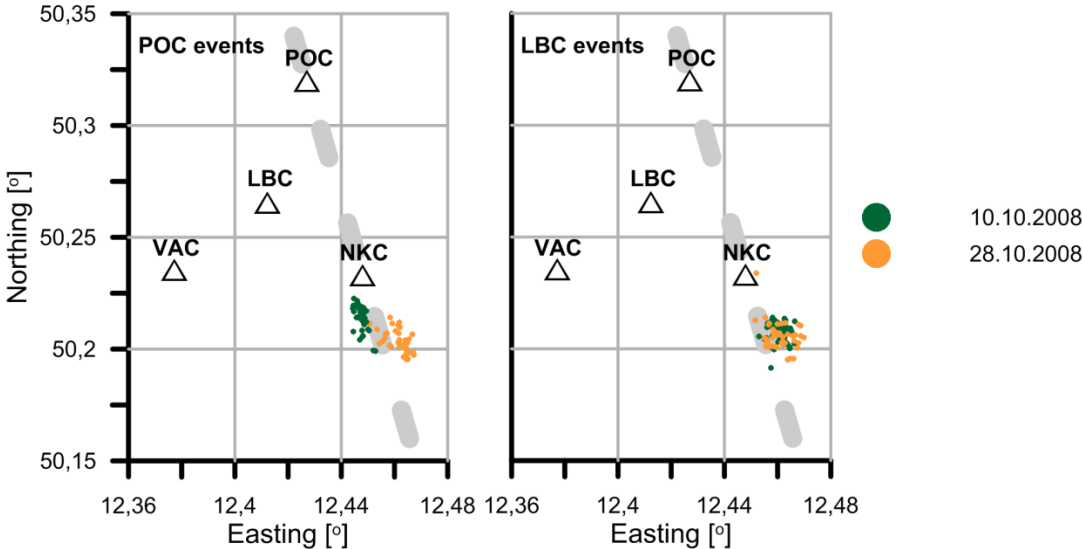
Figure. 4.11. Locations of epicenters of events used in measurements at POC and LBC stations. The thick grey dashed line indicates the Počátky-Plesná fault.

Chapter 5

Analysis of attenuation using induced seismicity in the region of High Agri Valley – Italy

5.1 Induced seismicity caused by wastewater disposal

Recently, attention to wastewater (usually saturated by salts) injections has been growing within the scientific community, especially due to the higher activity in the exploration of tight oil reservoirs and intensified hydraulic fracturing of the shale formations. As a consequence of injection of fluids, there is often seismicity induced/triggered by such activity (Grigoli et al. 2017). Magnitudes of these induced/triggered earthquakes may be large like the 2016 M_w 5.8 Pawnee earthquake in Oklahoma (Walsch and Zoback 2015). Altough exploration of unconventional reservoirs in Europe is not in an advanced stage, fluid injection is becoming a matter of widespread social concern (e.g., van Eck et al. 2006). European cases of seismicity induced or triggered by fluid injection/withdrawal are earthquakes (mostly with swarm-like character) that occurred in Basel and St. Gallen in Switzerland (Edwards et al. 2015), Blackpool in the UK (Clarke et al. 2014), Soultz-sous-Forêts in France (Baisch et al. 2010), Groningen in Netherlands (van Thienen-Visser and Breunese 2015), Castor in Spain (Cesca et al. 2014), and High Agri Valley in southern Italy (Stabile et al. 2014a; Improta et al. 2015). The latter case is rare in European context, since the seismicity is triggered by the injection of large volumes of wastewater in a place where the largest onshore oilfield in the western Europe is located, and the wastewater produced from the exploitation of the oil field is injected back into the subsoil through a single injection well, named Costa Molina 2 (CM2).

5.2 High Agri Valley

High Agri Valley is a Quaternary basin located in the axial zone of the southern Apennines thrust belt chain. From a seismotectonic point of view, High Agri Valley is bordered by two NW-SE trending normal fault systems: the Eastern Agri fault system

(EAFS) to the east (Cello et al. 2003) and the Monti della Maddalena fault system (MMFS) to the west (Maschio et al. 2005). Historical seismicity (Rovida et al. 2016) shows that High Agri Valley is one of the regions with high seismogenic potential, where the seismicity is characterized by historical presence of strong earthquakes esuch as the M_W 7, 1857 Basilicata earthquake. The NE-SW extensional stress regime is active as verified by different stress indicators (Cello et al. 2003; Montone et al. 2004) and space geodesy data provided by GPS network (Riguzzi et al. 2012).

The fluid-injection induced seismicity occurs in the southeastern part of High Agri Valley near the CM2 well in the municipality of Montemurro (Figure 5.1a) with onset of the swarm-like seismicity observed only after the disposal of wastewater was started (2nd of June, 2006). The seismicity is characterized by shallow (less than 5 km depth) microearthquakes (local magnitudes $M_L \leq 2$), which occur along a NE dipping
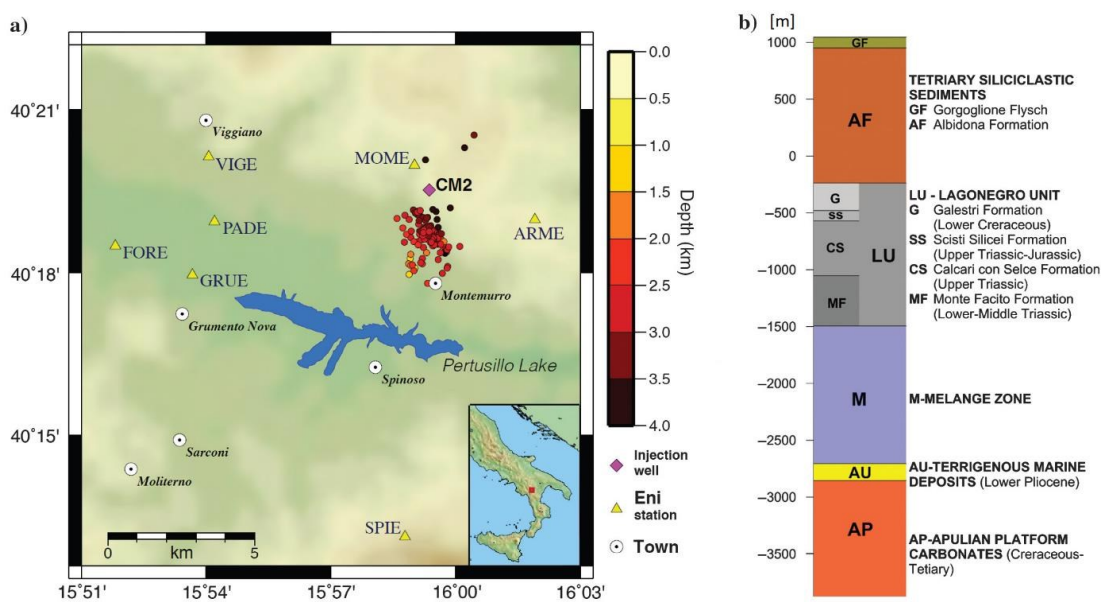
Figure 5.1. a) Fluid-injection induced/triggered seismicity (represented by small circles with varying colour indicating positions of hypocenters) in High Agri Valley (southern Italy) recorded by the company Eni seismic network between June 2006 and December 2012 (from Stabile et al. 2014a). Diamond labeled as CM2 represents the position of the wellhead of the wastewater disposal well. Triangles represent the positions of the seismic stations. White circles with black centers show the locations of settlements. Shading reflects the elevation. b) Stratigraphic log of the CM2 injection well (from Stabile et al. 2014a).

102

fault (Stabile et. al., 2014a). Considering the complex geological-structural setting and the high seismic hazard of the area where such fluid-induced seismicity started to occur, and considering the occurrence of hydrogeological instability phenomena, the area became a subject of great interest in seismological (Pischiutta et al. 2014; Stabile et al. 2014a, 2014b; Improta et al. 2015), seismotectonical (Giocoli et al. 2015; Buttinelli et al. 2016), hydrogeological (Gueguen et al. 2015), and environmental (Colella 2014) studies.

High Agri Valley is filled by Quaternary continental deposits of variable thickness that cover the pre-Quaternary substratum consisting of allochthonous units overlaying the Mesozoic-Tertiary carbonate sequence of the Apulian Platform (see AP in Figure 5.1b), which is 6-7 km thick (Menardi Noguera and Rea 2000, and references therein), and constitutes the reservoir unit for the biggest onshore oil field in western Europe. Geophysical investigation and deep well logs showed that in High Agri Valley, the top of Appulian Platform is between 2 and 4 km below sea level (b.s.l.) (Dell'Aversana 2003; Turrini and Rennison 2004). Effective decoupling between the allochthon and the buried Apulian unit is related to the rheological contrast produced by a clay-rich "mélange zone" (Mazzoli et al. 2001; Balasco et al., 2015), which is several hundreds of meters thick but locally it can be more than one kilometer thick (Shiner et al. 2004). The study area falls in the southeastern part of High Agri Valley, in the township of Montemurro (Fig. 5.1a). The pre-Quaternary substratum of this area (see Figure 5.1b) consists of Tertiary siliciclastic sediments (Albidona Formation and Gorgoglione Flysch), which crop out mainly in the northern sector of Montemurro (Giocoli et al. 2015), above pelagic successions (Lagonegro Units). Here the mélange zone is about 1.2 km thick and the top of the Apulian Platform gently dips (Turrini and Rennison 2004; Improta et al. 2015) from 2.8 km b.s.l. at MOME station to about 3 km depth b.s.l. at ARME station (for the location of stations, see Figure 5.1a).

5.3 Dataset

We investigate P- and S-wave attenuation of the southeastern sector of High Agri Valley, by using data from four seismic stations (MOME, ARME, VIGE and SPIE, see Figure 5.1a). The stations belong to the broader local seismic network composed of 15 stations installed by the operator of CM2 well, Eni company, in July 2001 (Stabile et al. 2014b) to monitor the seismic activity in the vicinity of the oil field. These four stations recording with sampling frequency of 125 Hz were operating even before the beginning of wastewater injections (June 2, 2006, Stabile et al. 2014a) and due to their location, they provided the highest quality records of seismic events connected to the wastewater injection in the region. We use data of 206 induced by fluid injection microearthquakes recorded between June 2006 and December 2012, which have their local magnitudes ranging from $M_L = 0.3$ to $M_L = 2.0$ (Stabile et al. 2014a). In our study, we use origin times of both Stabile et al. (2014a), who used a 1D velocity model proposed by Valoroso et al. (2009), and Improta et al. (2015), who used a 3D velocity model (both velocity models provide similar residual values in location process). Traveltimes computed in 3D model are slightly greater than computed in 1D model. We are unable to determine which model provide more accurate results, and therefore, we show values of Q and V_P/V_S that we also measured in this study using origin times from both catalogues.

We measured peak frequencies using direct wave arrivals to estimate t^* using eq. (3.6) and further calculate corresponding effective Q_P and Q_S factors in the region using eq. (3.7). Figure 5.2 shows representative examples of waveforms for all the stations used in the study. Figure 5.2 also shows the half-periods used for the measurement of peak frequency. At the most distant station (SPIE), the signal to noise ratio for the direct wave is not as high as in other stations. For stations MOME ARME and VIGE single arrivals could be identified. Direct arrivals for station SPIE included interferences of later arrivals. The analysis of the data recorded by SPIE station indicated, that first half-periods of direct arrivals are not affected by the following arrivals and, therefore, are suitable for the peak frequency measurements with the use of half-period method. In addition to measurement of the attenuation in the

region, we measure V_P/V_S ratio to see if the influence of the wastewater injected through CM2 manifest in changes of seismic velocities as well.
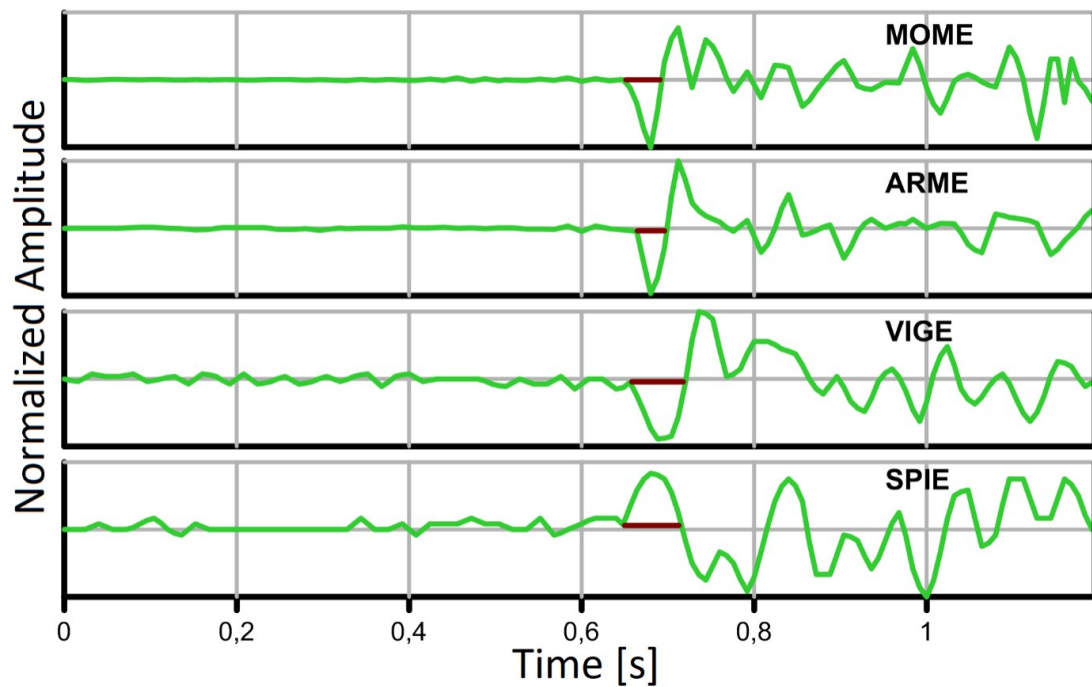
Figure 5.2. Examples of waveforms used in the study with the first-half period marked by dark horizontal line. Note that the time corresponding to 0 is chosen so that onsets at all 4 stations appear at approximately the same time.

5.4 Results

We used only events with maximum M_L = 1.0 to guarantee that corner frequencies did not affect peak frequencies as discussed in Chapter 3. Therefore, the number of useful events dropped to 127. The estimated corner frequencies for the selected events are above 35 Hz assuming conservative value of the stress drop equal 1MPa (higher stress drop results in higher value of corner frequency, for more details see, Kwiatek et al. 2011; Eisner et al. 2013). To measure peak frequencies, we used raw-unfiltered waveforms in order to not influence the form and, therefore, duration of the signal. Furthermore, after initial picking, we re-picked the arrivals again to reduce possible inconsistency among picks. The estimated values of t^* obtained from peak frequencies allowed us to calculate effective Q factors for each of the four stations. S-waves arrivals for more distant stations - VIGE and SPIE were not suitable

for peak frequency measurements; therefore, we did not determine Q_S for these stations. Moreover, the number of useful direct P-waves for station SPIE was significantly smaller in comparison to other stations due to lower signal-to-noise ratio at this station. Measured peak frequencies as a function of traveltimes determined using velocity model of Valoroso (2009) are shown in the Figure 5.3.
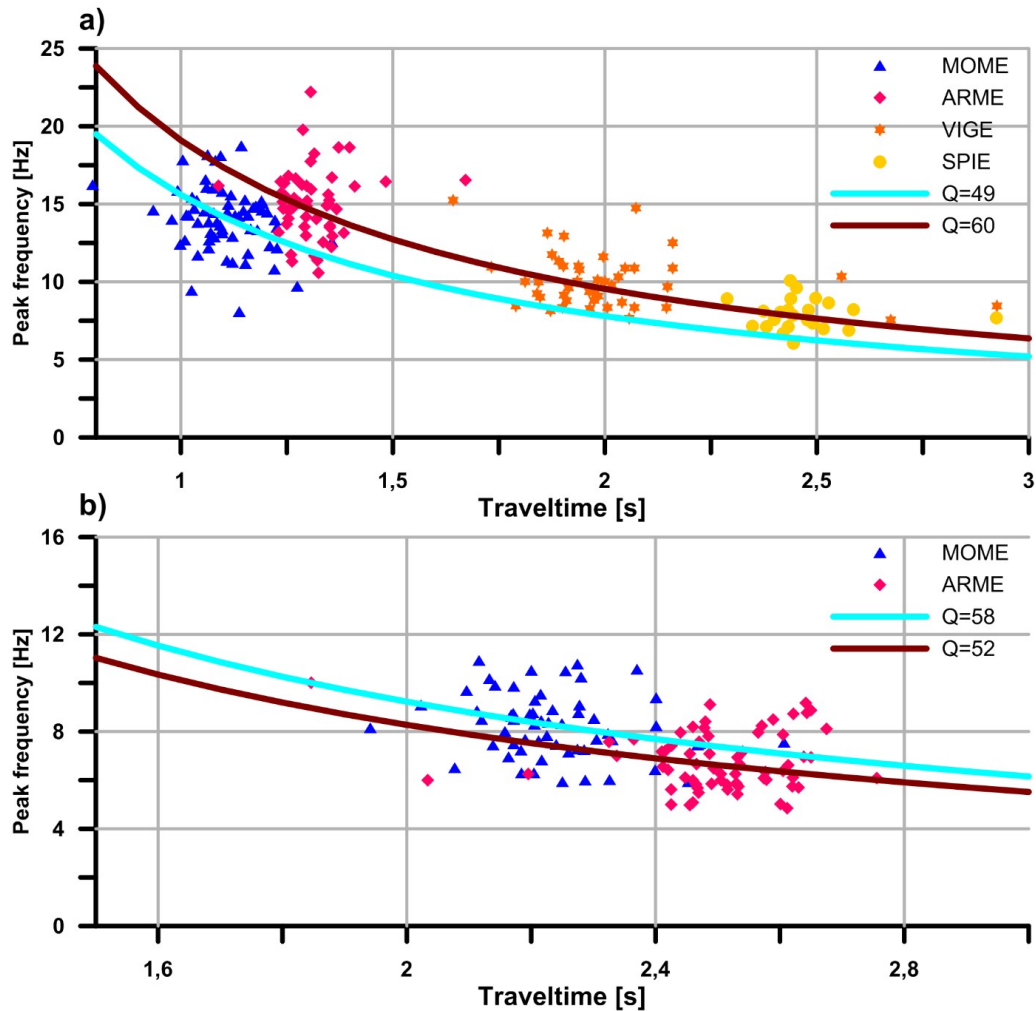
Figure 5.3. Measured peak frequencies (symbols) vs traveltimes of Stabile et al. (2014a) for a) P-waves, and b) S-waves. The cherry red and light blue curves represent peak frequencies predicted by eq. (3.6) for constant attenuation.

We can see that the measured peak frequencies, except one event, do not exceed 20 Hz. The highest peak frequencies are for P-waves recorded at station ARME with median value of 15 Hz, therefore significantly below estimated corner frequency of at least 35 Hz. Figure 5.4 shows measured peak frequencies versus M_L – the plot used to verify if eq. (3.-6) and (3.7) can be used to estimate t^* and Q as suggested in

Chapter 3, section 2. Fig 5.4 shows that there is not a relationship between measured peak frequencies and increasing magnitudes. We can thus consider that peak frequencies of the direct waves are not controlled by the corner frequency, but by attenuation effects only. Table 5.1 summarized values of effective Q estimated using measured values of peak frequencies. Station MOME has estimated effective Q_P factor ~49 for 1D model, ~44 for 3D model, which is significantly lower than Q_P for
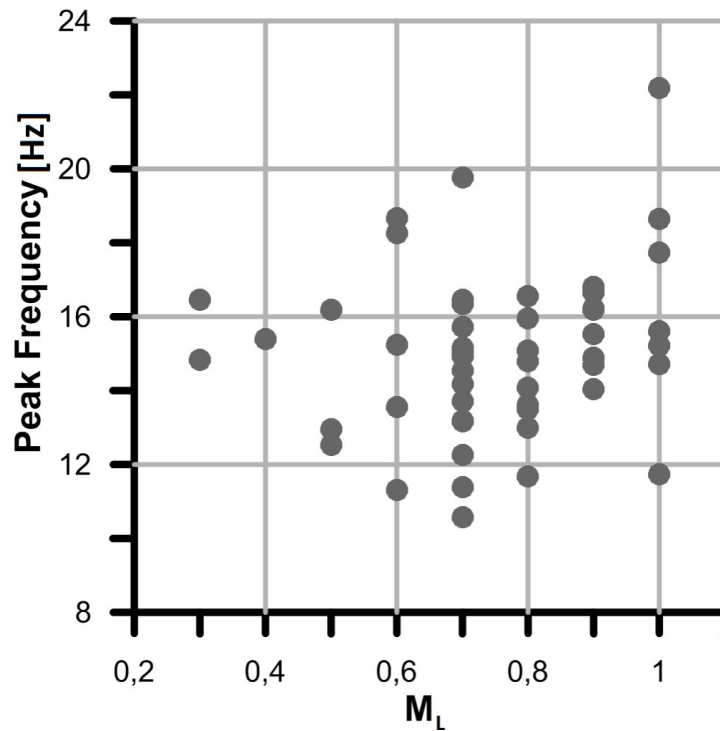
Figure 5.4. Measured peak frequencies versus magnitudes M_L for the ARME - station with the highest peak frequencies.

Wave type	Station	1D model			3D model		
		Q	STDEV	N	Q	STDEV	N
P-wave	MOME	49	7	65	44	8	63
	ARME	61	10	51	55	10	50
	VIGE	60	8	44	57	11	43
	SPIE	61	8	23	56	9	23
S-wave	MOME	58	9	58	54	9	58
	ARME	52	10	65	49	10	65
	VIGE	-	-	-	-	-	-
	SPIE	-	-	-	-	-	-

Table 5.1. Effective Q for P- and S-waves, and their standard deviations STDEV. Each Q was obtained by a different number of measurements N at each station.

stations ARME, VIGE and SPIE: ~60 for 1D model, ~56 for 3D model. The difference of estimated Q_P for the station MOME in comparison to other stations is statistically significant with the T-test confidence level above 99.9%. Therefore, most likely the anomaly is not due to the scatter of the data. The anomaly is also clearly visible in the measured P-wave peak frequency distribution (Figure 5.3a); in fact, the curve corresponding to the theoretical values for $Q_P=60$ fits well the peak frequencies of VIGE, ARME and SPIE, but not those of MOME. Interestingly, we observe that the estimated Q_S is higher for MOME than for ARME station. The difference between the S-wave attenuation factors at MOME and ARME is smaller than that for the P-wave attenuation factors and statistically less significant. Interestingly, Q_P/Q_S ratio for the MOME station is unusually low - below 1. We shall discuss the anomalous results obtained from the data recorded at the station MOME in more detail in the next section part of this chapter.

5.5 Interpretation of results

5.5.1 Influence of the fluid-injection on attenuation and V_P/V_S ratio

Since the seismicity occurring in the investigated area is due to the wastewater injection, the behavior of observed Q factors may naturally be interpreted as the effect of fluids, which affect the medium properties (Gregory 1976). Saturation and pore pressure influence medium properties, like velocity of seismic waves (Han and Batzle, 2004) and attenuation (O'Connel and Budiansky 1977). Since the bottom of the CM2 well is very close to the epicenters of the induced events, it is possible that the injected fluids affect the attenuation between the epicenters and the MOME station in the wastewater injection target layer of the Apulian Platform. According to Pham et al. (2002), the partial saturation leads to the increase of the seismic P-wave attenuation up to the so-called squirt-flow peak at the saturation of ~90% (Helle et al. 2003). A partial saturation may result in $Q_P/Q_S<1$ (Toksöz et al. 1979; Johnston et al. 1979). Such unusually low value of Q_P/Q_S was observed in the studies, which dealt with data gathered from arrays placed in boreholes for hydraulic stimulation of

hydrocarbon reservoirs e.g., Wandycz et al. (2019), but in particular Wcisło and Eisner (2016), who observed it in carbonate rocks. Waves propagating from source area to the station MOME pass the vicinity of the CM2 well. The rocks within Apulian Platform in the vicinity of the CM2 well have likely higher saturation during and after the injection of the waste water. This is consistent with observed higher attenuation of the P-waves at MOME station and lower Q_P/Q_S ratio, and may, at least, partially explain the obtained anomaly.

To confirm existence of anomalous medium properties in the vicinity of the MOME station and validate the above interpretation, we compare another property of a medium, V_P/V_S ratio. We do that at all considered stations to see if the assumed increased saturation and higher pore pressure lead to the increase of V_P/V_S, which was suggested by Audet et al. (2009); Peacock et al. (2011). For this purpose, we used the methodology of Lin and Shearer (2007), which utilizes the origin times calculated during locations and wave arrival times to measure effective (average along the path) V_P/V_S. Although the absolute values of the V_P/V_S ratio calculated using this method may not be fully accurate (due to inaccuracies of velocity models used for location), this method allows to measure the differences of V_P/V_S ratio between stations (Lucente et. al. 2011). To measure V_P/V_S ratio, we may use events with $M_W>1.0$, which were excluded from analysis of attenuation. The results of V_P/V_S measurements are shown in Table 5.2.

Station	1D model			3D model		
	V_P/V_S	STDEV	N	V_P/V_S	STDEV	N
MOME	**1.98**	0.06	183	**2.12**	0.13	175
ARME	**1.89**	0.05	198	**1.98**	0.12	188
VIGE	**1.90**	0.04	193	**1.96**	0.09	185
SPIE	**1.90**	0.05	184	**1.96**	0.10	177

Table 5.2. Values of the measured effective V_P/V_S, their standard deviations STDEV and number of measurements N per station for 1D and 3D models.

Using the 1D model origin times, all stations except MOME have effective V_P/V_S ~1.9, which agrees with the results of Valoroso et al. (2009). The anomalous value is found for MOME station (1.98) and the difference in V_P/V_S between the station MOME and other stations is significant with t-test confidence level above

99.9%. The V_P/V_S anomaly is confirmed as well by using Wadati method (Wadati, 1933, a,b). Wadati method allows determination of the V_P/V_S without determination of the origin time of a seismic event. Figure 5.5a shows a Wadati plot representative
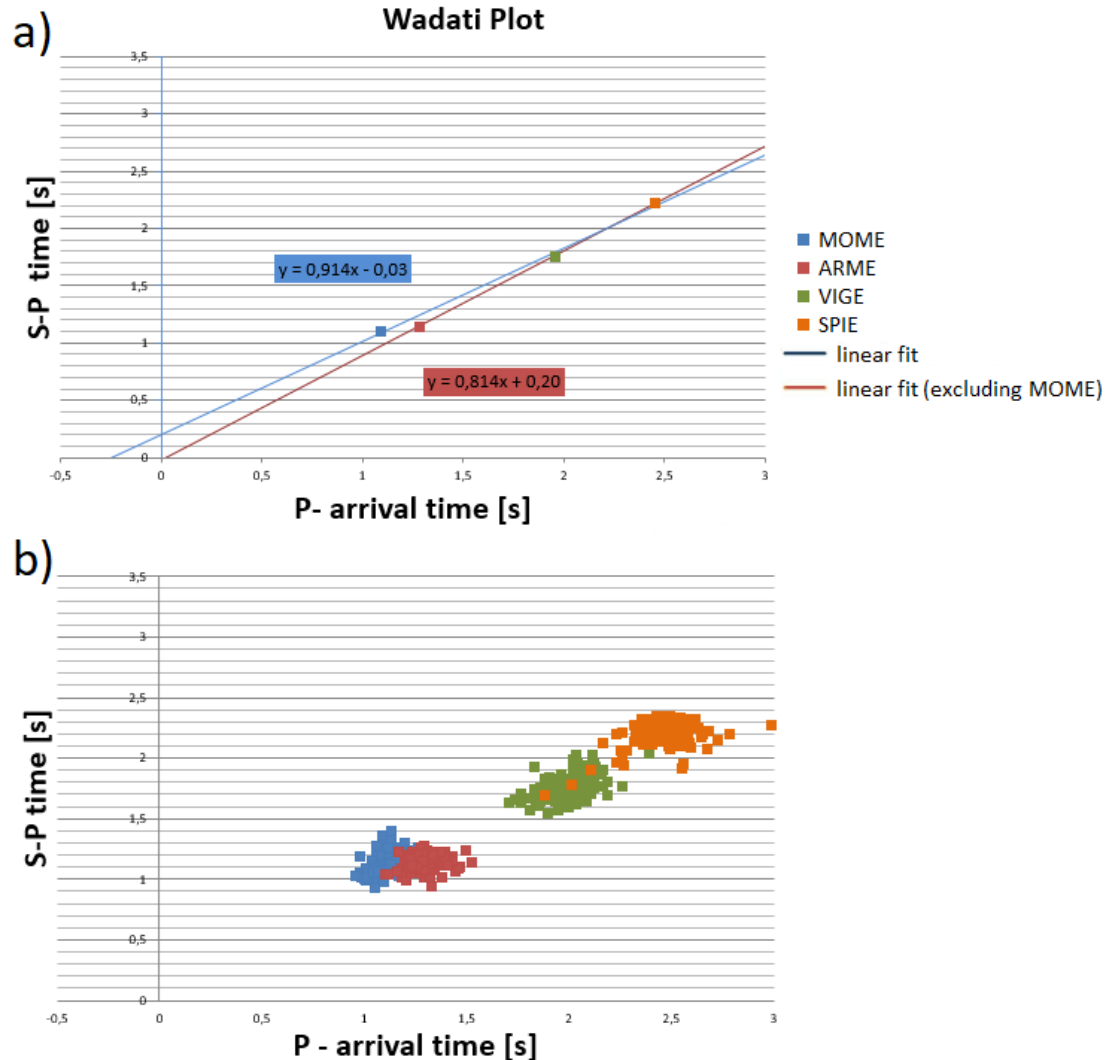
Figure 5.5. a) Wadati plot for a representative event in the dataset. The blue line is a linear regression computed using all four stations. The red line is a linear regression for times observed only at SPIE, VIGE and ARME stations b) S-P times as a function of P-wave arrival times for all events used in the study.

for the dataset used in this chapter. We see that the dot corresponding to the station MOME is not situated on the orange line that is a linear fit computed including datapoints of stations ARME, VIGE and SPIE. The average inverted V_P/V_S ratio computed using Wadati plots and the data recorded at ARME, VIGE and SPIE stations provides V_P/V_S ratio equal 1.89. Interestingly, since the anomalously high V_P/V_S is

110

measured at the station with the shortest traveltime, the measured V_P/V_S decreases when we include MOME station in the Wadati plot. It significantly changes the intercept time and also increases the error of the calculated linear fit used in the Wadati plot. Figure 5.5b shows Wadati type plot for all events used in the study.

Measured velocity ratios show another interesting feature – temporal evolution. Namely, V_P/V_S ratio correlates quite well with the injection pressure. Figure 5.6 shows the temporal evolution of measured V_P/V_S ratios along with the pressure of the wastewater injection measured at the head of the injection well at MOME and ARME stations that are closest to the injection well. V_P/V_S ratio seems to increase with the higher pressure of the wastewater injection. Station MOME is characterized by the greatest changes in the V_P/V_S ratio which is reflected in the highest value of standard deviation of V_P/V_S (greater average variations in relation to the mean value) and the greatest difference between the minimum and maximum
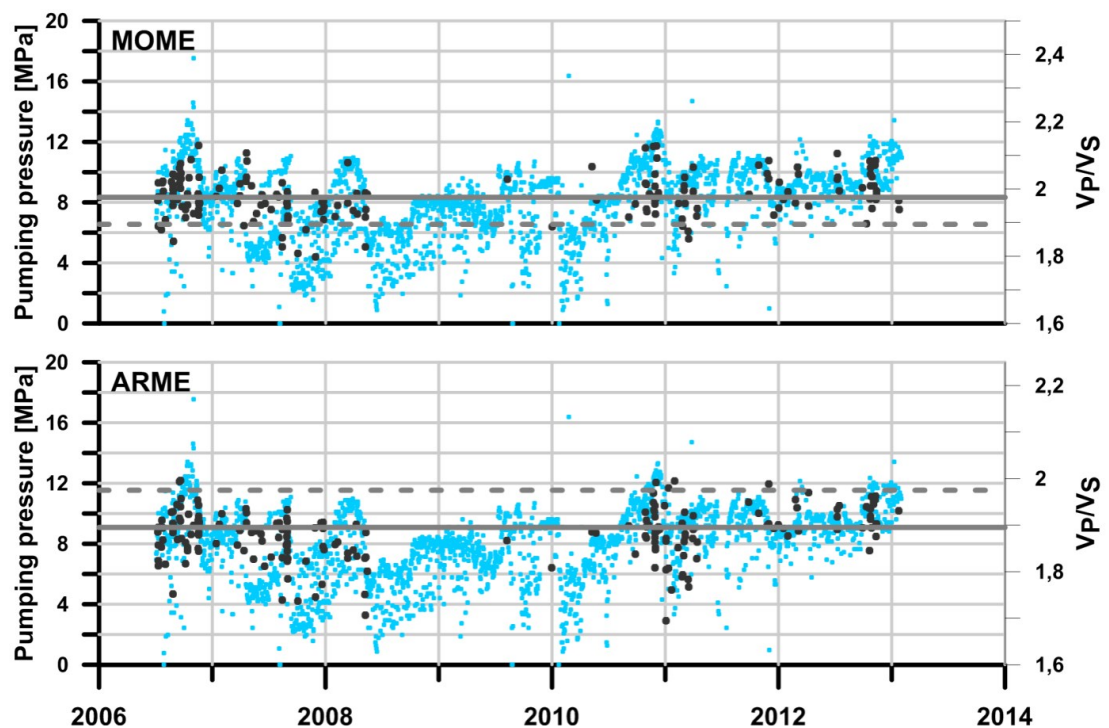
Figure 5.6. Temporal evolution of the measured V_P/V_S ratios (dark dots) and averaged daily pumping pressure (blue dots). Solid line shows the average of the V_P/V_S ratio for the indicated station, dashed line indicates the average of the V_P/V_S ratio for the station from the other plot.

values of V$_P$/V$_S$ (the difference of maximum and minimum for MOME is 0.33 while for ARME is 0.29). The variations of V$_P$/V$_S$ ratios are also observed at VIGE and SPIE stations, but the local effect of the injection seems to be less pronounced at these stations (differences between minimum and maximum values of V$_P$/V$_S$ are 0.19 and 0.20 respectively) as these stations are located further away from the injection well. Unfortunately, lower number of measurements and higher natural scatter of measured peak frequencies prevents us from performing similar analysis of temporal changes of attenuation.

5.5.2 Influence of the geology on attenuation and V$_P$/V$_S$ ratio

The mechanism related to medium saturation discussed at the beginning of the section 5.5.1 likely contributes to the decrease of the measured Q$_P$ and the increase of the V$_P$/V$_S$ ratio for MOME station. Nevertheless, we need to note, that the waves propagating from sources to stations spend only part of the total traveltime within the Apulian Platform – the layer where differences in saturation should be present. There might be other reasons that may contribute to Q and V$_P$/V$_S$ anomaly (e.g. 3D geological structure). Therefore, it is important to assess if, given the magnitude of the Q and V$_P$/V$_S$ anomaly found close to the station MOME, it is plausible to attribute the whole anomaly solely to variations in rock properties within the Apulian Platform due to the injection. Alternatively, additional explanation should be sought.

To do that we perform modelling of possible values of Q$_P$ within the Apulian Platform and in the overburden. We do that to check how large the differences of attenuation within Apulian Platform (assuming constant Q in the overburden) would be required to obtain estimated values of t*. We use MOME and ARME stations due to their relatively similar average epicentral distances, 2.3km and 3.7 km respectively. Similar distances to stations mean that: 1) the waves arriving at both stations spend similar portions of the whole traveltime to these stations within Apulian Platform; and 2) a possible VTI type of anisotropy does not play a significant role as the take-off angles towards both stations are similar. The portions of traveltimes towards MOME

112

and ARME stations within Apulian Platform account for ~25% (Improta et al., 2015) of the total traveltime. The modeling requires solving the simplest case of the set of equations (3.10) that was discussed in Chapter 3, section 5, with two layers only:

$$\frac{1}{Q_{P1}} t_1 + \frac{1}{Q_{P2}} t_2 = t_j^*, \qquad 1 \le j \le J. \qquad (5.1)$$

In our case Q_{P1} and t_1 is Q_P and P-wave traveltime in overburden and Q_{P2} and t_2 correspond to these parameters in Appulian Platform. J is total number of estimated t^* at given station (see Table 5.1). Traveltimes are given and the value of average Q_{P1} is set in each scenario. Value of the Q_{P2} inside the Apulian Platform is unknown. We solve the set of equations (5.1) separately for stations MOME and ARME, therefore we obtain two different values of Q_{P2} inside the Apulian Platform for these two stations that are placed in two different directions from the source zone. Table 5.3 shows the result of the modeling for subsequently lower Q_P in the overburden layers. The results illustrate what differences of Q inside of Apulian Platform are required to explain differences in average Q_P for stations MOME and ARME.

	Q_P				
Overburden (Q_{P1}) - fixed value	70	65	60	55	50
1D velocity model					
Q_{P2} calculated using data of station MOME	26	28	32	37	47
Q_{P2} calculated using data of station ARME	42	49	60	83	150
3D velocity model					
Q_{P2} calculated using data of station MOME	20	22	24	27	31
Q_{P2} calculated using data station of station ARME	33	37	41	52	74

Table 5.3. Results of the modeling of Q_{P2} – attenuation factor of Appulian Platform calculated at stations MOME and ARME for scenarios with several fixed values of attenuation factor Q_{P1} of the overburden.

We can see that to attribute the whole difference in measured effective Q_P between the stations to variations of medium property within Apullian Platform would imply either: (1) significantly lower Q_P for Apulian Platform when compared to the overburden, or (2) big differences in Q_P within the Apulian Platform. The first implication is not probable as Appulian Platform is high velocity layer, which is considered to be weakly attenuating (Zolezzi et al. 2007). Assuming low values of Q_P in the overburden, we obtain significant difference between Q_P within Apulian Platform in the direction of MOME and ARME. Technically such a strong difference in attenuation can be possible for rocks with different fluid saturation. For example, Tisato and Madonna (2012) showed that difference in Q_P between rocks saturated at 0% and rocks saturated at 90% may be significant, high enough to produce differences of Q_P within Apulian Platform shown in case of Q_P in the overburden set to 50. Nevertheless, we need to note that the waves propagating to both station in Apulian Platform are in relative proximity after they leave sources. Required strong contrast in saturation of the rocks in the area is not very likely as the injection is taking place for a long time. We have shown in Figure 5.6 that V_P/V_S at the station ARME reacts to the injection pressure with only slightly smaller amplitude of changes than at station MOME, which does not imply such significant difference in medium properties. Tisato and Madona (2012) show that even the difference between saturation of 60% and 90% would not be sufficient to explain the whole anomaly given the modeled theoretical values shown in the Table 5.3.

5.5.3 Explanation of the observed anomalies

Our findings show that the low effective Q_P measured at MOME station is most likely an effect of combination of two factors: (1) the differences in medium properties within the Apulian Platform caused by injection and (2) the spatial variation of medium properties in the overburden rocks around the station MOME – possibly due to more complicated geological setting. Improta et al. (2015) show that spatial variation of V_P/V_S ratio exists in High Agri Valley; they show that the high V_P/V_S ratio zone is present south-west from the CM2 well – direction which is not covered in this study. If this zone reaches closer to the station MOME than suggested by results

of Improta et al. (2017), it should be possible to fully explain the measured anomaly. The extension of this zone does not necessarily contradict the findings of Improta et al. (2017) because their 3D tomographic model was obtained by using another, temporarily installed seismic network, which did not include any station close to CM2 well that would be placed north of it. The direct cause of the anomaly may be different rock composition, stress regime (according to Improta et al. 2015, the waves propagating from the source zone towards the station MOME propagate along the minimum horizontal stress direction, thus decreasing the attenuation in this direction) or influence of different rock saturation. Increased saturation in overburden, which is clay rich, may also help to explain unusual, high Q_P/Q_S ratio measured for the MOME (Pham et al. 2002). Differences in overburden are supported as well by the fact, that as shown in Fig. 5.6, the anomaly manifesting through high values of V_P/V_S in the direction of MOME station was present since the beginning of the injection.

Chapter 6

Analysis of combined effects of source directivity and attenuation for induced event in North China

6.1 Rupture directivity – introduction

In chapter 4 and 5, we have shown results of application of the peak-frequency method to datasets, where selected arrivals had their peak frequencies controlled by attenuation only. Nevertheless, as we noted in Chapter 3, peak frequencies may, and often are, controlled by combined effects of source properties and attenuation. In Chapter 3, we noted that the peak frequencies of arrivals can be dependent on the size (magnitude of the event). Bigger earthquakes due to greater dimensions of the rupture area are characterized by lower corner frequencies f_c. Due to rupture propagating in particular direction, the perceived duration of the rupture duration and amplitudes of excited waves differ in different directions from the source. This phenomenon is called rupture directivity. Effect of rupture directivity on ground shaking was first identified for strong earthquakes that often cause significant damage, e.g., 1992 M_W 7.3 Landers (Ammon et al., 1993), 1995 M_W 6.9 Kobe (Furumura and Koketsu, 1998), 2009 MW5.9 L'Aquila (Calderoni et al., 2015), or 2015 M_W 7.8 Gorkha (Koketsu et al., 2016). Relatively rare earthquakes with high, supershear rupture velocity can be particularly dangerous (Bao et al. 2022). Rupture directivity affects the amplification of ground motion and, therefore, the damage distribution caused by large earthquakes. Therefore, modeling and determination of active fault orientation and expected rupture directions play a significant role in seismic hazard evaluation. In earthquake source analysis, directivity can be used for the determination of the fault plane from the two inverted nodal planes of source mechanism (both explaining the observed data equally well). Correct determination of the fault plane is important in studies of microseismicity and for further interpretation of microseismicity induced by hydraulic fracturing with geomechanical models (Staněk and Eisner, 2017; Eisner and Staněk, 2018).

Considering earthquakes as a self-similar phenomenon, directivity is expected for events of all magnitudes. While there is a growing body of observational evidence

demonstrating this effect for small events 2<M_W<5, (e.g., Pacor et al., 2016; Yoshida, 2019; Ameri et al., 2020; Chen et al., 2021; Colavitti et al., 2022; Seo et al., 2022), recorded waveforms for microseismic events (M_W<2) usually do not exhibit directivity effects. Microseismic sources are often described by simple radially symmetric crack models with point source radiation patterns while details of the source process, including effects of rupture direction, are obscured by propagation effects. Only few studies have indicated directivity for microseismic events, see, e.g., Lengliné and Got (2011), Kane et al. (2013), Folesky et al. (2016) for 1<M_W<3 events, or in acoustic emissions in laboratory experiments e.g. Kolář et al. (2020). In the previous studies concerning the directivity of small earthquakes, attenuation effects were either not considered (e.g., Ross et al., 2020) or eliminated by using source-stations pairs with similar distances (Lengliné and Got, 2011).

In this chapter, we reveal rupture directivity of microseismic event by using peak frequencies of direct P-waves and careful consideration of attenuation. Our analysis exploits high signal-to-noise ratio (SNR) data from a dense star-like surface array of geophones due to a microseismic event (Mw~1; Li et al., 2021) induced during hydraulic fracturing of shale in North China.

6.2 Dataset

The field dataset used in this chapter was acquired during the hydraulic fracturing of shale reservoir in China. Exact location and information about geological setting in the region are not available to us due to data confidentiality constraints. The geometry of the microseismic monitoring array covering approximately 36 km^2 is shown in Figure 6.1. A star-like surface array with 12 arms and a total of 1771 geophones was installed to gather passive seismic data (vertical component of particle velocity, 1 kHz sampling). The surface topography of the area varies between 300 m and 850 m above mean sea level (MSL). The vertical treatment well with wellhead in the center of the array reaches target reservoir at 3300–3700 m below MSL.
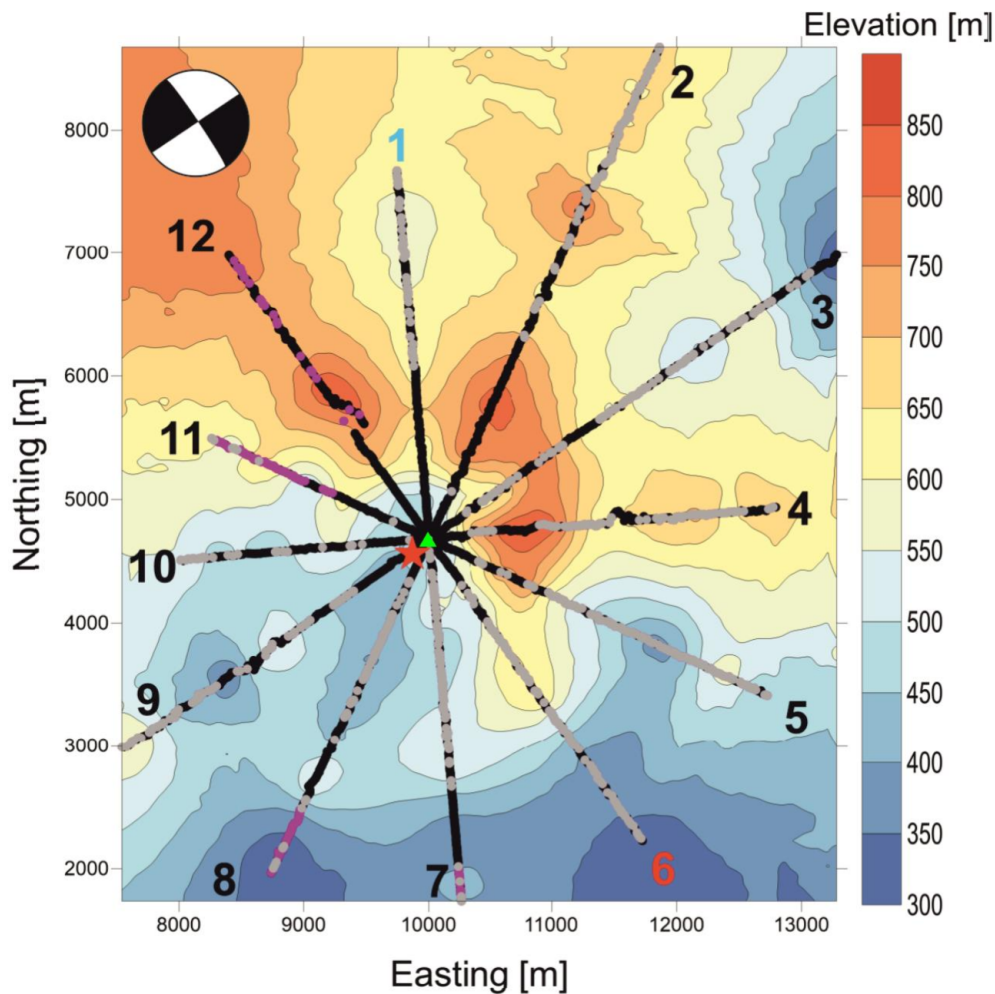
Figure 6.1. Star-like surface monitoring array with 12 arms. The green triangle indicates the location of the well. Dots (many of them overlapped) show the positions of 1771 receivers: receivers with clear single P-wave arrival are in gray, and receivers with picked P-wave amplitudes only are in magenta. Elevation map in the background is the interpolated elevation (above mean sea level) measured at the positions of receivers

We analyze one of the three induced microseismic events detected during the stimulation. The selected M_W~1 has the highest signal-to-noise ratio from detected events and is located approximately below the center of the array at the depth of 3300 m below MSL (Li et al. 2021), see the epicenter represented by the red star in Figure 6.1. The 1D P-wave velocity model was created from sonic log measurements (Wu et al., 2017), in our calculations we use smoothed version of that model, shown in Figure 6.2.
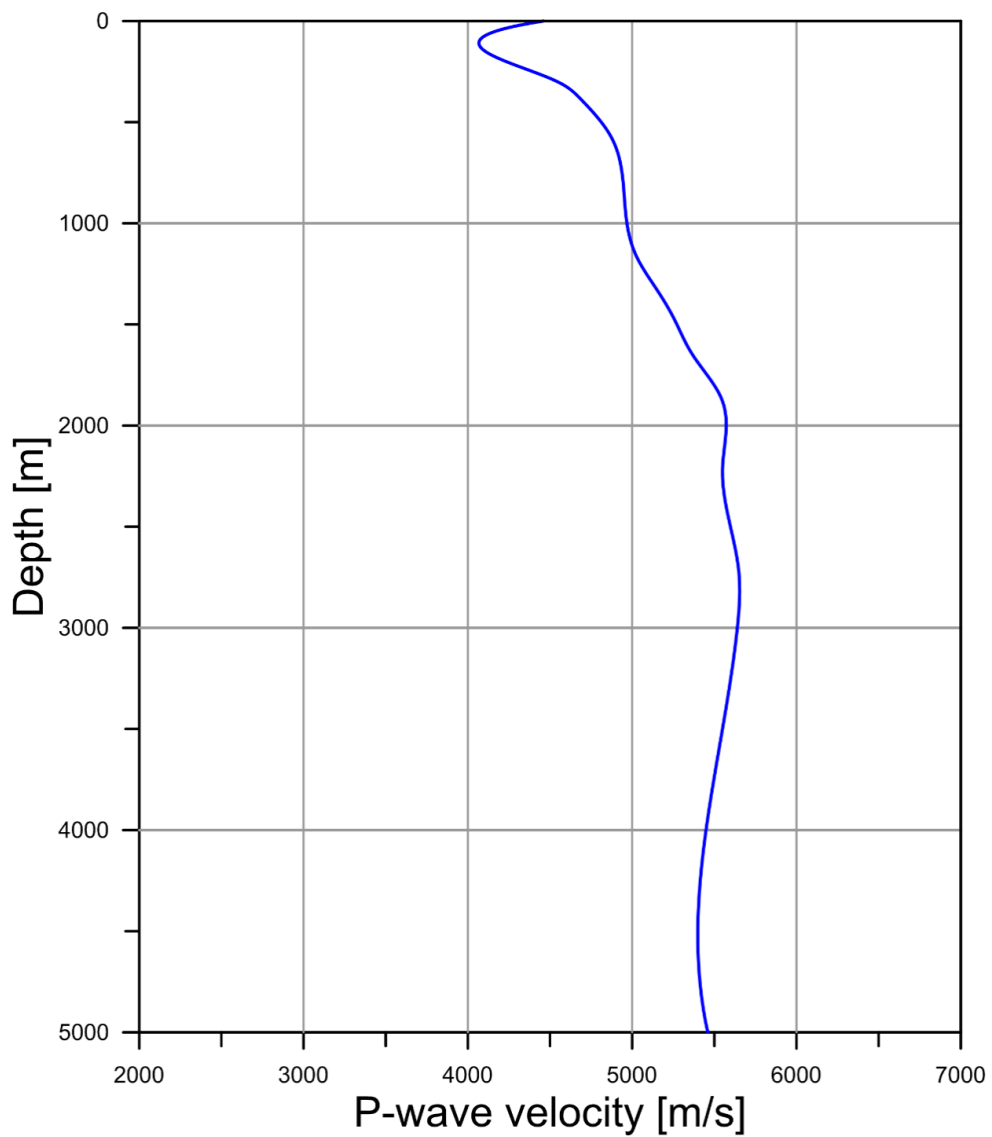
Figure 6.2. Smoothed velocity model used in the study.

Although the directivity effect is usually clearly manifested in S-waves, we only use P-waves because S-waves were not clearly recorded by the array of vertical geophones. Many geophones recorded clear, single direct P-wave arrival allowing measurement of the half-period on individual traces and source mechanism inversion from arrival amplitudes. Examples of traces with different quality of the arrivals are shown in Figure 6.3.
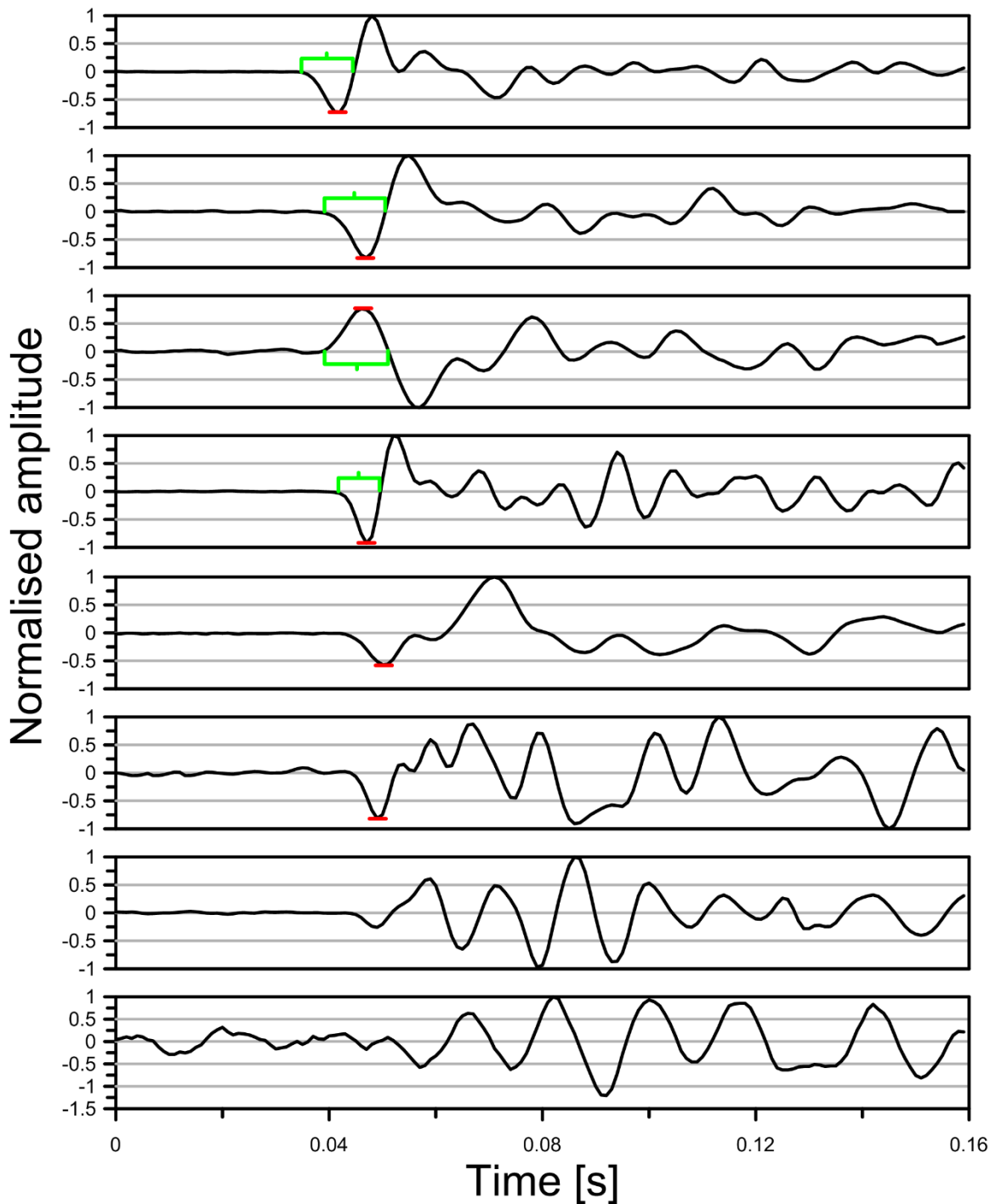
Figure 6.3. Examples of recorded P-wave arrivals. The top four traces show clear, single direct arrivals that allow determination of peak frequency (half-periods highlighted by the green brackets). Four bottom traces show noisier signals with more complex P-wave arrivals, two of them allowing reliable amplitudes picks. Picked amplitudes used for the source mechanism inversion are marked by the red dashes.

6.3 Source mechanism inversion

In this chapter, we use manually picked P-wave amplitudes for a full moment tensor representing a general source mechanism, following Staněk et al. (2014, 2017). The inversion procedure minimizes the L2 misfit between observed and synthetic P-wave amplitudes. We assume source and source time function to be a point source and a delta function, respectively (Aki and Richards, 2002). The Green's function derivatives are computed using ray theory (Červený, 2001; Moser and Červený, 2007) in the smoothed 1D isotropic velocity model. The resulting full-moment tensor is decomposed into shear double-couple (DC) component, and non-shear isotropic (ISO) and compensated linear vector dipole (CLVD) components (Hudson et al., 1989).

As shown by Staněk et al. (2014, 2017), star-like arrays like the one we work with in this chapter provide an ideal focal sphere coverage in a wide range of offsets and azimuths, allowing stable full moment tensor inversion for events located below the center of the array at a depth comparable to aperture of the array. The inversion result is sensitive mainly to the noise level in the data, which is in our case significantly lower than the noise levels tested by Staněk et al. (2014).

6.4 Rupture directivity and peak frequencies

The directivity of the seismic source due to the rupture propagation is similar to the Doppler effect. Observers in different positions do not perceive the actual rupture duration T_{RU}, with corresponding corner frequency $f_C \sim 1/T_{RU}$ (Aki & Richards, 2002). Instead, apparent rupture duration T_{ARU} varying with the angle between the ray take-off and rupture direction is perceived. As the rupture propagates along a fault at certain speed, the pulse in the rupture direction is the narrowest, i.e., T_{ARU} is the shortest, and its amplitude is the highest. Conversely, the greatest T_{ARU} and the lowest amplitude are in the opposite direction. Integral over the displacement source time function, proportional to seismic moment M_0, is independent of azimuth (Lay and Wallace, 1995). Simplified directivity effect of a source with unilateral rupture propagation on the apparent duration can be described by the Haskell model (Haskell, 1964):

$$T_{ARU}(\alpha) = T_{RU}(1 - b\cos\alpha). \tag{6.1}$$

Angle α is measured between the rupture direction and ray take-off direction that results in reaching the observation point; b is a ratio between the rupture velocity (V_{RU}) and P- or S-wave velocity (V_P or V_S) at the source. Directivity effects are stronger for S-waves because, in most cases, $V_{RU}<V_S<V_P$. In the spectral domain, displacement spectrum Ω_D in the source model with a single corner frequency described by eq. (3.2) is in the presence of directivity substituted by the version with corner frequency dependent on the angle α:

$$\Omega_D(f) = M_0 \qquad\qquad f < f_{AC}(\alpha),$$

$$\tag{6.2}$$

$$\Omega_D(f) = \frac{M_0}{\left(\frac{f^2}{f^2_{AC}(\alpha)}\right)} \qquad\qquad f \geq f_{AC}(\alpha).$$

Here $f_{AC}(\alpha)$ is the apparent corner frequency equal to $1/T_{ARU}(\alpha)$. The source velocity spectrum $\Omega_V(f) = 2\pi f \Omega_D(f)$ peaks at the corner frequency $f_{AC}(\alpha)$, and thus, the peak frequency at the source varies with α. Simple example of directivity effect is shown in Figure 6.4. It shows P-wave radiation pattern of a point source compared with radiation pattern of P-wave for a source with directivity effects included. The exact influence of the directivity is shown using a ratio between rupture time and apparent rupture time T_{RU}/T_{ARU} computed using eq. (6.1) in each direction.
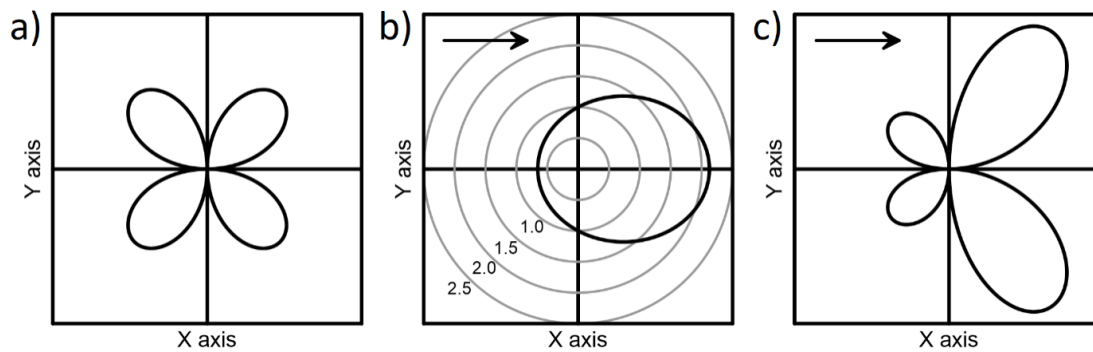
Figure 6.4. a) standard P-wave radiation pattern of a shear source – a cross section along the fault plane (situated in the horizontal, X-Y plane) with the horizontal rake direction (0 deg); b) relative directivity coefficient calculated for medium with V_P/V_S equal 1.7 and rupture velocity equal $V_{RU}=0.9V_S$ and rupture direction indicated by black arrow; c) deformed P-wave radiation pattern caused by seismic directivity.

As discussed in Chapter 3, in homogeneous medium, the effect of attenuation on spectral amplitudes causes exponential decrease $e^{-\pi f t^*}$. The exponential term reduces higher frequencies faster and thus distorts the directional variations caused by the rupture directivity. The expression for peak frequency for source model affected by rupture directivity similar to eq. (3.8):

$$f_{peak} = \min\left(f_{AC}(\alpha), \frac{1}{\pi t^*}\right).$$ (6.3)

It means that f_{peak} changes from $f_{AC}(\alpha)$ to $\frac{1}{\pi t^*}$ as the wave propagates to larger distances, once the total attenuation described by t^* exceeds $\frac{1}{\pi f_{AC}(\alpha)}$. In practice it means that values of peak frequencies that initially are different for waves propagating in different directions gradually converge with increasing distance. The behavior of peak frequencies in different directions for earthquakes with sources displaying rupture directivity is similar to behavior of peak frequencies for sources with different magnitudes.

Similarly to displacement spectrum described by (6.2), Brune source-displacement model, which is characterized by smoother shape around f_C and was discussed in Chapter 3 as well, is described by following expression:

$$\Omega_D(f) = \frac{M_0}{\left(1+\left(\frac{f}{f_{AC}(\alpha)}\right)^{2\gamma}\right)^{1/\gamma}}.$$ (6.4)

The behavior of peak frequencies for Brune model was described in Chapter 3, section 4. The effect of directivity on peak frequencies in this model is, again, similar to effects of different values of corner frequency due to different magnitudes.

The peak frequencies estimated from the first arrivals are only weakly affected by source radiation and/or complicated ray path effects, contrarily to maximum arrival amplitudes. Therefore, analysis of frequency content is more suitable than analysis of amplitudes when studying directivity effects.

6.5 Results

6.5.1 Inverted source mechanism

For the source mechanism inversion, we manually picked 717 amplitudes of the P-wave arrivals. The picks were done for 629 geophones selected also for the f_{peak}

measurement (Fig. 6.1, gray dots) and for additional 88 geophones (Fig. 6.1, magenta dots) used to increase source mechanism inversion stability. All the selected geophones provided sufficiently high SNR to pick reliable amplitude. The analyzed event is a strike-slip (presented as a beach ball in Fig. 6.1) with two nearly vertical nodal planes oriented in the NW-SE direction (strike: 326 deg, dip: 85 deg, rake: -180 deg) and in the NE-SW direction (strike: 236 deg, dip: 90 deg, rake: -5 deg), and with the double couple (DC) component of 66%. Both planes explain the observed amplitudes equally well, and we must seek an additional independent information (here, the directivity observation, which we present in the discussion section) to determine the fault plane and rupture direction. The square of the L2-misfit normalized by the root-mean-square of data is 0.39, corresponding to variance reduction of 85%. The resulting source mechanism is very similar to that of Li et al. (2021), who used the same dataset but different method.

We point out that we cannot determine seismic moment and moment magnitude of the microseismic event because the data owner has not provided us with precise geophone sensitivities needed to correct the amplitude values for the instrument response. Therefore, we adopt the magnitude 1.2 published by Li et al. (2021).

6.5.2 Measured peak frequencies

In total, 629 receivers from 11 arms (gray dots in Fig. 6.1) provide clear single, P-wave arrivals with high SNR allowing reliable f_{peak} measurements. Values of measured peak frequencies are shown in Figure 6.5. The f_{peak} values are higher in the southern than in the northern area from the source epicenter. Note that the receivers in the southern part of the array are located in a generally lower elevation than the receivers in the northern part (Fig. 6.1) and thus they have slightly shorter traveltimes for similar offsets.
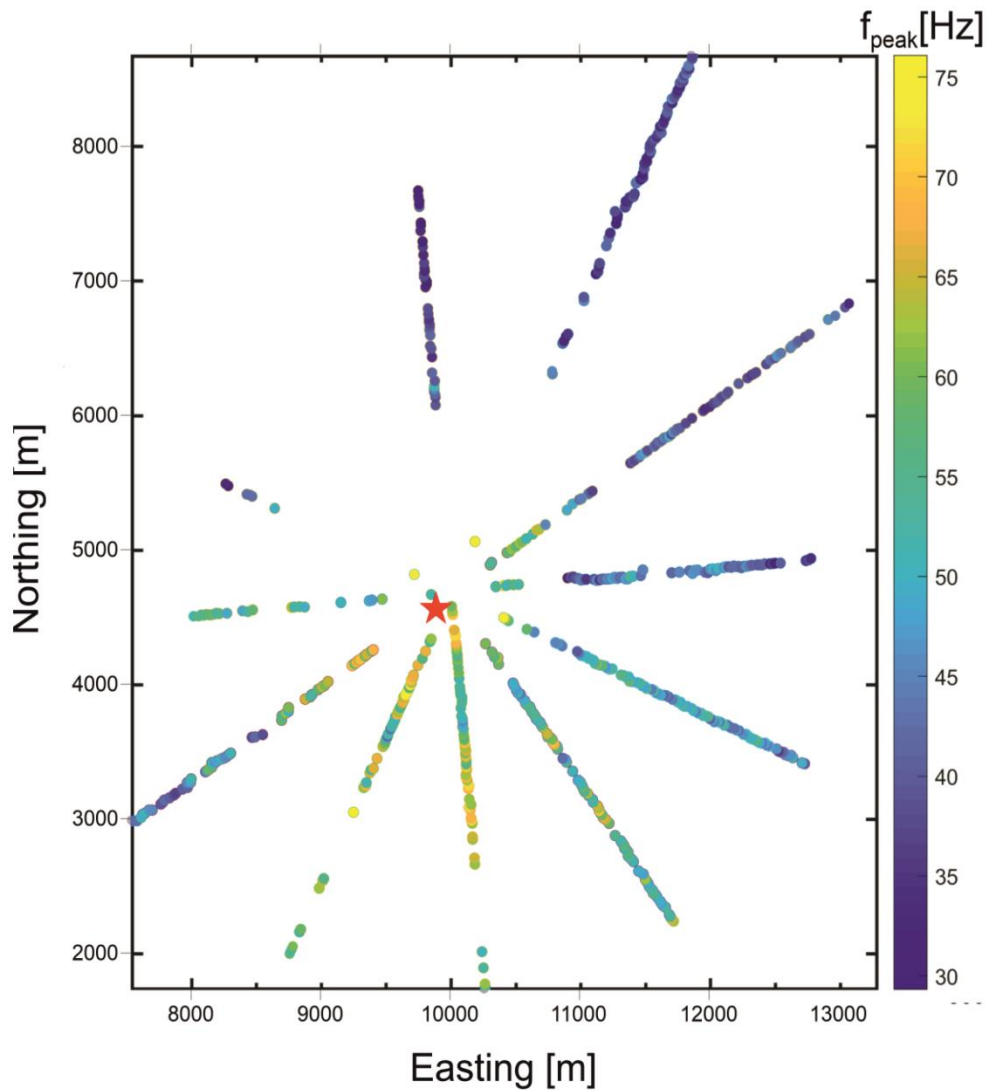
Figure 6.5. Peak frequencies measured at receivers with P-waves suitable for the peak frequency measurement.

6.5.3 Effects of attenuation on the observed peak frequencies

Figure 6.6a shows measured peak frequencies as a function of traveltime. For reference, curves indicating theoretical pattern of f_{peak} following $\frac{1}{\pi t^*}$ decrease with increasing traveltime are included. The curves are computed for effective P-wave quality factor $Q_P = 150$ (solid line), and its 10% standard deviations $Q_P = 165$ and $Q_P = 135$ (dashed lines). For a medium with constant effective Q, the traveltime can be used as a proxy to accumulated t^*. While the general trend of the measured peak frequencies is decreasing with the increasing traveltime (increasing t^*), significant variability in measured values, particularly for traveltimes up to 1s, indicates that changes in elevation are not the main cause of the distribution of peak frequencies

125

shown in Figure 6.5. If the peak frequencies were controlled by attenuation only, they could be used to evaluate effective Q_P by using equation (3.7) as shown in Figure 6.6b. The spatial variability of the f_{peak} values may indicate complicated geological setting/anisotropy in the area of interest. The attenuation strength is usually inversely proportional to seismic velocity (Zhang and Stewards, 2008). Therefore, in the presence of variable Q_P, we would expect evident variations of seismic velocities (Pham et al. 2002; Wcisło et al., 2018). However, the analysis of traveltimes (Fig. 6.7) indicates that differences in average velocities in the N-NW and S-SE directions are negligible. The lack of the azimuthal P-wave velocity variations also suggests insignificant anisotropy of the medium. Moreover, in a complicated medium, one might expect waveform complexity, which contradicts the high number of clear single P-wave arrivals found in our dataset. This suggests that the measured peak frequencies are unlikely to be controlled solely by attenuation or varying medium properties.
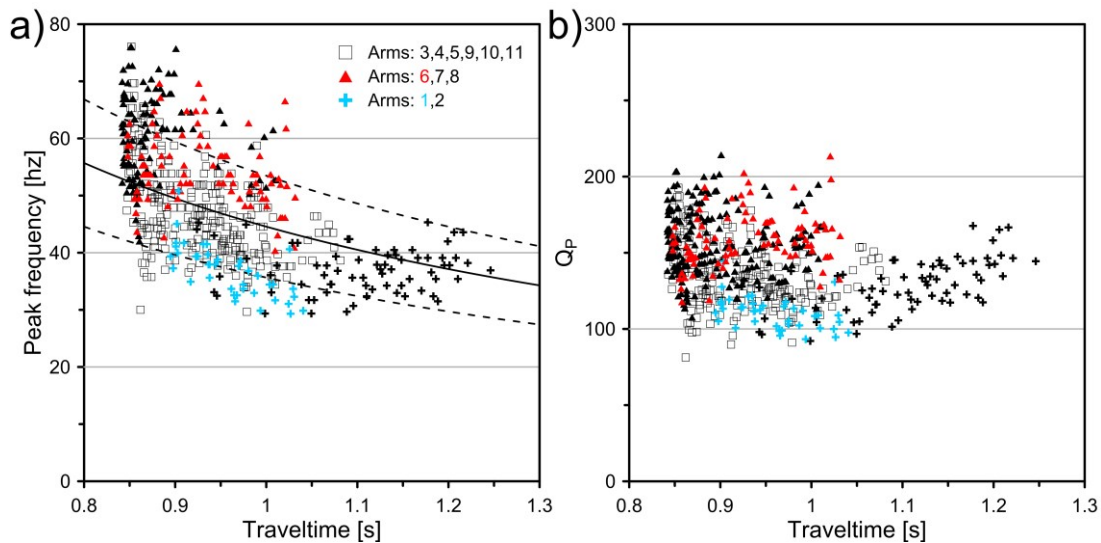
Figure 6.6. a) Measured peak frequencies f_{peak} as a function of traveltime. Symbols indicate results for receivers belonging to arms 1–2 (crosses), arms 6–8 (triangles), and arms 3–5 and 9–11 (squares). The blue indicates arm 1, and the red indicates arm 6. The curves indicate the theoretical decrease of f_{peak} when controlled by attenuation only (equation 3.6). The solid curve indicates Q = 150, and the upper and lower dashed curves indicate Q = 165 and Q = 135, respectively; b) Effective Q_P factors calculated from f_{peak} using equation (3.7), that is, neglecting the possible influence of source effects.
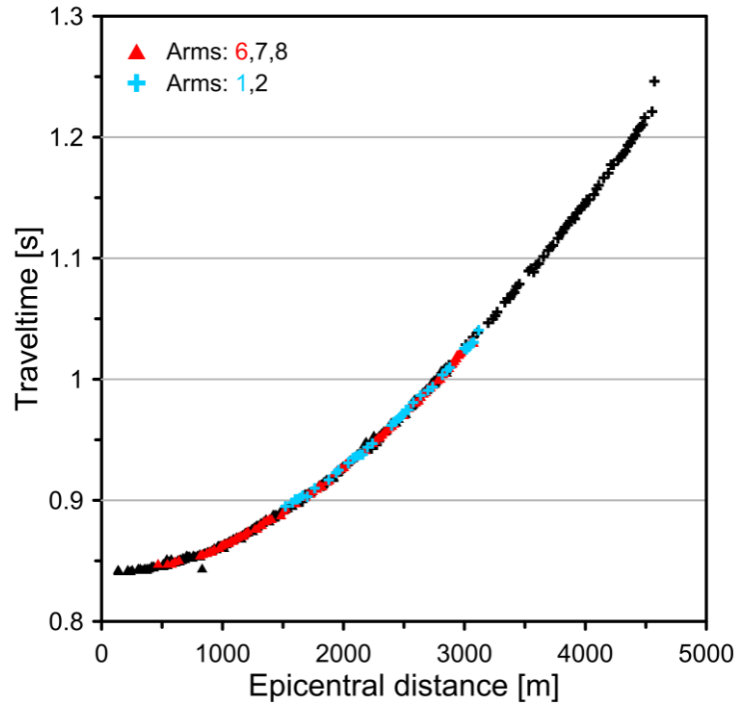
Figure 6.7. Distance dependence of the travel times for receivers of arms 1–2 and 6–8.

6.5.4 Effects of rupture directivity on the observed peak frequencies

Our interpretation of the measured peak frequencies is that we deal with a combination of rupture directivity and attenuation. First indication that rupture directivity influences the results is the observation of directionally dependent f_{peak} (Fig. 6.5), showing that the lowest peak frequencies are observed in the north and the largest in the south of the array. This agrees with the rupture plane having strike 326 deg with rupture direction tilted towards the south.

To examine how the rupture directivity combined with attenuation affects the peak frequencies, we consider several possible scenarios. We calculate synthetic spectra at the stations considering the Brune source spectrum (as we suspect that peak frequencies are close to corner frequency of the event) and grid-search for four free parameters: rupture direction (confined to the two above-described fault planes of the focal mechanism), T_{RU}, Q_P, and rupture velocity V_{RU}. In one scenario, we also allow the event to be supershear. Velocity ratio V_P/V_S is fixed at 1.7 as we do not have S-waves arrivals available that would allow velocity ratio analysis. Difference between synthetic peak frequencies and the measured peak frequencies is described by L2-misfit function defined as:

127

$$\text{misfit} = \frac{1}{n}\sum_{i=1}^{n}[\ln(f_{\text{peak modeled}_i}) - \ln(f_{\text{peak measured}_i})]^2 , \qquad (6.5)$$

where n is the number of the f_{peak} measurements (n=629). The misfit corresponds to the posterior variance of the logarithmic residuals. We note that in the case of Gaussian relative data errors and perfect modeling, misfit would correspond to the squared mean of data standard deviations.

Table 6.1 summarizes results of the modeling for the Brune model with $\gamma = 1$ (results for $\gamma = 2$ are very similar) for four scenarios of increasing complexity to show influence of particular factors in the data interpretation:

- Case 1: The peak frequency is affected neither by attenuation nor by the source directivity (best fit assumes directionally independent peak frequencies).

- Case 2: The attenuation is added to the modeling.

- Case 3: The effects of directivity (eq. 6.1) calculated for the common V_{RU}/V_S value of 0.9 are added.

- Case 4: A global grid-search with variable V_{RU}/V_S and possible supershear rupture propagation is performed.

For each case, Table 6.1 lists the value of the minimum L2-misfit, and minimum and maximum value of synthetic peak frequency (and its logarithm). The range of measured values is equal to 29 Hz (3.37) – 76 Hz (4.33). Due to the natural presence of the noise in the data, the true noise free range of the peak frequencies for the selected receivers is difficult to assess. We perform a simple estimation through cutting off 5% of the extreme values providing the range from 33 Hz (3.51) – 67 Hz (4.20). Note that this rough estimate does not consider a possible bias due to the uneven spatial receiver coverage (number of the receivers placed closer to the epicenter is higher than those placed further away as shown in Fig. 6.6a and thus more affected by attenuation).

Modeling scenario		V_{RU}/V_S	T_{RU} (s)	Q	Misfit	Misfit improvement	min / max modeled f_{peak} in Hz (logarithm)
No attenuation	No directivity	0 (fixed)	1/48	Not considered	0.0451	1.00	48 (3.87) / 48 (3.87)
Attenuation		0 (fixed)	1/200 (fixed)	140	0.0270	1.57	37 (3.61) / 52 (3.95)
	Directivity	0.9 (fixed)	1/34	495	0.0215	2.10	35 (3.56) / 54(3.99)
		1.25	1/33	235	0.0187	2.41	31 (3.43) / 57 (4.06)

Table 6.1. Summary of basic results of the modeling. Misfit improvement is computed in relation to the case where no attenuation and no directivity is considered. The min/max values of measured peak frequencies (logarithms) are equal 29 Hz (3.37) / 76 Hz (4,33), the range with a cut off of the 5% of the highest/lowest values is equal to 33 Hz (3.51) / 67 Hz (4.20).

Table 6.1 shows that just by introducing attenuation (Case 2) we significantly improve the fit in comparison to the fit for the constant f_{peak} model (Case 1) but the range of modeled peak frequencies is limited. Adding source directivity to the modeling (Case 3) decreases the misfit even more. Nevertheless, only if we allow the event to be supershear (Case 4), we get a broad range of modelled peak frequencies while still improving the misfit (2.4 times smaller than for the Case 1). The obtained variance for the best model corresponds to standard deviation of the peak frequency measurement equal to 14%. Such value agrees with the result of synthetic experiments with real noise published by Wcisło and Eisner (2019). The modeling indicates that the fault plane of the event is in the NW-SE direction (strike: 326 deg, dip: 85 deg, rake: -180 deg), and the rupture direction is tilted upwards from the inverted rake direction (see the Discussion section).

Figure 6.8 shows a map of natural logarithms of observed peak frequencies (Fig. 6.8a) and their synthetic equivalents for cases 2-4 (Fig. 6.8b-d). The Figure 6.8 indicates how consecutively increased complexity of the modeling improves the

129

modeling results. The best result is obtained for V_{RU}/V_S=1.25 and corner frequency of 33 Hz. The corresponding rupture duration T_R=1/33s is plausible for a M_w 1.2 event (Kwiatek et al., 2011). The optimal quality factor Q=235 is reasonable for compacted shale (Delle Piane et al., 2014). In the Figure 6.9 are measured and modeled peak frequencies as a function of the rupture direction (measured from the vertical in the fault plane) for the subshear (Case 3) and supershear (Case 4) cases. The latter case fits the data better as demonstrated by the lower scatter around the synthetic values, but more importantly better fit for both highest and lowest measured peak frequencies. Nevertheless, we will further deliberate about the modeling uncertainty in the section 6.6 that includes discussion.
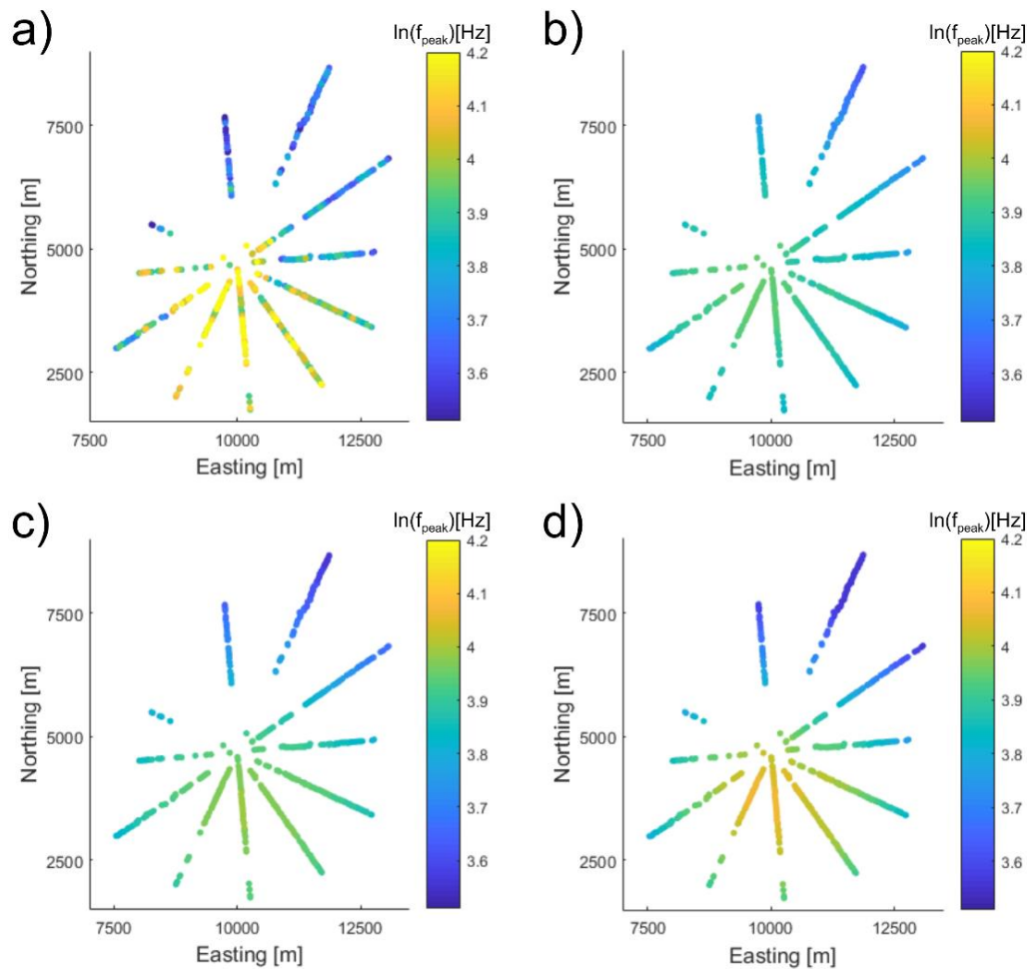
Figure 6.8. a) Logarithms of observed peak frequencies. The color scale corresponds to the range with a cutoff of the 5% of the highest/lowest values (3.51)/(4.20); (b–d) Logarithms of the peak frequencies for the best-fit models of three different scenarios, considering: b) only attenuation, c) attenuation and directivity for V_{RU}/V_S = 0.9, and d) attenuation and directivity with supershear rupture propagation.
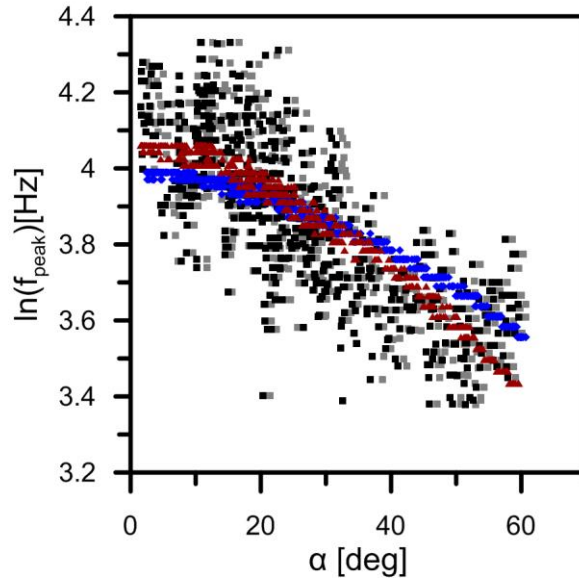
Figure 6.9. Measured (squares) and modeled (dots) peak frequencies as a function of angle α between the rupture direction and the ray take-off angle for model with $V_{RU}/V_S = 0.9$ (gray squares and blue dots) and best-fitting model with supershear rupture propagation $V_{RU}/V_S = 1.25$ (black squares and red dots).

6.6 Discussion

6.6.1 Uncertainty of the modeling

Table 6.1 shows results only for the best-fitting models in each Case. To examine the uncertainty, we compute misfit for the most general Case 4, while fixing selected parameters and optimizing the remaining ones. Figure 6.10a shows how the misfit changes with rupture direction for rupture-to-S-wave velocity ratios V_{RU}/V_S set to 0.95, 1.05, 1.15, and 1.25. The minimum misfit is around 10 deg from the vertical within the fault plane for V_{RU}/V_S, equal to 1.15 and 1.25. Assuming a misfit threshold of 10% of the global minimum (horizontal line in Fig. 6.10a), plausible rupture directions lie between 5 deg and 30 deg from the vertical. Note that such a misfit threshold also permits subshear value of V_{RU}/V_S =0.95. Figure 6.10b then shows the dependence of the misfit on the quality factor for the same fixed V_{RU}/V_S ratios. In all cases, the misfit increases abruptly for low values of Q (Q<150). For V_{RU}/V_S =1.25, the misfit attains its minimum for Q=235 (see also Table 1). Nevertheless, the misfit minimum is relatively flat for Q>200. For slower rupture velocities, the misfit is generally worse. The respective misfit curves are also flat for Q>200, having its

(formal) minimum at very large values of Q. Overall, the behavior of the misfit suggests that Q is greater than 150 and that the observed pattern of peak frequencies is primarily driven by the directivity only weakly concealed by attenuation, which in turn moderately reduced observed peak frequencies. The event
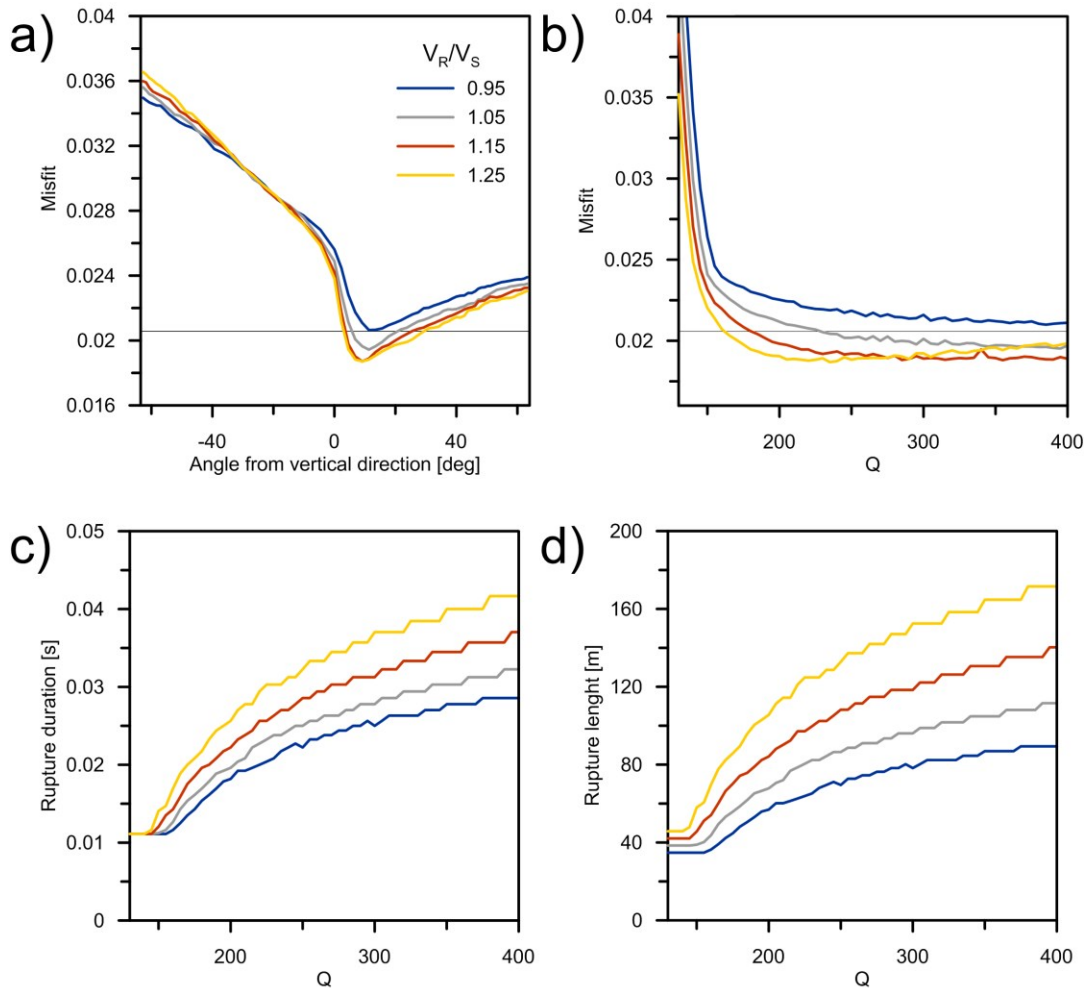
Figure 6.10. a) Misfit calculated for the best model assuming different rupture direction and V_{RU} within the plane with strike: 326 deg, dip: 85 deg, and rake: −180 deg. Note, that the minimal rupture time is limited to 0.005 s. The horizontal line indicates misfit threshold that is 10% larger than the global minimum. b) Misfit calculated for the best model as a function of Q and V_{RU}. c) Dependence of rupture duration on Q and V_{RU}. (d) Rupture length calculated from rupture durations a velocities in panel c). Note that the unmentioned modeling parameters are optimized in each case.

occurred in a sedimentary basin, which can be generally characterized as highly attenuative with Q values smaller than 200-300 (e.g., Delle Piane et al., 2014; Mikhaltsevitch et al. 2020; Takam Takougang and Calvaret, 2012; Wcisło et al. 2018). That indicates that the real Q should be in the lower range of our estimate, which supports the event rupture to be supershear. The subshear models which fit the data within the 10% treshhold imply high Q value which is less likely, although not entirely ruled out.

The low sensitivity of the misfit, particularly to the Q values, has implications for the rupture duration and the rupture length estimates. Figure 6.10c shows that the rupture durations for fixed V_{RU}/V_S increase with increasing Q. Combining the 10% data misfit threshold and the limit on Q being smaller than 300, the plausible rupture duration ranges between 1/30 s to 1/55 s. Figure 6.10d shows rupture length estimates calculated simply by multiplying the rupture duration by the respective rupture velocity. Assuming the same constraints as above, the plausible rupture lengths are between 70 m and 150 m. Nevertheless, we point out that the rupture length estimates in particular are based on the simplified assumption of the Haskell model with constant velocity, neglecting possible complexities of the true rupture propagation.

In summary, while only large strike-slip earthquakes have well-documented cases with supershear rupture propagation (e.g., Hu et al., 2019; Wang et al., 2012, 2016), the occurrence of a supershear microseismic event cannot be disregarded. We have shown that our data prefer supershear rupture with a pronounced directivity effect, although strictly speaking, fast yet subshear rupture cannot be ruled out. We point out that possibly more advanced modeling of the rupture directivity than using the kinematic Haskell model might shed light on the properties of this microseismic event. In particular, dynamic rupture simulations (Kaneko and Shearer, 2015) might provide additional arguments regarding the rupture velocity, direction, and size. For example, a supershear rupture would have to be inclined because the rupture velocity is limited to the S-wave speed for a vertical propagation of horizontal slip (anti-plane, mode III crack, Madariaga and Olsen, 2000).

6.6.2 Effects of rupture directivity on observed amplitudes

For revealing the effect of rupture directivity, we used peak frequencies and intentionally ignored P-wave arrival amplitudes and polarity changes due to radiation pattern. On the other hand, these changes were the main input in the source mechanism inversion. The resulting strike-slip source mechanism was inferred from manually picked P-wave arrival amplitudes without considering the directivity effect. Therefore, another analysis of directivity effects on amplitudes can be done by investigating the ratios between observed and synthetic amplitudes varying with angle α. In this analysis, we exclude amplitudes recorded from the arm 1 as the observed and synthetic amplitudes for this arm are very small due to the proximity to the nodal plane (small absolute differences translate into large variations of the computed ratios).

The calculated ratios are scattered but exhibit a trend, as summarized by histograms shown in Figure 6.11. The histograms are divided into three groups: with angle α (measured from the rupture direction determined above) below 20 deg (top panel), α between 20 deg and 40 deg (middle panel), and α above 40 deg (bottom panel). The distribution top panel has the most populated central interval. The ratios > 1.25 characterize more receivers than the ratios < 0.75. The middle panel distribution is similar, but the interval for ratios > 1.25 is less populated than for ratios < 0.75. The bottom panel, including receivers with α > 75 deg, has the most populated interval with ratios < 0.75. The number of receivers in the interval for higher ratios decreases. The median ratio values for selected α intervals decrease with decreasing α from 1.08 to 0.70. This is a similar result as for the peak frequencies - amplitudes for high α are smaller than the amplitudes predicted by a point source radiation. We generally see that the observed-to-synthetic amplitude ratios follow a decreasing trend with increasing α, proving that the rupture directivity affects the P-wave amplitudes in the studied dataset.

The rupture directivity effect on the observed microseismic data is exploitable for determining the event's fault plane orientation and rupture direction. Furthermore, we can use the ratios between the observed amplitudes affected by the directivity and modeled amplitudes to improve the source mechanism inversion
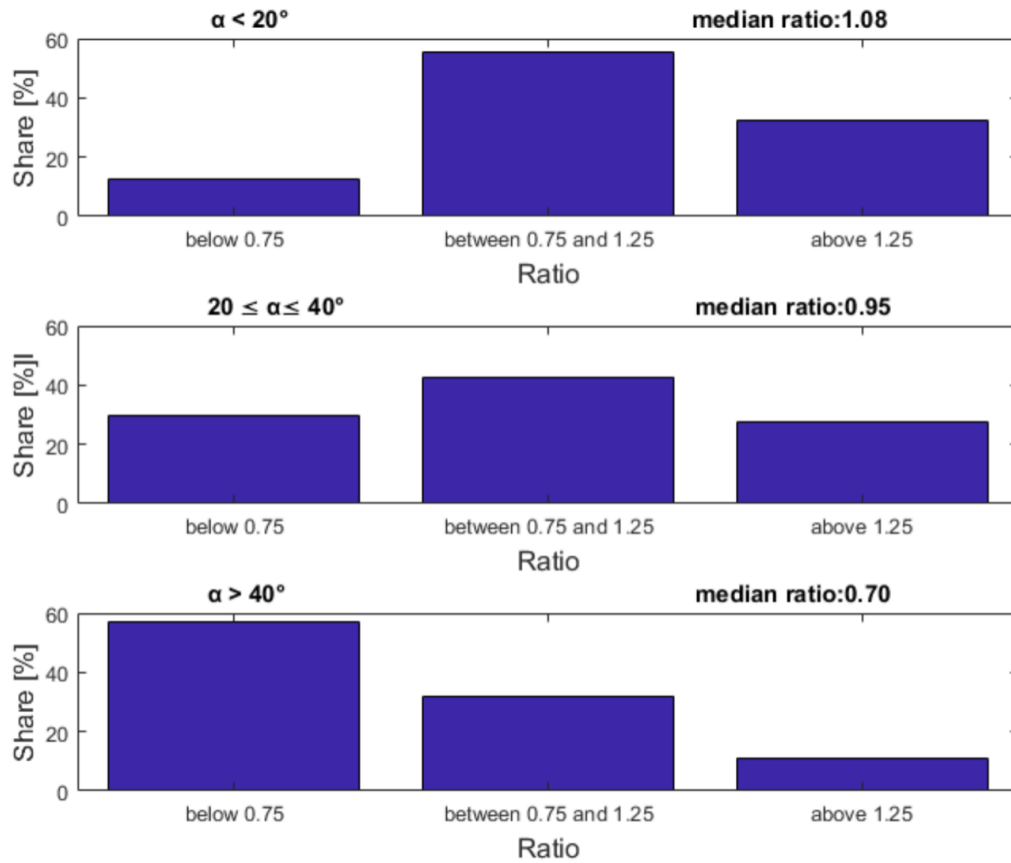
Figure 6.11. Distributions of the observed-to-synthetic amplitude ratios for the inverted source mechanism: a) Receivers with α less than 20 deg; b) Receivers with α between 20 deg and 40 deg; c) Receivers with α above 40 deg.

results. We propose a simple correction of amplitudes based on linear regression fit of the observed-to-modeled amplitude ratios as a function of α. In calculating a linear fit, we excluded 2.5% of the geophones that provided the highest and lowest ratios, as outliers may bias the fit based on the L2 norm. The regression coefficients are used to make a first-order correction to the observed amplitudes used as an input to the source mechanism inversion done with the code using a point source. The amplitude correction factors vary from ~1.15 (for receivers with α close to ~0 deg) to ~0.70 (for receivers with α close to ~60 deg).

Fault plane orientation inverted from the corrected amplitudes (strike: 324 deg, dip: 87 deg, rake: -179 deg) is very similar to the initial result, but the inverted DC component of 71% is slightly higher than the initial 66%. In other words, the full moment tensor inverted from a large star-like surface array is very stable (especially

135

for the strike-slip type of mechanism, as shown by Staněk et al., 2014). Note that several literatures (e.g., Staněk et al., 2014; Eyre and van der Baan, 2017; Li et al., 2021) have shown that the non-DC components (CLVD and ISO) of inverted source mechanisms may be artificially increased by uncertainties in the inversion, including rupture directivity effects treated erroneously as a seismic noise. Therefore, the DC component higher than for the initially inverted solution can be considered as an improvement. Nevertheless, the variance reduction of 86% is comparable to the solution inverted from the amplitudes not corrected for directivity results.

Conclusions

We approached the subject of the doctoral thesis from two directions: forward modelling of wavefields in attenuative media and estimation of attenuation from real datasets. First, we implemented Weak Attenuation Concept (WAC) using the correspondence principle into ray-based program package ANRAY that allows now computation of synthetic seismograms in layered, attenuative, isotropic and anisotropic media. Benchmark, with independent full-wave method showed that WAC provides satisfactory results for attenuation encountered in the Earth's crust studies. The problem of reflection/transmission at the interface between two attenuative layers has been studied by many authors without concluding results. Therefore, for tests of WAC, we choose the simplest case of SH-SH reflection/transmission in isotropic media. Using WAC, we have found expressions for reflection/transmission coefficients in attenuative media that were implemented in the program package SEIS. Package SEIS is designed for 2D computations of seismic wavefields in isotropic layered structures with laterally varying velocities. Tests that we have performed indicate that the use of correspondence principle is in certain cases problematic. The problems occur in the overcritical region for models with $\beta 1 < \beta 2$ and $Q_1 < Q_2$. In these cases, use of the correspondence principle leads to propagation vectors of the transmitted wave pointing back to the first layer and moduli of reflection/transmission coefficients exceeding maximum physically possible values. In these cases, we have proposed artificial modification of the formulae for reflection/transmission coefficients, which provides acceptable results. However, it is done at the costs of the violation of the equation of motion and Snell's law constraints.

We have performed number of tests, which included comparison of coefficients calculated with derived formulae and results obtained by independent method, which was not based on the use of the correspondence principle. We calculated seismograms using frequency dependent and frequency independent (calculated at the reference frequency) reflection/transmission coefficients in different attenuation models. We have also made comparison of seismograms

computed with ray method with seismograms computed using full-wave method. Our tests showed that:

-the influence of attenuation on the reflection/transmission coefficients at the interface between two attenuative media is negligible outside the critical region. In the critical region, where ray method does not provide correct results anyway, the effects of the attenuation are noticeable, but still they are much smaller than the effects of attenuation on propagation inside attenuative medium.

-the reflection/transmission coefficients are only weakly frequency dependent which dramatically simplifies ray computations in layered media.

-transmitted waves in attenuative media are inhomogeneous. Our tests showed that ignoring the inhomogeneity of transmitted waves, which cannot be calculated using ray method, does not affect in significant way the accuracy of the ray seismograms when compared with full-wave benchmark.

We have shown that the WAC implemented in the ray method can be applied in layered media even for relatively low values of Q. This implies that ray method with WAC can be used in modeling of wavefields in majority of realistic models. The full-wave method used for comparisons can only deal with isotropic models. Nevertheless, in both isotropic and anisotropic cases, a crucial quantity in determination of attenuation effect is global absorption factor t^*, therefore modelling of attenuation effects on waves in isotropic and anisotropic media is in principle very similar. Our tests indicate, that modified version of ANRAY will be applicable not only to isotropic, but also anisotropic models. This opens a possibility of performing detailed studies of realistic, attenuative media by the ray method.

Second part of the dissertation focuses on the estimation of attenuation from real datasets. We showed that due to the similarity of the shape of source spectra of earthquakes, peak frequencies of waves excited by microseismic events can be used to estimate total effect of attenuation described by the global absorption factor t^*. Knowledge of t^* allows us to determine effective (averaged) Q of the medium. t^* can be also used in detailed studies of attenuation of investigated medium, including

138

attenuation tomography. We have presented the analysis of the attenuation performed using peak frequencies on three datasets.

We have successfully applied peak frequency method to the dataset from West Bohemia where natural seismic swarms occur. We used the data recorded during 2008 swarm to evaluate attenuation in West Bohemia. Besides estimating effective values of Q_P and Q_S in the whole region, we performed the analysis, which allowed us to determine local Q_P and Q_S values in the source area. We have shown, that attenuation in the source area is stronger than in the surrounding medium, which is likely caused by presence of cracks in the focal zone and possible influence of fluids of lower crust/upper mantle origin. The influence of fluids is probable cause of seismic swarms in the region. We have also shown that during the swarm, the effective Q in the region decreased which further supports the role of fluids in the region.

Another dataset from High Agri Valley in South Italy included recordings of microseismic events that were induced by wastewater injection. Determined values of effective Q_P have shown anomaly in the vicinity of the injection well. The presence of anomaly was supported by analysis of the V_P/V_S ratio in the region. The anomaly is likely due to the influence of wastewater injection and its varying volume and pressure. Partial saturation can help to explain unusually low P- to S-wave attenuation ratio ($Q_P/Q_S<1$) found in the vicinity of the injection well. Combining analysis of V_P/V_S ratio and attenuation provides improved picture of the medium in the region.

Last dataset that we analyzed was acquired during hydraulic stimulation of shales in North China. Single event was recorded by the star-like array with high number of receivers. Analysis of spatial distribution of peak frequencies of P-wave arrivals combined with analysis of source mechanism indicated that recorded peak frequencies were controlled by combined effects of attenuation and source properties. The spatial distribution of peak frequencies revealed presence of source directivity. Analysis of peak frequencies allowed us to uniquely determine the fault plane of the event and rupture direction. Our results indicate that the event had fast,

possible supershear rupture. Despite peak frequencies not being solely controlled by attenuation, we were able to estimate the minimum value of Q in the region.

Studies of real datasets have shown that attenuation is important factor in studies that include microseismic data. Attenuation provides useful insight into medium properties, but also can be helpful in analysis of the source properties of analyzed events. Analysis of peak frequencies of waves excited by microseismic events is relatively simple, but robust method in estimation of attenuation that is often more suitable than analysis of amplitudes of arrivals.

References

Abercrombie, R.E. (1995). Earthquake source scaling relationships from M_L -1 to 5 using seismograms recorded at 2.5-km depth, *Journal of Geophysical Research*, 100(B12), 15-36, doi: 10.1029/95JB02397

Adam, L., Batzle, M., Lewallen, K. and van Wijk, K. (2009). Seismic wave attenuation in carbonates, *Journal of Geophysical Research: Solid Earth*, 114(B6), doi: 10.1029/2008JB005890.

Ameri, G., Martin, Ch. and Oth, A. (2020). Ground-Motion Attenuation, Stress Drop, and Directivity of Induced Events in the Groningen Gas Field by Spectral Inversion of Borehole Records, *Bulletin of the Seismological Society of America*, 110(5), 2077-2094, doi: 10.1785/0120200149.

Aki, K., and P. G. Richards (2002). Quantitative seismology, 2nd ed. (pp.491-534), University Science Books.

Ammon, Ch. J., Velasco, A. A., Lay, T. (1993). Rapid estimation of rupture directivity: Application to the 1992 Landers (MS=7.4) and Cape Mendocino (MS=7.2), California earthquakes, *Geophysical Research Letters*, 20(2), 97-100, https://doi.org/10.1029/92GL03032.

Audet, A., Bostock, M., Christensen, N. and Peacock, M. (2009). Seismic evidence for overpressured subducted oceanic crust and megathrust fault sealing, *Nature*, 457, 76-78, doi: 10.1038/nature07650.

Bachura, M., T. Fischer (2015). Coda Attenuation Analysis in the West Bohemia/Vogtland Earthquake Swarm Area, *Pure and Applied Geophysics*, 173(2) 425-437, doi: 10.1007/s00024-015-1137-3.

Bachura, M., T. Fischer (2016). Detailed velocity ratio mapping during aftershock sequence as a toll to monitor the fluid activity within the fault plane, *Earth and Planetary Science Letters*, 453, 215-222, doi: 10.1016/j.epsl.2016.08.017.

Baisch, S, Vörös, R., Rothert, E., Stang, H., Jung, R. and Schellschmidt, R. (2010). A numerical model for fluid injection induced seismicity at Soultz-sous-Forêts, *International Journal of Rock Mechanics and Mining Sciences*, Volume 47(3), 405-413, doi: 10.1016/j.ijrmms.2009.10.001.

Balasco, M., Giocoli, A., Piscitelli, S., Romano, G., Siniscalchi, A., Stabile, T.A., Tripaldi, S., (2015). Magnetotelluric investigation in the High Agri Valley (southern Apennine, Italy), *Natural Hazards and Earth System Sciences*, 15(4), 843-852, doi: 10.5194/nhess-15-843-2015.

Bao, H. Xu, L., Meng, L., Ampuero, J.P., Gao, L. and Zhang, H. (2022). Global frequency of oceanic and continental supershear earthquakes, *Nature Geoscience*, 15, 942-949, doi: 10.1038/s41561-022-01055-5.

Beckwith, J., Clark, R. and Hodgson, L. (2017). Estimating frequency-dependent attenuation quality factor from prestack surface seismic data, *Geophysics*, 82(1), 011-022, doi: 10.1190/geo2016-0169.1.

Benjumea, B., Macau, A., Gabàs, A. and Figueras, S. (2016). Characterization of a complex near-surface structure using well logging and passive seismic measurements, *Solid Earth*, 7(2), 685-701, doi: 10.5194/se-7-685-2016.

Ben-Menahem, A. and Singh, S.J. (1981). Seismic waves and sources, Springer-Verlag, New York.

Bland, D. (1960). The theory of linear viscoelasticity. Pergamon Press, New York.

Borcherdt, R.D. (1977). Reflection and refraction of type IIS waves in elastic and anelastic media, *Bulletin of Seismological Society of America*, 67(1), 43–67, doi: 10.1785/BSSA0670010043.

Borcherdt, R.D. (2020). Viscoelastic waves and rays in layered media. Cambridge University Press, Cambridge.

Bräuer, K., Kämpf, H. and Strauch, G. (2003). Isotopic evidence (3HE/4HE, 13CCO2) of fluid triggered interpolate seismicity, *Journal of Geophysical Research*, 108(B2), ESE 3-1-ESE3-11, doi:10.1029/2002JB002077.

Bräuer, K., Kämpf, H. and Strauch, G. (2009). Earthquake swarms in non-volcanic regions: What fluids have to say, *Geophysical Research Letters*, 36(17), L17309, doi:10.1029/2009GL039615.

Bräuer, K., Kämpf, H., Koch, U. and Strauch, G. (2011). Monthly monitoring of gas and isotope compositions in the free gas phase at degassing locations close to the Nový Kostel focal zone in the western Eger Rift, Czech Republic, *Chemical Geolology*, 290(3-4), 163-173, doi: 10.1016/j.chemgeo.2011.09.012.

Brokešová, J. and Červený, V. (1998). Inhomogeneous plane waves in dissipative, isotropic and anisotropic media. Reflection/transmission coefficients, *Seismic waves in complex 3-D structures*, 7, 57–146.

Brune, J. N. (1970). Tectonic stress and spectra of seismic shear waves from earthquakes, *Journal of Geophysical Research*, 75(26), 4997–5009, doi: 10.1029/JB075i026p04997.

Buchen, P.W. (1971). Reflection, transmission and diffraction of SH-waves in linear viscoelastic solids, *Geophysical Journal of Royal Astronomical Society*, 25, 97–113, doi: 10.1111/j.1365-246X.1971.tb02333.x.

Buttinelli, M., Improta, L., Bagh, S. and Chiarabba, C. (2016). Inversion of inherited thrusts by wastewater injection induced seismicity at the Val d'Agri oilfield (Italy), *Scientific Reports*, 6, 37165, doi: 10.1038/srep37165.

Caffagni, E., Eaton, D., Jones, L. and van der Baan, M. (2016). Detection and analysis of microseismic events using a Matched Filtering Algorithm (MFA), *Geophysical Journal International*, 206(1), 644-658, doi: 10.1093/gji/ggw168.

Calderoni, G., Rovelli, A., Ben-Zion, Y. and Di Giovambattista, R. (2015). Along-strike rupture directivity of earthquakes of the 2009 L'Aquila, central Italy, seismic sequence, *Geophysical Journal International*, 203(1), 399-415, doi: 10.1093/gji/ggv275.

Caleap, M., Aristegui, C. and Angel Y.C. (2009). Effect of crack opening and orientation on dispersion and attenuation of antiplane coherent wave, *Geophysical Journal International*, 177(3), 1151-1165, doi: 10.1111/j.1365-246X.2009.04127.x.

Carcione, J.M. (2001). Wave fields in Real Media: Wave Propagation in Anisotropic, Anelastic and Porous Media, Pergamon, Amsterdam.

Carcione, J.M. and Helle, B.H. (2004). The physics and simulation of wave propagation at the ocean bottom, *Geophysics*, 69(3), 825-839, doi: 10.1190/1.1759469.

Carcione, J. M., Gei, D., Botelho, M. A. B., Osella, A. and de la Vega, M. (2006). Fresnel reflection coefficients for GPR-AVO analysis and detection of seawater and NAPL contaminants, *Near Surface Geophysics*, 4(4), 253-263, doi: 10.3997/1873-0604.2005049.

Carcione, J.M. (2014). Wave fields in real media: wave propagation in anisotropic, anelastic, porous and electromagnetic media. Handbook of Geophysical Exploration, 3rd edn., revised and extended, Oxford.

Castiello, A., Ren, Y., Greenwood, S., Martin, T., Luo, Z. and Buchan, I. (2015). Seismic imaging in gas obscured areas – Q anomaly detection and Q migration applied to broadband data, 77th EAGE Conference & Exhibition, Extended Abstract, Th N107 11, doi: 10.3997/2214-4609.201413252.

Chiarabba, C., Piccinini, D. and De Gori, P. (2009). Velocity and attenuation tomography of the Umbria Marche 1997 fault system: Evidence of a fluid-governed seismic sequence, *Tectonophysics* ,476(1-2), 73-84, doi: 10.1016/j.tecto.2009.04.004.

Cipta, A., Cummins, P., Irsyam, M. and Hidati, S. (2018). Basin Resonance and Seismic Hazard in Jakarta, Indonesia, *Geosciences*, 8(4), 128, doi: 10.3390/geosciences8040128.

Cello, G., Tondi, E., Micarelli, L. and Mattioni, L. (2003). Active tectonics and earthquake sources in the epicentral area of the 1857 Basilicata earthquake (southern Italy), *Journal of Geodynamics*, 36(1-2), 37–50, doi: 10.1016/S0264-3707(03)00037-1.

Cesca, S., Grigoli, F., Heimann, S., Gonzalez, A., Buforn, E., Maghsoudi, S. and Dahm, T. (2014). The 2013 September-October seismic sequence offshore Spain: a case of seismicity triggered by gas injection?, *Geophysical Journal International*, 198(2), 941-953, doi: 10.1093/gji/ggu172.

Chen, H., He, X., Yang, H. and Zhang, J. (2021). Fault-Plane Determination of the 4 January 2020 Offshore Pearl River Delta Earthquake and Its Implication for

Seismic Hazard Assessment, *Seismological Research Letters*, 92(3), 1913-1925, doi: 10.1785/0220200232.

Clarke, H., Eisner, L., Styles, P. and Turner, P. (2014). Felt seismicity associated with shale gas hydraulic fracturing: The first documented example in Europe, *Geophysical Research Letters*, 41(23), 8308-8314, doi: 10.1002/2014GL062047.

Colavitti, L., Lanzano, G., Sgobba, S., Pacor, F., and Gallovič, F. (2022). Empirical Evidence of Frequency-Dependent Directivity Effects from Small-to-Moderate Normal Fault Earthquakes in Central Italy, *Journal of Geophysical Research: Solid Earth*, 127(6), e2021JB023498, doi: 10.1029/2021JB023498.

Colella, A. (2014). Anomalous deep waters gurgling to the surface and impacting soils in the Val d'Agri oil field, southern Italy, International Journal of *Ecosystems and Ecology Science*, 4(4), 533-542.

Červený, V. (2001). Seismic ray theory. Cambridge University Press, Cambridge, United Kingdom.

Červený, V., and Pšenčík, I. (1984). Documentation of earthquake algorithms. SEIS83 - Numerical modeling of seismic wave fields in 2-D laterally varying layered structures by the ray method, E.R.Engdahl edit., Report SE-35, Boulder, 36–40.

Červený, V. and Pšenčík, I. (2005). Plane waves in viscoelastic anisotropic media—I. Theory, *Geophysical Journal International*, 161(1), 197-212, doi: 10.1111/j.1365-246X.2005.02589.x.

Červený, V. and Pšenčík, I. (2008). Quality factor Q in dissipative anisotropic media, *Geophysics*, 73(4), 63-75. doi: 10.1190/1.2937173.

Daley, P.F. and Krebes, E.S. (2015). Anelastic (poroviscoelastic) medium - the SH-wave problem, *Journal of Seismic Exploration*, 24, 103–120.

Das, S. (2015). Supershear Earthquake Ruptures – Theory, Methods, Laboratory Experiments and Fault Superhighways: An Update. In: Ansal, A. (eds) Perspectives on European Earthquake Engineering and Seismology. Geotechnical, Geological and Earthquake Engineering, vol 39. Springer, doi: 10.1007/978-3-319-16964-4_1.

Dell'Aversana, P. (2003). Integration loop of 'global offset' seismic, continuous profiling magnetotelluric and gravity data, *First Break*, 21(11), 32–41, doi: 10.3997/1365-2397.2003019.

Delle Piane, C., Sarout, J., Madonna, C., Seanger, E.H., Dewhurst, D.N and Raven, M. (2014). Frequency-dependent seismic attenuation in shales: experimental results and theoretical analysis, *Geophysical Journal International*, 198(1), 504-515, doi: 10.1093/gji/ggu148.

Drwiła, M., Wcisło, M., Anikiev, D., Eisner, L. and Keller, R. (2019). Passive seismic measurement of seismic attenuation in Delaware Basin, *The Leading Edge*, 38(2), 138-143, doi: 10.1190/tle38020138.1.

Ebrom, D. (2004). The low-frequency gas shadow on seismic sections, *The Leading Edge*, 23(8), doi:10.1190/1.1786898.

Edwards, B., Kraft, T., Cauzzi, C., Kästli, P. and Wiemer, S. (2015). Seismic monitoring and analysis of deep geothermal projects in St. Gallen and Basel. Switzerland, *Geophysical Journal International*, 201(2), 1022–1039, doi: 10.1093/gji/ggv059.

Eisner, L., Abott, D., Barker, W., Lakings, J. and Thornton, M. (2008). Noise suppression for detection and location of microseismic events using a matched filter, SEG Technical Program Expanded Abstracts 2008, 1431-1435, doi: 10.1190/1.3059184.

Eisner, L., Husley, B.J., Duncan, P., Jurick, D., Wener, H. and Keller, W. (2010). Comparison of surface and borehole locations of induced seismicity, *Geophysical Prospecting*, 58(5), 809-820, doi: 10.1111/j.1365-2478.2010.00867.x.

Eisner, L., Williams-Stroud, A., Hill, P. Duncan, P. and Thornton, M. (2013). Beyond the dots in the box: Microseismicity-contrained fracture models for reservoir simulation, *The Leading Edge*, 29(3), 326-333, doi: 10.1190/1.3353730.

Eisner, L., Gei, D., Hallo, M., Opršal I. and Ali M.Y. (2013). The peak frequency of direct waves for microseismic events, *Geophysics* 78(6), A45-A49, doi: 10.1190/geo2013-0197.1.

Eisner, L., Gei, D., Hallo, M., Opršal, I. and Ali, M.Y. (2014). Reply to "The peak frequency of direct waves for microseismic events" (Leo Eisner, Davide Gei, Miroslav Hallo, Ivo Opršal, and Mohammed Y. Ali, Geophysics, 78(6), A45–A49, *Geophysics*, 79(4), X23–X25, doi: 10.1190/2014-0053.2.

Eisner, L. and Stanek, F. (2018). Microseismic data interpretation—what do we need to measure first?, First Break, 36(2), 55-58, doi: 10.3997/1365-2397.n0069.

Einziger, P. and Felsen, L. (1982). Evanescent waves and complex rays, *IEEE Transactions on Antennas and Propagation*, 30(4), 594-605, doi: 10.1109/TAP.1982.1142865.

Eyre, T. S., and van der Baan, M. (2017). The reliability of microseismic moment-tensor solutions: Surface versus borehole monitoring, *Geophysics*, 82(6), KS113–KS125, doi: 10.1190/geo2017-0056.1.

Faber, E., Horálek, J., Boušková, A., Teschner, M., Koch, U. and Poggenburg J. (2009). Continuous gas monitoring in the west bohemia earthquake area, Czech Republic: first results, *Studia Geophysica et Geodaetica*, 53(3), 315-328, doi: 10.1007/s11200-009-0020-z.

Furumura, T. and Koketsu, K. (1998). Specific distribution of ground motion during the 1995 Kobe earthquake and its generation mechanism, *Geophysical Research Letters*, 25(6), 785-788, doi: 10.1029/98GL50418.

Futterman, W.I. (1962). Dispersive body waves, *Journal Geophisical Research*, 67(11), 5279-5291, doi: 10.1029/JZ067i013p05279.

Fischer, T., and Horálek J. (2005). Slip-generated pattern of swarm microearthquakes from West Bohemia/Vogtland (central Europe): Evidence of their triggering mechanism?, *Journal of Geophysical Research*, 110(5), B05S21, doi:10.1029/2004JB003363.

Fischer, T., and Michálek J. (2008). Post 2000-swarm microearthquake activity in the principal focal zone of West Bohemia/Vogtland: space-time distribution and waveform similarity analysis, *Studia Geophysica et Geodaetica*, 52(4), 493-511, doi: 10.1007/s11200-008-0034-y.

Fischer, T., Horálek, J., Hrubcová, P., Vavryčuk, V., Bräuer, K. and Kämpf, H. (2014). Intra-continental earthquake swarms in West-Bohemia and Vogtland: a review, *Tectonophysics*, 611(6), 1-27, doi: 10.1016/j.tecto.2013.11.001.

Fischer. T., Heinicke, J., Matyska, C. and Vlcek, J. (2015). 2014 earthquake sequence in West Bohemia/Vogtland responsible for the sudden increase of CO_2 flow rate?, Geophysical Research Abstracts 17, EGU2015-8499-2.

Fischer. T., Matyska C. and Heinicke, J. (2017). Earthquake-enhanced permeability – evidence from carbon dioxide release following the M_L 3.5 earthquake

in West Bohemia, Earth *Planetary Science Letters*, 460(15), 60-67, doi: 10.1016/j.epsl.2016.12.001.

Folesky, J., Kummerow, J., Shapiro, S.A., Häring, M. and Asanuma, H. (2016). Rupture directivity of fluid-induced microseismic events: Observations from an enhanced geothermal system, *Journal of Geophysical Research: Solid Earth*, 121(11), 8034-8047, doi: 10.1002/2016JB013078.

Forghani-Arani, F., Behura, J., Haines, S. and Batzle, M. (2013). An automated cross-correlation based event detection technique and its application to a surface passive data set, *Geophysical Prospecting*, 61(4), 778-787, doi: 10.1111/1365-2478.12033.

Fuchs, K. and Müller, G. (1971). Computation of Synthetic Seismograms with the Reflectivity Method and Comparison with Observations, *Geophysical Journal International*, 23(4), 417-433, doi: 10.1111/j.1365-246X.1971.tb01834.x.

Gajewski, D. and Pšenčík, I. (1987). Computation of high-frequency seismic wavefield in 3-D laterally inhomogeneous media, *Geophysical Journal International*, 91(2), 383-411, doi: 10.1111/j.1365-246X.1987.tb05234.x.

Gajewski, D. and Psencik,I. (1992). Vector wave fields for weakly attenuating anisotropic media by the ray method, *Geophysics*, 57(1), 27-38, doi: 10.1190/1.1443186.

Giocoli, A., Stabile, T.A., Adurno, I., Perrone, A., Gallipoli, M.R., Gueguen, E., Norelli, E. and Piscitelli, S. (2015). Geological and geophysical characterization of the south-eastern side of the High Agri Valley (southern Apennines, Italy), *Natural Hazards and Earth System Sciences*, 15(2), 315-323, doi: 10.5194/nhess-15-315-2015.

Gladwin, M.T., Stacey, F. D. (1974). Anelastic degradation of acoustic pulses in rock, *Physics of the Earth and Planetary Interiors*, 8(4), 332-336, doi: 10.1016/0031-9201(74)90041-7.

Gregory, A., (1976). Fluid saturation effects on dynamic elastic properties of sedimentary rocks, *Geophysics*, 41, 895-921, doi: 10.1190/1.1440671.

Grigoli, F., Cesca, S., Priolo, E., Rinaldi, A.P., Clinton, J., Stabile, T.A., Dost, B., Garcia-Fernandez, M., Wiemer, S. and Dahm, T. (2017). Current challenges in monitoring, discrimination and management of induced seismicity related to

underground industrial activities: a European perspective, *Reviews of Geophysics*, 55(2), 310-340, doi: 10.1002/2016RG000542.

Grinsted, A., Moore, J.C. and Jevrejeva, S. (2004). Application of the cross wavelet transform and wavelet coherence to geophysical time series, *Nonlinear Proceedings of Geophysics*, 11(5/6), 561-566, doi: 10.5194/npg-11-561-2004.

Gueguen, E., Bentivenga, M., Colaiacovo, R., Margiotta, S., Summa, V. and Adurno, I. (2015). The Verdesca landslide in the Agri Valley (Basilicata, southern Italy): a new geological and geomorphological framework, *Natural Hazards and Earth System Sciences*, 15(11), 2585-2595, doi: 10.5194/nhess-15-2585-2015.

GURALP, CMG-3ESPC Seismometer: Datasheet, Retrieved from: https://www.guralp.com/documents/DAS-C3E-0001.pdf.

Guo, P. and McMechan, G. (2017). Sensitivity of 3D 3C synthetic seismograms to anisotropic attenuation and velocity in reservoir models, *Geophysics*, 82(2), T79-T95, doi: 10.1190/geo2016-0321.1.

Helle, H., Pham, N. and Carcione, J. (2003). Velocity and attenuation in partially saturated rocks: poroelastic numerical experiments, *Geophysical Prospecting*, 51(6), 551-566, doi: 10.1046/j.1365-2478.2003.00393.x.

Hallo, M. (2012). Microseismic surface monitoring network design – Sensitivity and accuracy. 74th EAGE Conference & Exhibition Extended Abstract, P021, doi: 10.3997/2214-4609.20148336.

Hainzl, S. and Fischer, T. (2002). Indications for a successively triggered rupture growth underlying the 2000 earthquake swarm in Vogtland/NW-Bohemia, *Journal of Geophysical Research*, 107(B12), ESE5-1-ESE 5-9, doi:10.1029/2002JB001865.

Han, D.H. and Batzle, M. (2004). Gassmann's equation and fluid-saturation effects on seismic velocities, *Geophysics*, 69(2), 398–405, doi: 10.1190/1.1707059.

Haskell, N.A. (1964). Total energy and energy spectra density of elastic waves from propagating faults, *Bulletine of Seismological Society of America*, 54(6a), 1811-1841, doi: 10.1785/BSSA05406A1811

Horálek, J., Boušková, A., Hampl, F. and Fischer, T. (1996). Seismic regime of the West-Bohemian earthquake swarm region: preliminary results, *Studia Geophysica et Geodaetica*, 40(4), 398-412, doi: 10.1007/BF02300767.

Horálek, J. and Fischer, T. (2008). Role of crustal fluids in triggering the West Bohemia/Vogtland earthquake swarms: just what we know (a review), *Studia Geophysica et Geodaetica*, 52(4) 455-478, doi:10.1007/s.11200-008-0032-0.

Hu, F., Oglesby, D.D., Chen, X. (2019). The sustainability of free-surface-induced supershear rupture on strike-slip faults, *Geophysical Research Letters*, 46(16) 9537-9543, doi: 10.1029/2019GL084318

Huang, G., Chen, X., Luo, C., Li, J. and Dai, H. (2018). AVA inversion based on the wave equation with attenuation compensation, SEG Technical Program Expanded Abstracts, 620-624, doi: 10.1190/segam2018-2994004.1.

Hudson, J., Pearce, R. and Rogers, R. (1989). Source type plot for inversion of the moment tensor, *Journal of Geophysical Research*, 94(B1), 765-774, doi: 10.1029/JB094iB01p00765.

Ide, S., Beroza, G.C, Prejean, S.G. and Ellsworth, W.L. (2003). Apparent break in earthquake scaling due to path and site effects on deep borehole recordings, *Journal of Geophysical Research*, 108(B5), 2271, doi: 10.1029/2001JB001617.

Improta, L., Valaroso, L., Piccinini, D. and Chiarabba, C. (2015). A detailed analysis of wastewater-induced seismicity in the Val d'Agri oil field (Italy), *Geophysical Research Letters*, 42(8), 1-9, doi: 10.1002/2015GL063369

Improta, L., Bagh, S., De Gori, P., Valoros, L., Pastori, M., Piccinini, D., Chiarabba, C., Anselmi, M. and Butinelli, M. (2017). Reservoir Structure and Wastewater-Induced Seismicity at the Val d'Agri Oilfield (Italy) Shown by Three-Dimensional Vp and Vp/Vs Local Earthquake Tomography, *Journal of Geophysical Research: Solid Earth*, 122(11), 9050-9082, doi: 10.1002/2017JB014725.

Jakobsen, M. and Hudson, J.H. and Johansen, T. (2003). T-matrix approach to shale acoustics, *Geophysical Journal International*, 154(2), 533-558, doi: 10.1046/j.1365-246X.2003.01977.x.

Jech, J. and Pšenčík, I. (1989). First-order perturbation method for anisotropic media, *Geophysical Journal International*, 99(2), 369–376, doi: 10.1111/j.1365-246X.1989.tb01694.x.

Jechumtálova, Z. and Eisner, L. (2008). Seismic source mechanism inversion from linear array of receivers reveal non-double-couple seismic events induced by

hydraulic fracturing in sedimentary formation, *Tectonophysics*, 460(1-4), 124-133, doi: 10.1016/j.tecto.2008.07.011.

Johnston, D., Toksoz, M. and Timur, A. (1979). Attenuation of seismic waves in dry and saturated rocks: II. Mechanisms, *Geophysics*, 44(4), 691-711, doi: 10.1190/1.1440970.

Lay, T. and Wallace, T.C. (1995). Modern global seismology, San Diego, Academic Press.

Lei, X. am Xue, Z. (2009). Ultrasonic velocity and attenuation during CO_2 injection into water-saturated porous sandstone: Measurements using difference seismic tomography, *Physics of the Earth and Planetary Interiors*, 176(3-4), 224-234, doi: 10.1016/j.pepi.2009.06.001.

Lengliné, O. and Got J.L. (2011). Rupture directivity of microearthquake sequences near Parkfield, California, *Geophysical Research Letters*, 38(8), doi: 10.1029/2011GL047303.

Lin, G., and Shearer, P. (2007). Estimating local V_p/V_s ratios within similar earthquake clusters, *Bulletin of the Seismological Society of America*, 97(2), 379-388, doi: 10.1785/0120060115.

Lucente, F., De Gori, P., Margheriti, L., Piccinini, D., Di Bona, M., Chiarabba, C. and Agostinetti, N. (2010). Temporal variation of seismic velocity and anisotropy before the 2009 M_W 6.3 L'Aquila earthquake, Italy, *Geology*, 38(11), 1015-1018, doi: 10.1130/G31463.1.

Kane, D.L., Shearer, P.M., Goerts-Allman, D.P. and Vernon, F.L. (2013). Rupture directivity of small earthquakes at Parkfield, *Journal of Geophysical Research: Solid Earth*, 118(1), 212-221, doi: 10.1029/2012JB009675.

Kaneko, Y. and Shearer P.M. (2015). Variability of seismic source spectra, estimated stress drop, and radiated energy, derived from cohesive-zone models of symmetrical and asymmetrical circular and elliptical ruptures, J*ournal of Geophysical Research: Solid Earth*, 120(2), 1053-1079, doi: 10.1002/2014JB011642.

Kelly, C.M., Rietbrock, A., Faulkner, D.R. and Nadeau, M.R. (2013). Temporal changes in attenuation associated with the 2004 M6.0 Parkfield earthquake, *Journal of Geophysical Research: Solid Earth*, 118(2), 630-645, doi: 10.1002/jgrb.50088g.

Kjartansson, E. (1979). Constant Q-wave propagation and attenuation. 10.1002/2014JB011642, *Journal of Geophysical Research: Solid Earth*, 84(B9), 4737-4748. doi: 10.1029/JB084iB09p04737.

Koch, U., and Heinicke, J. (2011). Seismohydrological effects related to the NW Bohemia earth- quake swarms of 2000 and 2008: similarities and distinctions, *Journal of Geodynamics*, 51(1), 44–52, doi: 10.1016/j.jog.2010.07.002.

Koketsu, K., Miyake, H., Guo, Y. et al. (2016). Widespread ground motion distribution caused by rupture directivity during the 2015 Gorkha, Nepal earthquake, *Scientific Reports*, 6, 28536, doi: 10.1038/srep28536.

Kolář, P., Petružálek, M., Lokajíček, T., Šílený, J., Jechumtálová, Z., Adamova, P. and Boušková, A. (2020). Acoustic Emission Events Interpreted in Terms of Source Directivity, *Pure and Applied Geophysics*, 177(2), 1-18, doi: 10.1007/s00024-020-02517-w.

Kravtsov, Y.A. and Orlov, Y.I. (1990). Geometrical optics of inhomogeneous media. Springer, New York.

Krebes, E.S. (1983). The viscoelastic reflection/transmission problem: two special cases, *Bulletin of the Seismological Society of America*, 73(6a), 1673–1683, doi: 10.1785/BSSA07306A1673

Krebes, E.S. and Daley, P.F. (2007). Difficulties with computing anelastic plane-wave reflection and transmission coefficients, *Geophysical Journal International*, 170(1), 205–216, doi: 10.1111/j.1365-246X.2006.03349.x

Kriegierowski, M., Cesca, S., Ohrnberger, M., Dahm, T. and Krueger, F. (2019). Event couple spectral ratio Q method for earthquake clusters: Application to northwest Bohemia, *Solid Earth*, 10(1), 317-328. doi: 10.5194/se-10-317-2019.

Kwiatek, G., Plenkers, K. and Dresen, G. (2011). Source parameters of pico-seismicity recorded at Mponeng Deep Gold Mine, South Africa: Impli-cations for Scaling Relations, *Bulletin of Seismological Society of America*, 101(6), 2592-2608, doi: 10.1785/0120110094.

Lay, T. and Wallace, T.C. (1995). Modern global seismology, San Diego: Academic Press.

Lei, X. and Xue, Z. (2009). Ultrasonic velocity and attenuation during CO_2 injection into water-saturated porous sandstone: Measurments using difference

seismic tomography, *Physics of the Earth and Planetary Interiors*, 176(3-4), 224-234, doi: 10.1016/j.pepi.2009.06.001.

Lengliné, O. and Got, J.L., (2011). Rupture directivity of microearthquake sequences near Parkfield, California, *Geophysical Research Letters*, 38(8), L0831, doi: 10.1029/2011GL047303.

Li, H., Chang, X.-B., Xie, X. and Wang, Y. (2021). Microseismic moment-tensor inversion and sensitivity analysis in vertically transverse isotropic media, *Geophysics*, 86(2), 1MA-W19, doi: 10.1190/geo2020-0098.1.

Lucente, F., De Gori, P., Margheriti, L., Piccinini, D., Di Bona, M., Chiarabba, C. and Agostinetti, N. (2010). Temporal variation of seismic velocity and anisotropy before the 2009 MW6.3 L'Aquila earthquake, Italy, *Geology*, 38(11), 1015-1018, doi: 10.1130/G31463.1.

Madariaga, R. and Olsen, K.B. (2000). Criticality of Rupture Dynamics in 3-D, *Pure and Applied Geophysics*, 157, 1981-2000, doi: 10.1007/PL00001071.

Málek, J., Horálek, J. and Janský, J. (2005). One-Dimensional qP-wave velocity model of the, upper crust for the West Bohemia/Vogtland earthquake swarm region, *Studia Geophysica et Geodaetica*, 49(4), 501-524, doi: 10.1007/s11200-005-00242.

Maschio, L., Ferranti, L. and Burrato, P. (2005). Active extension in Val d'Agri area, Southern Apennines, Italy: Implications for the geometry of the seismogenic belt, *Geophysical Journal International*, 162(2), 591–609, doi: 10.1111/j.1365-246X.2005.02597.x.

Matheney, M.P. and Nowack, R.L. (1995). Seismic attenuation values obtained from instantaneous-frequency matching and spectral ratios. *Geophysical Journal International*, 123(1), 1-15, doi: 10.1111/j.1365-246X.1995.tb06658.x.

Maxwell S.C., Rutledge J., Jones R. and Fehler M. (2010). Petroleum reservoir characterization using downhole microseismic monitoring, *Geophysics*, 75(5), 129-137, doi: 10.1190/1.3477966.

Mazzoli, S., Barkham, S., Cello, G., Gambini, R., Mattioni, L., Shiner, P. and Tondi, E. (2001). Reconstruction of continental margin architecture deformed by the contraction of the Lagonegro Basin, southern Apennines, Italy, *The Quaterly journal of the Geological Society of London*, 158, 309–319, doi: 10.1144/jgs.158.2.30.

Menardi Noguera, A., and Rea, G. (2000). Deep structure of the Campanian-Lucanian Arc (Southern Apennine, Italy), *Tectonophysics*, 324(4), 239–265, doi: 10.1016/S0040-1951(00)00137-2.

Michálek, J., and Fischer, T. (2013). Source parameters of the swarm earthquakes in West Bohemia/Vogtland, *Geophysical Journal International*, 195(2), 1196–1210, doi: 10.1093/gji/ggt286.

Mikhaltsevitch, V., Lebedev, M., Pervukhina, M. and Gurevich, B. (2020). Seismic dispersion and attenuation in Mancos shale - laboratory measurements, *Geophysical Prospecting*, 69(2), 568-585, doi: 10.1111/1365-2478.13056.

Moczo, P., Bard, P.Y. and Pšenčík, I. (1987). Seismic response of 2-Dabsorbing structures by the ray method, *Journal of Geophysics*, 62, 38–49(1).

Montone, P., Mariucci, M.T, Pondrelli, S. and Amato, A. (2004). An improved stress map for Italy and surrounding regions (central Mediterranean), *Journal of Geophysical Research*, 109(B10), B10410, doi: 10.1029/2003JB002703.

Mousavi, S., Haberland, C., Bauer, P., Hejrani, B. and M. Korn (2017). Attenuation tomography in West Bohemia/Vogtland, *Tectonophysics*, 695(B2), 64-75, doi: 10.1016/j.tecto.2016.12.010.

Morozov, I., B. (2014). Discussion and Reply: Source reverberations, near-surface resonances, or Q? Comment on "The peak frequency of direct waves for microseismic events" (Leo Eisner, Davide Gei, Miroslav Hallo, Ivo Opršal, and Mohammed Y. Ali, Geophysics 288 78, no. 6, A45–A49), *Geophysics*, 79(4), X19–25, doi: 10.1190/GEO2014-0053.1.

Morozov, I. (2020). mment on "Attenuation in West Bohemia: Evidence of High Attenuation in the Nový Kostel Focal Zone and Temporal Change Consistent with CO2 Degassing" by M. Wcisło, L. Eisner, J. Málek, T. Fischer, J. Vlček, and G. Kletetschka, *Bulletin of the Seismological Society of America*, 110(1), 368-374, doi: 10.1785/0120180143.

Moser, T.J. and Červený, V. (2007). Paraxial ray methods in anisotropic inhomogeneous media, *Geophysical Prospecting*, 55(1), 21–37, doi: 10.1007/s11200-009-0013-y.

Nickschick, T., Kämpf, H., Flechsig, C., Mrlina, J., and Heinicke, J. (2015). CO2 degassing in the Hartoušov mofette area, western Eger Rift, imaged by CO2 mapping

and geoelectrical and gravity surveys, *International Journal of Earth Science*, 104(8), 2107-2129, doi: 10.1007/s00531-014-1140-4.

Novotný, O., Málek, J. and Boušková, A. (2016). Wadati method as a simple tool to study seismically active fault zones: a case study from the West-Bohemia/Vogtland region, central Europe, *Studia Geophysica Geodaetica*, 60(2), 248-267, doi:10.1007/s11200-015-1206-1.

O'Connell, R. and Budiansky, B. (1977). Viscoelastic properties of fluid-saturated cracked solids, *Journal of Geophysical Research*, 82(36), 5719-5735, doi: 10.1029/JB082i036p05719

Pacor, F., Gallovič, F., Puglia, R., Luzi, L. and D'amico, M. (2016). Diminishing high-frequency directivity due to a source effect: Empirical evidence from small earthquakes in the Abruzzo region, Italy, *Geophysical Research Letters*, 43(10), 5000-5008, doi: 10.1002/2016GL068546.

Peacock, S., Christensen, N., Bostock, M. and Audet, P. (2011). High pore pressures and porosity at 35 km depth in the Cascadia subduction zone, *Geology*, 39(5), 471-474, doi: 10.1130/G31649.1.

Pham N., Carcione, J., Helle, H. and Ursin, B. (2002). Wave velocities and attenuation of shaley sandstones as function of pore pressure and partial saturation, *Geophysical Prospecting*, 50(6), 615-627, doi: 10.1046/j.1365-2478.2002.00343.x

Pischiutta, M., Pastori, M., Improta, L., Salvini, F., and Rovelli, A. (2014). Orthogonal relation between wavefield polarization and fast S wave direction in the Val d'Agri: An integrating method to investigate rock anisotropy, *Journal of Geophysical Research Solid Earth*, 119(1), 396-408, doi: 10.1002/2013JB010077.

Portier, S., and Vuataz (Eds), E.D. (2009). Studies and support for the EGS reservoirs at Soultz-sous-Forêts: Final report April 2004–May 2009, Project financed by State Secretariat for Education and Research (SER/SBF) and Swiss Federal Office of Energy (OFEN/BFE).

Prudencio, J., Ibáñez, J.M., Del Pezzo, E. and De La Siena, L. (2015). 3D Attenuation Tomography of the Volcanic Island of Tenerife (Canary Islands), *Surveys in Geophysics*, 36(5), 693–716, doi: 10.1007/s10712-015-9333-3.

Prudencio, J., De Siena, L., Ibanez, J., Del Pezzo, E., Garcia-Yeguas, A. and Diaz-Moreno, A. (2015). The 3D Attenuation Structure of Deception Island (Antarctica), *Surveys in Geophysics*, 36(3), 371-390, doi: 10.1007/s10712-015-9322-6.

Pšenčík, I., Wcisło, M. and Daley, P.F. (2022). SH plane-wave reflection/transmission coefficients in isotropic, attenuating media, *Journal of Seismology*, 26(1), 15-34, doi: 10.1007/s10950-021-10052-x.

Pšenčík, I., Wcislo, M. and Carcione, J. (2022). Comparison of ray and full-wave synthetic seismograms of reflected SH waves in attenuating media, *Seismic waves in complex 3-D structures*, 31, 55-68.

Quan, Y. and Harris, J.M. (1997). Seismic attenuation tomography using the frequency shift method, *Geophysics*, 62(3), 895-905, doi: 10.1190/1.1444197.

Rao, Y. and Wang, Y. (2019). Stabilised inverse-Q filtering for seismic characterization of carbonate reservoirs, Journal of Geophysics and Engineering, 16(1), 190-197, doi: 10.1093/jge/gxy016.

Richards, P.G. (1984). On wavefronts and interfaces in anelastic media, *Bulletin of the Seismological Society of America*, 74(6), 2157–2165, doi: 10.1785/BSSA0740062157.

Riguzzi, F., Crespi, M., Devoti, R., Doglioni, C., Pietrantonio, G. and Pisani, A.R. (2012). Geodetic strain rate and earthquake size: New clues for seismic hazard studies, *Physics of the Earth Planetary Interiors*, 206, 67–75, doi: 10.1016/j.pepi.2012.07.005.

Ross, Z.E., Trugman, D.T., Azizzadenesheli, K. and Anandkumar, A. (2020). Directivity modes of earthquake populations with unsupervised learning, Journal of *Geophysical Research: Solid Earth*, 125(2), 2019JB018299, doi: 10.1029/2019JB018299.

Rovida A., Locati, M., Camassi, R., Lolli, B. and Gasperini P., (2016). CPTI15, the 2015 version of the Parametric Catalogue of Italian Earthquakes: Istituto Nazionale di Geofisica e Vulcanologia.

Ross, Z.E., Trugman, D.T., Azizzadenesheli, K. and Anandkumar, A. (2020). Directivity modes of earthquake populations with unsupervised learning, *Journal of Geophysical Research: Solid Earth*, 125(2), doi: 10.1029/2019JB018299.

Rutledge, J.T and Phillips, W.S (2003). Hydraulic stimulation of natural fractures as revealed by induced microearthquakes, Carthage Cotton Valley gas field, east Texas, *Geophysics*, 68(2), 441-452, doi: 10.1190/1.1567214.

Ruud, B.O. (2006). Ambiguous reflection coefficients for anelastic media, *Studia Geophysica et Geodaetica*, 50(3), 479–498, doi: 10.1007/s11200-006-0030-z.

Schaff, D. and Richards, P.G. (2014). Improvements in magnitude precision, using the statistics of relative amplitudes measured by cross correlation, *Geophysical Journal International*, 197(1), 335-350, doi: 10.1093/gji/ggt433.

Seo, M., Kim, W., and Kim, Y. (2022). M_L 2.2 Gwangyang, Korea, Microearthquake: Toward Resolving High-Resolution Rupture Process of a Small Earthquake, *The Seismic Record*, 2(4), 227-236, doi: 10.1785/0320220030.

Shekar, B. and Tsvankin, I. (2014). Point-source radiation in attenuative anisotropic media, Geophysics, 79(5), WB25-WB34, doi: 10.1190/GEO2013-0417.1

Sidler, R. and Carcione, J.M. (2007). Wave reflection at an anelastic anisotropicocean bottom, *Geophysics*, 72(5), SM139–SM146, doi: 10.1190/1.2750423.

Sidler, R., Carcione, J. M., and Holliger, K. (2008). On the evaluation of the plane-wave reflection coefficients in anelastic media, *Geophysical Journal International*, 175(1), 94–102, doi: 10.1111/j.1365-246X.2008.03796.x.

Stabile, T. A., Giocoli, A., Perrone, A., Piscitelli, S. and Lapenna, V. (2014a). Fluid injection indeced seismicity reveals a NE dipping fault in the southeastern sector of the High Agri Valley (southern Italy), *Geophysical Research Letters*, 41(16), 5847-5854, doi: 10.1002/2014GL060948

Stabile, T. A., Giocoli, A., Lapenna, V., Perrone, A., Piscitelli, S. and Telesca, L. (2014b). Evidences of low-magnitude continued reservoir-induced seismicity associated with the Pertusillo artificial lake (southern Italy), *Bulletin of the Seismological Society of America*, 104(4), 1820-1828, doi: 10.1785/0120130333.

Staněk, F., Eisner, L. and Moser, T.J. (2014). Stability of source mechanism inverted from P-wave amplitude microseismic monitoring data acquired at the surface, *Geophysical Prospecting*, 62(3), 475-490, doi: 10.1111/1365-2478.12107.

Staněk, F. and Eisner, L. (2017). Seismicity Induced by Hydraulic Fracturing in Shales: A Bedding Plane Slip Model, *Journal of Geophysical Research: Solid Earth*, 122(10), 7812-7926, doi: 10.1002/2017JB014213.

Staněk, F., Eisner, L. and Vesnaver, A. (2017). Theoretical assessment of the full-moment tensor resolvability for receiver arrays used in microseismic monitoring, *Acta Geodynamica et Geomaterialia*, 14(2), 233-240, doi: 10.13168/AGG.2017.0006.

Shekar, B. and Tsvankin, I. (2012). Anisotropic attenuation analysis of crosshole data generated during hydraulic fracturing, *The Leading Edge*, 31(5), 588-593, doi: 10.1190/tle31050588.1.

Stabile, T.A., Giocoli, A., Perrone, A., Piscitelli, S. and Lapenna, V. (2014) Fluid injection induced seismicity reveals a NE dipping fault in the southeastern sector of the High Agri Valley (southern Italy), *Geophysical Research Letters*, 41(16), 5847-5854, doi: 10.1002/2014GL060948.

Shiner, P., Beccacini, A. and Mazzoli, S. (2004). Thin-skinned versus thick-skinned structural models for Apulian carbonate reservoirs: Constraints from the Val d'Agri Fields, S Apennines, Italy, *Marine and Petroleum Geology*, 21(7), 805–827, doi: 10.1016/j.marpetgeo.2003.11.020.

Takam Takougang E.M. and Calver A.J. (2012). Seismic velocity and attenuation structures of the Queen Charlotte Basin from full-waveform tomography of seismic reflection data, *Geophysics*, 77(3), B107-B124, doi: 10.1190/geo2011-0243.1.

Tarantola, A. (2005). Inverse Problem Theory and Methods for Model Parameter Estimation. SIAM: Society for Industrial and Applied Mathematics, doi: 10.1137/1.9780898717921.

Tisato, N., and Madonna, C. (2012). Attenuation at low seismic frequencies in partially saturated rocks: Measurements and description of a new apparatus, *Journal of Applied Geophysics*, 86, 44–53, doi: 10.1016/j.jappgeo.2012.07.008.

Tisato, N., Quintal, B., Chapman, S., Podladchikov, Y. and Burg J.P. (2015). Bubbles attenuate elastic waves at seismic frequencies: First experimental evidence, *Geophysical Research Letters*, 42(10), 3880-3887, doi:10.1002/2015GL063538.

Tomic, J., Abercrombie, R.E. and Do Nascimiento A.F. (2009). Source parameters and rupture velocity of small M≤ 2.1 reservoir induced earthquakes,

Geophysical Journal International, 179(2), 1013-1023, doi: 10.1111/j.1365-246X.2009.04233.x.

Toksöz, M., Johnston, D. and Timur, A. (1979). Attenuation of seismic waves in dry and saturated rocks: I. Laboratory measurments, *Geophysics*, 44(4), 681-690, doi: 10.1190/1.1440969.

Thomson, C.J. (1997). Complex rays and wave packets for decaying signals in inhomogeneous, anisotropic and anelastic media, *Studia Geophysica et Geodaetica*, 41, 345–381, doi: 10.1023/A:1023359401107.

Tonn, R. (1989). Comparison of seven methods for the computation of Q, *Physics of the Earth and Planetary Interiors*, 55(3-4), 259-268, doi: 0.1016/0031-9201(89)90074-5.

Tselentis, G., Paraskevopoulos, P. and Martakis, N. (2010). Intrinsic Q_P seismic attenuation from the rise time of microearthquakes: a local scale application at Rio-Antirrio, Western Greece, *Geophysical Prospecting*, 58(5), 845-859, doi: 10.1111/j.1365-2478.2010.00885.x.

Turrini, C., and Rennison, P. (2004). Structural style from the Southern Apennines' hydrocarbon province – An integrated view: in K. R. McClay, ed., Thrust tectonics and hydrocarbon systems: AAPG Memoir, 82, 558–578.

Ursin, B. and Toverud, T. (2002). Comparison of seismic dispersion and attenuation models, *Studia Geophysica et Geodaetica*, 46(2), 293-320, doi: 10.1023/A:1019810305074.

Valaroso, L., Improta, L., Chiaraluce, L., Di Stefano, R., Ferranti, L., Govoni, A. and Chiarabba, C. (2009). Active faults and induced seismicity in the Val d'Agri region (southern Apennines, Italy), *Geophysical Journal International*, 178, 488-502, doi: 10.1111/j.1365-246X.2009.04166.x

van Eck, T., Goutbeek, F., Haak, H. and Dost, B. (2006). Seismic hazard due to small-magnitude, shallow-source, induced earthquakes in The Netherlands, *Engineering Geology*, 87(1-2), 105-121, doi: 10.1016/j.enggeo.2006.06.005.

van Thienen-Visser, K. and Breunese, J.N. (2015). Induced seismicity of the Groningen gas field: History and recent developments, *The Leading Edge*, 34(6), 664-671, doi: 10.1190/tle34060664.1.

Vavryčuk, V. (2007). Ray velocity and ray attenuation in homogeneous anisotropic viscoelastic media, *Geophysics*, 72(6), D119-D127, doi: 10.1190/1.2768402.

Vavryčuk, V. (2010) Behaviour of rays at interfaces in anisotropic viscoelastic media, *Geophysiscal Journal International*, 181, 1665–1677.

Vlček, J., Fischer, T. and Heinicke J. (2016). Carbon-dioxide flow measurement in geodynamically active area of West Bohemia, *Geophysical Research Abstracts*, 18, EGU2016-8088.

Wadati, K. (1933a) On the travel time of earthquake waves. Part II, *The Geophysical Magazine*, 7, 101–111.

Wadati, K. (1933b) On the travel time of earthquake waves. Part II, *The Geophysical Magazine*, 7, 113–137.

Walsh, R., and Zoback, M.D. (2015). Oklahoma's recent earthquakes and saltwater disposal, *Science Advances*, 1(5), e1500195, doi: 10.1126/sciadv.150019

Walls J., Taner, M.T, Uden, R., Singleton, S., Derzhi, N., Mavko, G. and Dvorkin, J. (2006). Novel Use of P- and S-wave Seismic Attenuation for Deep Natural Gas Exploration and Development, Final Report, Rock Solid Images, DE-FC26-04NT42243.

Wandycz, P., Święch, E., Eisner, L., Pasternacki, A., Wcisło, M. and Maćkowski, T. (2019). Estimation of the quality factor based on the microseismicity recordings from Northern Poland, *Acta Geophysica*, 67(4), 2005-2014, doi: 10.1007/s11600-019-00362-7.

Wang, D., Mori, J. and Koketsu, K. (2016). Fast Rupture Propagation for Large Strike-slip Earthquakes, *Earth and Planetary Science Letters*, 440, 115-126, doi: 10.1016/j.epsl.2016.02.022

Wcisło, M. and Eisner, L. (2016). Attenuation from microseismic datasets by the peak frequency method benchmarked with the spectral ratio method, *Studia Geophysica et Geodaetica*, 60 547-564, doi: 10.1007/s11200-015-0577-7.

Wcisło, M. and Pšenčík, I. (2017). Seismic waves in inhomogeneous, weakly dissipative, anisotropic media; preliminary tests with P waves, *Seismic Waves in Complex 3-D Structures*, 27, 83-92.

Wcisło, M. (2018). Effects of attenuation, velocity and density on SH-wave reflection/transmission coefficients in isotropic, weakly attenuating media, *Seismic waves in complex 3-D structures*, 28, 113-134.

Wcisło, M. and Eisner, L. (2018). Assessment of Possibility of Performing 1D Attenuation Tomography from Induced Microseismicity, 81st EAGE Conference and Exhibition 2019, doi: 10.3997/2214-4609.201900790

Wcisło, M., Eisner, L., Málek, J., Fischer, T., Vlček, J. and Kletetschka. G. (2018). Attenuation in West Bohemia: Evidence of high attenuation in the Nový Kostel focal zone and temporal change consistent with CO_2 degassing, *Bulletin of the Seismological Society of America*, 108(1), 450–458, doi: 10.1785/0120170168.

Wcisło, M., Stabile, T.A., Telesca, L. and Eisner, L. (2018). Variations of attenaution and V_P/V_S ratio in the vicinity of wastewater injection: a case study of Costa Molina 2 well (High Agri Valley, Italy), *Geophysics*, 83(2), B25-B31, doi: 10.1190/geo2017-0123.1.

Wcisło, M. and Eisner, L. (2019). Fast Determination of Attenuation From Microseismicity for Large Datasets, *Acta Geodynamica et Geomaterialia*, 16(3), 257-268, doi: 10.13168/AGG.2019.0022.

Wcisło, M., Eisner, L., Málek, L., Fischer, T., Vlček, J. and Kletetschka, G. (2020). Reply to "Comment on 'Attenuation in West Bohemia: Evidence of High Attenuation in the Nový Kostel Focal Zone and Temporal Change Consistent with CO_2 Degassing' by M. Wcisło, L. Eisner, J. Málek, T. Fischer, J. Vlček, and G. Kletetschka" by Morozov, *Bulletin of the Seismological Society of America*, 110 (1), 375–380, doi: 10.1785/0120190100.

Weinlich F.H., Bräuer, K., Kämpf, H., Strauch, G., Tesar, J. and Weise, S.M. (1999). An active subcontinental mantle volatile system in the western Eger rift, Central Europe: gas flux, isotopic (He, C, and N) and composi- tional fingerprints, *Geochimica et Cosmochimica Acta*, 63(21), 3653–3671, doi: 10.1016/S0016-7037(99)00187-8.

Wu, S., Wang, Y. and Chang, X. (2017). Microseismic source locations with deconvolution migration, *Geophysical Journal International*, 212 (3), 2088-2115, doi: 10.1093/gji/ggx518.

Wüstefeld, A., Lecomte, I., Oye, V., Kühn, D. and Kværna, T. (2014). Quantitative network design optimization, 5th EAGE Passive Seismic Workshop, doi: 10.3997/2214-4609.20142171.

Yoshida, K. (2019). Prevelance of assymetrical rupture in small earthquakes and its effect on the estimation of stress drop: a systematic investigation in inland Japan, *Geoscience Letters*, 6, 16, doi: 10.1186/s40562-019-0145-z.

Zhang, Z. and Stewart, R.R. (2008). Seismic attenuation and well log analysis in a heavy oilfield, SEG Technical Program Expanded Abstracts 2008, doi: 10.1190/1.3059251.

Zhu Y.P. and Tsvankin I. (2007). Plane-wave attenuation anisotropy in orthorhombic media, *Geophysics*, 72(1), D9–D19, doi: 10.1190/1.2387137.

Zhu, T., Ajo-Franklin, J.B. and Daley, J.M. (2017). Spatiotemporal changes of seismic attenuation caused by injected CO_2 at the Frio-II pilot site, Dayton, TX, USA, *Journal of Geophyical Research: Solid Earth*, 122(9), 7156-7171, doi: 10.1002/2017JB014164.

Zolezzi, F., Morasca, P., Mayeda, K., Phillips, W. and Eva, C. (2008). Attenuation tomography of the Southern Appenines (Italy), *Journal of Seismology*, 12(3), 355-365, doi: 10.1007/s10950-007-9079-6.